UNIVERSITA' DEGLI STUDI DI NAPOLI

"FEDERICO II"

FACOLTA' DI FARMACIA

DIPARTIMENTO DI CHIMICA FARMACEUTICA E TOSSICOLOGICA

DOTTORATO DI RICERCA IN SCIENZA DEL FARMACO

XXIV CICLO

Interaction of peptides and small molecules with biological targets

Coordinatore
Chiar.ma Prof.ssa
MARIA VALERIA D'AURIA

Supervisore
Chiar.mo Prof.
ALFONSO CAROTENUTO

Candidato
DIEGO BRANCACCIO

CONTENTS

Abstract

During my PhD course, I focused my attention on the conformational analysis of peptides that interact with GPCR and ligand-receptor interactions from NMR spectroscopy with possible application to cytotoxic agents binding to DNA.

In particular, I investigated the conformational behaviour of peptide analogues of Urotensin, Melanocortin and Somatostatin in water solution and membrane mimetic environment (SDS and DPC micelles).

Another research field was the NMR-based screening as potent technique for the identification of small molecules that interact with macromolecule targets. Several methods based on the ligand observation have been proposed in the literature, among these WaterLOGSY (water-ligand observed via gradient spectroscopy), and STD-NMR (saturation transfer difference) experiments. I applied these NMR techniques for the evaluation of the DNA interactions of a new series of thiophen-naphthoquinones with interesting cytotoxic activity.

Abbreviations

Abbreviations used for amino acids and designation of peptides follow the rules of the IUPAC-IUB Commission of Biochemical Nomenclature in *J. Biol. Chem.* 1972, *247*, 977-983. Amino acid symbols denote L-configuration unless indicated otherwise. The following additional abbreviations are used:

1D, 2D and 3D, one-, two- and three-dimensional;
ACTH, adreno-corticotropic hormone;
AGRP, agouti-related protein;
Boc, tert-butyloxycarbonyl;
Bzl, benzyl;
cAMP, Cyclic adenosine monophosphate;
Cpa, p-chloro-phenylalanine;
DBU, 1,8-Diazabicyclo(5.4.9)undec-7-ene;
DCM, dichloromethane;
DF, differential frequency;
dh-DSA- N, dehydrodiaminosuberic acid, N-terminus;
dh-DSA-C, dehydrodiaminosuberic acid, C-terminus;
DIPEA, *N,N*-diisopropylethyl-amine;
DMF, *N,N*dimethylformamide;
DMSO, dimethylsulfoxide;
DOTA, 1,4,7,10-tetraazacyclododecane-1,4,7,10-tetraacetic acid; EDT, 1,2-ethanedithiol;
DPC, dodecyl phosphocholine;
DQF-COSY, double quantum filtered correlated spectroscopy;
EL, extracellular loop;
EM, energy minimization;
ESI-MS, electrospray ionization-mass spectrometry;
Fmoc, 9-fluorenylmethoxycarbonyl;
GH, growth hormone; Hag, L-2-allyl-Gly;
GPCR, G-protein-coupled receptor;
HATU, exafluorophosphate salt of the O-(7-Azabenzotriazol-yl)-tetramethyl uranium cation (this acronym does not longer correspond to the true structure);
HBTU, 2-(1*H*-benzotriazole-1-yl)-1,1,3,3-tetramethyluronium hexafluorophosphate;
h-MCR, *human* Melanocortin Receptor;
HOBt, *N*hydroxy-benzotriazole;
*h*U-II, human Urotensin-II peptide;

h-UTR, human Urotensin II receptor;
IL, intracellular loop;
LC, liquid chromatography;
MD, molecular dynamic;
MSH, melanocyte stimulating hormones;
MW, molecular weight;
Nal, Naphtylalanine;
NMM, N-methyl morpholine;
NMR, nuclear magnetic resonance;
NOE, nuclear Overhauser effect;
NOESY, nuclear Overhauser enhancement spectroscopy;
Orn, Ornitine;
PE COSY, primitive exclusive correlated spectroscopy;
Pen, penicillamine;
POMC, proopiomelanocortin;
RCM, ring closing metathesis;
RMSD, root mean square deviation;
ROESY, rotating-frame Overhauser effect spectroscopy;
RP-HPLC, reverse phase-high performance liquid chromatography; SPE, Solid Phase Extraction;
r-UTR, rat Urotensin II receptor;
SAR, Structure activity relationship;
SD, standard deviation;
SDS, sodium dodecylsulphate;
SPPS, solid phase peptide synthesis;
SRIF, somatostatin; sst, somatostatin receptor;
STD, saturation transfer difference;
TES, triethylsilane;
TFA, trifluoroacetic acid;
THF, tetrahydrofuran;
Tic, tetrahydroisoquinoline;
TLC, thin-layer chromatography;
TM, trans-membrane domain;
TOCSY, total correlated spectroscopy;
TSP, 3-(trimethylsilanyl)propionic acid;
U-II, Urotensin-II peptide;
WaterLOGSY, water-ligand observed via gradient spectroscopy.

Chapter 1 - CONFORMATIONAL ANALYSIS OF PEPTIDES THAT INTERACT WITH GPCR

1.1 New Insight into the Binding Mode of Peptide Ligands at Urotensin-II Receptor: Structure-Activity Relationships Study on P5U and Urantide

Urotensin II (U-II) is a disulfide bridged peptide-hormone identified as the ligand of a G protein-coupled receptor. Human U-II (H-Glu-Thr-Pro-Asp-c[Cys-Phe-Trp-Lys-Tyr-Cys]-Val-OH) has been described as the most potent vasoconstrictor compound identified to date.

We have recently identified both a superagonist of *h*U-II termed P5U (H-Asp-c[Pen-Phe-Trp-Lys-Tyr-Cys]-Val-OH) and the compound termed Urantide (H-Asp-c[Pen-Phe-DTrp-Orn-Tyr-Cys]-Val-OH), which is the most potent UT receptor peptide antagonist described to date.

In the present study, we have synthesized several analogues of P5U and Urantide in which the Asp^4 residue in N-terminus position was replaced with coded and non-coded amino acids. The replacement of the Asp^4 residue by Tic led to an analogue, compound **14**, more potent as antagonist (pK_B = 8.94) compared to Urantide. Furthermore, a different SAR was observed for the P5U compared to the Urantide analogues. NMR and docking studies revealed a different binding

mode for the agonist and antagonist ligands which could explain the observed SAR.

1.1.1. Introduction

Urotensin-II (U-II) is a cyclic peptide originally isolated from goby fish urophysis.[1] Subsequently, it has been found that U-II is also present in tetrapods and that its gene is expressed in the CNS.[2] The U-II precursor has now been cloned in various vertebrate species including frog, rat and mouse, pig, monkey, and human.[3-6] U-II was identified as the natural ligand of an orphan G-protein-coupled receptor [7] now referred to as UT receptor.

Recently, an analogue of U-II, called urotensin-related peptide (URP), has been identified in mammals.[8] In all U-II and URP isoforms known so far, the sequence of the cyclic C-terminal hexapeptide has been fully conserved across species.[9] The U-II and URP genes are primarily expressed in motoneurons located in discrete brainstem nuclei and in the ventral horn of the spinal cord.[10-13] U-II and URP mRNAs have also been detected, although at a much lower level, in various peripheral tissues including the pituitary, heart, spleen, thymus, pancreas, kidney, small intestine, adrenal, and prostate.[3, 8, 14]

The U-II/UT receptor system seems to play an important role in cardiovascular functions; in fact, *h*U-II has been shown to be 1-2 orders of magnitude more potent than endothelin-1 in producing vasoconstriction in mammals and thus is one of the most effective

vasoconstrictor compounds identified to date.[7, 15, 16] On the basis of its spectrum of activities, *h*U-II has been postulated to contribute as modulator to cardiovascular homeostasis and possibly to be involved in certain cardiovascular pathologies.[15, 17] It has been recently demonstrated that U-II is involved in inhibition of insulin release [18] in the perfused rat pancreas and may play an important role in pulmonary hypertension.[19] Central nervous effects of U-II have also been described.[20] Hence, the *h*U-II ligands could be of therapeutic value in a number of pathological disorders. It has been demonstrated that the C-terminal octapeptide of U-II retains full biological activity and binding properties.[21-26]

The (patho)physiological role(s) of the U-II/UT receptor system and, most importantly, the potential interest of UT receptor ligands as drug candidates prompted the development of low molecular weight compounds as non peptide UT receptor agonists and antagonists (Figure 1).[27]

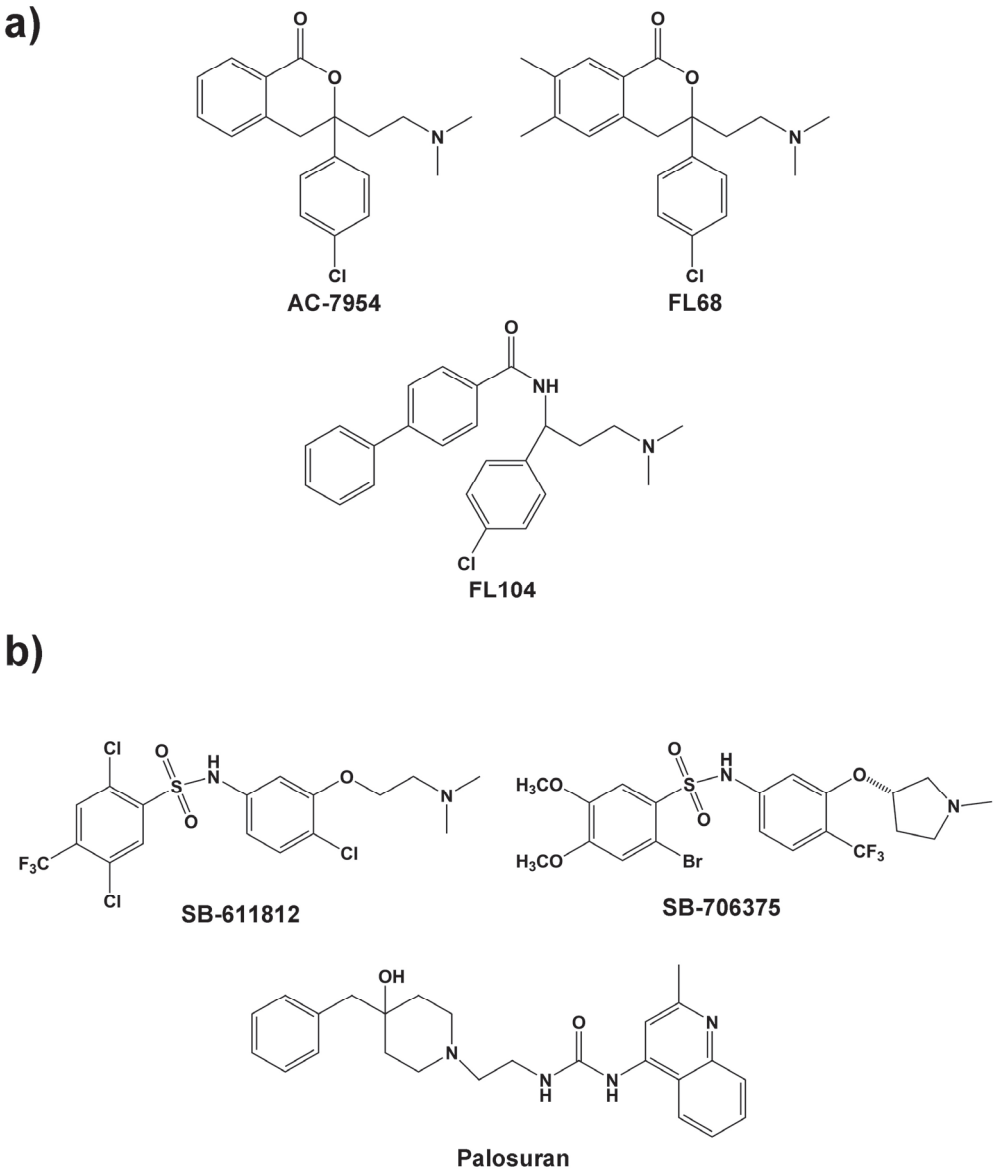

Figure 1. Some representative structures of non-peptide UTR agonists (a), and antagonists (b).

Our research group has been involved for a long time in the development of UTR peptide ligands. The optimization of a peptide as a lead structure is important to improve its pharmacokinetic properties, and in identifying the pharmacophore elements, that is, to determine the key amino acid residues that are involved in the

biological activity.[28] Interestingly, some common features are observable (two aryl moieties and a protonable nitrogen atom) in organic and peptide UTR ligands.[29] Hence, the structural information obtained by the peptide investigation might be useful for the design of both small-molecules and peptide ligands.

In previous studies, we have identified both a superagonist named P5U (H-Asp-c[Pen-Phe-Trp-Lys-Tyr-Cys]-Val-OH) [30] and an antagonist, Urantide (H-Asp-c[Pen-Phe-DTrp-Orn-Tyr-Cys]-Val-OH) [31] of *h*U-II. The latter is the most potent peptide antagonist at UT receptor described to date. Actually, Urantide behaves as a pure antagonist in the rat aorta bioassay,[31] and as a full agonist in a calcium mobilization assay performed in CHO cells expressing the *h*-UTR.[32] This point has been widely discussed elsewhere.[33] For sake of simplicity, we will refer to Urantide as an antagonist throughout the manuscript.

Recently, we performed extensive NMR and computational studies on both P5U and Urantide that allowed us to formulate a hypothesis about the structural changes that determine the switching from agonist to antagonist activity.[33, 34]

To aim to identify new leads for the development of both agonists and antagonists at UT receptor, we have studied the structure-activity relationships of a series of novel P5U and Urantide analogues based

on the chemical substitution of the Asp^4 residue, with several other amino acid residues with different physicochemical properties (Figure 2 and Figure S1). The most interesting analogues were then analysed by NMR and their structures fitted within *h*-UTR models to gain insight into the agonist and antagonist binding modes.

1.1.2 Results

Chemistry. Peptides were synthesized according to the solid phase approach using standard Fmoc methodology in a manual reaction vessel (Experimental Section). [35]

The purification was achieved using a semi-preparative RP-HPLC C-18 bonded silica column (Vydac 218TP1010). The purified peptide was 98% pure as determined by analytical RP-HPLC. The correct molecular weight of the peptide was confirmed by mass spectrometry and amino acid analysis (Supporting Information).

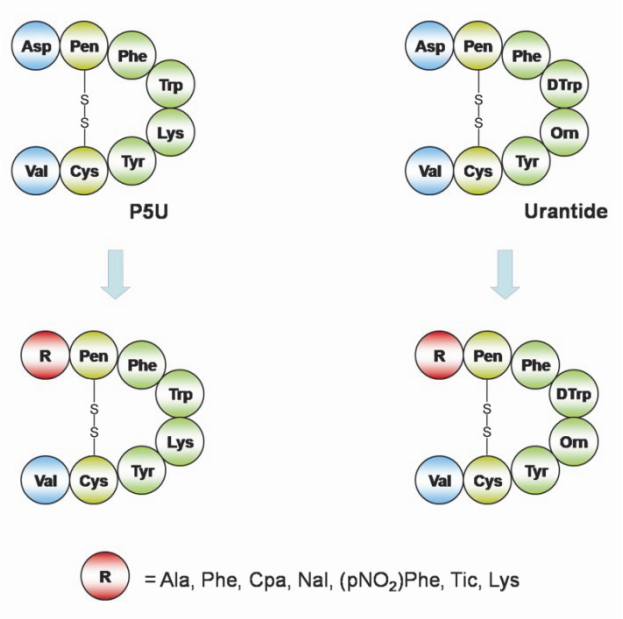

Figure 2. New synthesized compounds

Biological Data. Receptor affinity at *h*-UTR and biological activity (rat aorta bioassay) of the synthesized compounds are reported

in Table 1. Substitution of the native Asp^4 residue in P5U by an Ala residue (compound **1**), which generated an URP analogue, slightly reduced the contractile potency of the peptide (pEC_{50}=8.04). Similar modification in Urantide sequence produced compound **2** with antagonist activity but slightly less potent than Urantide (pK_B 7.84). Subsequently, to evaluate the role of an aromatic residue in position 4 we replaced Asp^4 with a Phe residue in both sequence of P5U and Urantide. Compound **3** showed to be a superagonist as P5U (pEC_{50}=9.18) while the same substitution in Urantide sequence generated compound **4** with a reduced binding affinity but with an increased antagonist activity (pK_i 7.71 and pK_B 8.68). Then, the Asp^4 residue was replaced with some uncoded aromatic amino acids (Figure 2). Compound **5**, in which Asp^4 was replaced with a Cpa residue resulted to be less potent as agonist compared to P5U (pEC_{50} 8.86). Similar trend was observed in compound **6** with a reduced antagonist potency (pK_B 7.85). Analogue **7**, containing in position 4 a Nal(1) residue, showed a sensible reduction both in binding (pK_i 7.58) and functional activity (pEC_{50} 6.99), while the same substitution in Urantide sequence (compound **8**) resulted in a conserved antagonist activity (pK_B 8.50). Interestingly, Nal(2) derivative of P5U (compound **9**) regained high agonist activity (pEC_{50} 8.28). On the

other hand, compound **10** resulted to be slightly less potent compared to compound **8** and Urantide (pK_B 7.89).

Table 1. Receptor Affinity and Biological Activity of P5U and Urantide Analogues of General Formula:

R-c[Pen[a]-Phe-*Xaa*-*Yaa*-Tyr-Cys]-Val-OH

Peptide	Xaa	Yaa	R	pK_i [b]	pEC_{50} [c]	pK_B [d]
*h*U-II	Trp	Lys	*	9.10 ±0.08	8.30 ±0.06	-
*h*U-II(4-11)	Trp	Lys	Asp	9.60±0.07	8.60 ± 0.04	-
P5U	Trp	Lys	Asp	9.70±0.07	9.60 ± 0.07	-
Urantide	DTrp	Orn	Asp	8.30 ± 0.04	Inactive	8.30
1	Trp	Lys	Ala	9.10±0.08	8.04±002	-
2	DTrp	Orn	Ala	8.78±0.08	-	7.84
3	Trp	Lys	Phe	9.55±0.05	9.18±0.17	-
4	DTrp	Orn	Phe	7.71±0.10	-	8.68
5	Trp	Lys	Cpa	9.05±0.04	8.86±0.05	-
6	DTrp	Orn	Cpa	8.02±0.06	-	7.85
7	Trp	Lys	Nal(1)	7.58±0.06	6.99±0.13	-
8	DTrp	Orn	Nal(1)	8.41±0.01	-	8.50
9	Trp	Lys	Nal(2)	8.19±0.10	8.28±0.10	-
10	DTrp	Orn	Nal(2)	7.93±0.01	-	7.89
11	Trp	Lys	(pNO_2)Phe	7.87±0.08	7.14±0.09	-
12	DTrp	Orn	(pNO_2)Phe	7.80±0.10	-	7.90
13	Trp	Lys	Tic	8.58±0.03	8.87±0.18	-
14	DTrp	Orn	Tic	8.03±0.07	-	8.94
15	Trp	Lys	Lys	8.03±0.11	8.22±0.24	-
16	DTrp	Orn	Lys	6.66±0.01	-	7.49

[a] Cys in *h*U-II and *h*U-II(4-11). [b] pKi: -log Ki [c] pEC_{50}: -log EC_{50}. [d] pK_B (-log K_B) values are from experiments in the rat thoracic aorta. Each value in the table is mean ± s.e.m. of at least 4 determinations. * H-Glu-Thr-Pro-Asp-

Replacing the Asp^4 residue with the amino acid pNO_2Phe in both parent peptides, led to compounds with reduction in activity. In fact, compound **11** resulted to have a reduced binding affinity at UT receptor (pKi 7.87) and a more considerable reduction in functional activity (pEC_{50} 7.14). Compound **12**, resulted to be slightly less potent respect to Urantide showing a pK_B of 7.90. Analogue **13**, in which Asp^4 residue was replaced with a Tic residue, showed a slightly reduced activity (pEC_{50} 8.87). Surprisingly, the same substitution in Urantide sequence produced analogue **14** with increased antagonist potency showing a pK_B value of 8.94. This compound represents a new potent antagonist discovered by this study. Finally, the replacement of Asp^4 with a Lys residue in P5U (analogue **15**) resulted in a reduced activity (pEC_{50} 8.22). Worthy of note, the same modification in Urantide sequence produced an analogue (compound **16**) showing a dramatic reduction in binding affinity and antagonist activity (pK_i 6.66 and pK_B 7.49), being by far the weakest ligand among the synthesized compounds.

NMR Analysis. A whole set of 1D and 2D NMR spectra in 200 mM aqueous solution of SDS were collected for compounds **14,** and **16**. These peptides were chosen since **14** is the most potent antagonist of the series while **16** has very low binding affinity and antagonist potency (Table 1). Micelle solution was employed since we have

recently reported the NMR structure of UT agonists (among which P5U) [34] and antagonist (among which Urantide) [33] in this *medium*. Complete ^{1}H NMR chemical shift assignments were effectively achieved for the two peptides according to the Wüthrich procedure[36] via the usual systematic application of DQF-COSY,[37, 38] TOCSY,[39] and NOESY [40] experiments with the support of the XEASY software package (Supporting Information).[41] Peptides **14** and **16** differs from Urantide only for the N-terminal residue substitution and show diagnostic NMR parameters (H_α proton chemical shifts, NOE contacts, $^{3}J_{\text{NH-H}\alpha}$ and $^{3}J_{\text{H}\alpha\text{–H}\beta}$ coupling constants, NH exchange rates and temperature coefficients) all similar to those observed in the parent peptide (Supporting Information). In particular, NOE contacts between H_α-NH_{i+2} of D-Trp^{7} and Tyr^{9} and between NH-NH_{i+1} of Orn^{8} and Tyr^{9} indicated the presence of a β-turn. This result was supported by the observation of slowly exchanging NH resonance of residue 9, and low value of the temperature coefficient for this proton ($-\Delta\delta/\Delta T$ < 3.0 ppb/K). A short stretch of antiparallel β-sheet involving residues 5-6 and 10-11 is inferred from a number of long-range NOEs including H_α-NH connectivities between residues 5, 11 and 10, 6 and a NH-NH connectivity between residues 6 and 9. All the

data indicated the preservation, in **14** and **16**, of the *β*-hairpin structure.

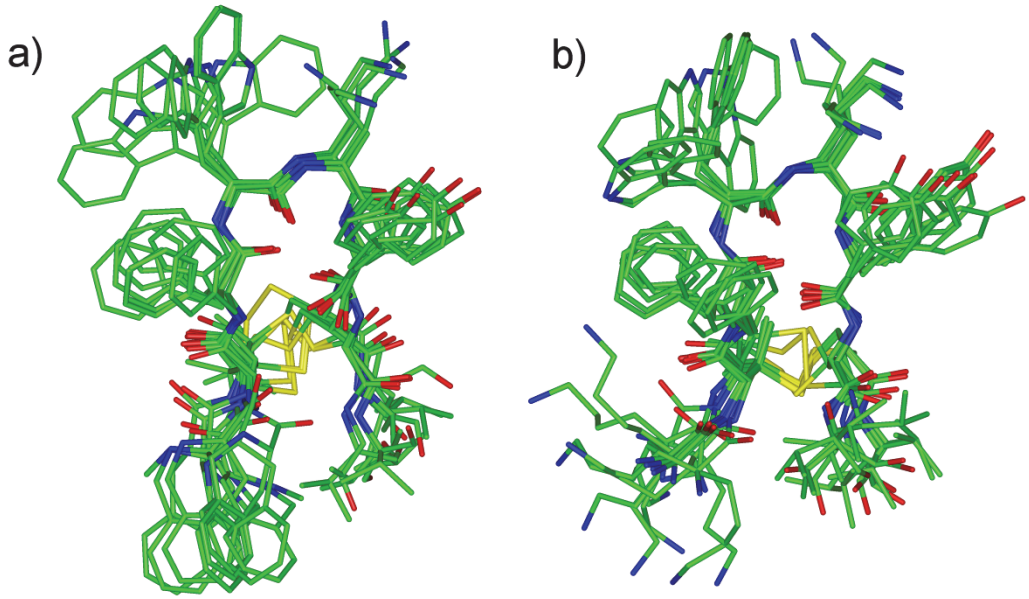

Figure 3. Superposition of the 10 lowest energy conformers of **14** (a), **16** (b). Structures were superimposed using the backbone heavy atoms of residues 5-10. Heavy atoms are shown with different colours (carbon, green; nitrogen, blue; oxygen, red; sulfur, yellow). Hydrogen atoms are not shown for clarity.

NMR-derived constraints obtained for the analyzed peptides (Supporting Information) were used as the input data for a simulated annealing structure calculation. For each peptide, 20 calculated structures satisfying the NMR-derived constraints (violations smaller than 0.40 Å) were chosen (Figure 3 a-b). As shown, both the peptides **14**, and **16** show a well defined type II' *β*-hairpin structure encompassing residue 5-10 (backbone rmsd values are 0.41 and 0.37 Å, respectively). In contrast, the N- and C-terminal residues were

highly flexible. Considering the side chains orientation, Phe[6], Orn[8], and Tyr[9] side chains showed a large preference for *trans*, g^-, and g^- rotamers, respectively, while D-Trp[7] side chain is found both in *trans* and g^+ conformation.

Docking Studies of Urantide and its Analogues. The theoretical structure of the *h*-UT receptor (Figure 4) was generated by homology modeling based on the crystal structure of bovine rhodopsin (PDB code 1F88),[42] as described previously.[43] The resulting structure represents an inactive form of the *h*-UT receptor (h-UTR_i) with an overall conformation very similar to that of bovine rhodopsin (1.22 Å rmsd between the backbone atoms of the transmembrane domains).

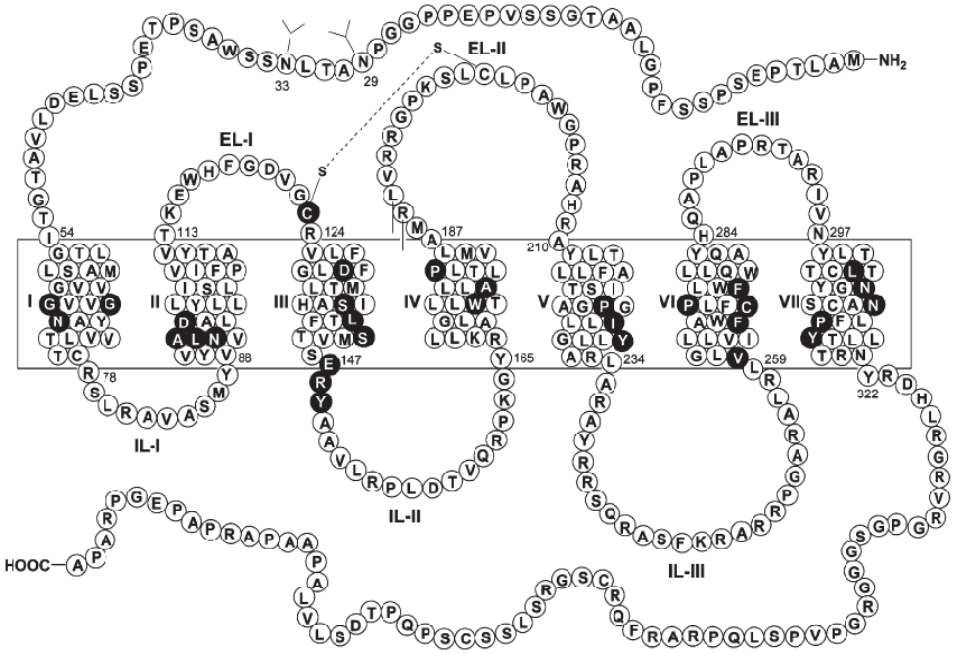

Figure 4. Serpentine model of the *h*-UTR sequence. The black lines represent the boundaries of the membrane. Filled circles indicate the residues highly conserved among the GPCRs superfamily. The TM helices are denoted by roman numerals. The arabic numbers indicate the position of the residues inside the TM domain. The glycosilation sites on the N-terminal region are also shown.

Since the currently available docking programs may not work very well for peptide compounds, manual docking was conducted for Urantide. The NMR-derived Urantide structure [33] was placed in between the trans-membrane domains of the *h*-UTR_i, employing the following criteria to achieve meaningful docking modes: (i) The positively charged amino group of Orn^8 had to be close to and pointing in the direction of the carboxylate group of Asp130, which is conserved in many GPCRs and positioned in the TM-III region; (ii) N-terminal residues should point towards extracellular loops as experimentally determined [44]; (iii) No steric clashes should occur between any atom. To assess the stability of the Urantide/*h*-UTR_i complex and to analyze the potential ligand/receptor interactions, energy minimization and MD simulations of 2 ns at a constant temperature of 300 K were run. During the MD simulation, the ligand, the EL's, and all the receptor side chains were allowed to relax, while the TM's and IL's backbone atoms were held frozen. The distances between the peptide and the key receptor residues were monitored along the complete 2 ns MD trajectory (Supporting Information).

To inspect the variations in the ligand conformation, rmsd with respect to the starting structure was calculated. Interestingly, the rmsd of Urantide backbone atoms turned out to be remarkably stable

throughout all the MD simulations ($0 < rmsd < 0.6$), indicating that the peptide settles into the receptor-binding site in a stable β-hairpin conformation. Also the side chain orientations are those described by NMR. Interestingly, D-Trp^7 prefers a *trans* orientation about χ_1 angle ($\chi_1 \approx 180°$, $\chi_2 \approx -70°$). As shown in Figure 5a, the hypothetical binding site of Urantide is located among TM-III÷TM-VII, and EL-II. The β-hairpin is oriented along the receptor helical axis, with the N- and C-terminal residues pointing towards the extracellular side. The binding mode of the peptide is determined mainly by the interactions showed in Figure 5b and Table 2.

Table 2. Urantide/*h*-UTR$_i$ Interactions

Residue*	Surrounding residue
Asp^4	Ala187 (EL-II), Met188 (EL-II), Cys199 (EL-II), Arg206 (EL-II), Ala207 (EL-II)
Pen^5	Gln278 (TM-VI), Pro287 (EL-III)
Phe^6	Cys123 (EL-I), Val184 (TM-IV), Met188 (EL-II)
D-Trp^7	Phe131 (TM-III), Met134 (TM-III), His135 (TM-III), Leu212 (TM-V), Leu215 (TM-V), Phe216 (TM-V), Ile220 (TM-V), Trp275 (TM-VI), Gln278 (TM-VI)
Orn^8	Asp130 (TM-III), Thr301 (TM-VII), Thr304 (TM-VII)
Tyr^9	Phe127 (TM-III), Phe274 (TM-VI), Asn297 (TM-VII), Thr301 (TM-VII)
Cys^{10}	Cys199 (EL-II), Pro287 ((EL-III)
Val^{11}	Cys123 (EL-I), Arg189 (EL-II), Cys199 (EL-II), Leu288 (EL-III).

* For sake of clarity, the residue numbers of the ligands are reported as apex while those of the receptor are not.

In particular, (i) a tight charge-reinforced hydrogen-bonding network involving the carboxylate group of Asp130 and the protonated δ-amino group of Orn^8 of Urantide is established. Such an interaction, which we assume to be an anchoring point of the ligand to *h*-UTR, remained stable during the whole production run (Supporting Information, Figure S2). (ii) Three hydrophobic pockets, delimited by residues listed in Table 2, host the aromatic side chains of Phe^6, D-Trp^7, and Tyr^9 of Urantide. Particularly, the indole system of D-Trp^7 appears to be optimally oriented for a π-stacking interaction with the aromatic indole system of Trp275. Furthermore, the phenolic OH of Tyr^9 is at hydrogen-bonding distance with the side chain CO of Asn297, and OH of Thr301. (iii) Asp^4 in Urantide is involved in a hydrogen-bonding network. Particularly, the oxygen atoms of the carboxylate form two charge-reinforced hydrogen bonds with Arg206 guanidinium group. In addition, the protonated N-terminal group of Asp^4 engages additional hydrogen bonds with the backbone CO of Ala187, Cys199 and Met188. (iv) Finally, the negatively charged C-terminal group establishes two hydrogen bonds with backbone HN of Cys123 and Cys 199, and a salt bridge with the protonated guanidinium moiety of Arg189 (EL-II). All the aforementioned interactions resulted to be quite stable during the whole MD production run (see Figure S2-S11 for details). The mean structure of

the last 1 ns of MD was extensively minimized and used for subsequent analysis.

Since the NMR results indicate that the 3D structure of the Urantide analogues **14** and **16** did not change after the replacement of the N-terminal residue, we used the energy-minimized structure

of the Urantide/*h*-UTR_i complex as starting point for the docking procedure of these derivatives. After replacing Asp^4 of Urantide with Tic^4 to give compound **14** and with Lys^4 to give **16**, the complexes were minimized and then subjected to a 200 ps MD simulation. The mean structures of the last 100 ps of the MD trajectory were then minimized and used for subsequent analysis.

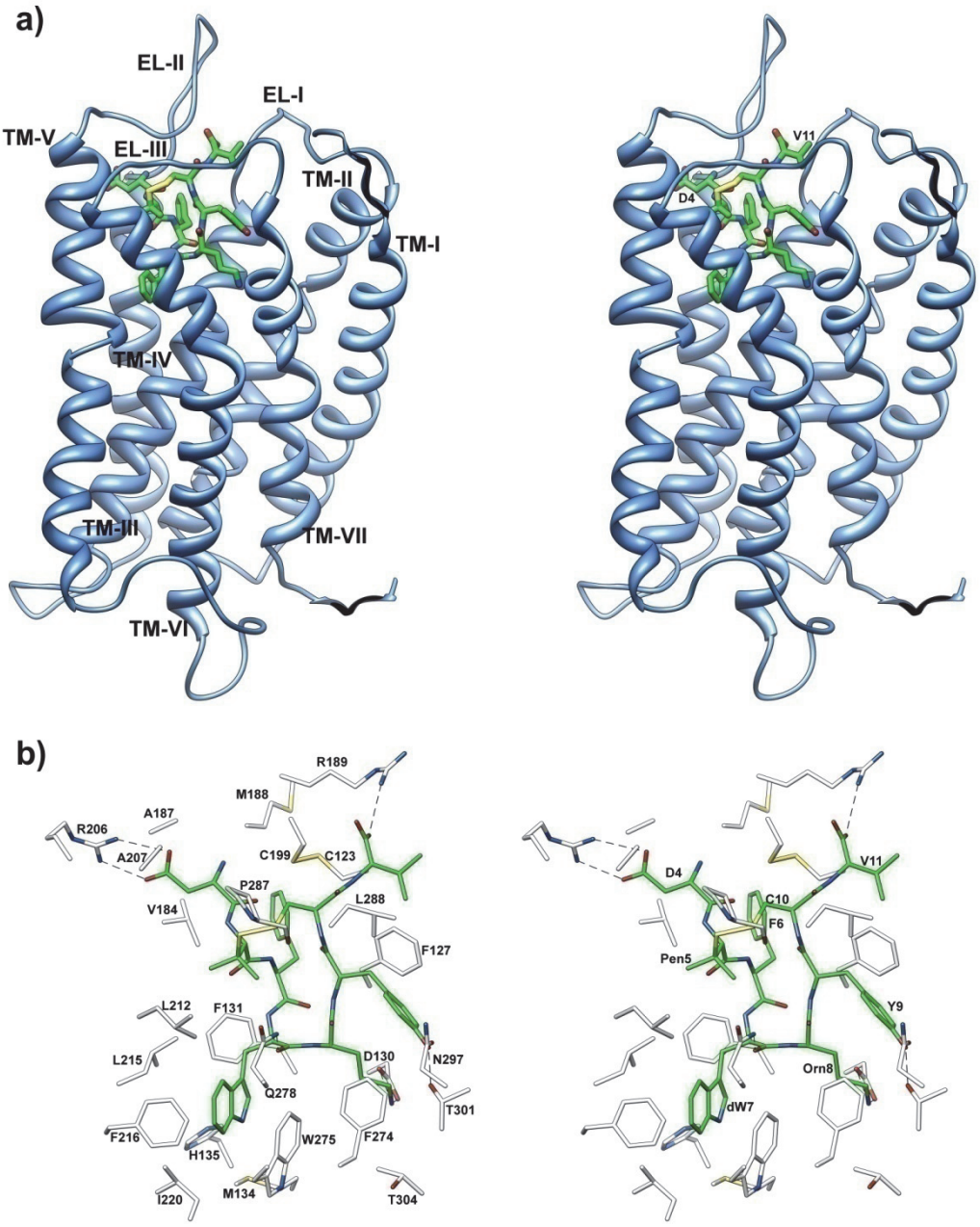

Figure 5. (a) Stereoview of *h*-UTR$_i$ model complexed with Urantide. Urantide heavy atoms are colour coded as in Figure 2. Receptor backbones are represented in azure and labeled. (b) Stereoview of Urantide within the binding pocket of *h*-UTR$_i$. Hydrogen bonds are represented with dashed lines.

While the same interactions with *h*-UTR$_i$ were recorded for the unchanged residues, in the **14**/UTR$_i$ complex, Tic^4 interacts with Val184 (TM-IV), Ala187 (EL-II), Leu200 (EL-II), Pro201 (EL-II), and Tyr211 (TM-V); while in the **16**/UTR complex Lys^4 residue takes

contact with Leu200 (EL-II), and Tyr211 (TM-V). In Table 3 ligand/receptor ΔG_{bind} values are reported as calculated employing the AutoDock4 program native scoring function.[45-47] Interestingly, there is a clear, although qualitative, correlation between the predicted ΔG_{bind} values and the experimental binding constants (Table 1).

Docking of P5U and its Analogues. The three-dimensional model of the *h*-UTR, in the active state (*h*-UTR_a), was constructed from the model structure of the bovine rhodopsin, proposed by Mosberg,[48] and was generated by homology modeling following the same steps described for the inactive model.[43]

Table 3. Binding free energies (ΔG_{AD4}) calculated for the energy minimized averaged complexes deriving from the MD simulations.

Receptor	Ligand	ΔG_{bind}[a]	Electr[b]	H-Bond[b]	VdW[b]	Desolv[b]	Tors[b]
h-UTR_i[c]	Urantide	-24.33	-4.99	-5.90	-26.50	7.09	5.97
h-UTR_i	**14**	-23.01	-3.21	-3.83	-26.98	5.94	5.07
h-UTR_i	**16**	-21.10	-3.31	-5.77	-25.16	6.28	6.86
h-UTR_a	P5U	-24.53	-4.99	-6.11	-25.89	6.69	5.76
h-UTR_a	**13**	-23.53	-3.35	-4.19	-27.40	6.03	5.37
h-UTR_a	**15**	-23.01	-4.11	-6.77	-25.40	6.31	6.96
h-UTR_a	Urantide	-20.65	-5.92	-6.42	-21.39	7.11	5.97
h-UTR_i	P5U	-18.68	-3.60	-3.47	-24.67	6.80	6.26

[a] ΔG_{bind}: free energy of binding. [b] Energy terms contributing to the AutoDock4 scoring function. Electr: electrostatic; H-Bond: H-Bonding; VdW: Van der Waals; Desolv: desolvation; Tors: torsional entropy. All terms are given in kcal/mol. [c] *h*-UTR_i: receptor in the inactive state. *h*-UTR_a: receptor in the active state.

A comparison of models for the active and inactive states of *h*-UTR reveals the structural changes that accompany activation.

Overall, the rmsd between these models is 2.3 Å calculated for the backbone atoms of all the TM's, but decreases to 1.7 Å after excluding TM-VI, which experiences a rearrangements upon receptor activation. Indeed, TM-VI shifts outward and rotates counterclockwise (viewed from the extracellular side) during activation, moving its intracellular end away from TM-III and toward TM-V. As a result of this and other changes, the receptor structure tightens near its extracellular surface but opens up at the cytoplasmic side, providing a cavity for binding of the Gαs subunit.

The NMR-derived P5U structure [34] was placed in between the trans-membrane domains of the *h*-UTR_a model, following the same criteria used for Urantide (see above) to achieve meaningful binding poses. Energy minimization and MD simulations (2 ns) were run to assess the stability of the P5U/*h*-UTR_a complex and to analyze the potential ligand/receptor interactions.

To inspect the variations in the ligand conformation, rmsd with respect to the starting structure was calculated. Interestingly, the rmsd of P5U backbone atoms turned out to be really stable throughout all the MD simulations ($0 < \text{rmsd} < 0.5$), indicating that the peptide settles into the receptor-binding site in a stable *β*-hairpin conformation. Also the side chain orientations are those described by NMR.[34]

As shown in Figure 6a, the hypothetical binding site of P5U is located among TM-III÷TM-VII, EL-II and EL-III. The *β*-hairpin is oriented along the receptor helical axis, with the N- and C-terminal residues pointing towards the extracellular side. The binding mode of P5U is determined mainly by the interactions showed in Figure 6b and Table 4.

Table 4. P5U/*h*-UTR_a Interactions

Residue	Surrounding residue
Asp^4	Pro201 (EL-II), Gln285 (EL-III)
Pen^5	His208 (EL-II), Trp277 (TM-VI), Ala281 (TM-VI), Ala286 (EL-III)
Phe^6	Val184 (TM-IV), Met188 (EL-II), Leu212 (TM-V)
Trp^7	Phe131 (TM-III), Met134 (TM-III), Phe274 (TM-VI), Trp275 (TM-VI), Gln278 (TM-VI)
Lys^8	Asp130 (TM-III), Tyr305 (TM-VII)
Tyr^9	Trp116(TM-II), Cys123 (EL-I), Leu126 (TM-III), Phe127 (TM-III), Cys199 (EL-II)
Cys^{10}	Trp277 (TM-VI)
Val^{11}	Arg189 (EL-II), Cys199 (EL-II)

As for Urantide, a stable (Figure S12) charge-reinforced hydrogen-bonding network involved the carboxylate group of Asp130 and the protonated *ε*-amino group of Lys^8 of P5U is observed. Three hydrophobic pockets, delimited by residues listed in Table 4, host the aromatic side chains of Phe^6, Trp^7, and Tyr^9. These hydrophobic pockets only partially overlap with those of Urantide. For instance, Tyr^9 OH group is not engaged in any hydrogen bond. Again, the

negatively charged C-terminal group of Val^{11} establishes a hydrogen bond with Cys199 backbone NH, and a salt bridge with the protonated guanidinium moiety of Arg189.

Differently from Urantide, Asp^4 in P5U is involved in a hydrogen-bond with the Gln285 (EL-III) NH_2 group. This H-bond is not stable during the MD trajectory (Figure S13). The mean structure of the last 1 ns of MD was extensively minimized and used for subsequent analysis.

Replacing the Asp^4 residue of P5U with Tic or Lys residue (obtaining the derivatives **13** and **15**, respectively) in the P5U/*h*-UTR model complex, and following the same optimization steps used for the complexes of Urantide analogues (see above), we obtained the two models: **13**/*h*-UTR_a and **15**/*h*-UTR_a, showing similar binding energy (Table 3) in accordance with the experimental binding data (Table 1).

Switching the ligands. To assess the predictive value of the receptor models the ligands were switched, i.e. urantide was docked within *h*-UTR_a and P5U within *h*-UTR_i model (Figure S14). For the docking of urantide, we started from the optimized P5U/UTR_a complex and superposed the NMR derived urantide structure with that of P5U (backbone atoms of residues 5-10). Then, we removed the P5U structure and optimized the urantide/UTR_a complex. Analogous

steps were taken for the P5U/UTR$_i$ complex. In Table 3, the binding energies of the two complexes are reported.

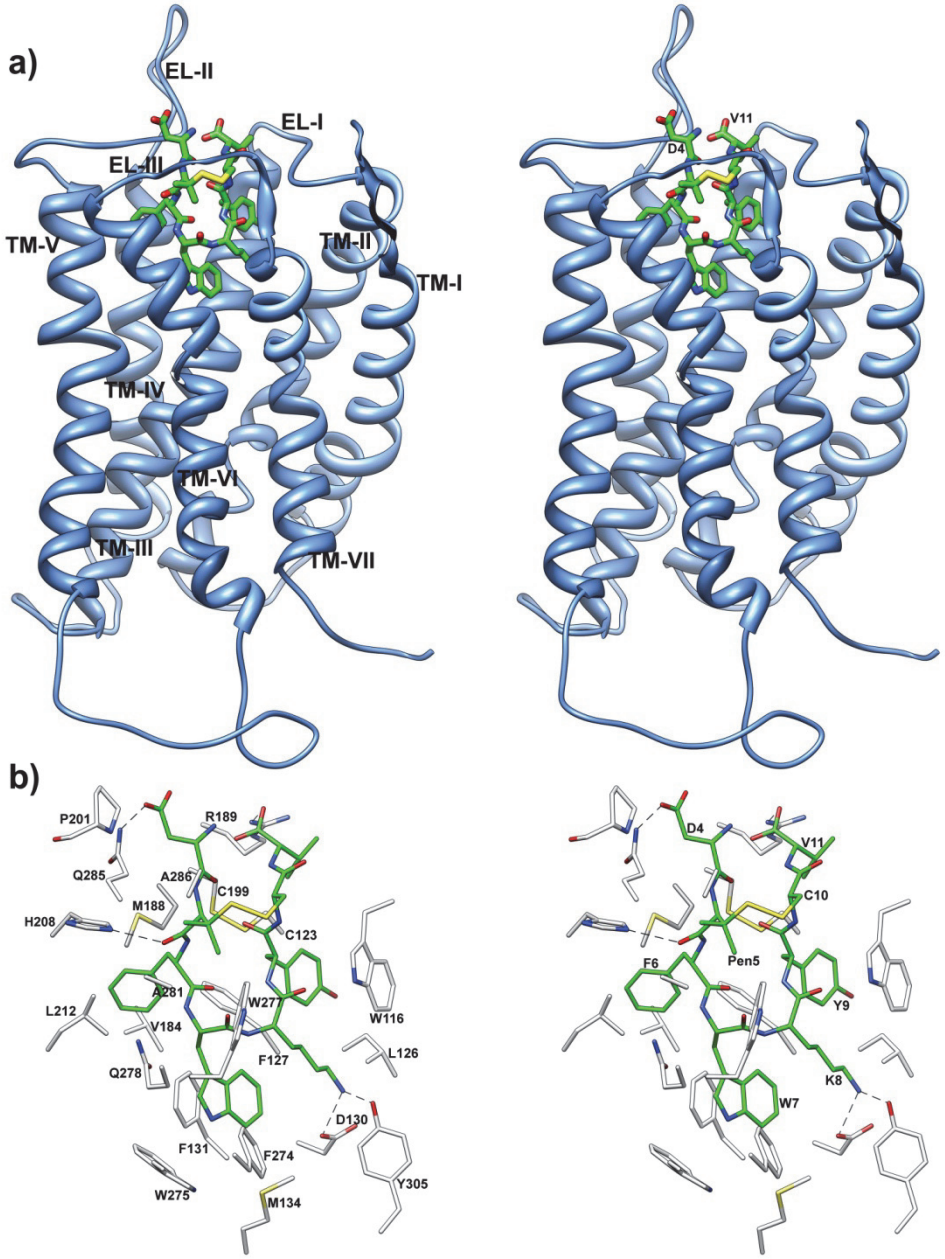

Figure 6. (a) Stereoview of h-UTRa model complexed with P5U. P5U heavy atoms are colour coded as in Figure 2. Receptor backbones are represented in azure and labeled. (b) Stereoview of P5U within the binding pocket of h-UTRa. Hydrogen bonds are represented with dashed lines.

1.1.3. Discussion

Previous studies have demonstrated that the C-terminal octapeptide of *h*U-II [U-II(4-11), Table 1] mimicked the effects of U-II on intracellular calcium concentration in UTR-transfected cells and contraction of rat aortic rings.[22, 24, 25] Recently, Coy et coll. have examined the role of the N-terminal Asp residue in UII(4–11) since this acidic amino acid embodies one of the main structural differences between the UII(4–11) and somatostatin octapeptides which results in little somatostatin affinity for the UT receptor.[26] They found that the N-terminal amino acid does not require a negatively charged side chain, merely one which has a hydrogen bond acceptor CO group. The side chain can be constrained into a trans-olefinic configuration and can also contain an aromatic ring substituted with polar groups such as OH and NO_2. Afterwards, Salvadori et coll. examined the same position of *h*U-II(4-11) using a number of aromatic residues.[49] They found that all of the new analogues behaved as full agonists, and that aromaticity is well tolerated; size, length and chirality of the side chain are not important, while substituents with a nitrogen atom are preferred. On bases of these considerations and to further investigate the contribution of the N-terminal Asp residue in the biological activity, we synthesized 16 analogues of P5U and Urantide substituted at this position with amino acids bearing different physicochemical

properties (Table 1). In particular, Urantide was used as lead compound to investigate the N-terminal position in analogues with potential antagonist activity. All synthesized compounds were tested for their binding affinity on *h*-UTR-transfected CHO cells and for their contractile activity on de-endothelialized rat aortic rings (Table 1).[31]

Overall, the biological data indicate that in the "agonist series" (i.e. derived from P5U) the N-terminal substitutions of Asp^4 with uncharged, aromatic or positively charged residues are generally well tolerated. The consistent reduction in binding and activity is probably due to the lost of a hydrogen bond acceptor/donor group, in accordance with previous results.[26, 49] Concerning the "antagonist series" (i.e. derived from Urantide), while a positively charged amino acid (Lys) strongly reduces the binding and the activity (compound **16**), an aromatic residue is well tolerated and can increase the potency. In particular, compound **14**, in which a Tic residue replaces the Asp^4 of Urantide, showed the highest antagonist potency in the functional rat aorta bioassay (pK_B 8.94). Since the binding constant of **14** to *h*-UTR is slightly reduced compared to Urantide, the enhanced functional potency should derive from improved tissue penetration of the more hydrophobic Tic amino acid in **14** replacing an Asp residue in Urantide. Species differences between *h*-UTR and *r*-UTR could

also be invoked. To check the last hypothesis, the sequences of *h*-UTR and *r*-UTR were compared (Figure S15). Since only minimal residue differences were observed near the bound ligand and, in particular, near to the Tic residue (EL2 is unchanged in the two receptors), the hypothesis was rejected.

To determine whether the different biological activities of Urantide analogues were driven by different conformational properties of the peptides or by the different chemical functionalities at the N-terminus, we performed an NMR study on the interesting analogues **14** and **16** in SDS micelles solution. The use of SDS micelles to study the conformational properties of *h*U-II analogues is motivated on the basis of their interaction with a membrane receptor. For peptides acting as ligands of membrane receptors (such as GPCR), the use of membrane mimetic media, such as SDS or DPC, is suggested hypothesizing a membrane-assisted mechanism of interactions between the peptides and their receptors.[50] According to this model, the membrane surface plays a key role in facilitating the transition of the peptide from a random coil conformation adopted in the extracellular environment to a conformation that is recognized by the receptor. The increase of the local concentration of the peptide and the reduction of the rotational and translational freedom of the neuropeptide are membrane-mediated events acting as determinant

steps for the conformational transition of the peptide.[51, 52] NMR has proven useful to examine the structures of bioactive peptides that cross membrane barriers.[53-55] Actually, we succeeded in correlating the SDS-bound conformation of *h*U-II analogues with their biological activity.[33, 34]

We showed that *h*U-II analogues, which retain high affinity for UT receptor, all possess a type II' β-hairpin backbone conformation regardless their agonist or antagonist activity, indicating that such backbone conformation is necessary for the UT recognition.[33, 34] The main conformational difference observed in the structures of the antagonists and the agonists was established in a different orientation of the (D/L)-Trp^7 side chain. In particular, while in the agonists the (D/L)-Trp^7 indole moiety is close to the Lys^8 side chain, in the antagonists (D/L)-Trp^7 side chain is more flexible and further from the ornitine side chain. The structural features of the "antagonist series" were found also for the analogues **14**, and **16** (Figure 3) indicating that the different affinity-activity of the two compounds do not depend on a different spatial disposition of the "pharmacophoric" residues (i.e. (D/L)-Trp^7, Lys/Orn^8, Tyr^9) [22, 23] but must depend on different interaction of the N-terminal residue with the receptor.

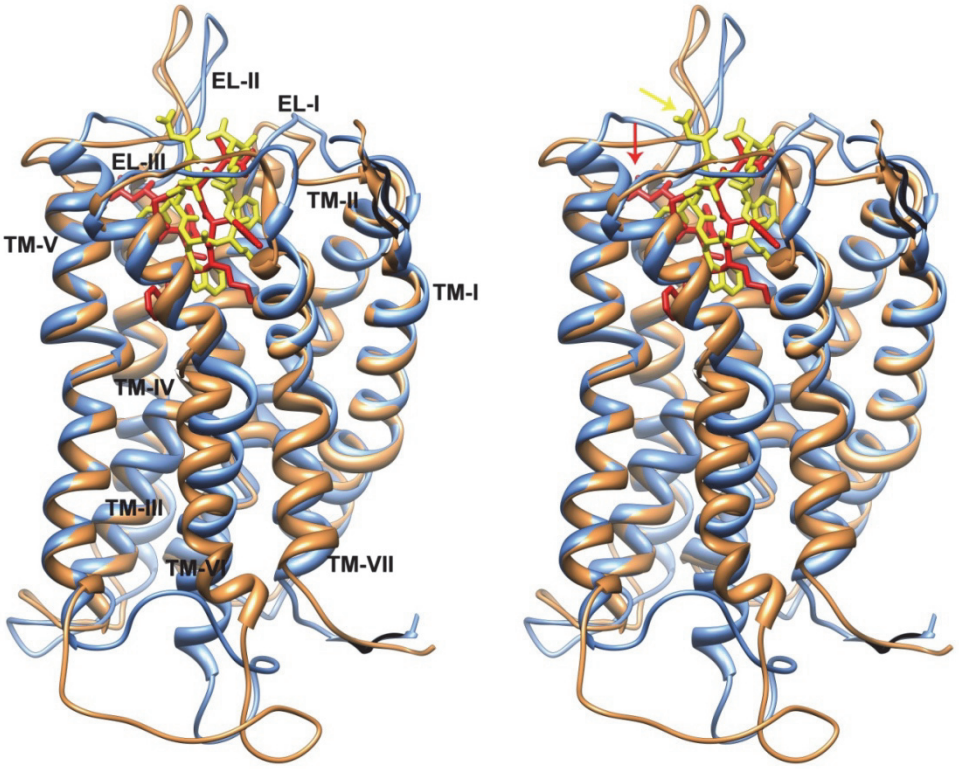

Figure 7. Stereoview of *h*-UTR models in the inactive (azure) and active (sienna) conformations complexed with Urantide (red) and P5U (gold), respectively. The *h*-UTR models are superimposed using the backbone heavy atoms of TM residues apart from TM-VI. Asp^4 residue is evidenced by an arrow.

To gain insight into this interaction mode we first undertook a docking study between the parent Urantide and *h*-UT receptor model. It is worth noting that, while docking studies regarding peptide agonist have been performed,[23, 43, 44, 56] the docking of peptide antagonist at UT receptor is unprecedented. Since the crystal structure of a GPCR in the active conformation is not yet disposable, we used the "active state" rhodopsin model developed by Mosberg *et al.* as template to build an *h*-UTR_a model.[48] Hence, the rhodopsin receptor template was also chosen for the inactive state model (*h*-UTR_i) to allow a direct comparison of the two models. The structures of other

mammalian GPCR's in inactive state have been solved.[57-59] Interestingly, our *h*-UTR$_i$ model and the β_2-adrenergic receptor (β_2AR, PDB code 2RH1) are quite similar around the urantide binding site showing an rmsd of the backbone heavy atoms of 1.5 Å (helices II÷VII, Figure S16).

Urantide/*h*-UTR$_i$ complex (Figure 5) and the MD simulations indicated that: (i) the β-hairpin structure adequately fits the binding site and is stable during the MD trajectory; (ii) the binding site, situated in the entrance of the TM bundle on the extracellular side, is formed by TM-III÷TM-VII, and EL-II; (iii) particularly important for the present study, the N-terminal Asp^4 residue interacts with EL-II, mostly by stable electrostatic interactions with the Arg206. Replacement of Asp^4 with a Lys residue (analogue **16**), in the model complex, increase the binding energy (Table 3) since the favorable interactions are lost and, in contrast, electrostatic repulsions between N$^\varepsilon$ of Lys^4 and the guanidinium group of five arginine and the N$^\varepsilon$ of one lysine residues located on the EL-II can occur. In contrast, the loss of favorable electrostatic interaction, upon the replacement of the Asp^4 of Urantide with a Tic residue (analogue **14**), is partially compensated by van der Waals interactions of the phenyl ring of Tic and by a reduced desolvation energy.

Docking study between P5U and *h*-UTR$_a$ was also performed. The obtained complex (Figure 6) and the MD simulations indicated that: (i) the β-hairpin structure adequately fits the binding site and is stable during the MD trajectory; (ii) the binding site, situated in the entrance of the TM bundle on the extracellular side, is formed by TM-III÷TM-VII, EL-II; and EL-III; (iii) the N-terminal Asp^4 residue lies between EL-II and EL-III. We found similarities, but also some differences, with previous reports describing the docking of peptide agonists (*h*U-II, and P5U) into an UTR model.[23, 43, 44, 56] In regards to our previous work,[43] the different docking results obtained for the P5U/*h*-UTR complex is ascribable to the different conformation of both the receptor and the ligand. In fact, in the present study the *h*-UTR structure is based on an active model of rhodopsin,[48] while in the previous work the receptor was constructed starting from the X-ray inactivated form of rhodopsin.[42] Moreover, herein the presented P5U 3D structure is obtained from a NMR study in SDS micelle solution,[34] while the one used in 2005 was derived from a NMR study in DMSO solution.[30]

To assess the predictive value of the models the ligands were switched, i.e. urantide was docked within *h*-UTR$_a$ model and P5U within *h*-UTR$_i$ (Figure S14). Both urantide/UTR$_a$ and P5U/UTR$_i$ complexes show negative binding energies (Table 3), but these are

significantly lower (absolute value) than the ones of urantide/UTR_i and P5U/UTR_a complexes, respectively. These results are not surprising. In fact, urantide still retains agonist activity being a full agonist in a calcium mobilization assay.[32] Interestingly, D-Trp^7 aromatic moiety of urantide within UTR_a binding site is close to the Orn^8 side chain in a conformation which characterizes the agonist peptide ligands (Figure S14).[33] As concern P5U/UTR_i complex, the negative value of the binding energy can be explained admitting that, in a first step, even the agonists bind the receptor in its inactive (ground) state. Then, the system moves to a minimum of free energy which is reached with the receptor activation.

Urantide/*h*-UTR_i and P5U/*h*-UTR_a interactions found in our models (Table 2, Table 4 and Figure 7) are different. In particular, Urantide plunges more deeply into the TM's bundle compared to P5U, probably due to the ornitine side chain length reduction, and to the D-Trp^7 higher flexibility. As a consequence, the exocyclic carboxylate group of Asp^4 of P5U, lying at the interface between EL-II and EL-III, is more external compared to the corresponding residue in Urantide, and establishes only non-stable hydrogen bond with the receptor. In accordance with SAR data obtained by us and others,[26, 49] the presence of both aromatic (**13**) or positively charged (**15**) residues at

position 4 of P5U leads to compounds with similar binding energy (Table 3).

Recently published experimental results, reporting that the agonists and antagonists (partial agonists) interact differently with the UT receptor, are in accordance with our models.[44, 60] Boivin *et al.* measured the interactions of *h*U-II, URP and Urantide with separately synthesized *h*-UT receptor EL's.[60, 61] They observed that agonist *h*U-II and URP bind EL-II and EL-III while the binding of Urantide was observed only with EL-II. None of these ligands were able to interact with EL-I. These results are fully consistent with our models. Leduc *et al.* found various interactions between photoreactive *h*U-II and Urantide analogues and *r*-UTR.[44, 62] Also, these interactions are compatible with our models.

The proposed binding modes are also in qualitative agreement to the observed SAR at the core -Phe-Trp-Lys-Tyr- sequence. In fact, pharmacophoric residues Trp^{7}, $Lys(Orn)^{8}$, and Tyr^{9}, whose substitution with Ala significantly reduces or abolishes the binding affinity of U-II analogues, show a high number of receptor interactions. In contrast, Phe^{6} shows only a few interactions in accordance with SAR indicating that its substitution with Ala results in a still full agonist peptide. Furthermore, substitution of the hydroxyl group of Tyr^{9} of U-II with methoxy, nitro, amino, methyl,

fluoro, or a hydrogen atom does not affect the potency and the efficacy of the U-II analogues in the rat aorta bioassay.[63] These observations agree with our model since the phenolic OH is not involved in receptor binding in the P5U/UTR_a model. Substitution of the Tyr residue by bulky aromatic amino acids such as (2-naphthyl)-L-alanine, biphenylalanine,[23] or 3-iodo-tyrosine [25] may even increase the binding affinity and the biological activity. Consistently, the tyrosine-binding pocket of our model can accommodate a bulkier side chain with an enhancement of the hydrophobic interactions. SAR data suggest that the presence of an aliphatic amine at position 9 is mandatory for U-II activity.[63] The position of the NH_2^{ε} from the peptide backbone has been investigated using ornithine, 2,4-diaminobutyric acid (Dab), and 2,3-diaminopropionic acid (Dap), i.e. with distances of 3, 2 and 1 carbon atoms, respectively. Reduction of the distance between the primary aliphatic amine and the peptide backbone of 3 and 2 methylene groups gradually reduces the potency and efficacy of the analogs and switch the activity towards antagonism. Further shortening of the amino acid side-chain increases potency and restores efficacy. Interestingly, the Dab^8-urantide analogue UFP-803 behaves as a pure antagonist (pA_2 7.46).[64] Our model can explain these results. In fact, a distance of 3 methylene groups is suitable for both UTR_i and UTR_a ligands, such as urantide

($\Delta\Delta G_{bind}$ = -3.88 Kcal/mol, Table 3). A distance of 2 methylene groups is also suitable for the two receptor states but with a much preferred antagonist mode (for UFP-803, $\Delta\Delta G_{bind}$ = -5.41 Kcal/mol; data not shown). Little attention has been paid to the Trp^9 residue in the SAR studies of U-II apart from the Ala- and D-scan approaches. Replacement of the Trp residue with 2-Nal,[23] or 4-benzoyl-L-phenylalanine (Bpa) [62] significantly decreased agonist binding affinity and potency. This would suggest that the indole NH function may establish a hydrogen bond with some UTR residue. We don't observe this postulated H-bond and believe that the indole electron rich system is more suitable for a cation-π interaction with the Lys^8 side chain observed in the peptide agonist ligands.[33]

Based on the binding mode of UTR peptide agonists and antagonists, we derived new 3D pharmacophore models illustrated in Figure 8. The distances between the pharmacophoric residues (i.e. mean distances observed during the 2 ns MD simulations) are in good accordance with those previously reported both for peptide agonists and antagonists.[33] These pharmacophore models might be useful for the next design cycle and, in particular, for the design of small-molecule ligands.

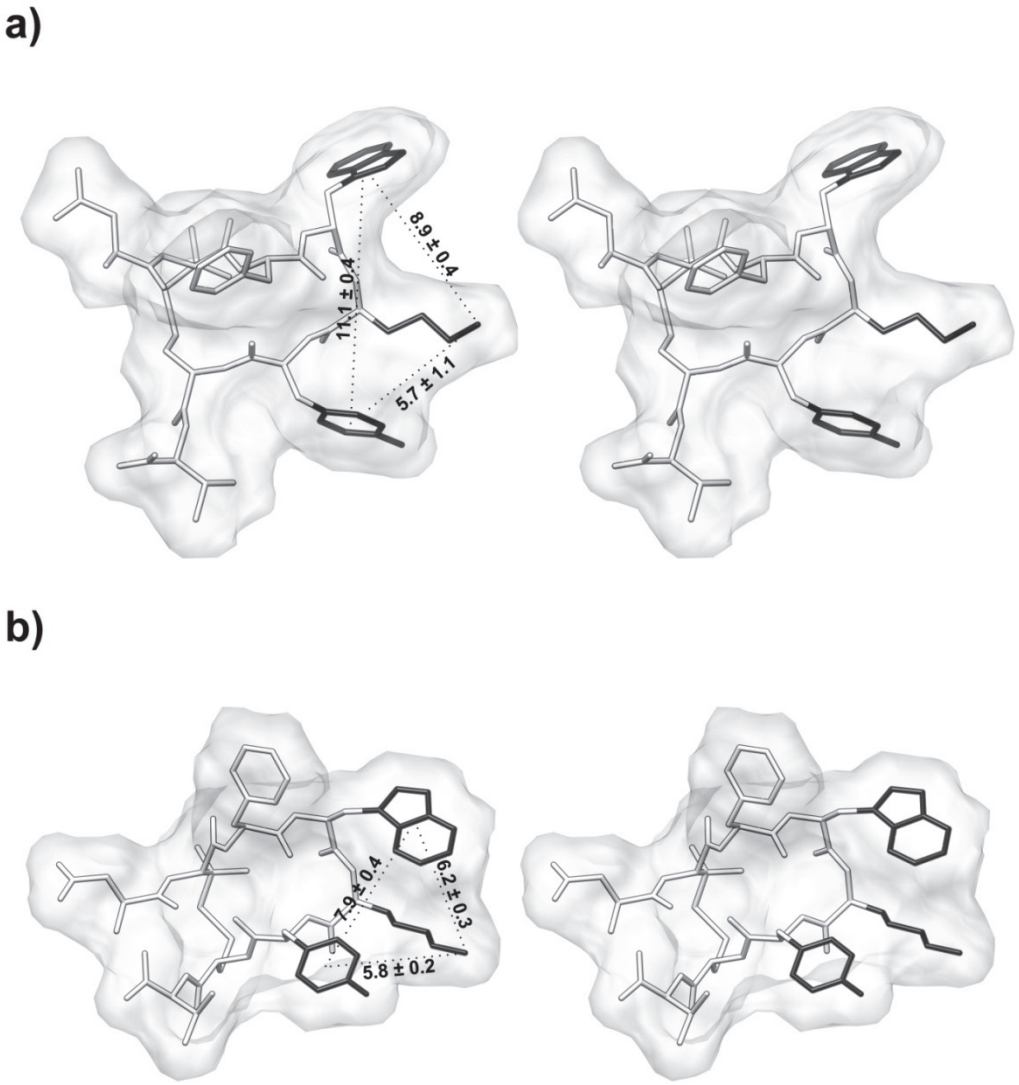

Figure 8. Stereoview of the pharmacophore model for peptide antagonists (a) and agonists (b). The distances between the aryl ring centroids of (D)Trp7 and Tyr9, and the Nε/δ of Lys(Orn)8, are displayed. Distances and standard deviations are obtained from one hundred structures saved every 20 ps of the MD simulations.

1.1.4 Conclusions

In conclusion, we observed a different SAR at the N-terminus for P5U compared to Urantide analogues. P5U shows a high degree of tolerance upon N-terminal substitutions. In Urantide analogues, an aromatic residue is well tolerated and can increase the potency. In fact, replacement of the Asp^4 residue by Tic led to an analogue, compound **14**, more potent as antagonist (pK_B = 8.94) compared to Urantide. Conversely, a positively charged amino acid (Lys) drastically reduces the binding and the activity. The results could be explained on the basis of the different receptor binding mode of the agonist P5U *vs* the antagonist Urantide. Understanding of the impact of amino acid substitutions in position 4, combined with information regarding the interactions between UT receptor and its ligands, is crucial to increase the knowledge of structure-function relationships focused to the design of new potent UT receptor ligands.

1.1.5. Experimental Section

Synthesis. *N*$^{\alpha}$-Fmoc-protected amino acids, HBTU and HOBt were purchased from Inbios (Naples, Italy). Wang resin was purchased from Advanced ChemTech (Louisville, KY). Protected Pen was purchased from Bachem (Basel, Switzerland). Peptide synthesis solvents, reagents, as well as CH_3CN for HPLC were reagent grade and were acquired from commercial sources and used without further purification unless otherwise noted. The synthesis of *h*U-II analogues was performed in a stepwise fashion via the solid-phase method. N$^{\alpha}$-Fmoc-Val-OH was coupled to Wang resin (0.5 g, 0.7 mmol NH_2/g). The following protected amino acids were then added stepwise N$^{\alpha}$-Fmoc-Cys(Trt)-OH, N$^{\alpha}$-Fmoc-Tyr(OtBu)-OH, N$^{\alpha}$-Fmoc-Yaa(N$^{\varepsilon}$-Boc)-OH (Yaa: Lys, Orn), N$^{\alpha}$-Fmoc-Xaa(N^{in}-Boc)-OH (Xaa: Trp, DTrp), N$^{\alpha}$-Fmoc-Phe-OH, N$^{\alpha}$-Fmoc-Pen(Trt)-OH and N$^{\alpha}$-Fmoc-R-OH (R = Phe, Cpa, Ala, (pNO_2)Phe, Tic, Nal(1), Nal(2), Lys). Each coupling reaction was accomplished using a 3-fold excess of amino acid with HBTU and HOBt in the presence of DIEA.

The N$^{\alpha}$-Fmoc protecting groups were removed by treating the protected peptide resin with a 25% solution of piperidine in DMF, (1x5 min and 1x20 min). The peptide resin was washed three times with DMF and the next coupling step was initiated in a stepwise manner. All reactions were performed under an Ar atmosphere. The

peptide resin was washed with DCM (3x), DMF (3x) and DCM (4x), and the deprotection protocol was repeated after each coupling step. The N-terminal Fmoc group was removed as described above and the peptide was released from the resin with TFA/ Et_3SiH /H_2O (90:5:5) for 3 h. The resin was removed by filtration and the crude peptide was recovered by precipitation with cold anhydrous ethyl ether to give a white powder which was purified by RP-HPLC on a semi-preparative C18-bonded silica column (Vydac 218TP1010, 1.0 x 25 cm) using a gradient of CH_3CN in 0.1% aqueous TFA (from 10 to 90% in 45 min) at a flow rate of 1.0 mL/min. The product was obtained by lyophilization of the appropriate fractions after removal of the CH_3CN by rotary evaporation. Analytical RP-HPLC indicated a purity > 98% and molecular weights were confirmed by FAB-MS (Fisons mod. Prospec) or HR-MS (Kratos Analytical mod. Kompact) (Supporting Information).

General Method of Oxidation and Cyclization. The peptides were oxidized by the syringe pump method previously reported.[65] The linear peptide (300-500mg) was dissolved in 40ml of 50%H_2O/25% acetonitrile/25% methanol, and nitrogen gas was passed through the solution for 20 min. Five milliliters of saturated ammonium acetate solution were added, and the pH was taken to 8,5 with NH_4OH. The peptide solution was then added at room

temperature via syringe pump to a stirred oxidant solution. The oxidant solution was prepared as follows: 2 equiv of potassium ferricyanide were dissolved in 400ml of H_2O/200ml of acetonitrile /200ml of methanol. To this solution was added 100 ml of saturated ammonium acetate, and the pH was then taken to 8,5 with NH_4OH. The peptide solution was added at such a rate that approximately 10mg of peptide were delivered per hour per liter of the oxidant. After the addition of peptide was complete, the reaction mixture was stirred for an additional 5-6h and then taken to pH 3.5 with glacial acetic acid. Amberlite IRA-68 (Cl - form) was added to remove the iron ions and the solution stirred for 20min and then filtered. The solution was concentrated using a rotary evaporator at 30°C and then lyophilized. The material thus obtained was dissolved in glacial acetic acid, filtered to remove inorganic salts, and relyophilized. The crude cyclic peptides were purified by preparative HPLC on the system described above, using a gradient of 100% buffer for 20min, then 0-20% acetonitrile in 5 min, followed by 20-60% acetonitrile in 40 min, all at 40ml/min. Again the peptides eluted near 50% organic /50% buffer. The purity of the cyclic peptides was checked by analytical HPLC (C-18 column, Vydac 218TP104, 4,6mm X 25cm), using a Shimadzu SPD 10A vp with detection at 230 and 254 nm and by TLC in four solvent systems in silica gel with detection by UV light, iodine

vapours, and ninhydrin. The analytical data of the compounds synthesized in this work are given in the Supporting Information.

Organ Bath Experiments. The experimental procedures employed in this study were approved by Institutional Animal Care and Use Committee and carried out in accordance with the legislation of Italian authorities (D.L. 116 27/01/1992), which complies with European Community guidelines (CEE Directive 86/609) for the care and use of experimental animals.

Male albino rats (Wistar strain, 275–350 g) were euthanized by cervical dislocation, under ether anaesthesia. The thoracic aorta was cleared of surrounding tissue and excised from the aortic arch to the diaphragm. From each vessel, a helically cut strip was prepared, and then it was cut into two parallel strips. The endothelium was removed by gently rubbing the vessel intimal surface with a cotton-tip applicator; the effectiveness of this manoeuvre was assessed by the loss of relaxation response to acetylcholine (1 μM) in noradrenaline (1 μM) precontracted preparations. All preparations were placed in 5ml organ baths filled with normal Krebs solution warmed at 37° C and oxygenated with 95% O_2, 5% CO_2. The tissues were connected to isotonic force transducers (Ugo Basile, VA, Italy) under a constant load of 5mN and motor activity was digitally recorded by an Octal Bridge Amplifier connected to PowerLab/8sp hardware system and

analyzed using the Chart 4.2 software (AD Instruments, Australia). After 60 min equilibration, tissue responsiveness was assessed by the addition of 1 μM noradrenaline followed by a further equilibration of 60 min.

To assess the agonist activity cumulative concentration-response curves to *h*U-II and to the agonist peptide under examination were constructed in paired aortic strips and responses obtained were normalized towards the control *h*U-II maximal contractile effect (E_{max}).

To assess the antagonist activity concentration–response curves to *h*U-II were constructed cumulatively in paired aortic strips. One strip was pretreated with vehicle (DMSO; 1-3 μl/ml) and used as a control, while the other strip was pretreated with the antagonist peptide under examination and, after a 30-min incubation period, *h*U-II was administered cumulatively to both preparations.

In each preparation only one cumulative concentration-response curve to *h*U-II was carried out and only one concentration of antagonist was tested. Concentration-response curves were analyzed by sigmoidal nonlinear regression fit using the GraphPad Prism 4.0 program (San Diego, CA, U.S.A.) to determine the molar concentration of the agonist producing the 50% (EC_{50}) of its maximal effect. Agonist activity of all compounds was expressed as pEC_{50}

(−log EC_{50}). The antagonist potency was expressed as apparent pK_B (−logK_B) calculated from the equation: pK_B = − (log [CR - 1] - log [antagonist concentration]) where the concentration-ratio (CR) is the ratio of equieffective concentrations (EC_{50}) of hU-II in the presence and absence of antagonist.[66, 67] The nature of the antagonism was checked by means of Schild analysis.

Binding experiments. All experiments were performed on membranes obtained from stable CHO-K1 cells expressing the recombinant human UT receptor (Euroscreen ES-440-M, Bruxelles, Belgium). Assay conditions were: TRIS-buffer (20mM, pH 7.4 at 37° C) added with $MgCl_2$ (5mM) and 0.5% BSA. Final assay volume was 0.1 ml, containing 1 μg membrane proteins. The radioligand used for competition experiments was [^{125}I]Urotensin II (specific activity 2000 Ci/mmol; Amersham Biosciences, Buckinghamshire, U.K.) in the range 0.07–1.4 nM (corresponding to 1/10–1/5 of its KD). Non-specific binding was determined in the presence of 1 μM of unlabelled *h*U-II, and ranged between 10–20% of total binding. Competing ligands were tested in a wide range of concentrations (1 pM – 10 μM). The incubation period (120 min at 37° C) was terminated by rapid filtration through UniFilter-96 plates (Packard Instrument Company), pre-soaked for at least 2 h in BSA 0.5%, and using a MicroMate 96 Cell Harvester (Packard Instrument Company). The filters were then

washed 4 times with 0.2 ml aliquots of Tris-HCl buffer (20mM, pH 7.4, 4°C). Filters were dried and soaked in Microscint 40 (50 µl in each well, Packard Instrument Company), and bound radioactivity was counted by a TopCount Microplate Scintillation Counter (Packard Instrument Company). Determinations were performed in duplicate. All binding data were fitted by using GraphPad Prism 4.0 in order to determine the equilibrium dissociation constant (K_d) from homologous competition experiments, the ligand concentration inhibiting the radioligand binding of the 50% (IC_{50}) from heterologous competition experiments. K_i values were calculated from IC_{50} using the Cheng-Prusoff equation ($K_i = IC_{50}/(1 + [\text{radioligand}]/K_d)$ according to the concentration and K_d of the radioligand.[56]

NMR Sample Preparation. 99.9% ^2H_2O were obtained from Aldrich (Milwaukee, USA), 98% SDS-d_{25} was obtained from Cambridge Isotope Laboratories, Inc. (Andover, USA), [(2,2,3,3-tetradeuterio-3-(trimethylsilanyl)]propionic acid (TSP) from MSD Isotopes (Montreal, Canada).

NMR Spectroscopy. The samples for NMR spectroscopy were prepared by dissolving the appropriate amount of peptide in 0.45 ml of ^1H_2O (pH 5.5), 0.05 ml of ^2H_2O to obtain a concentration 1-2 mM of peptides and 200 mM of SDS-d_{25}. NH exchange studies were performed dissolving peptides in 0.50 ml of ^2H_2O and 200 mM of

SDS-d_{25}. NMR spectra were recorded on a Varian INOVA 700 MHz spectrometer equipped with a z-gradient 5 mm triple-resonance probe head. All the spectra were recorded at a temperature of 25 °C. The spectra were calibrated relative to TSP (0.00 ppm) as internal standard. One-dimensional (1D) NMR spectra were recorded in the Fourier mode with quadrature detection. The water signal was suppressed by gradient echo.[68] 2D DQF-COSY,[37, 38] TOCSY [39], NOESY [40] and PE-COSY [69] spectra were recorded in the phase-sensitive mode using the method from States.[70] Data block sizes were 2048 addresses in t_2 and 512 equidistant t_1 values. Before Fourier transformation, the time domain data matrices were multiplied by shifted $\sin^2$ functions in both dimensions. A mixing time of 70 ms was used for the TOCSY experiments. NOESY experiments were run with mixing times in the range of 150-300 ms. The qualitative and quantitative analyses of DQF-COSY, TOCSY, and NOESY spectra, were obtained using the interactive program package XEASY.[41] $^3J_{\mathrm{HN\text{-}H\alpha}}$ coupling constants were obtained from 1D ^{1}H NMR and 2D DQF-COSY spectra. $^3J_{\mathrm{H\alpha\text{–}H\beta}}$ coupling constants were obtained from 1D ^{1}H NMR and 2D PE-COSY spectra, the last performed with a β flip angle of 35°. The temperature coefficients of the amide proton chemical shifts were calculated from 1D ^{1}H NMR and 2D TOCSY

experiments performed at different temperatures in the range 25°-40 °C by means of linear regression.

Structural Determinations. The NOE-based distance restraints were obtained from NOESY spectra collected with a mixing time of 200 ms. The NOE cross peaks were integrated with the XEASY program and were converted into upper distance bounds using the CALIBA program incorporated into the program package DYANA.[71] Cross peaks which were overlapped more than 50% were treated as weak restraints in the DYANA calculation. In a first step only NOE derived constraints (Supporting Information) were considered in the annealing procedures. Overall, 76 meaningful NOE-derived restraints (9 NOEs per residue; that is: 32 intraresidue, 32 sequential, 11 medium-range, and 1 long-range) for peptide **14**, and 73 (9 NOEs per residue; that is: 34 intraresidue, 29 sequential, 9 medium-range, and 1 long-range) for peptide **16**, were used as input for the calculation. For each examined peptide, an ensemble of 200 structures was generated with the simulated annealing of the program DYANA. An error-tolerant target function (tf-type=3) was used to account for the peptide intrinsic flexibility. Non standard Pen, D-Trp, Orn, and Tic residues were added to DYANA residue library using MOLMOL.[72] From these structures we could univocally determine the hydrogen bond atom acceptors corresponding to the slowly exchanging NH's

previously determined for each peptide. In a second DYANA run these hydrogen bonds were explicitly added as upper and lower limit constraints (NH of Phe^6 with CO of Tyr^9, and NH of Tyr^9 with CO of Phe^6), together with the NOE derived upper limit constraints (Supporting Information). The second annealing procedure produced 200 conformations from which 50 structures were chosen, whose interprotonic distances best fitted NOE derived distances, and then refined through successive steps of restrained and unrestrained EM calculations using the Discover algorithm (Accelrys, San Diego, CA) and the consistent valence force field (CVFF) [73] as previously described.[34] Coupling constants were not used in the constrained simulated annealing calculation, however, backbone and side chain conformations are in accordance with the experimental $^3J_{HN-H\alpha}$ and $^3J_{H\alpha-H\beta}$ coupling constants, respectively. The final structures were analyzed using the InsightII program (Accelrys, San Diego, CA). Graphical representation were carried out with the InsightII program (Accelrys, San Diego, CA). RMS deviation analysis between energy minimized structures were carried out with the program MOLMOL.[72]

h-UTR Models and Docking. The theoretical structure of the *h*-UT receptor, in the inactive state, was generated by homology modeling based on the crystal structure of bovine rhodopsin (PDB

code 1F88),[42] as previously described.[43] The three-dimensional model of the the *h*-UTR, in the active state, was constructed from the model structure of the bovine rhodopsin, proposed by Mosberg,[48] and was generated by homology modeling following the same steps described for the inactive model.[43] To validate the reliability of the calculated models, the program PROCHECK,[74, 75] which automatically checks the stereochemical accuracy, packing quality, and folding reliability, was employed. All amino acids in the α-helices were located in the favored region of the right-handed α-helix in the Ramachandran plot. From calculated ω angles, there were no cis peptide bonds in the calculated *h*-UTR model. All Cα atoms except Cys displayed *S*-chirality. For the packing quality, there were no bump regions in the calculated *h*-UTR models.

The peptides Urantide and P5U were manually docked in the suspected binding site of the *h*-UTR_i and *h*-UTR_a, respectively. Employing the criteria described in the Results section, we generated 10 poses for both urantide/*h*-UTR_i and P5U/*h*-UTR_a complexes. Refinement of each pose was achieved by in vacuo energy minimization with the Discover algorithm (50 000 steps; ε = 1). The backbone atoms of the TM and IL domains of the *h*-UTR were held in their position; the ligand and EL's were free to relax. Minimization was followed by a brief MD simulation period (200 ps). After this

period, many poses (7 and 8 out of the 10 poses for urantide and P5U, respectively) were discarded since the ligand was driven away from its starting position and lost the salt-bridge with the conserved Asp residue. The other poses (3 for urantide and 2 for P5U) converged to a very similar conformation (rmsd of the backbone atoms < 1 Å) and the lowest energy complex for each ligand was chosen as starting point for subsequent 2 ns MD simulations (time step = 1 fs, T = 300 K). The backbone coordinates of the TM helices were fixed during the MD simulations because, without environmental constraints (i.e. lipid bilayer and water solution), they can move away from each other and can lose their helical structure. Fixing TM helices should still allows for sufficient spatial/conformational sampling of the docked complexes since the ligand, in the discarded poses (see above), significantly changed both the initial position and conformation, after the MD simulations. An average structure was calculated from the last 1 ns trajectory and energy-minimized using the steepest descent and conjugate gradient methods until a rmsd of 0.05 Kcal/mol per Å was reached. Starting from these energy minimized structures, the model complexes of the Urantide and P5U analogues **13-16** were obtained. The Asp^4 was replaced with a Lys or a Tic residue and the complex was minimized first relaxing only the replaced residue (10 000 steps); then relaxing all the ligand (40 000 steps). Whereupon, a 200 ps MD

simulations was performed. The average structure of the last 100 ps was re-minimized until a rmsd of 0.05 Kcal/mol per Å was reached. For the docking of urantide within UTR_a (switching of the ligands), we started from the optimized P5U/UTR_a complex and superposed the NMR derived urantide structure with that of P5U (backbone atoms of residues 5-10). Then, we removed the P5U structure. The complex was minimized relaxing the ligand (40 000 steps). Whereupon, a 200 ps MD simulations was performed. The average structure of the last 100 ps was re-minimized until a rmsd of 0.05 Kcal/mol per Å was reached. Analogous steps were taken for the P5U/UTR_i complex. All the MD trajectories were analyzed by means of the Analysis module of InsightII package. Molecular graphics images of the complexes were produced using the UCSF Chimera package.[76] Rescoring of the ligand/receptor models according to the AutoDock4 (AD4) [45-47] scoring function was attained using a script provided within the MGLTools software package (http://mgltools.scripps.edu/).

1.2 Conformational Study on Cyclic Melanocortin Ligands and New Insight into their Binding Mode at the MC4 Receptor

The melanocortin receptors are involved in many physiological functions, including pigmentation, sexual function, feeding behavior, and energy homeostasis, making them potential targets to treat obesity, sexual dysfunction, etc. Understanding the basis of the ligand-receptor interactions is crucial for the design of potent and selective ligands for these receptors.

The conformational preferences of the cyclic melanocortin ligands MTII (Ac-Nle^4-c[Asp^5-His^6-*D*Phe^7-Arg^8-Trp^9-Lys^{10}]-NH_2) and SHU9119 (Ac-Nle^4-c[Asp^5-His^6-*D*Nal(2')^7-Arg^8-Trp^9-Lys^{10}]-NH_2), which show agonist and antagonist activity at the *h*-MC4R, respectively, were comprehensively investigated by solution NMR spectroscopy in different environments. In particular, water and water/DMSO (8:2) solutions were used as isotropic solutions and an aqueous solution of DPC (dodecylphosphocholine) micelles was used as a membrane mimetic environment. NMR derived conformations of these two ligands were docked within *h*-MC4R models. NMR and docking studies revealed intriguing differences which can help explain the different activities of these two ligands.

1.2.1 Introduction

The melanocortin family contains five human receptors (*h*-MC1R-*h*-MC5R) cloned to date and stimulates the cAMP second messenger and other signal transduction pathways.[77-84] Melanocortin receptors belong to the class A superfamily of rhodopsin-like G-protein-coupled receptors (GPCRs), characterized by having seven transmembrane α-helices (TM1-TM7) linked by three extracellular and three intracellular loops.[78, 81, 82] The endogeneous agonists of the MCRs, the melanocortins, are a family of peptides comprised of α, β-, and γ-melanocyte stimulating hormones (MSH) and adreno-corticotropic hormone (ACTH). They are derived from post-translational modification of a common precursor, proopiomelanocortin (POMC).[85] The natural melanocortins are all agonist for *h*-MCRs with exception of the *h*-MC2R, for which only ACTH is a full agonist.[86] Also, synthetic melanocortins have different pharmacological profiles for the five *h*-MCRs. For example, NDP-α-MSH [87] and MTII [88] are agonist for all *h*-MCRs except the *h*-MC2R.[89] There are also the endogeneous protein antagonists known as agouti and agouti-related protein (AGRP).[90, 91] Interaction of these effectors with MCRs results in the modulation of numerous biological functions which include among others regulation of skin pigmentation (MC1R), steroid production (MC2R), the

immune response, thermoregulation, food intake, sexual function (MC3R and MC4R), and stress-induced anxiety and depression.[92-97] The MC4R subtype is regarded as a potential drug target, because it is involved in feeding and sexual behaviour.[90, 97-100] Mammals with a defective MC4R gene, which is expressed in the brain, are characterized by obese phenotype and increased food intake.[101-103] Pharmacological studies indicate that activation of the MC4R in rodents [100] and humans [93] modulates erectile function. Consequently, research efforts have been focused on the development of potent and MC4R-selective agonists as potential antiobesity drugs or as treatments for sexual dysfunction. [104] On the other hand, a MC4R antagonist that blocks the satiety-inducing effect of α-MSH could be helpful for treatment of anorexia or cancer cachexia.[105]

A molecular understanding of MTII and SHU9119 activity at the *h*-MC4R may have important implications in the design of drugs. In addition, the identification of the essential amino acid residues of the *h*-MC4R responsible for MTII agonism and SHU9119 antagonism should be important for understanding the signalling events that regulate the melanocortin system under physiologic conditions.[106, 107]

Hence, we first studied the conformational preferences of the cyclic melanocortin ligands MTII, and SHU9119 (Table 5), agonist

and antagonist at *h*-MC4R, respectively. Conformational analysis was carried out by NMR spectroscopy in water, water/DMSO solutions, and 200 mM aqueous solution of DPC as membrane mimetic environment. Then, NMR derived structures of MTII and SHU9119 were docked within the *h*-MC4 receptor model, in the active and inactive state, respectively.

Table 5. Ligand Sequences

Peptide	Sequence
MTII	Ac-Nle^4-c[Asp^5-His^6-***D*Phe**^{7}-Arg^8-Trp^9-Lys^{10}]-NH_2
SHU9119	Ac-Nle^4-c[Asp^5-His^6-***D*Nal(2')**^{7}-Arg^8-Trp^9-Lys^{10}]-NH_2
NDP-MSH	Ser^1-Tyr^2-Ser^3-Nle^4-Glu^5-His^6-***D*Phe**^{7}-Arg^8-Trp^9-Gly^{10}-Lys^{11}-Pro^{12}-Val^{13}-Gly^{14}

1.2.2 Results

Chemistry. Peptides were synthesized using the solid phase approach and standard Fmoc methodology in a manual reaction vessel (Experimental Section).[35]

The purification was achieved using a semi-preparative RP-HPLC C-18 bonded silica column (Vydac 218TP1010). The purified peptide was 98% pure as determined by analytical RP-HPLC. The correct molecular weight and composition of the peptide was confirmed by mass spectrometry and amino acid analysis (Table S5, Supporting Information).

NMR Analysis. Complete ^{1}H NMR chemical shift assignments were achieved for MTII and SHU9119 according to the Wüthrich procedure [36] via the usual systematic application of DQF-COSY [37, 38], TOCSY [39], and NOESY [40] experiments (Tables S6-S13, Supporting Information) with the support of the XEASY software package.[41] The conformational preferences for the two peptides were investigated by solution NMR spectroscopy in different solvent environments. In particular, water and water/DMSO (8:2) solutions were used as isotropic solutions and 200 mM aqueous solution of DPC (dodecylphosphocholine micelles) was used as a membrane mimicking environment.

Water solution. NMR analysis was performed in water at pH 5

and a peptide concentration of about 2 mM. First, we analyzed the peptides at 25 °C. Both peptides showed similar NMR parameters (Tables S6-S7) as previously reported.[108, 109] Almost all NMR parameters indicate structural flexibility: a) temperature effects $|\Delta\delta/\Delta T| > 6$ ppb/K; b) $^{3}J_{HN\text{-}H\alpha}$ coupling constants are all within the range 6-8 Hz; c) No standard α-helix or *β*-sheet structure from Hα CSI (chemical shift index) values [110] (Figure S17, Supporting Information); d) No unambiguous medium- or long-range backbone NOE connectivities were found in the ROESY or NOESY. Strong $d_{\alpha N}(i, i+1)$ NOEs, which are generally observed in extended structures, appeared along almost the entire length of the peptides.

To reduce the conformational flexibility, we acquired the spectra also at 5°C. At this temperature, most of the NMR parameters did not change significantly (Tables S8-S9), though improvements of the signal quality in the NOESY spectra were observed. Weak $d_{\alpha N}(i, i+2)$ NOEs between Nle^{4} and His^{6} and between His^{6} and Arg^{8} could be observed. Also the methyl protons of the N-terminal acetyl group show a weak NOE contact with the Hα of Asp^{5}. Medium $d_{NN}(i, i+1)$ NOE between *D*Phe^{7} (*D*Nal(2')^{7}) and Arg^{8} was observed. Among the possible observable contacts, the $d_{\alpha N}(i, i+2)$ NOE between Asp^{5} and *D*Phe^{7} could not be observed due to spectral overlap.

Cryoscopic solution. To further reduce the peptide

conformational flexibility, NMR spectra were acquired at -10 °C in a cryomixture solution of water/DMSO 8:2. Such cryomixtures have been shown to produce physico-chemical conditions compatible with those of biological fluids.[111] Again, most of the NMR parameters did not change significantly (Tables S10-S11). Apart from the two $d_{\alpha N}(i, i+2)$ NOEs observed also in water (5 °C) the NOESY spectra showed $d_{\alpha N}(i, i+2)$ NOEs between Asp^5 and $D\text{Phe}^7$ ($D\text{Nal}(2')^7$). Furthermore, $d_{\beta N}(i, i+3)$ NOEs between Asp^5 and Arg^8 and $d_{NN}(i, i+2)$ NOEs between His^6 and Arg^8 also were observed.

DPC micelles. Several NMR parameters indicate that MTII and SHU9119 are highly structured in DPC solution. In particular, $^3J_{\text{HN-H}\alpha}$ coupling constants (Tables S12-S13) and Hα CSI values (Figure S17) and many NOE signals (Tables S14-S15, Supporting Information) clearly point to a folded structure encompassing the N-terminal residues (4-7) and extended conformation of residues 8-9. Non-trivial medium range NOE interactions, among which $d_{\alpha N}(i, i+2)$ 4-6, 5-7, 6-8, $d_{NN}(i, i+2)$ 6-8, and $d_{\beta N}(i, i+3)$ 5-8, are observed indicating that the membrane mimetic environment stabilizes intrinsic conformational tendencies of the peptide. Additional *medium* and *long* range NOE contacts were observed. In particular, various NOEs connected the Nle^4 side chain with both $D\text{Phe}^7$ ($D\text{Nal}(2')^7$) and Trp^9 aromatic moieties indicating spatial proximity of these side chains. Other

interesting contacts were observed between the methyl protons of the N-terminal acetyl group and the HN of Asp^5, and between amide protons of the C-terminal NH_2 group and the Hδ1 and Hε1 of Trp^9.

Structure Determination. NOE distance restraints obtained for MTII and SHU9119 in DPC micelles were used as the input data for a simulated annealing structure calculation using the program DYANA.[71] The annealing procedure produced 100 conformations from which 20 structures were chosen, whose interprotonic distances best fitted the NOE derived distances, and then refined through successive steps of restrained and unrestrained EM calculations using the Insight/Discover package (Accelrys Inc, San Diego, CA).

Structure Description. Superposition of the 10 lowest energy conformers of MTII and SHU9119 are shown in Figure 9. Since a *β*-turn may be defined as four consecutive non-helical residues that have a Cα(i)-Cα(i+3) distance < 7 Å, two *β*-turns that involve Nle^4 to *D*Phe^7 (*D*$Nal(2')^7$) and Asp^5 to Arg^8, can be identified. Examination of the backbone dihedral angles at the central (i+1, and i+2) residues of the turns showed that these turn structures most closely resembled type I (residue 4 to 7) and type II (residue 5 to 8) *β*-turns, although deviations from the standard dihedral angles of these two types of *β*-turn occurred (Table S16, Supporting Information). Residues 8 to 10 are in extended conformations. The side chain χ_1-angles of Asp^5,

Arg[8], Trp[9] and Lys[10] are also well defined, preferring *trans*, *gauche*-, *trans* and *gauche*- orientations, respectively. Side chains of Nle[4] and His[6] are more flexible. The *D*Phe[7] orientation in MTII is also well defined as *trans*. The *D*Nal(2')[7] orientation in SHU9119 is less defined showing an equilibrium between *trans* and *gauche*+ rotamers. These results are consistent with the measured $^{3}J_{H\alpha H\beta}$ coupling constants (Tables S12-S13).[112, 113]

The peptide surface has amphipathic nature. In fact, considering the *pseudo*-plane defined by the backbone atoms (green ribbon, Figure 9) the hydrophobic residues Nle[4], *D*Phe[7] (*D*Nal(2')[7]) and Trp[9] lie on one side (right in Figure 9) while the positively charged residues His[6] and Arg[8] lie on the other side.

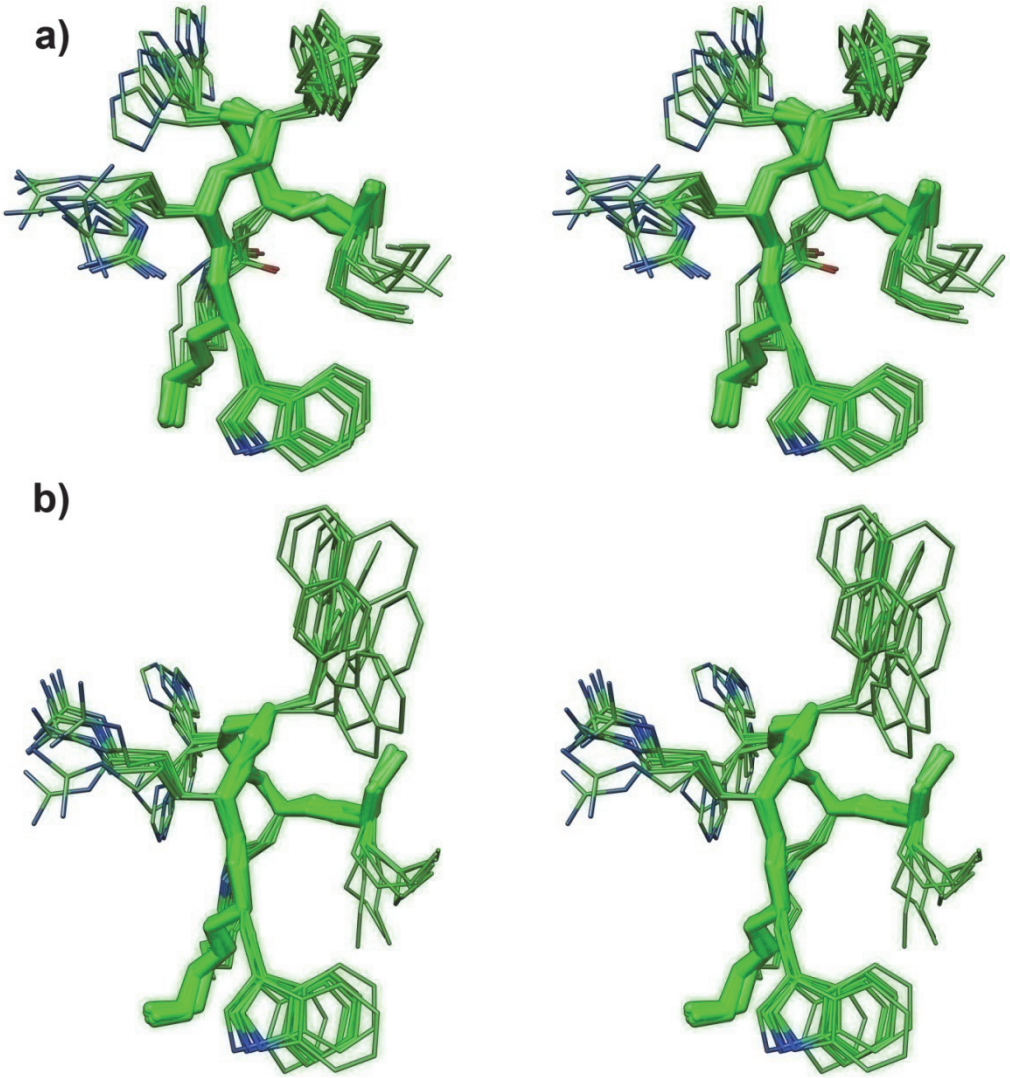

Figure 9. Stereoviews of the 10 lowest energy conformers of MTII (a), and SHU9119 (b). Structures were superimposed using the backbone heavy atoms of residues 5-10. Heavy atoms are shown with different colours (carbon, green; nitrogen, blue; oxygen, red). Hydrogen atoms are not shown for clarity.

Docking Studies. NMR derived structures of MTII and SHU9119 were docked within the *h*-MC4R models proposed by Mosberg.[114, 115] In particular, the agonist MTII was docked within an "active state" model (*h*-MC4R$_a$), while the antagonist SHU9119 was docked within an "inactive state" model (*h*-MC4R$_i$). Figure 10 shows a snake-like diagram of the *h*-MC4R sequence.

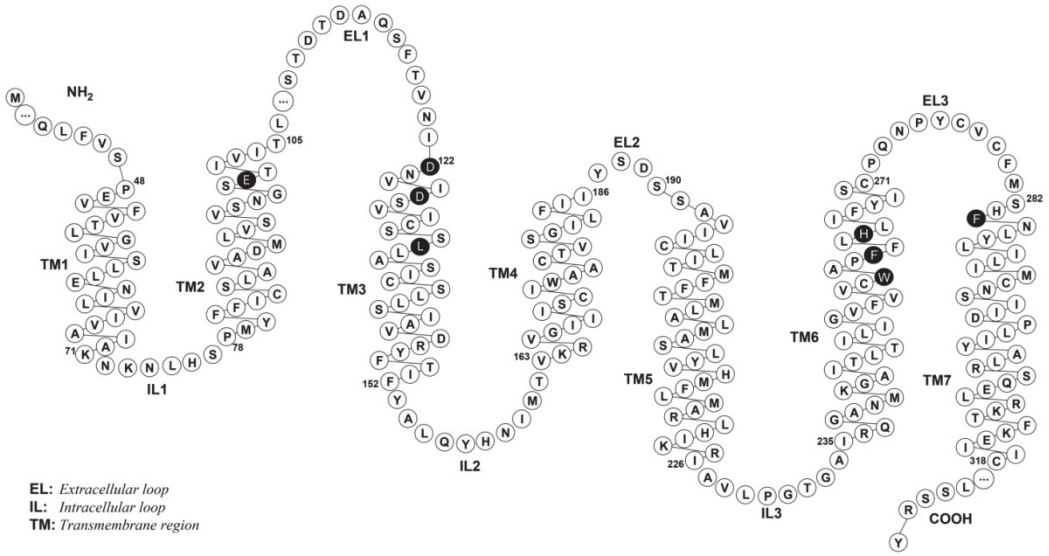

Figure 10. Snake-like diagram of the h-MC4R sequence. This plot was generated with the RbDe software.[116] Black residues indicate that mutation data are available. The ' . . .' indicates hidden residues (see reference [114] for the complete sequence).

Since the currently available docking programs may not work very well for peptide compounds (more than eight rotatable bonds) [117], manual docking was conducted. The NMR-derived MTII structure was placed in between the trans-membrane domains of the *h*-MC4R$_a$. The following criteria were employed to achieve meaningful docking modes: (i) The positively charged side of the amphipathic surface of the peptides should be close to the carboxylate groups of Asp122, Asp126, and Glu100, as suggested by several mutagenesis studies [114, 115, 118-125]; (ii) *D*Phe^7 residue should point towards Leu133 residue as suggested by a mutagenesis study [118]; (iii) No steric clashes should occur between any atom. To assess the stability

of the MTII/*h*-MC4R$_a$ complex we analyzed the potential ligand/receptor interactions, energy minimization and MD simulations for 1 ns at a constant temperature of 300°K. During the MD simulation, the ligand, the EL's, and all the receptor side chains were allowed to relax, while the TM's and intracellular loops (ILS) backbone atoms were held frozen. The distances between the peptide and the key receptor residues were monitored along the complete 1 ns MD trajectory (Supporting Information). The mean structure of the last 0.5 ns of MD was energy minimized and used for subsequent analysis.

Table 6. MTII/*h*-MC4R$_a$ Interactions

Residue[a]	Surrounding residue
Nle[4]	Val193(TM5), **His264**[b] (TM6), **Leu265** (TM6), **Tyr268** (TM6)
Asp[5]	
His[6]	**Asp122** (TM3), Asn123(TM3), **Asp126** (TM3)
*D*Phe[7]	**Asp126** (TM3), **Ile129** (TM3), **Leu133** (TM3), **Phe184** (TM4), **Phe261** (TM6), **Phe284** (TM7), **Leu288** (TM7)
Arg[8]	**Glu100** (TM2), **Asp122** (TM3), **Ile125** (TM3), **Asp126** (TM3), **Ile129**(TM3)
Trp[9]	**His264** (TM6), **Phe267** (TM6), Pro272 (EL3), Val278 (EL3), Phe280 (EL3), **Phe284** (TM7)
Lys[10]	Tyr276 (EL3), Val278 (EL3), Met281 (EL3)

[a] For sake of clarity, the residue numbers of the ligands are reported as superscript while those of the receptor are not. [b] Receptor residues involved in mutagenesis studies are shown in bold.

To inspect the variations in the ligand conformation, the rmsd with the respect to the starting structure was calculated. Interestingly, the rmsd of the MTII backbone atoms turned out to be stable throughout all of the MD simulations ($0 < \text{rmsd} < 0.8$ Å), indicating that the peptide settles into the receptor-binding site in a stable conformation. Also the side chain orientations are those described by NMR. In particular, the *D*Phe^7 and Trp^9 side chain prefer a *trans* orientation about χ_1 angle ($\chi_1 \approx 160°$ for *D*Phe^7, $\chi_1 \approx -163°$ for Trp^9). As shown in Figure 11a, the hypothetical binding site of MTII is located among TM2-TM7, and EL3. C- and N-terminal residues point towards the extracellular side. The binding mode of the peptide is determined mainly by the interactions shown in Figure 11b and summarized in Table 6.

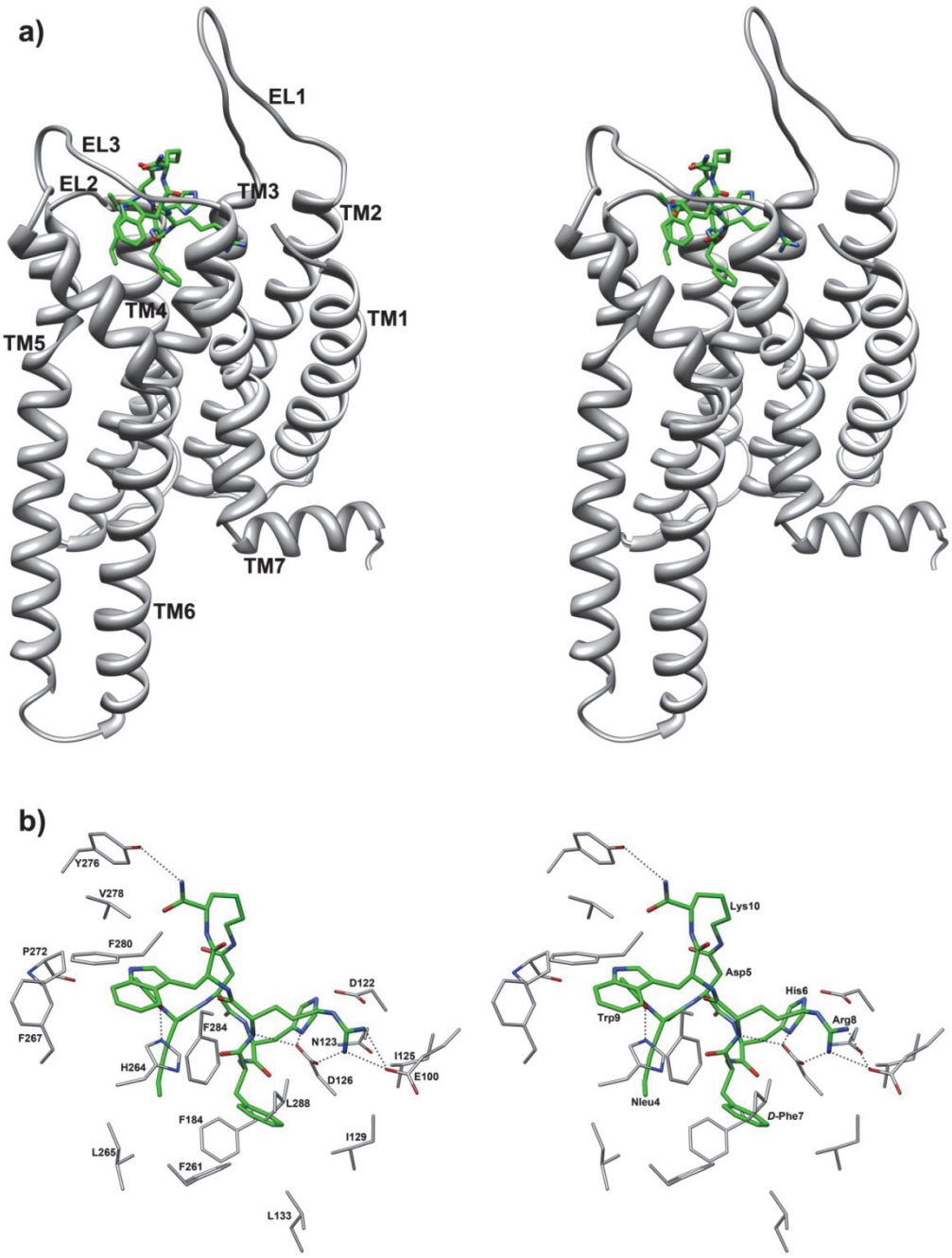

Figure 11. (a) Stereoview of *h*-MC4R$_a$ model complexed with MTII. MTII heavy atoms are shown with different colours (carbon, green; nitrogen, blue; oxygen, red). Hydrogen atoms are not shown for clarity. Receptor backbones are represented in gray and labeled. (b) Stereoview of MTII within the binding pocket of *h*-MC4R$_a$. Hydrogen bonds are represented with dashed lines.

In particular, (i) a tight charge-reinforced hydrogen-bonding network involving the carboxylate groups of Glu100 and Asp126 with the protonated guanidinium group of Arg^8 of MTII are established. The guanidinium group of Arg^8 is also involved in an electrostatic interaction with the carboxylate group of Asp122. Such interactions, which we assume to be anchoring points of the ligand to the *h*-$MC4R_a$, remained stable during the entire MD simulation (Figure S18, Supporting Information). The oxygen atoms of the carboxylate of Asp126 form a charge-reinforced hydrogen bond with the protonated imidazole group of His^6, which was not stable during the MD simulation (Figure S18). (ii) Two hydrophobic pockets, delineated by residues listed in Table 6, host the side chains of *D*Phe^7, and Trp^9 of MTII. Particularly, the side chain of *D*Phe^7 occupies the hydrophobic pocket involving residues Ile129, Leu133, Phe184, Phe261, Phe284, while the indole system of Trp^9 is surrounded by Phe280, Pro272, Phe267, Phe284 and appears to be optimally oriented for a π-stacking interaction with the imidazolic system of His264. iii) Terminal groups also contribute to the complex stabilization. The Nle^4 side chain is close to Val193 and Tyr268. The acetyl group CO of Nle^4 (N-terminal) engages hydrogen bonds with imidazole NHε of His264. Amide group NH_2 of Lys^{10} (C-terminal) established a hydrogen bond with the phenolic OH of Tyr276. These H-bonds are not stable during

the MD production run (data not shown).

The NMR-derived SHU9119 structure was placed within the trans-membrane domains of the *h*-MC4R$_i$ model, following the same criteria used for MTII (see above) to achieve meaningful binding interactions. Energy minimization and MD simulations (1 ns) were run to assess the stability of the SHU9119/*h*-MC4R$_i$ complex and to analyze the potential ligand/receptor interactions. The mean structure of the last 0.5 ns of MD was extensively minimized and used for subsequent analysis. SHU9119 backbone atoms turned out to be stable throughout all of the MD simulations ($0 < \text{rmsd} < 0.9$ Å), indicating that the peptide settles into the receptor-binding site in a stable conformation. Also the side chain orientations are those described by NMR. In particular, Trp^9 prefers a *trans* orientation about the χ_1 angle ($\chi_1 \approx 175°$). Finally, the *D*Nal(2')^7 side chain adopts a *gauche*+ conformation ($\chi_1 \approx 80°$).

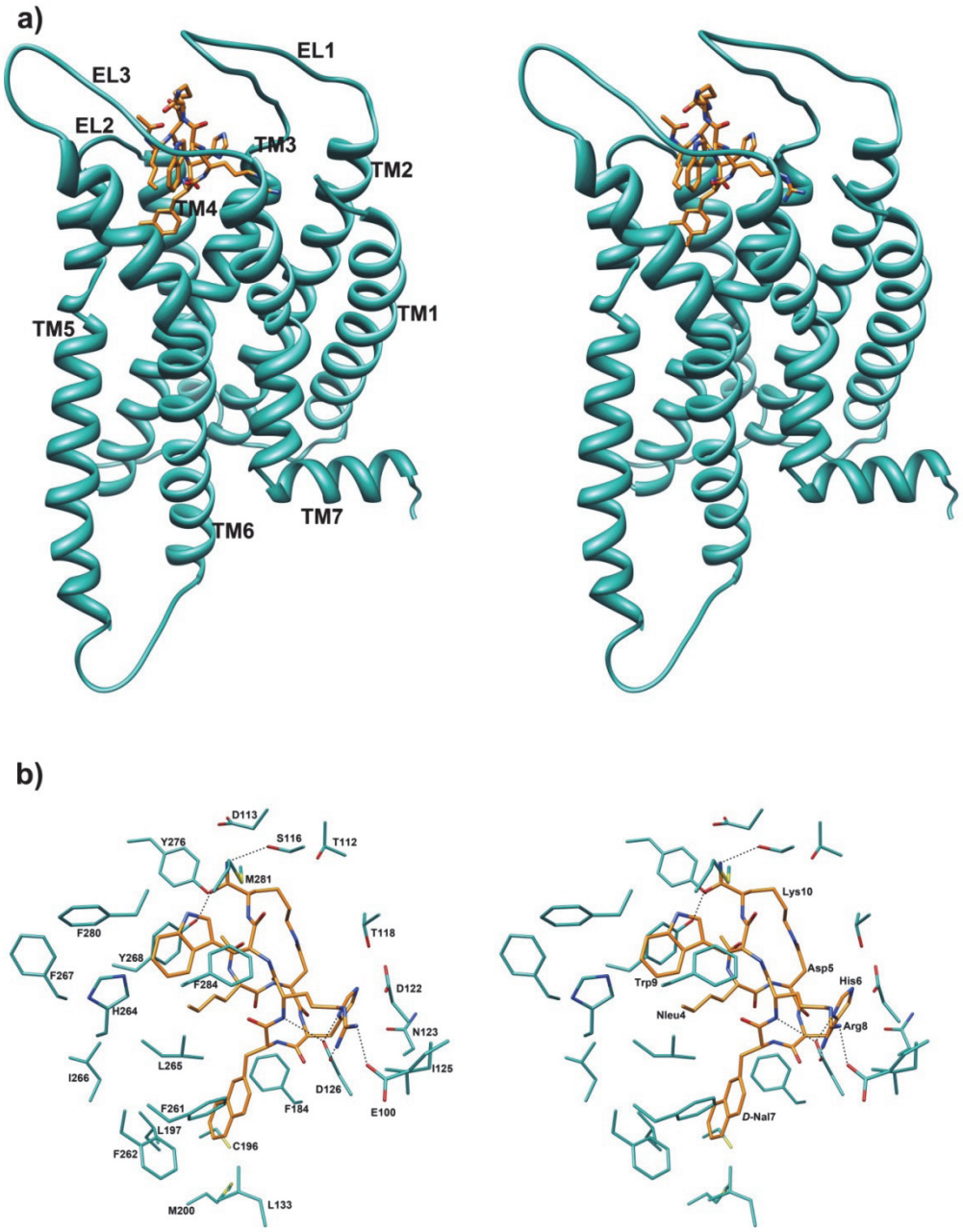

Figure 12. (a) Stereoview of *h*-MC4R$_i$ model complexed with SHU9119. SHU9119 heavy atoms are shown with different colours (carbon, orange; nitrogen, blue; oxygen, red). Hydrogen atoms are not shown for clarity. Receptor backbones are represented in cyan and labeled. (b) Stereoview of SHU9119 within the binding pocket of *h*-MC4R$_i$. Hydrogen bonds are represented with dashed lines.

Table 7. SHU9119/*h*-MC4R$_i$ Interactions

Residue[a]	Surrounding residue
Nle[4]	**His264**[b] (TM6), **Leu265** (TM6), **Tyr268** (TM6), Tyr276(EL3)
Asp[5]	**Phe184** (TM4)
His[6]	Thr118 (EL1), **Asp122** (TM3), Asn123 (TM3), **Asp126** (TM3), **Phe184** (TM4)
*D*Nal[7]	**Leu133 (TM3)**, **Phe184** (TM4), Cys196 (TM5), Leu197 (TM5), Met200 (TM5), **Phe261** (TM6), **Phe262** (TM6), Leu265 (TM6)
Arg[8]	**Glu100** (TM2), **Asp122** (TM3), Ile125 (TM3), **Asp126** (TM3),
Trp[9]	**His264** (TM6), Leu265 (TM6), **Tyr268** (TM6), **Phe267** (TM6), Phe280 (EL3), Met281 (EL3), **Phe284** (TM7)
Lys[10]	Thr112 (EL1), Asp113 (EL1), Ser116 (EL1), Thr118 (EL1), **Tyr268** (TM6), Tyr276 (EL3), Val278 (EL3), Met281 (EL3)

[a] For sake of clarity, the residue numbers of the ligands are reported as superscript while those of the receptor are not. [b] Receptor residues involved in mutagenesis studies are evidenced in bold.

As shown in Figure 12a, the hypothetical binding site of SHU9119 is located among TM2-TM7, and EL3. C- and N-terminal residues point towards the extracellular side. The binding mode of the peptide is determined mainly by the interactions showed in Figure 12b and Table 7. In particular, (i) considering Arg[8] and His[6], the same interactions observed in the MTII/h-MC4Ra complex are observed also for SHU9119. Again, Hbonds involving the Arg[8] guanidinium group remained stable during the whole MD production run (Figure S19, Supporting Information), while those of His[6] were not. (ii) Two hydrophobic pockets, involving the residues listed in Table 7, host the aromatic side chains of *D*Nal(2')[7], and Trp[9] of SHU9119. These

pockets only partially overlap with those hosting the aromatic side chains of MTII. Particularly, the side chain of *D*Nal(2')[7] occupy the hydrophobic pockets involving residues Leu133, Phe184, Cys196, Leu197, Met200, Phe261, Phe262, Leu265, while the indole group of Trp[9] is surrounded by His264, Phe267, Met281, Phe284 and appears to be optimally oriented for a π-stacking interaction with the aromatic group of Tyr268. This is different from MTII, because Trp[9] in MTII makes π-stacking with His264. The Nle[4] side chain is close to Leu265, Tyr268, and Tyr276. The acetyl group CO of Nle[4] (N-terminal) in SHU9119 isn't involved in hydrogen-bonding. Finally, the amide group NH_2 and the oxygen atom of the terminal carboxamide group of Lys[10] (C-terminal) established two hydrogen bonds: with the OH of Ser116 and with the phenolic OH of Tyr268. These Hbonds are not stable during the MD production run (data not shown).

1.2.3 Discussion

We investigated the conformational preferences of the cyclic melanocortin ligands MTII and SHU9119 by solution NMR spectroscopy in different environmental situations: water, water/DMSO (8:2) and an aqueous solution of DPC (dodecylphosphocholine). In water and water/DMSO cryoscopic mixture, NMR parameters were very similar for both peptides and indicate structural flexibility. A few NOEs, however, point to a tendency of the peptides to form a turn-helical conformation at the N-terminus (residue 4-8). The data could be indicative of a nascent helix in solution.[126] The nascent helix consists of a population of different conformations, in which a significant proportion contains backbone conformations in the α-region of (ϕ, ψ) space in the Ramachandran plot, rather than of any single defined solution conformation.

In DPC micelle solution, the peptides exhibited a higher conformational stability. The use of micelles to study the conformational properties of peptides has been described in section 1.1.3.[50-55]

Two consecutive β-turns that involved Nle^4 to *D*Phe^7/*D*Nal(2')^7 (distorted type I) and Asp^5 to Arg^8 (distorted type II) and a short extended segment along residues Trp^9 and Lys^{10} were observed in the

calculated structures of MTII and SHU9119 (Figure 9 and Table S16). It is noteworthy that an amphiphilic molecular surface was obtained for the message sequence residues in both peptides. The main conformational difference observed in the structures of the two ligands was established in a different orientation of the *D*Phe^7 and *D*Nal(2')^7 side chains. *D*Phe^7 of MTII preferred the *trans* rotamer, while the *D*Nal(2')^7 side chain of SHU9119 was more flexible.

A type II β-turn structure encompassing residues 5-8 was already found by NMR analysis of MTII and SHU9119 in water solution.[108, 109] This β-turn led to stacking between the aromatic rings of His^6 and *D*Phe^7 in MTII while no aromatic stacking between His^6 and *D*Nal(2')^7 was found in SHU9119. This stacking was not observed in the structures obtained in DPC micelles. Considering the β-turn encompassing residues 4-7, it has never been observed in the structure of MTII or SHU9119. Interestingly, the presence of this turn is in accordance with the results of N-methylation of MTII backbone amide bonds. In fact, N-methylation of *D*Phe^7, which should destabilize this β-turn, caused a total loss of binding as well as adenylate cyclase activity at the *h*-MC4R (*h*-MC1R, *h*-MC3R and *h*-MC5R).[127] N-Methylation of Arg^8 caused a dramatic reduction of the binding (about 500-fold at the *h*-MC4R) but yielded a compound that retained full agonist activity toward all subtypes of melanocortin receptors.

To gain insight into the interaction mode of these ligands with the *h*-MC4R, we first undertook a docking study between MTII and *h*-MC4R model. Since the crystal structure of a GPCR in the active conformation has not yet been obtained, we used a *h*-MC4R model in the "active state" proposed by Mosberg *et al*. (*h*-MC4R$_a$).[114] According to these authors, upon activation, the receptor experiences a rearrangement which involves mainly the TM6 helix. The TM6 helix shifts outward and rotates counterclockwise (viewed from the extracellular side) during activation, moving its intracellular end away from TM3 and toward TM5. As a result of this and other changes, the receptor structure tightens near its extracellular surface but opens up at the cytoplasmic side, providing a cavity for binding of the $G_{\alpha s}$ subunit. In the active state model, several side chains change their orientation among which Trp258, in accordance with earlier spectroscopic results.[128] Similar conformational changes upon activation of the MC4R were subsequently proposed also by Hogan *et al*.[121] During the manuscript preparation another model of the *h*-MC4R$_a$ has been published.[129] This model was based on recent crystal structures of the GPCR opsin in the ligand-free and in the G-protein-interacting conformations.[130, 131] Interestingly, our *h*-MC4R$_a$ model and that built by Chapman *et al*. are quite similar showing an rmsd of the TM's backbone heavy atoms of 2.0 Å (Figure S20, Supporting Information).

For the MTII/*h*-MC4R$_a$ complex, docking and the MD simulations (Figure 11) indicated that: (i) the structure adequately fits the binding site and is stable during the MD trajectory; (ii) the binding site, situated in the entrance of the TM bundle on the extracellular side, is formed by TM2-TM7, and EL3 (Figure 11a); (iii) the pharmacophore residues *D*Phe^7, the Arg^8 and Trp^9 side chains establish the highest number of interactions with the receptor. In particular, Arg^8 residue is involved in a charge-reinforced hydrogen bonding network with carboxylate groups of Glu100, Asp122, and Asp126 which was stable during the MD simulations (Figure S18). In contrast, the His^6 imidazole group participates only in an unstable hydrogen bond with Asp126 (Figure S18). Two wide hydrophobic pockets host the side chains of *D*Phe^7, and Trp^9 of MTII (Figure 11b). The N- and C-terminal groups point towards the extracellular side and are involved only in limited interactions with the receptor consistent with the observation that these termini can be substituted with retention of potent binding affinity.

The proposed binding mode is in qualitative accordance with the known structure-activity relationships of MTII. In fact, substitution of *D*Phe^7 or Trp^9, which show a large number of receptor interactions, with alanine resulted in compounds with very low affinities for *h*-MC4R (*h*-MC3R and *h*-MC5R).[132] The Arg^8 involved in stable

interactions with the receptor, its replacement with the neutral residue, alanine, led to an active analogue but with more than a 1000-fold reduced affinity at *h*-MC4R compared to the parent compound, in accordance with the stable interactions exhibited by this residue. In contrast, the substitution of His^6 with alanine yielded a peptide with activation and binding affinity similar to MTII towards the *h*-MC4R (*h*-MC3R and *h*-MC5R). Therefore, the imidazole group was shown not to be essential to binding of MTII with the *h*-MC4R (*h*-MC3R and *h*-MC5R). A similar result was reported for the 'core' peptide Ac-His^6-*D*Phe^7-Arg^8-Trp^9-amide in which the omission of histidine resulted in the tripeptide that was only 2-fold less potent at *h*-MC4R than the tetrapeptide.[124] Considering N-terminal acetyl group, an analogue of MTII without the acetyl group was as potent as MTII at the *h*-MC4R (*h*-MC3R and *h*-MC5R).[133] Replacement of Ac-Nle^4 with Ala or Ac-Ala yielded compounds with agonist potencies at *h*-MC4R similar to that of MTII. The analogue without both acetyl group and norleucine was 200-fold less active at *h*-MC4R. Also replacement of MTII residues with proline (Pro-scan) gave similar results. Proline replacement was acceptable only at Nle^4 and His^6 positions yielding compounds with agonist potencies at the *h*-MC4R similar to that of MTII.[133]

Interestingly, many residues of the receptor involved in the interaction with MTII were identified as molecular determinants of ligand binding by mutagenesis studies (Table 6).[107, 115, 118-124] In particular, His264 has been demonstrated to be essential for melanocortin peptide activation of the MC4R.[134] π-stacking interaction of imidazolic nucleus of His264 and indole system of Trp^9 can trigger the MC4R activation. Interestingly, this π-stacking interaction is not observed in the SHU9119/*h*-$MC4R_i$ complex described below.

A docking study between SHU9119 and *h*-$MC4R_i$ also was performed. The *h*-$MC4R_i$ model, built by Mosberg *et al*. and based on the rhodopsine crystal structure, was used.[115] The main differences between inactive and active models of *h*-MC4R were discussed above. The obtained complex (Figure 12) and the MD simulations indicated that SHU9119 positioning within the *h*-$MC4R_i$ is similar to that observed for MTII/*h*-$MC4R_a$ (Figure 12 and Figure 13). In particular, backbone atoms of MTII and SHU9119 are almost superimposable lying inside the TM2-TM7 bundle. Also the side chains of the positively charged residues His^6 and the Arg^8 show the same orientation and the Arg^8 residue is involved in a charge-reinforced hydrogen bonding network with carboxylate groups of Glu100,

Asp122, and Asp126 which was stable during the MD simulations period (Figure S19).

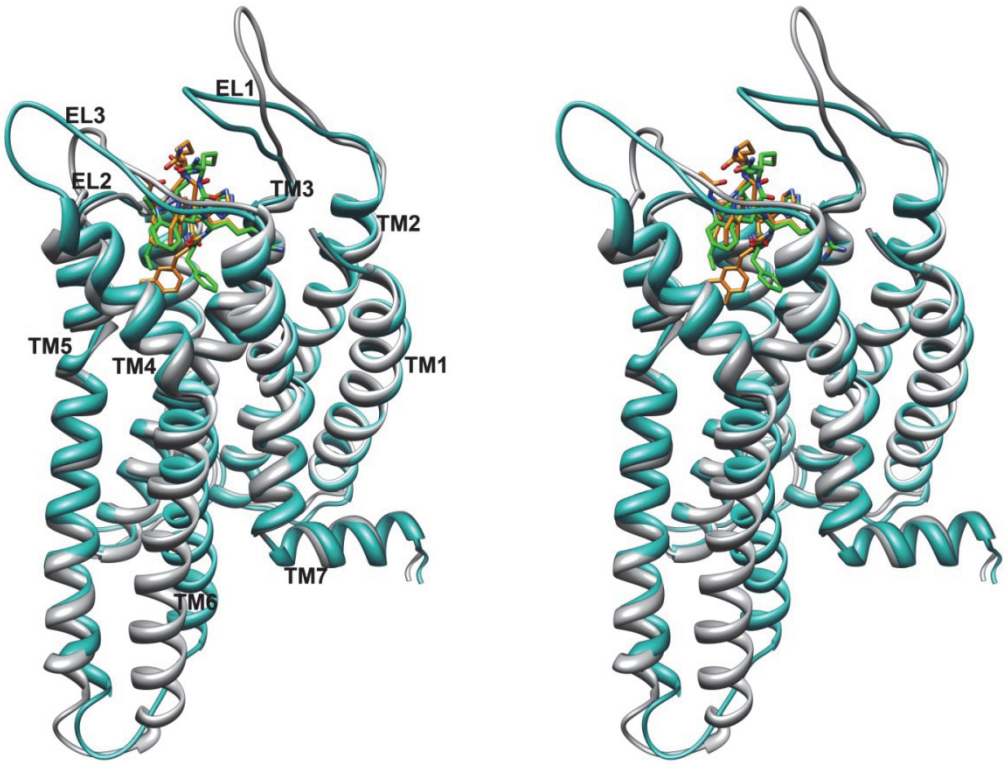

Figure 13. Stereoview of *h*-MC4R models in the active (gray) and inactive (cyan) conformations complexed with MTII (carbon, green; nitrogen, blue; oxygen, red) and SHU9119 (carbon, orange; nitrogen, blue; oxygen, red), respectively. The *h*-MC4R models are superimposed using the backbone heavy atoms of TM residues apart from TM6. Hydrogen atoms are not shown for clarity.

In contrast, the *D*Nal(2')^7 and Trp^9 binding pockets are quite different compared to those of the corresponding residues of MTII. These differences depend on the different orientations of the *D*Nal(2')^7 and Trp^9 side chains and on the movement of TM6 during activation.[115] In the SHU9119/*h*-MC4R$_i$ complex the *D*Nal(2')^7 prefers a *gauche*+ orientation due to steric interaction with Leu133, while in the MTII/*h*-MC4R$_a$ complex the *D*Phe^7 side chain could adopt a *trans* orientation. Furthermore, the χ_2 torsion angle of Trp^9 rotates from 9,7° in the MTII/*h*-MC4R$_a$ to -56,0° in SHU9119/*h*-MC4R$_i$. Interestingly, the 2'-naphthalene and indole moieties of SHU9119 show many van der Waals interactions with hydrophobic residues of the TM6 helix which could stabilize the inactive state of the *h*-MC4R (Table 7). As a matter of fact, different groups have proposed that large aromatic side chain substitutions at the Phe^7 position of α-MSH analogues can interfere with MC4R activation by interacting with receptor residues within TM6, physically hindering the conformational changes necessary to elicit full efficacy.[120, 125] Our model is also supported by the observation that the *D*Nal(2')^7 naphthalene external ring fills the same cleft as the Phe^{113} benzene ring of AGRP (Agouti related protein, an endogenous antagonist) in a model of AGRP/*h*-MC4R$_i$ complex (Figure 14).[115] It can be observed in the same Figure 14 that also the Arg^8 guanidinium group

of SHU9119 is perfectly overlapped with the same groups of Arg^{111} of AGRP.

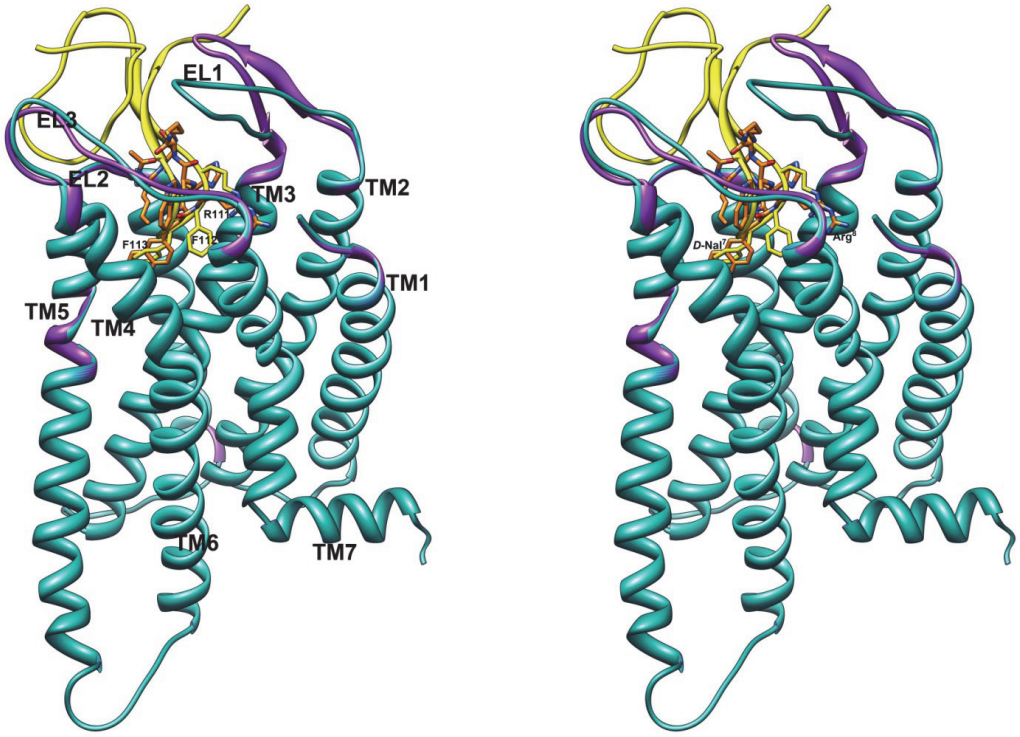

Figure 14. Stereoview of SHU9119/*h*-MC4R$_i$ (orange-cyan) and AGRP/*h*-MC4R$_i$ (gold-purple) models in the inactive conformations. On the left side, AGRP's labels are shown; on the right side, SHU9119's labels are shown. The *h*-MC4R models are superimposed using the backbone heavy atoms of TM residues. Hydrogen atoms are not shown for clarity.

Similar conformation and positioning of MTII and SHU9119 within the MC4R are not surprising since it was shown that the single substitution of Leu133 with a methionine residue in the receptor converted SHU9119 from an antagonist into an agonist at the *h*-MC4R.[118] Probably, according to our model, when Leu133 was replaced with methionine, which is more flexible than leucine, the hindering amino acid was removed and the *D*Nal(2')^7 bulky aromatic

side chain could be accommodated in the same cleft occupied by *D*Phe^7 of the agonist MTII. An analogous point mutation in the *h*-MC3R had the same effect on SHU9119 activity.[135] Interestingly, SHU9119 behaves as an agonist at the *h*-MC1R and *h*-MC5R where a methionine or a (smaller) valine residue, respectively, occupies the position corresponding to Leu133 according to the sequence alignment reported in the reference.[115]

Other groups have suggested modeled docked conformations of melanotropin peptides with the MC4R for both agonist and antagonist ligands. In particular concerning the agonists, a few models of the NDP-MSH,[114, 129, 136] a model of α-MSH-ND (the open analogue of MTII),[137] and a model of the tetrapeptide His-*D*Phe-Arg-Trp [121] complexed with *h*-MC4R have been proposed. It is noteworthy that different ligand conformations were employed for the peptide agonist/MC4R models proposed (Table 8). As a consequence of the lack of an accepted melanocortin peptide active conformation, all the models proposed in literature, included the MTII/*h*-MC4R presented here, were only partially superposable.

Table 8.

Peptide	Conformation	Central Residues	Reference
NDP-MSH	type II (hairpin)	6-7	[112]
NDP-MSH	type I'	6-7	[135]
NDP-MSH	type II'	7-8	[127]
α-MSH-ND	type I	6-7	[136]
Core[a]	type II'	7-8	[118]

[a] His-*D*Phe-Arg-Trp tetrapeptide core sequence.

For example, considering the NDP-MSH/*h*-MC4R complex proposed by Mosberg *et al.*,[114] it is quite different from our MTII/*h*-MC4R model described above (Figure 15). NDP-MSH [87] and MTII [88] differ by cyclization at Asp^5-Lys^{10} residues (in MTII), but share the same pharmacophoric sequence His^6-*D*Phe^7-Arg^8-Trp^9.

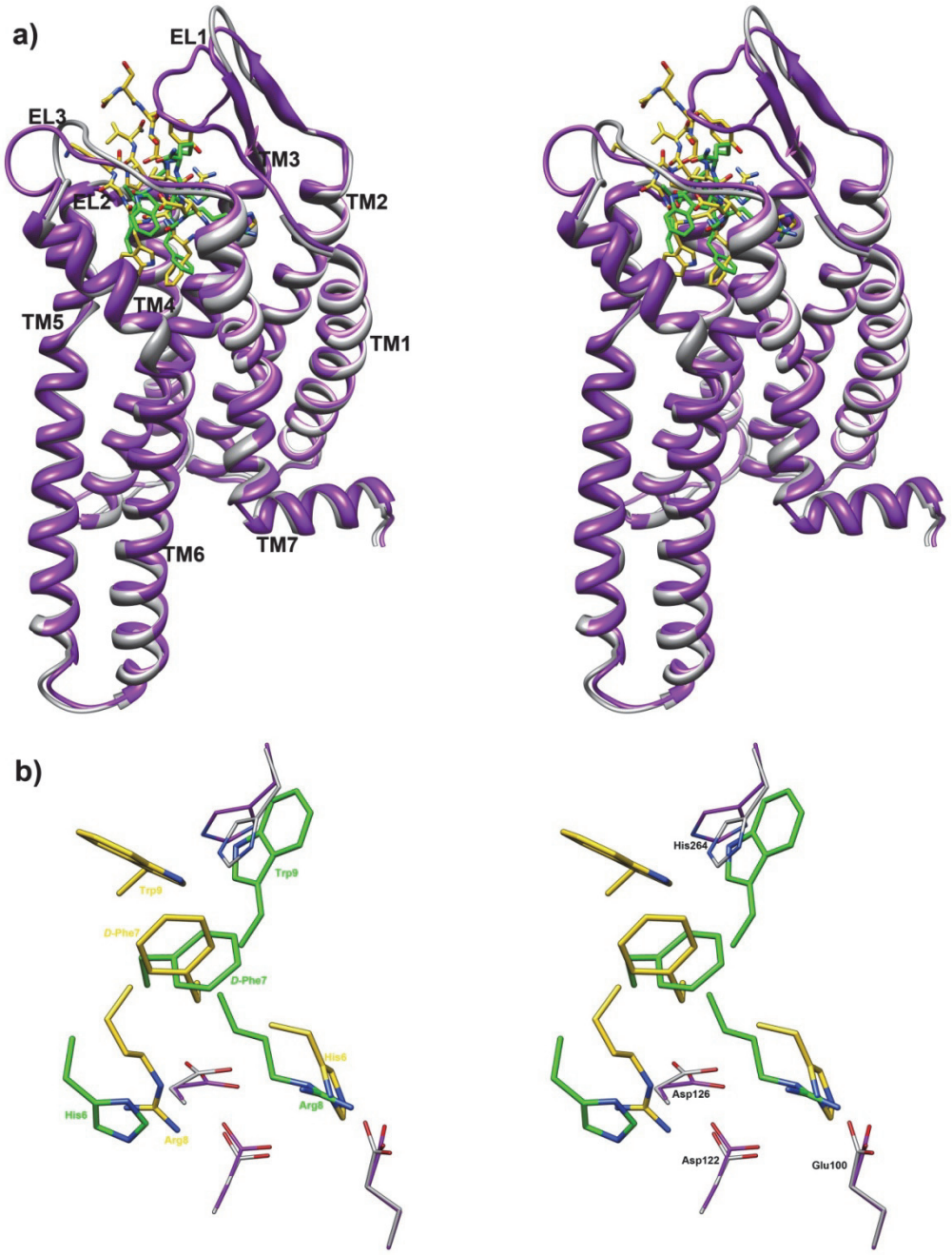

Figure 15. (a) Stereoview of MTII/*h*-MC4R$_a$ (green-gray) and NDP-MSH/*h*-MC4R$_a$ (gold-purple) models in the active conformations. (b) Bottom stereoview of MTII and NDP-MSH within the binding pocket of *h*-MC4R$_a$. Only pharmacophoric side chains of ligands (His6-Arg9) are showed for clarity. Important residues of receptors are represented. The *h*-MC4R models are superimposed using the backbone heavy atoms of TM residues. Hydrogen atoms are not shown for clarity.

The receptor coordinates of the two complexes are very similar; indeed, we started from the Mosberg's *h*-MC4R$_a$ coordinates, and

only marginal changes of the extracellular loops could be observed after the MTII/*h*-MC4R$_a$ complex optimization (Figure 15). In contrast, ligand conformations are different considering the common tetrapeptide fragment. A β-hairpin-like structure with a distorted type II β-turn spanning His^6-*D*Phe^7 was proposed for Mosberg's NDP-MSH, while our NMR-derived MTII structure shows two consecutive β-turns spanning residues Asp^5-His^6 and His^6-*D*Phe^7 (see above). Also side chain orientation of Trp^9 was different in the two peptides being *trans* in MTII and *gauche*- in NDP-MSH. Hence, even if both peptides are located within the TM2-TM7 bundle at the extracellular side, their interactions with *h*-MC4R$_a$ appear to be different. In particular, in the MTII/*h*-MC4R$_a$ model His^6 and Arg^8 are swapped compared to NDP-MSH/*h*-MC4R$_a$ in Mosberg's model. In Mosberg's model, His^6 forms the most stable interactions with the Glu100, Asp122, and Asp126 negatively charged side chains, while Arg^8 is more solvent exposed. Furthermore, in the NDP-MSH/*h*-MC4R$_a$ model, the indole group of Trp^9 roughly occupies the same position as *D*Nal(2')^7 or Phe^{113} of the antagonists SHU9119 and AGRP, respectively. Finally, the *D*Phe^7 residues are located in similar positions within the receptor.

Some differences in the SAR data of NPD-MSH and MTII were observed both in terms of binding affinity: alanine substitutions were

generally better tolerated in linear NDP-MSH than in cyclic MTII [119, 125, 132]; and in terms of efficacy: the *D*-(4-Cl)Phe^7 substitution in NDP-MSH substantially reduces E_{max} but does not appreciably affect MC4R activation by the cyclic MTII.[106, 125] Different SARs could indicate different orientations of MTII and NDP-MSH (or other linear peptides) within the binding pocket thus justifying the different interactions found in the complex models. Finally, Mosberg *et al.* also proposed a MTII/*h*-MC4R$_a$ complex model.[138] In this complex, the receptor model was the same as previously developed by the authors while the MTII structure was modeled from that of NDP-MSH. The lack of details about the interactions within this complex model does not allow any comparison with our model.

Considering the peptide antagonists, a SHU9119/*h*-MC4R complex model has been very recently proposed.[139] Apart from Arg^8 which was close to Glu100, Asp122, and Asp126 also in this model, other side chain interactions were different from those observed in our model. Again, a different backbone conformation of the bound peptide, a type-I β-turn in that case, can explain these differences. A few AGRP derived peptides were also docked within MC4R models. The triplet peptide Arg-Phe-Phe, the smallest conserved motif of AGRP which mediates the key interactions with

MC4R, was docked into the *h*-MC4R.[140] A bicyclic *h*AGRP derivative was docked into the mouse MC4R (*m*-MC4R).[141] The refined averaged NMR structure of *h*AGRP(87-132) was docked both into a *h*-MC4R [115] and a *m*-MC4R [142] model. When considered the Arg^{111}-Phe^{112}-Phe^{113} triad, the docked structures of AGRP derivatives all maintain similar putative ligand-receptor locations, which are illustrated in Figure 14.

1.2.4 Conclusions

In conclusion, NMR-derived MTII and SHU9119 structures show two consecutive β-turns spanning residues Asp^5-His^6 and His^6-*D*Phe^7 (or *D*Nal(2')^7) with some differences in the Phe/Nal^7 side chain orientation. Computational docking experiments of these structures, using three-dimensional homology molecular model of the *h*-MC4R, identified the main interactions between MC4 receptor and its peptide ligands. These findings may be crucial to increase our knowledge of structure-function relationships focused on the design of new potent MC4 receptor ligands.

1.2.5 Experimental Section

Synthesis. N^{α}-Fmoc-protected amino acids, HBTU and HOBt were purchased from Inbios (Naples, Italy). Wang resin was purchased from Advanced ChemTech (Louisville, KY). Synthesis of MT-II and SHU-9119 were performed by standard FMOC Strategy.[35]

NMR Sample Preparation. 99.9% $^{2}H_2O$ were obtained from Aldrich (Milwaukee, USA), 98% SDS-d_{25} was obtained from Cambridge Isotope Laboratories, Inc. (Andover, USA), [(2,2,3,3-tetradeuterio-3-(trimethylsilanyl)]propionic acid (TSP) from MSD Isotopes (Montreal, Canada).

NMR Spectroscopy. The samples for NMR spectroscopy were prepared by dissolving the appropriate amount of peptide to obtain a concentration 1-2 mM in 0.55 ml of $^{1}H_2O$ (pH 5.5), 0.05 ml of $^{2}H_2O$ for water samples, 0.48 mL of $^{1}H_2O$ (pH 5.5), 0.12 mL of $DMSO_{d6}$ for cryoscopic solution, 200 mM of SDS-d_{25} or DPC-d_{38} for micelle samples. NMR spectra were recorded on a Varian INOVA 700 MHz spectrometer equipped with a z-gradient 5 mm triple-resonance probe head. All the spectra were recorded at a temperature of 25 °C. The spectra were calibrated relative to TSP (0.00 ppm) as internal standard. One-dimensional (1D) NMR spectra were recorded in the Fourier mode with quadrature detection. Water suppression was

achieved by using the double-pulsed field gradient spin-echo (DPFGSE) scheme [68]. 2D DQF-COSY [37, 38], TOCSY [39], NOESY [40], and PE-COSY [69] spectra were recorded in the phase-sensitive mode using the method of States.[70] Data block sizes were 2048 addresses in t_2 and 512 equidistant t_1 values. Before Fourier transformation, the time domain data matrices were multiplied by shifted $\sin^2$ functions in both dimensions. A mixing time of 70 ms was used for the TOCSY experiments. NOESY experiments were run with mixing times in the range of 150-300 ms. The qualitative and quantitative analyses of DQF-COSY, TOCSY, and NOESY spectra, were obtained using the interactive program package XEASY.[41]. $^3J_{\mathrm{HN\text{-}H\alpha}}$ coupling constants were obtained from 1D ^{1}H NMR and 2D DQF-COSY spectra. The temperature coefficients of the amide proton chemical shifts were calculated from 1D ^{1}H NMR and 2D TOCSY experiments performed at different temperatures by means of linear regression.

Structural Determinations. The NOE-based distance restraints were obtained from NOESY spectra collected with a mixing time of 200 ms. The NOE cross peaks were integrated with the XEASY program and were converted into upper distance bounds using the CALIBA program incorporated into the program package DYANA.[71] Cross peaks which overlapped more than 50% were

treated as weak restraints in the DYANA calculation. For each examined peptide, an ensemble of 200 structures was generated with the simulated annealing of the program DYANA. An error-tolerant target function (tf-type=3) was used to account for the peptide intrinsic flexibility of the peptide. The annealing procedure produced 200 conformations from which 50 structures were chosen, whose interprotonic distances best fitted NOE derived distances, and then refined through successive steps of restrained and unrestrained EM calculations using the Discover algorithm (Accelrys, San Diego, CA) and the consistent valence force field (CVFF) [73] as previously described. Coupling constants were not used in the constrained simulated annealing calculation, however, backbone and side chain conformations are in accordance with the experimental $^{3}J_{\mathrm{HN-H\alpha}}$ and $^{3}J_{\mathrm{H\alpha-H\beta}}$ coupling constants, respectively. The PROMOTIF program, was used to extract details on the location and types of structural secondary motifs.[143] Graphical representation were carried out with the InsightII program (Accelrys, San Diego, CA). RMS deviation analysis between energy minimized structures were carried out with the program MOLMOL.[72]

Docking Procedures. The peptides MTII and SHU91119 were manually docked in the proposed binding site of the *h*-MC4R$_a$ and *h*-MC4R$_i$, respectively. Employing the criteria described in the Results

section, we generated 10 structures for both MTII/*h*-MC4R$_a$ and SHU9119/*h*-MC4R$_i$ complexes. Refinement of each structure was achieved by in vacuo energy minimization with the Discover algorithm (50 000 steps; $\varepsilon = 1$). The backbone atoms of the TM and IL domains of the *h*-MC4R were held in their position; the ligand and EL's were free to relax. Minimization was followed by a brief MD simulation period (200 ps). After this period, many poses (7 and 8 out of the 10 poses for MTII and SHU9119, respectively) were discarded since the ligand was driven away from its starting position and lost the salt-bridge with the conserved Asp residues. The other structures (3 for MTII and 2 for SHU9119) converged to a very similar conformation (rmsd of the backbone atoms < 1 Å) and the lowest energy complex for each ligand was chosen as the starting point for subsequent 1 ns MD simulations (time step = 1 fs, T = 300 K). The backbone coordinates of the TM helices were fixed during the MD simulations because, without environmental constraints (i.e. lipid bilayer and water solution), they can move away from each other and can lose their helical structure. Fixing TM helices should still allows for sufficient spatial/conformational sampling of the docked complexes since the ligand, in the discarded poses (see above), significantly changed both the initial position and conformation, after the MD simulations. An average structure was calculated from the last

0.5 ns trajectory and energy-minimized using the steepest descent and conjugate gradient methods until a rmsd of 0.05 Kcal/mol per Å was reached. All the MD trajectories were analyzed by means of the Analysis module of the InsightII package. Molecular graphics images of the complexes were produced using the UCSF Chimera package.[76] Rescoring of the ligand/receptor models according to the AutoDock4 (AD4) [45-47] scoring function was attained using a script provided within the MGLTools software package (http://mgltools.scripps.edu/).

1.3 Novel Octreotide Dicarba-Analogues with High Affinity and Different Selectivity for Somatostatin Receptors.

A limited set of novel octreotide dicarba-analogues with non-native aromatic side-chains in positions 7 and/or 10 were synthesized. Their affinity towards the $ssts_{1-5}$ was determined. Derivative 4 exhibited a pan-somatostatin activity, except sst_4, and derivative 8 exhibited high affinity and selectivity towards sst_5. Actually, compound 8 has similar sst_5 affinity (IC_{50} 4.9 nM) to SRIF-28 and octreotide. Structure-activity relationships suggest that the *Z* geometry of the double bond bridge is that preferred by the receptors. The NMR study on the conformations of these compounds in SDS_{-d25} micelles solution shows that all these analogues have the pharmacophore β-turn spanning Xaa^7-d-Trp^8-Lys^9-Yaa^{10} residues. Notably, the correlation between conformation families and affinity data strongly indicates that the sst_5 selectivity is favored by a helical conformation involving the C-terminus triad, while a pan-SRIF mimic activity is based mainly on a conformational equilibrium between extended and folded conformational states.

1.3.1 Introduction

The cyclic tetradecapeptide somatostatin (H–Ala[1]–Gly[2]-*c*[Cys[3]–Lys[4]–Asn[5]–Phe[6]–Phe[7]–Trp[8]–Lys[9]–Thr[10]–Phe[11]–Thr[12]–Ser[13]–Cys[14]]–OH, SRIF-14) was first isolated from mammalian hypothalamus. [144] This hormone is widely distributed in the human body and is found in the gut, pancreas, nervous system and in some exocrine and endocrine glands. By interactions with a family of five SRIF receptors (ssts), the native peptide exerts a great number of regulatory effects, especially those related to GH release. Different receptor subtypes mediate various functions but only sst_2 and sst_5 activities have been precisely related to specific physiological activities.[145] SRIF receptors are strongly expressed in various types of malignant cells, particularly in some neuroendocrine or neuroendocrine-like tumors. Over the last three decades, this has prompted researchers to prepare a huge number of new cyclic and acyclic analogues, which are more stable than SRIF in physiological conditions. Amongst these, a large number of reduced-size cyclic analogues, with or without the disulfide bridge, were synthesized and tested for their affinity towards the ssts. Furthermore, their pharmacological behaviour was studied and several NMR investigations on their affinity/conformations relationships were carried out. J. E. Rivier's group, at the Salk Institute of La Jolla, carried out a careful structure/affinity study on SRIF analogues,

introducing non natural aminoacids in the sequence and preparing variably sized S-S bridged cyclopeptides. These authors related the structure/conformation of the cyclopeptides to the sst_{1-4} specific affinity by means of NMR studies.[146-149]

Octreotide [150] (compound 1, Figure 16), a cyclic octapeptide analogue of somatostatin, containing a disulfide tether, and showing high affinity and selectivity for sst_2, was the first analogue to be used in clinical protocols. Following the enormous growth in preparation and application of radiolabelled peptides for tumor imaging and therapy, the somatostatin analogues thus far obtained were designed mainly for the targeting of malignant cells with γ- or β-emitting radionuclides.[147, 151, 152] As a matter of fact, octreotide derivatives [^{111}In-DTPA]octreotide (OctreoScan) and [^{90}Y-DOTA-Tyr^3]octreotide (OctreoTher) are both quite successfully used in the clinical diagnosis and therapy of neuroendocrine tumors, respectively.[153] Nevertheless, the vulnerability of the S-S bridge to endogenous and exogenous oxidating and reducing agents, such as those employed in the experimental conditions of labelling with the radioisotopes ^{99m}Tc or ^{188}Re,[154] prompted us to synthesize dicarba-analogues of similar ring size, by the RCM reaction on two allylglycines, substituting the relevant Cys^{3,14} residues in the linear peptide. Compound 2, reported in Figure 16 as an example, is the first

octreotide dicarba-tethered analogue synthesised by us and has the same aminoacid sequence of the corresponding, S-S bridged, molecule.[155, 156]

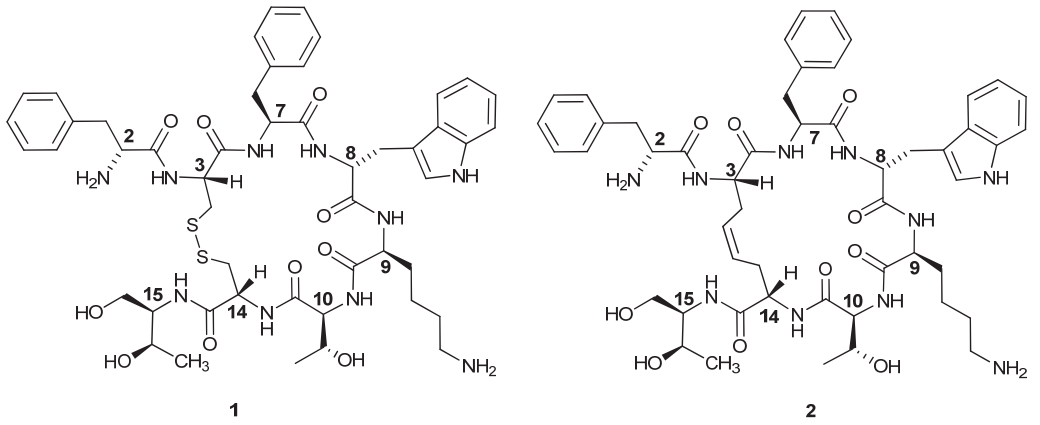

Figure 16. Structure of Octreotide (SMS201-995) (**1**) and of the first dicarba SRIF mimetic (**2**).[155] (Note: numbering of the residues follows that of the native SRIF).

The resulting unsaturated dicarba bridge proved to be insensitive to the conditions used for ^{99m}Tc or ^{188}Re labelling (unpublished results) and the molecules obtained were very stable in human serum.[155, 156] Recently, the stability of these compounds was exploited in the successful conjugation of cytotoxic dichloroplatinum complexes to analogue 2 as well as to the double bond hydrogenated derivative.[157] The same reaction, attempted with the octreotide molecule, failed. When the affinities of these analogues towards the five ssts were determined, we ascertained that some of them showed unexpected specific affinity for the sst_5 subtype, which led us to define a novel pharmacophore model for this receptor.[156]

This study reports the synthesis of new cyclooctapeptide dicarba-analogues, that have structures similar to those depicted in Figure 16, but are designed to carry different aromatic residues in positions 7 and/or 10 (Table 9). In the following, ssts subtypes affinities found for the new compounds 4-8 are correlated with the C=C bridge geometry and with the conformational behaviour in SDS_{-d25} micelles solution, investigated by NMR experiments. Characteristic structure/affinity relationships of this class of somatostatin analogues are widely discussed.

Table 9. Peptide Sequences; General Formula: d-Phe^{2}-*c*[dhDSA-N^{3}-Xaa^{7}-d-Trp^{8}-Lys^{9}-Yaa^{10}-dhDSA-C^{14}]-Thr(ol)^{15}-OH.

Peptide	*Xaa^{7}*	*Yaa^{10}*	*Double bond geometry*
2[a]	Phe	Thr	*Z*
3[a]	Phe	Tyr(Bzl)	*E*
4	Phe	Tyr(Bzl)	*Z*
5	1-Nal	Thr	*Z*
6	Phe	Tyr	*E*
7	Phe	Tyr	*Z*
8	1-Nal	Tyr(Bzl)	*Z*

[a] These compounds were previously reported.[156]

1.3.2 Results

Peptide Synthesis and Purification. The synthesis of dicarba-analogues followed the procedure described in our previous articles. [155, 156] Starting from H–L-Thr(*t*Bu)–ol–2-chlorotrityl resin (0.5 mmol/g) already containing [Thr(ol)^{15}], the elongation of the peptide sequence was stopped after the coupling of Hag^3 residue, with the aim of removing any possible interference of the aromatic ring of D-Phe in the correct orientation of the allylglycine side chains. After the Fmoc-Hag^3 coupling, the resin loading (0.5 mmol/g) already met the requirements of the pseudo-dilution effect, minimizing the risk of the formation of intermolecular bonds. The linear heptapeptides were then converted by RCM by the 2nd generation Grubbs catalyst (**9**) (Figure 17) to the corresponding cyclic analogues.

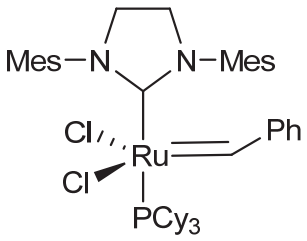

9

Figure 17. 2nd Generation Grubbs Catalyst.

The D-Phe^2 terminal residue was added only after ring-closing, thus facilitating the cyclization step. Cleavage of the crude peptides

from the resin was obtained using the standard cleavage mixture TFA/H_2O/EDT/Phenol (94:2:2:2, 3 h) for compounds **5**, **6** and **7** and with the new percentage mixture (70:26:2:2, 2,30 h) for compounds **4** and **8**, in order to overcome the loss of the benzyl group of the Tyr(Bzl) residue by hydrolysis, as described in our previous article.[156] All compounds obtained by RCM with **9** were pre-purified by SPE. The concentrated compound adsorbed on the SPE was eluted with an increased percentage of CH_3CN in H_2O (from 0% to 100%). The fractions enriched with each desired compound were then purified by semi-preparative RP-HPLC and characterized by ESI-MS. For each peptide, with the exception of **5** and **8**, the HPLC chromatogram showed two peaks with the same MW, corresponding to the geometric isomers (*Z*/*E* ratio ≈ 90:10). In particular, the *E* structure of the C−C=C−C tether of the sample eluted at lower R_t and the *Z* structure one of the second, more intense, peak, was ascertained by ^{1}H NMR inspection. The HPLC purity of each compound studied was > 97% and the isolated compounds showed unique *E* or *Z* configuration, confirmed by NMR analysis. No oligomer by-products were observed.

Binding Affinity to sst$_{1-5}$ Receptors. All compounds were tested for their ability to bind to the five human sst_{1-5} receptors subtypes in complete displacement experiments using the universal somatostatin

radioligand [^{125}I]-[Leu^{8},D-Trp^{22},Tyr^{25}]-somatostatin-28. SRIF-28 was run in parallel as control. IC_{50} values were calculated after quantification of the data using a computer-assisted image processing system. Binding data indicate that all compounds show sub-μM binding affinities towards the sst_5 (Table 10). Compounds **2** and **3** have already been described [156] and are reported for comparison. While peptide **3** was a potent and selective sst_5 ligand, its *Z*-isomer, peptide **4**, exhibited a pan-somatostatin affinity, apart from sst_4. In fact, the analogue **4** doubled the affinity toward sst_5 but completely lost the selectivity of **3**.

Peptide **5** is the 1-Nal^{7} analogue of **2** (Table 9). This peptide exhibited a low nanomolar $sst_{2,5}$ affinity. Actually, it is the most potent sst_2 ligand among the dicarba analogues prepared to date. The double-bond isomer analogues **6** (*E*) and **7** (*Z*), in which the phenolic group of Tyr^{10} replaces the Tyr(Bzl) residue of **3** and **4**, respectively, did not show any significant affinity toward sst_{1-5} subtypes apart from a slight affinity of **7** to sst_2.

Finally, analogue **8** shared Tyr(Bzl)^{10} residue with peptide **4** and 1-Nal^{7} residue with peptide **5**. Like compound **4**, it showed affinity for all the receptor subtypes except sst_4. However, the significant enhancement of the sst_5 affinity (nearly 3-fold compared to compound **4**) and the simultaneous reduction of affinity towards sst_{1-4} make

compound **8** a strong and selective sst_5 ligand. Indeed, compound **8** is the most potent sst_5 dicarba-analogue synthesized so far, showing an affinity close to the value found for the reference compound SRIF-28 (Table 10).

Table 10. Receptor affinities of the somatostatin analogues.

	IC_{50} (nM)[a]				
No.	sst_1	sst_2	sst_3	sst_4	sst_5
SRIF-28	2.3 ± 0.4 (7)	3.0 ± 0.2 (7)	3.6 ± 0.5 (7)	1.6 ± 0.3 (7)	2.4 ± 0.2 (6)
2[b]	> 1000 (2)	44 ± 1 (2)	> 1000 (2)	412 ± 68 (2)	28 ± 2 (2)
3[b]	> 1000 (2)	> 1000 (2)	892 ± 245 (2)	> 1000 (2)	29 ± 1 (2)
4	25 ± 1 (3)	46 ± 3 (3)	25 ± 4 (3)	346 ± 23 (3)	12.3 ± 0.3 (3)
5	> 1000 (3)	9.6 ± 0.9 (3)	> 1000 (3)	249 ± 51 (3)	16.5 ± 4.5 (3)
6	1000 (3)	355.5 ± 45.5 (3)	1000 (3)	1000 (3)	418 ± 56 (3)
7	> 1000 (3)	87 ± 18 (3)	> 1000 (3)	> 1000 (3)	161 ± 27 (3)
8	57.5 ± 12.5 (3)	101 ± 9 (3)	92.5 ± 0.5 (3)	> 1000 (3)	4.9 ± 1.0 (4)

[a] The number of independent repetitions to obtain the mean values ± SEM are indicated between brackets. SRIF-28 is used as internal control. [b] Corresponds to data published previously.[155]

NMR Analysis. NMR analysis of the analogues **3-8** was performed by means of 1D and 2D proton homonuclear experiments. NMR experiments were recorded on a Varian Inova-Unity 700 MHz spectrometer. Spectra were collected in SDS_{-d25} (200 mM) micelles solution. All samples (about 2 mM) were kept at 308 K and at pH ≅ 5.

Complete ^{1}H NMR chemical shift assignments were effectively achieved for all the analyzed molecules according to the Wüthrich procedure,[36] via the usual systematic application of TOCSY [39] and NOESY [40] experiments with the support of the XEASY software package (Tables S19-S24, Supporting Information).[41] NMR-derived constraints obtained for all compounds were used as the input data for a simulated annealing structure calculation, as implemented within the standard protocol of the DYANA program.[71]

*Compound **3***. The analogue **3** bears Tyr(Bzl) in position 10. We have already analyzed this peptide in our previous work in water/DMSO-d_6 solution.[156] The geometry of the double bond was confirmed as *trans* (*E*) from the coupling constant ($^{3}J_{CH=CH}$ = 15.1 Hz) between the two olefinic protons of the bridge and NOE contacts between the same olefinic and the H_{β}s of residue 14 (3). A qualitative analysis of short- and medium-range NOEs, $^{3}J_{NH\text{-}H\alpha}$ coupling constants, and temperature coefficients for exchanging NH was used to characterize the secondary structure of **3**. Spectra analysis pointed to the presence of a β-turn about residues 7–10. Interestingly, the upfield shift observed for H_{γ}s of Lys^{9} (δ = 0.52, 0.43 ppm) has been used for decades as diagnostic for biological activity.[158] NOE-derived constraints obtained for **3** were used as the input data for a

simulated annealing structure calculation (Table S25, Supporting Information). The backbone arrangement of **3** was well-defined, possessing an average root mean square deviation (rmsd) of the heavy atoms equal to 0.15 Å. No violation higher than 0.1 Å was observed again indicating conformational stability (Table S25). Main backbone features were a type II' β-turn spanning residues D-Trp^{8}-Lys^{9}, followed by a short 3_{10}-helix along residues Tyr(Bzl)^{10}-dhDsa-C^{14}-Thr(ol)^{15} (Figure 18) The turn structure is stabilized by hydrogen bonds between Phe^{7}-CO and Tyr(Bzl)^{10}-NH. The helical structure is stabilized by H-bonds between D-Trp^{8}-CO and dhDsa-C^{14}-NH and between Lys^{9}-CO and Thr(ol)^{15}-NH. These bonds are typical of 3_{10}-helix structure (i, i+3). The side chains of dhDsa-N^{3}, D-Trp^{8}, Lys^{9}, Tyr(Bzl)^{10}, and dhDsa-C^{14} showed well-defined χ1 values (i.e., *trans*, *trans*, *gauche*$^{-}$, *gauche*$^{-}$, and *gauche*$^{+}$ orientations, respectively). These orientations allowed a close spatial proximity between D-Trp^{8}/Lys^{9} side chains; moreover, the tyrosyl group of the residue 10 points toward the Lys^{9} side chain. In contrast, D-Phe^{2} and Phe^{7} side chain showed almost free rotation about the χ1 torsion angle. Also, the Bzl group of residue 10 was highly flexible.

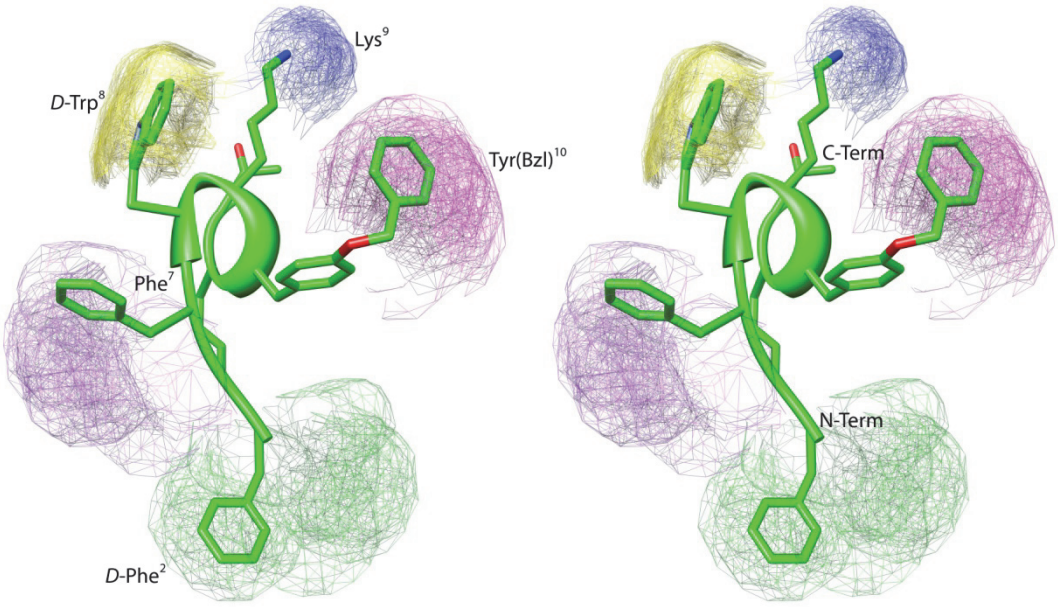

Figure 18. Stereoview of the lowest energy conformer of compound 3. Backbone is evidenced as a ribbon. Side chains of the ten lowest energy conformers are also shown as mesh surface. Surfaces are distinguished with different colors. N-Term, N-terminus; C-Term, C-terminus.

Compound 4. The analogue **4** is the geometric (*Z*) isomer of **3** as established by the coupling constant ($^3J_{CH=CH}$ = 8.1 Hz) between the two olefinic protons of the bridge and the relative strong NOE between the same olefinic H$_\gamma$s. This analogue shows spectral features similar to those found in **3** but with a greater tendency to conformational heterogeneity. In fact, NOESY spectra of **4** showed, simultaneously, both diagnostic connectivities consistent with folded structures: $d_{\alpha N}$(i, i+2) between H$_\alpha$-8/NH-10, H$_\alpha$-9/NH-14, H$_\alpha$-10/NH-15 and $d_{\alpha N}$(i, i+3) between H$_\alpha$-9/NH-15; and NOE contacts characteristic of extended regions: strong $d_{\alpha N}$(i, i+1) between H$_\alpha$-9/NH-10, H$_\alpha$-10/NH-14, and H$_\alpha$-14/NH-15 (Table S26, Supporting

Information). The apparently contradictory NOEs are indicative of the presence of at least two conformations in solution. The impossibility of resuming all the data in a single structure prompted us to consider incompatible NOEs separately in different calculation cycles (Experimental Section). Hence, we obtained two families of conformations. The first calculation cycle gave an ensemble of structures (family I) showing a similar conformation to compound **3**, with a type II' β-turn spanning residues D-Trp^{8}-Lys^{9}, followed by a short 3_{10}-helix along residues Tyr(Bzl)^{10}-dhDsa-C^{14}-Thr(ol)^{15} (Figure 19a). Moreover, side chain orientations were the same as those described for **3**. The main difference was a better definition of the Phe^{7} side chain which preferred the *trans* rotamer. For this set of structures, a number of consistent violations were observed (Table S26). In a second MD cycle, the violated upper limit constraints were upweighted for the contribution to the target function. Thus, a second conformational family (family II) was obtained which differed from the first mainly in that C-terminal residues were in extended conformations (Figure 19b). Furthermore, the side chain orientation of Tyr(Bzl)^{10} was *trans*. Hence, the tyrosyl nucleus was further from the Lys^{9} side chain. This is in accordance with the down-field shifts of the H_{γ} resonances of Lys^{9} compared to the corresponding shifts of compound **3**. Interestingly, the complete ensemble of structures (helix

and extended) fulfilled the NOE restraints, with no violations exceeding 0.5 Å (Table S26).

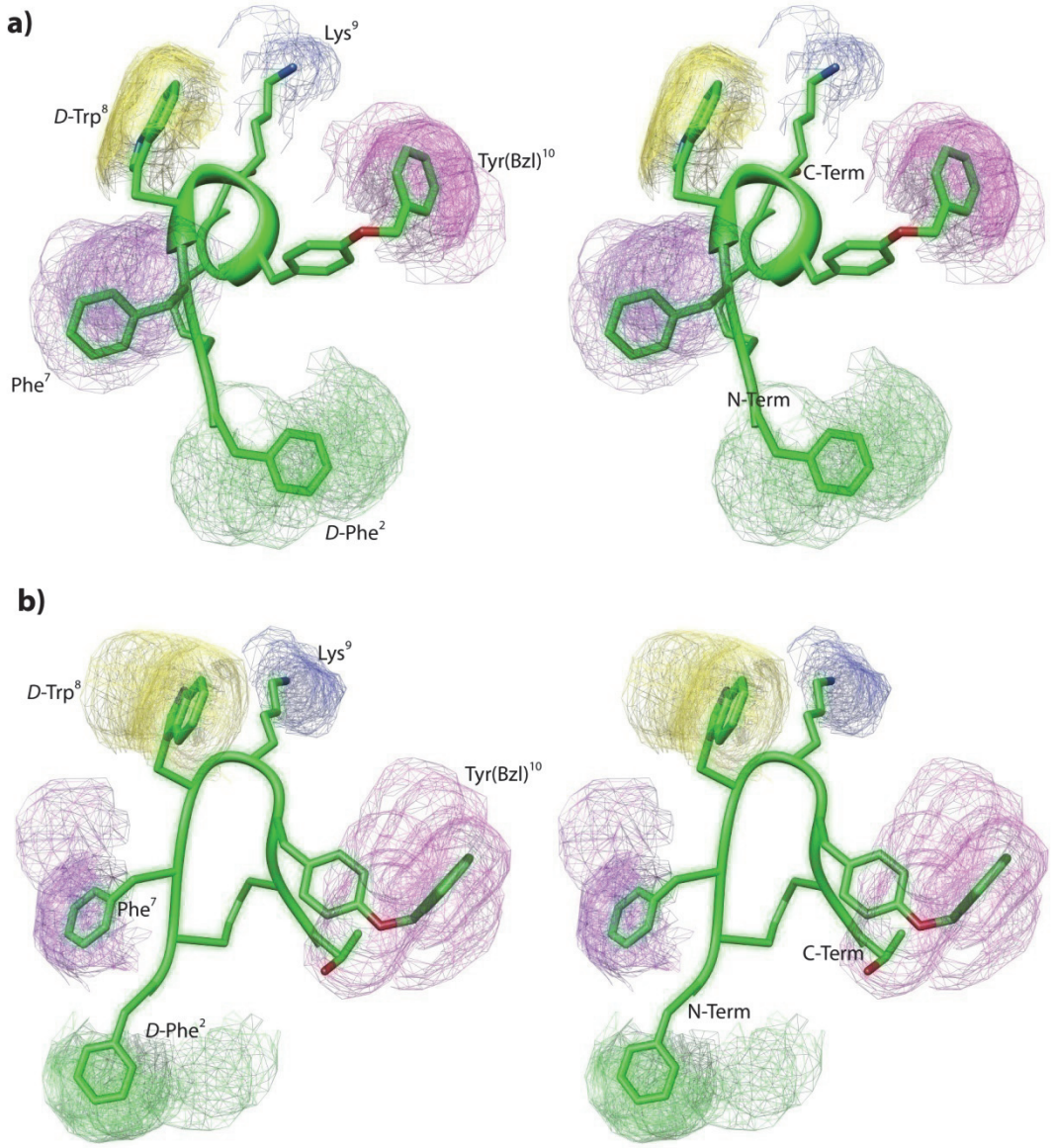

Figure 19. Stereoview of the lowest energy conformer of compound 4: family I (a), family II (b). Backbone is evidenced as a ribbon. Side chains of the ten lowest energy conformers are also shown as mesh surface. Surfaces are distinguished with different colors. N-Term, N-terminus; C-Term, C-terminus.

Compound ***5***. Compound **5** maintains the same octreotide scaffold, but position 7, which bears 1-Nal. Apart from the dicarba bridge, it has the same peptide sequence of the analogue NOC,

formerly prepared and studied as DOTA-conjugate by Maecke, Reubi and co-workers.[159] The coupling constant ($^3J_{CH=CH}$ = 8.1 Hz) between the two olefinic protons of the bridge and the relative strong NOE between the same olefinic H_γs established (*Z*) configuration for compound **5**. Only one isomer is obtained from RCM.

NMR-based structure calculations gave two conformational families, like compound **4**. Family I, obtained by a first run of MD calculation, showed a type II' *β*-turn spanning residues D-Trp^8-Lys^9, followed by a short 3_{10}-helix along residues Thr^{10}-dhDsa-C^{14}-Thr(ol)^{15} (Figure 20a). As found with compound **4**, a number of consistent violations were observed (Table S27, Supporting Information). In a second MD run, we obtained a second conformational family (II), which differed from the first mainly because the C-terminal residues were in extended conformations (Figure 20b). In both the families, residue 7 showed a defined *trans* orientation which forces 1-Nal^7 naphthyl moiety close to D-Trp^8 residue. This orientation is in accordance with the intense up-field shift observed for many D-Trp^8 proton resonances.

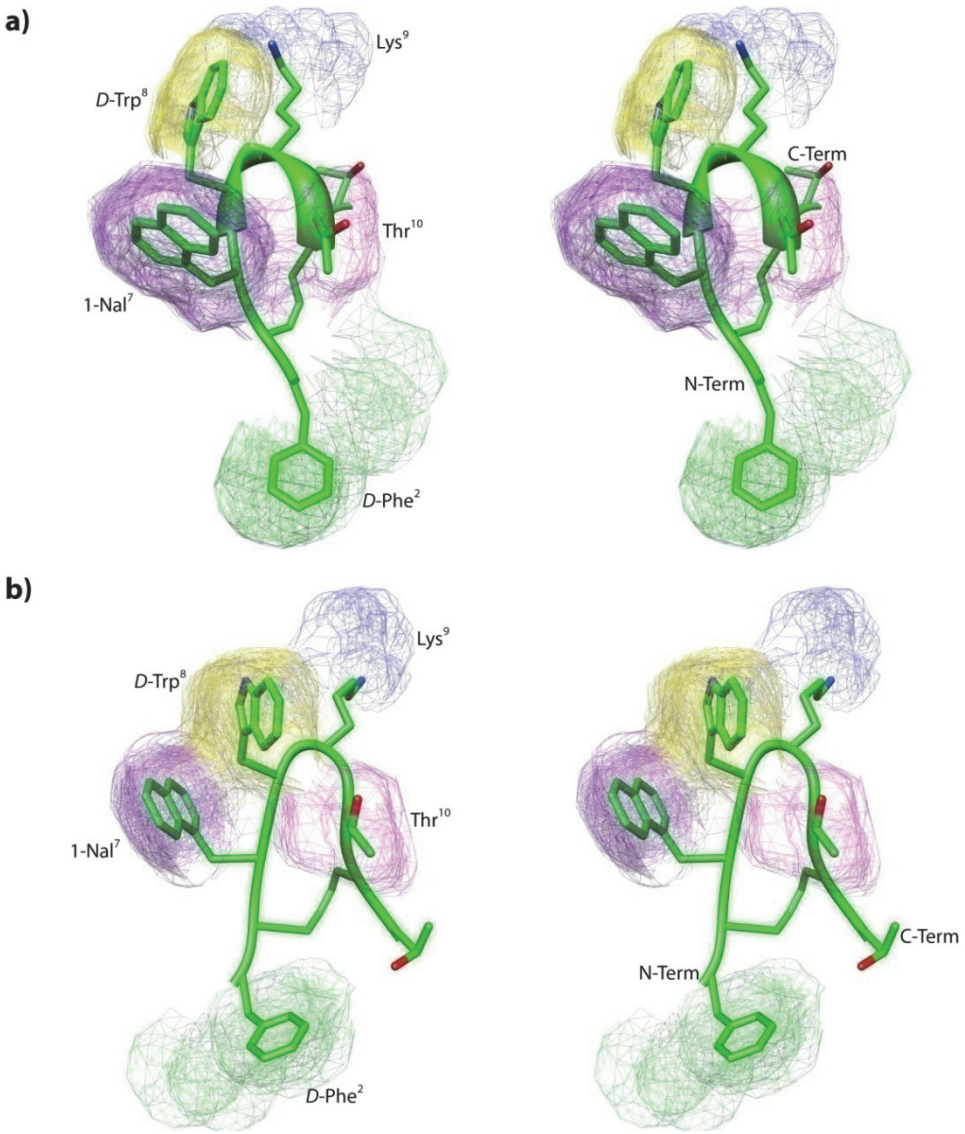

Figure 20. Stereoview of the lowest energy conformer of compound 5: family I (a), family II (b). Backbone is evidenced as a ribbon. Side chains of the ten lowest energy conformers are also shown as mesh surface. Surfaces are distinguished with different colors. N-Term, N-terminus; C-Term, C-terminus.

*Compounds **6** and **7**.* The analogues **6** and **7** differ from compounds **3** and **4** in that the Tyr(Bzl)[10] residue was replaced by a Tyr (i.e. without the Bzl group). Following the same arguments given for **3** and **4**, an *E* configuration was assigned to compound **6** and a *Z* configuration to the compound **7** at the double bond.

Many potential diagnostic NOEs could not be observed in the NOESY spectra of these analogues due to signal overlapping and this precluded structure calculations. For instance, H_α protons of Lys[9] and Thr-ol[15] resonated at the same chemical shift for both peptides. Actually, the NMR parameters of **6** (H_α shifts, coupling constants, and temperature coefficients) are very similar to those of compound **3**, and this was also true for **4** and **7**. Therefore, it could be hypothesized that 3D structures should be similar too.

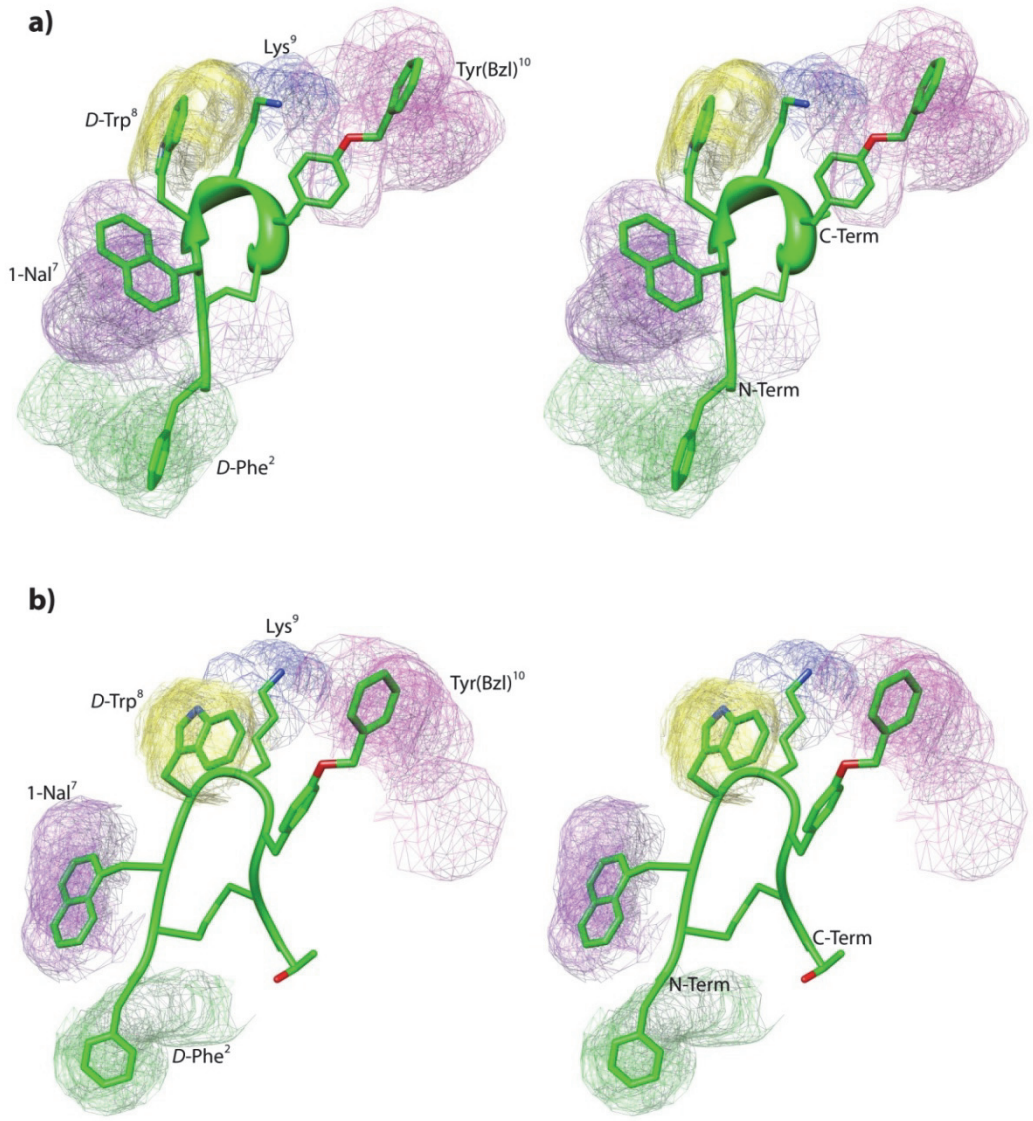

Figure 21. Stereoview of the lowest energy conformer of compound **8**: family I (a), family II (b). Backbone is evidenced as a ribbon. Side chains of the ten lowest energy conformers are also shown as mesh surface. Surfaces are distinguished with different colors. N-Term, N-terminus; C-Term, C-terminus.

*Compound **8***. The analogue **8** structure was rationalized starting from the peptide sequence of the previous compounds **4** and **5**. In fact, it bears both 1-Nal^7 and Tyr(Bzl)^{10}. For compound **8**, a *Z* configuration was established from the NOEs and coupling constant ($^3J_{CH=CH}$ = 8.1 Hz) between the two olefinic protons. NMR-based structure calculation (Table S28, Supporting Information), gave two

conformational families, as it did for compounds **4** and **5**, the first (family I) showing a short 3_{10}-helix along the Thr[10]-dhDsa-C[14]-Thr(ol)[15] residues (Figure 21a), and the second (family II) an extended conformation along the same residues (Figure 21b). In both families, the D-Trp[8], Lys[9] and Tyr(Bzl)[10] side chains were spatially closed in accordance with the increased up-field shift of the H_γ and H_β resonances of Lys[9]. Differently from compound **5**, 1-Nal[7] residue could not adopt a *trans* conformation, probably due to steric hindrance with Tyr(Bzl)[10]. In fact, 1-Nal[7] side chain was preferentially in a *gauche*$^-$ conformation.

1.3.3 Discussion

In our ongoing efforts to develop new somatostatin ligands with improved stability and affinity towards sst receptors, we have rationally designed and analyzed a limited set of peptides (Table 9). In these peptides the labile disulfide bridge was replaced by a dicarba-bridge, through the RCM reaction. As can be seen from Table 10, variation of the residues 7 and 10 results in analogues having a low sub-μmolar potency and a range of sst receptor subtype selectivities.

Recently, we have investigated some octreotide analogues, including compound **3**, in a water/DMSO-d_6 8:2 solution.[156] Here, an NMR study was performed on the developed analogues of octreotide in SDS micelles solution (see section 1.1.3).

Some apparently contradictory NOEs were indicative of the presence of at least two conformations in solution for analogues **4**, **5**, and **8**. To deal with this incongruence we used a practical approach. Incompatible NOEs were considered separately in different calculation cycles. Hence, two families of conformations were obtained which differed mainly in that C-terminal residues were in 3_{10}-helix (family I) or extended (family II) conformation. Eventually, the experimental restraints were fulfilled over the entire ensemble. It is noteworthy that the NMR data of the cognate molecule octreotide, using a single average conformation reveal several important

inconsistencies, including severe violations of mutually exclusive backbone-to-backbone NOEs.[160]

On the basis of the NMR results, some general conformation-affinity relationships concerning the binding to the sst receptors can be outlined. Similar to most of the bioactive analogues of SRIF reported so far,[161] the structures of the peptidomimetics presented here have a β-turn of type II′ spanning residues D-Trp^8 and Lys^9. The side chain of D-Trp^8 is in the *trans* conformer, and the side chain of Lys^9 is in the *gauche*$^-$ conformer, bringing the two side chains adjacent to each other in close proximity. Analogues with the *Z* configuration at the double bond can adopt both helical and extended structures at the C-terminus, showing a conformational equilibrium (Figures 19-21). As a consequence of this conformational behavior, *Z* analogues show greater potency compared to the corresponding *E* isomers (**4** *vs* **3** and **7** *vs* **6**) although it can go to the detriment of the selectivity, as in the case of compound **4** compared to **3**. It could be argued, from the data of Table 10, that *Z*-geometry of the double bond is a better mimic of the S-S bridge which, in turn, was hypothesized to be directly involved in the interaction with the sst receptors.[162, 163]

Analogues **3** and **4** bear a Tyr(Bzl) residue in position 10. The side chain of Tyr(Bzl)^{10} was designed to replace Phe^6, Phe^7, and Phe^{11} of SRIF14.[164] Compound **3** (*E*-isomer) selectively binds sst_5 while

its *Z*-isomer, **4**, showed a pan-SRIF-activity, apart from sst_4. In compound **3**, the *β*-turn motif is followed by a short 3_{10}-helix along residues Tyr(Bzl)^{10}- dhDsa-C^{14}-Thr(ol)^{15}. The side chain of Tyr(Bzl)^{10} is in the *gauche*$^-$ conformer and is located in close proximity to the D-Trp^8-Lys^9 pair (Figure 18). This is in accordance with our recent results which correlates sst_5 selectivity to conformationally restricted helical structure at the C-terminus.[156] The conformational properties of **3** in SDS micelles are similar to those observed in water/DMSO solution (data not shown). Only N-terminal residue D-Phe^2 is more flexible in the SDS solution compared to DMSO.

In addition to high-affinity binding to $sst_{2,3,5}$ like octreotide (**1**), compound **4** also exhibited a low nanomolar binding to sst_1, hence its affinity pattern resembles that of the hexa-cyclic peptide SOM230 (pasireotide) which also bears a Tyr(bzl)^{10} residue.[164] Since compound **4** fits 4/5 receptor binding sites, it was expected to display a high degree of flexibility. In fact, a dynamical equilibrium between extended and helical conformations was observed. Moreover, Tyr(Bzl)^{10} side chain orientation was different in the two conformations (Figure 19). Notably, NMR [160] and X-ray crystallography analyses have already suggested an equilibrium between extended and folded conformational states for the parent peptide **1**.[165] Furthermore, SOM230 exhibited similar backbone

conformational equilibrium in a theoretical MD study; the side chain of Tyr(Bzl) of SOM230 underwent great flexibility which was associated with low selectivity.[166] Although sst_2 is probably the most abundantly expressed SRIF receptor in human cancer,[167] recent literature data indicates that also sst_1 and sst_{3-5} may also be present in some human tumors.[168] Hence, peptides with an improved receptor binding profile are desirable in order to extend the spectrum of tumors accessible to diagnosis and internal radiotherapy. As a matter of fact, SOM230 is being investigated in clinical trials as a potential treatment for acromegaly, neuroendocrine tumors and Cushing's disease.[169, 170]

Among the tested compounds, peptide **5** showed the highest affinity towards sst_2 and also a good affinity towards sst_5. The sequence of this cyclopeptide is the same as the S-S bridged NOC,[159] whose DOTA derivative, DOTA-NOC, exhibited high affinity towards $sst_{2,3,5}$. The loss of sst_3 affinity in **5** is probably due to the absence of the D-Phe^2-bonded DOTA chelating group. Insertion of different arms at the N-terminus may, in fact have, a dramatic effect particularly on sst_3 affinity.[171] Compound **5** is also closely related to the previously described compound **2**, sharing its configuration at the double bond and the amino acid sequence but with Nal^7 in replacing Phe^7.[155] The activity profile of analogues **2** and **5** is

similar, showing an increase in the sst_2 (~4-fold) and sst_5 affinity (~2-fold) of **5** compared to **2** (Table 10). Since **2** showed similar conformational properties as **5** (data not shown), the improved affinity towards sst_2 and sst_5 is probably attributable to the 1-Nal^7 aromatic side chain which, oriented in a *trans* conformation, adequately fits the binding pocket of both receptors.

Compounds **6** and **7** are analogues to **3** and **4**, respectively, with the Tyr(Bzl)^{10} residue replaced by a tyrosine. This change renders compounds **6** and **7** strictly related to U-II. Analogue **6** showed a marked reduction of affinity towards sst_5 compared to the correlated compound **3**. Analogously, compound **7** showed a marked reduction of affinity towards $sst_{1,3,5}$ and a 2-fold reduction towards sst_2 compared to **4**. NMR data of the analogue couples pointed to similar conformational behavior, hence it can be argued that the Tyr^{10} phenol group is detrimental for binding to the sst receptors. This is in accordance with the low affinity of U-II to the sst_{2A} receptor.[172] On the other hand, residual affinity of compound **7** towards sst_2 and sst_5 (Table 10) parallels the capability of U-II to activate these two receptors at high doses.[173]

By combining 1-Nal^7 and Tyr(Bzl)^{10} residue replacements, we obtained compound **8** as a pure *Z*-isomer. Compound **8** showed the highest affinity towards sst_5 (Table 10) with at least a 10-fold

selectivity compared to the other ssts. Compound **8** is closely related to compound **4**, sharing its configuration at the double bond and the amino acid sequence but with 1-Nal^7 replacing Phe^7. Actually, the activity profile of the two analogues is similar (pan-SRIF-activity, apart from sst_4) with a decrease of the $sst_{1\text{-}3}$ affinity (2- to 4-fold) and increase of the sst_5 activity (~3-fold) of **8** compared to **4**. The conformational behavior of **8** also resembles that of **4**, in accordance to the activity similarity (Figure 19 and Figure 21). Since the helical-extended conformational equilibrium is also observable in the case of analogue **8**, the affinity changes could be tentatively attributed to the orientation of the 1-Nal^7 side chain which was differently oriented in the two peptides. In particular, it passed from a *trans* conformation observed in **4**, to a *gauche*$^-$ conformation in **8**. Such g*auche* orientation of the naphthyl group is likely still suitable (or preferred) for sst_5 but not for $sst_{1\text{-}3}$ binding.

Based on the results reported above, we updated the previously proposed pharmacophore model for sst_5-selective analogues.[156] The model involves the classical four side chains of the $sst_{2/3/5}$ pharmacophore,[162] namely, those of residues D-Phe^2, Phe^7 (Nal^7), D-Trp^8 and Lys^9, plus the Tyr(Bzl)^{10} side chain. The distances between the C_γ atoms of these side chains, observed in the potent sst_5 ligands **3**-**5**, **8** are reported in Table 11. The C_γ-C_γ distances found by

Melacini *et al*. for the $sst_{2/3/5}$-selective SRIF analogues are also reported in the same table.[162] It can be observed that the distances found in our derivatives agree with the $sst_{2/3/5}$ pharmacophore.

Table 11. Cγ-Cγ distances (Å) between putative pharmacophoric residues.[a]

Compd	**3**	**4**	**5**	**8**	**$sst_{2/3/5}$**[b]
Ar^2-Ar^7	8.5±0.8[c]	9.0±1.2	9.5±0.5	8.4±1.0	5-11
Ar^2-Ar^8	14.3±0.6	14.0±0.5	14.3±0.6	13.4±0.5	11-15
Ar^2-Lys^9	14.8±0.9	14.4±1.0	13.9±1.0	14.5±1.0	12-15
Ar^2-Ar^{10}	8.1±1.1	7.8±1.2	-	13.4±1.0	-
Ar^7-Ar^8	7.8±0.8	7.6±0.3	6.8±0.2	8.2±0.5	7-9
Ar^7-Lys^9	10.9±0.6	9.8±0.7	9.7±0.3	11.0±0.6	9-11
Ar^8-Lys^9	5.5±0.2	5.6±0.2	4.7±0.3	5.2±0.4	5
Ar^8-Ar^{10}	8.8±0.2	8.9±0.2	-	8.1±0.1	-
Lys^9-Ar^{10}	7.2±0.2	7.2±0.1	-	5.9±0.2	-

[a] Only the family I of peptides **4**, **5**, **8** were considered. [b]Pharmacophore for the sst_2, sst_3, sst_5 selective SRIF analogues [162] [c]Average distance and standard deviation calculated from the ensemble of ten structures.

1.3.4 Conclusions

A limited set of compounds of biostable SRIF analogues with dicarba bridge replacing the disulfide bridge of the parent octreotide (**1**) were prepared. Compounds were obtained by on-resin RCM by second generation Grubbs catalyst. All the analogues were tested for their affinity toward the sst_{1-5} receptor subtypes. Among the synthesized compounds, derivative **4** exhibited a pan-somatostatin activity (except sst_4) and derivative **8** exhibited high affinity and selectivity towards sst_5. Actually, compound **8** had a similar sst_5 affinity (IC_{50} 4.9 nM) to SRIF-28 and octreotide. Conformation-affinity relationships confirmed that helical propensity correlates with the peptide sst_5-affinity while a pan-SRIF activity is obtained by conformational equilibria. Both pan- and selective-SRIF analogues are potentially useful for the diagnosis and internal radiotherapy of tumors.

1.3.5 Experimental Section

General Procedures. Fmoc protected amino acids were purchased from Calbiochem-Novabiochem (Laufelfingen. Switzerland). 2nd generation Grubbs catalyst was obtained from Aldrich. Fmoc-Hag, Fmoc–O–benzyl-L-tyrosine and H–l-Thr(tBu)–ol–2–chlorotrityl resin were purchased from Iris Biotech (Marktredwitz, Germany). HATU was obtained from Chempep (Miami, USA). Peptide grade DMF was from Scharlau (Barcelona, Spain). All the other solvents and reagents used for SPPS were of analytical quality and used without further purification. Analytical RP-HPLCs were performed on a Waters instrument equipped with a UV detector on a Phenomenex Juppiter C18 column (5 μm, 250 x 4.6 mm) using a flow rate of 1 ml/min, with the following solvent system: 0.1% TFA in H_2O (A), 0.1% TFA in MeCN (B)). Semi-preparative RP-HPLC analyses were performed on the same instrument using a flow rate of 4 ml/min with the same solvent system, on a Phenomenex Juppiter C18 column (10 μm, 250 x 10 mm). Mass spectra were registered on an ESI LCQ Advantage mass spectrometer (Thermo-Finnigan). LC-ESI-MS analyses were performed on a Phenomenex Juppiter C18 column (5 μm, 150 x 2.0 mm) using a flow rate of 500 μL/min on a ThermoFinnigan Surveyor HPLC system coupled to ESI-MS, using the solvent system: H_2O (A), MeCN (B), 1% TFA in H_2O

(C). Routine NMR spectra were acquired on a Varian Inova 700 apparatus. TSP was purchased from MSD Isotopes (Montreal, Canada). ^2H_2O was obtained from Aldrich. SDS-d_{25} was obtained from Cambridge Isotope Laboratories, Inc. (Andover, MA). SPPS was performed in Teflon reactor on a manual synthesizer PLS 4x4 (AdvancedChemTech). Receptor autoradiography was performed on 20-μm thick cryostat (Microm HM 500, Walldorf, Germany).

Synthesis and Purification of Compounds 3-8. Peptides were synthesized following the method reported in the preceding work.[156] Briefly, the peptides were prepared using the general Fmoc-SPPS strategy on pre-swelled H–L-Thr(*t*Bu)–ol–2–chlorotrityl resin. Couplings were performed by adding two equivalents of protected amino acid activated by HATU and four equivalents of NMM in DMF. Each coupling was monitored by the qualitative ninhydrin (Kaiser) test.[35] At the end of the linear peptides synthesis, a microscale cleavage was performed. RP-HPLC analysis of the crude products revealed the presence of the linear peptides in approximately 95% purity, without traces of isomers due to amino acid racemization. The cyclization was performed on-resin by 2nd generation Grubbs catalyst (0.5 mole equiv. calculated on the basis of 0.5 mmol/g of peptide). After swelling, NH_2 terminal Fmoc–Hag was deprotected and coupled with Fmoc–D-Phe affording the on-resin peptides **4-8**

which were deprotected and cleaved [**5**, **6** and **7** with TFA/H_2O/EDT/phenol (94:2:2:2, 3 h) while **4** and **8** with TFA/H_2O/EDT/phenol (70:26:2:2, 2.30 h)]. The aqueous solutions of the peptides **4-8** were pre-purified by SPE, and after subjected to the purification by semi-preparative RP-HPLC and subsequently characterized by ESI-MS. Analytical RP-HPLC and ESI-MS analysis of the crude compounds revealed two chromatographic peaks with the same MW for compounds **4**, **- 7**, corresponding to the geometric isomers (*Z*/*E* ratio ≈ 90:10). Compounds were then purified by semi-preparative RP-HPLC and the most abundant chromatographic peaks were collected. For all the products HPLC purity was ≥ 97%.. Further experimental data are reported in the Supporting Information.

NMR Spectroscopy. The samples for NMR spectroscopy were prepared by dissolving the appropriate amount of peptide in 0.55 ml of ^1H_2O (pH 5), 0.05 ml of ^2H_2O to obtain a concentration 1-2 mM of peptides and 200 mM of SDS-d_{25}. TSP was used as internal chemical shift standard. The water signal was suppressed by gradient echo.[68] NMR experiments were recorded on a Varian Inova-Unity 700 MHz at 308.1 K. Complete ^1H NMR chemical shift assignments were effectively achieved for all the analyzed peptides (Supporting Information, Tables S19-S24) according to the Wüthrich procedure [36] via the usual systematic application of TOCSY [39] and NOESY

[40] experiments recorded in the phase-sensitive mode using the method from States.[70]

Typical data block sizes were 2048 addresses in t_2 and 512 equidistant t_1 values. Before Fourier transformation, the time domain data matrices were multiplied by shifted $\sin^2$ functions in both dimensions. A mixing time of 70 ms were used for the TOCSY experiments. NOESY experiments were run with mixing times of 100 and 200 ms. The qualitative and quantitative analyses of TOCSY and NOESY spectra were obtained with the support of the XEASY software package.[41]

Structural Determinations and Computational Modeling. The NOE-based distance restraints were obtained from NOESY spectra collected with the mixing time of 100 ms. The NOE cross peaks were integrated with the XEASY program and were converted into upper distance bounds using the CALIBA program incorporated into the program package DYANA.[71] Only NOE derived constraints (Supporting Information, Tables S25-S28) were considered in the annealing procedures. In a first calculation run, all the upper distance bounds were used, generating an ensemble of 100 structures with the simulated annealing standard protocol of the program DYANA. For peptides **4**, **5**, and **8**, a number of consistent (i.e. in all calculated structures) violated upper limit constraints (> 0.1 Å) were observed

(Supporting Information, Tables S25-S28). These violations were discarded in a subsequent MD run. This step was repeated till no violation was observed (two runs were enough for all peptides). Thus, we obtained a first family of structures (family I). In a second MD cycle, the violated upper limit constraints of the first cycle were upweighted (10-fold) for the contribution to the target energy function of DYANA. Hence, we obtained a new set of violated constraints which were discarded in the subsequent MD runs. After two MD runs, no violations were observed. In the final calculation run, we applied the same weight to the undiscarded constraints and obtained a second family of structures (family II). Since, the two sets of violations had no common member we did not repeat further the described procedure.

Finally, 20 structures for peptide **3**, and 20 structures for each family of peptides **4**, **5** and **8** were chosen, whose interprotonic distances best fitted NOE derived distances, and then refined through successive steps of restrained and unrestrained energy minimization calculations using the Discover algorithm (Accelrys, San Diego, CA) and the consistent valence force field (CVFF).[73]

The minimization lowered the total energy of the structures. The final structures were analyzed using the InsightII program (Accelrys, San Diego, CA). Graphical representation were carried out with the

UCSF Chimera package.[76] The root-mean-squared-deviation analysis between energy-minimized structures were carried out with the program MOLMOL.[72]

Determination of Somatostatin Receptor Affinity Profiles. Cell membrane pellets were prepared from human sst_1-expressing CHO cells, sst_2-, sst_3-, sst_4-expressing CCL39 cells and sst_5-expressing HEK293 cells and stored at -80°C. Receptor autoradiography was performed on 20-μm thick cryostat (Microm HM 500, Walldorf, Germany) sections of the membrane pellets, mounted on microscope slides, and then stored at -20°C as previously described.[174, 175] For each of the tested compounds, complete displacement experiments with the universal SRIF radioligand [Leu^8, D-Trp^{22}, ^{125}I-Tyr^{25}]-SRIF-28 (^{125}I-[LTT]-SRIF-28) (2,000 Ci/mmol; Anawa, Wangen, Switzerland) using 15,000 cpm/100 μL and increasing concentrations of the unlabelled peptide ranging from 0.1 – 1000 nM were performed. As control, unlabelled SRIF-28 was run in parallel using the same increasing concentrations. The sections were incubated with ^{125}I-[LTT]-SRIF-28 for 2 hours at room temperature in 170 mmol/L Tris-HCl buffer (pH 8.2), containing 1% BSA, 40 mg/L bacitracin, and 10 mmol/L $MgCl_2$ to inhibit endogenous proteases. The incubated sections were washed twice for 5 min in cold 170 mmol/L Tris-HCl (pH 8.2) containing 0.25% BSA. After a brief dip in 170 mmol/L Tris-

HCl (pH 8.2), the sections were dried quickly and exposed for 1 week to Kodak BioMax MR film. IC_{50} values were calculated after quantification of the data using a computer-assisted image processing system as described previously.[175] Tissue standards (Autoradiographic [^{125}I] and/or [^{14}C] microscales, GE Healthcare; Little Chalfont, UK) that contain known amounts of isotope, cross-calibrated to tissue-equivalent ligand concentrations were used for quantification.[146]

Chapter 2 - LIGAND-RECEPTOR INTERACTIONS FROM NMR SPECTROSCOPY. APPLICATION TO CYTOTOXIC AGENTS BINDING TO DNA

2.1 Design, Synthesis, and Cytotoxic Evaluation of Acyl Derivatives of 3-Aminonaphtho[2,3-*b*]thiophene-4,9-dione, a Quinone-Based System

A series of 3-acyl derivatives of dihydronaphtho[2,3-*b*]thiophen-4,9-dione system were studied with respect to cytotoxicity and topoisomerase II inhibitory activity. These analogues were designed as electron-deficient anthraquinone analogues with potential intercalation ability. Derivatives 3-(diethylamino)-N-(4,9-dioxo-4,9-dihydronaphtho[2,3-*b*]thiophen-3-yl)propanamide (**11m**) and 3-(2-(dimethylamino)ethylamino)-N-(4,9-dioxo-4,9-dihydronaphtho[2,3-*b*]thiophen-3-yl) propanamide (**11p**) showed a high efficacy in cell lines that were highly resistant to treatment with doxorubicin, such as MDA-MB435 (melanoma), IGROV (ovarian), SF-295 (glioblastoma) human cell lines. Both compounds inhibit topoisomerase II mediated relaxation of DNA, while only **11p** incites arrest at S phase in Caco-2 cells, inducing a delay of cell cycle progression and an increase of cell differentiation. The ability of these derivatives of modulate small heat shock proteins and the cardiotoxicy effects were also explored. In addition, DNA-binding properties of these compounds were investigated and discussed.

2.1.1 Introduction

Anthracyclines are among the most effective and useful anti-cancer agents developed, and they are used to treat more types of cancer than any other chemotherapy agent.[176, 177] Their clinical importance has stimulated wide research [178-181] directed to the development of new structurally related compounds with the goal of bypassing significant problems that limit their utility, such as their failure in resistant tumors expressing the ABCB1 (MDR1) gene [182-184] and the emergence of severe short- and long-term side effects associated with bone marrow and myocardial cell toxicity.[185, 186] With this aim, our research group has developed different series of quinone-based compounds containing the 3-amino-3-(ethoxycarbonyl)-2,3-dihydrothieno[2,3-*b*]naphtho-4,9-dione system (**4**, DTNQ) as chromophore (Figure 22).[187] The effected modifications on this template and the analysis of the structure-activity relationship (SAR) on the different synthesized series showed that the incorporation of a distal protonated alkyl amine linked to chromophore DTNQ system through a five- or six-membered heterocycle or the presence of a cycloalkyl as the fifth ring were effective approaches to identify new compounds endowed with potent cytotoxic activity, and able to overcome multidrug resistance of tumor cells. Thus, the 3-glycyl-amino-3-(ethoxycarbonyl)-2,3-

dihydrothieno[2,3-*b*]naphtho-4,9-dione (**5**),[188] the spirohydantoin derivatives 3-[2-(*N*,*N*-dimethylamino)ethyl or propyl]-spiro[(dihydroimidazo-2,4-dione)-5,3′-(2′,3′-dihydrothieno[2,3-*b*]naphtho-4′,9′-dione)] (**6a,b**) [189] as well as the spirodiketopiperazine derivatives 4-[(2-*N*,*N*-dimethyl)amino]ethylspiro[(dihydropirazin-2,5-dione)-6,3′-(2′,3′-dihydrothieno[2,3-*b*]naphtho-4′,9′-dione) (**7**) [190] and spiro [(hexahydropyrrolo[1,2-*a*]pyrazine-1,4-dione)-6,3′-(2′,3′-dihydrothieno[2,3-*b*]naphtho-4′,9′-dione)] (**8**) [191] showed remarkable cytotoxic activity against several solid tumors and doxorubicin- and *cis*-platinum-resistant human cell lines.

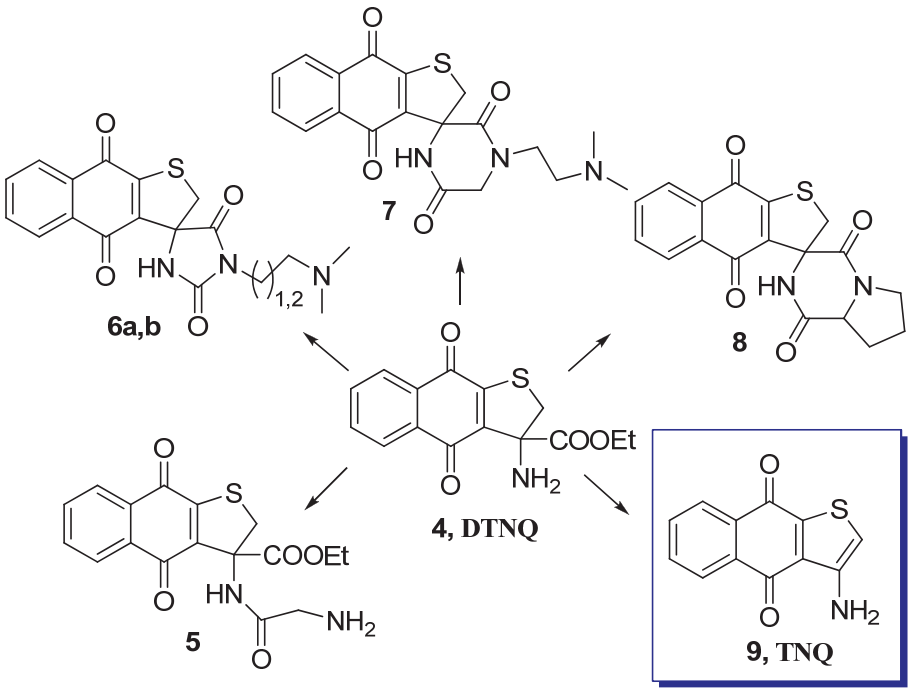

Figure 22. Structure of some DTNQ derivatives and the new TNQ system.

In addition, STD-NMR spectroscopy investigation performed on compounds **7** and **8** demonstrated that these derivatives interact with DNA with a dual binding mode: intercalative for the dihydrothieno[2,3-*b*]naphtho-4,9-dionetricyclic core and external considering the side-chain moiety.[190, 191] However, even though these derivatives had many of the structural characteristics of classical quinone-based DNA intercalating agents, they were not able to inhibit topoisomerase II (topo II) at equicytotoxic concentrations, indicating that other factors such as differences in cellular uptake, distribution within the cell, and additional targets within the cell might also affect the cytotoxicity of these derivatives.[192]

Now we have considered the possibility of using a new DTNQ derivative, the 3-aminonaphtho[2,3-*b*]thiophene-4,9-dione (**9**, TNQ) recently synthesized in our laboratories,[193] as a more planar chromophore. This quinone-based amine system showed interesting cytotoxic activity toward the MCF-7 human breast carcinoma (IC_{50} = 3.2 μM) and SW 620 human colon carcinoma cell lines (IC_{50} = 4.0 μM) indicating its potential as a template in the development of efficient cytotoxic agents. The new system presents a more “planar core” compared to initial DTNQ structure and an amine group able to be functionalized with appropriate side chain in a defined orientation with respect to the chromophore, thus guaranteeing two of the main

structural requisites for the antineoplastic activity of intercalating agents. According to literature data, among heterocyclic quinones endowed with cytotoxic activity, those containing a thiophene nucleus fused to a quinone system have received little attention, despite the antitumoral activity of thiophene analogues of daunomycin and mitoxantrone described by the work groups of Kita [194] and Krapcho,[195] respectively.

Thus, we developed a series of 3-substituted-aminonaphtho[2,3-*b*]thiophene-4,9-dione derivatives in which the amine group of the planar chromophore (TNQ) was linked to several amino acids (Gly, Ala, Phe, Lys, Pro, *β*-Ala), substituted-alkylcarbonyl chains (hydroxyacetyl, hydroxypropionyl, (*N*,*N*-diethyl)aminoacetyl, (*N*,*N*-diethyl)aminopropionyl, 2-morpholinacetyl, 3-morpholinpropionyl, (*N'*,*N'*-methyl)(*N*-aminoethyl)-aminopropionyl, thioacetyl, thiopropionyl) and carbamoyl chains (propyl, aminoethyl), which represent the side chain functionalities of the more active compounds of the precedent series. The objectives of this investigation are: a) validation of TNQ system as template in the development of new quinone-based antitumoral agents exploring so new chemical spaces; b) identification of the structural parameters which are important for the cytotoxic activity, through a comparative study of the structure activity relationships (SARs) of TNQ derivatives; and c) exploration

of the basic biochemical events correlated to cytotoxic activity of new derivatives. The present work deals with the preliminary studies concerning the synthesis of novel TNQ derivatives, the cytotoxic activity, the interaction with topo II and DNA, and their influence on cell cycle progression.

2.1.2 Results and Discussion

Chemistry. The synthetic approach to new 3-substituted-aminonaphtho[2,3-*b*]thiophene-4,9-dione derivatives was based on the capacity of DTNQ system and its 3-N-acyl derivatives to undergo oxidative decarboxylation in hydrolytic basic way, as we recently described.[193] Condensation of 3-amino-3-ethoxycarbonyl-2,3-dihydrothieno[2,3-*b*]naphtho-4,9-dione (**4**, DTNQ) with different Boc-amino acids (**a** = Gly, **b**= Ala, **c** = Phe, **d** = Lys, **e** = Pro, **f** = *β*-Ala,) using HBTU, HOBt, and DIPEA in DMF afforded, with high yields (50-65%), the appropriate pseudodipeptide intermediates **10'a-f**, as shown in Figure 23. Treatment with DBU in MeOH/H_2O medium gave directly the corresponding decarboxylated intermediates **11' a-f** in 76-82% yields. Finally, after removal of the Boc protecting group using 20% TFA in dichloromethane and triethylsilane as scavanger, the final compounds **11a-f** were obtained as trifluoroacetate salts in 40-48 % overall yields.

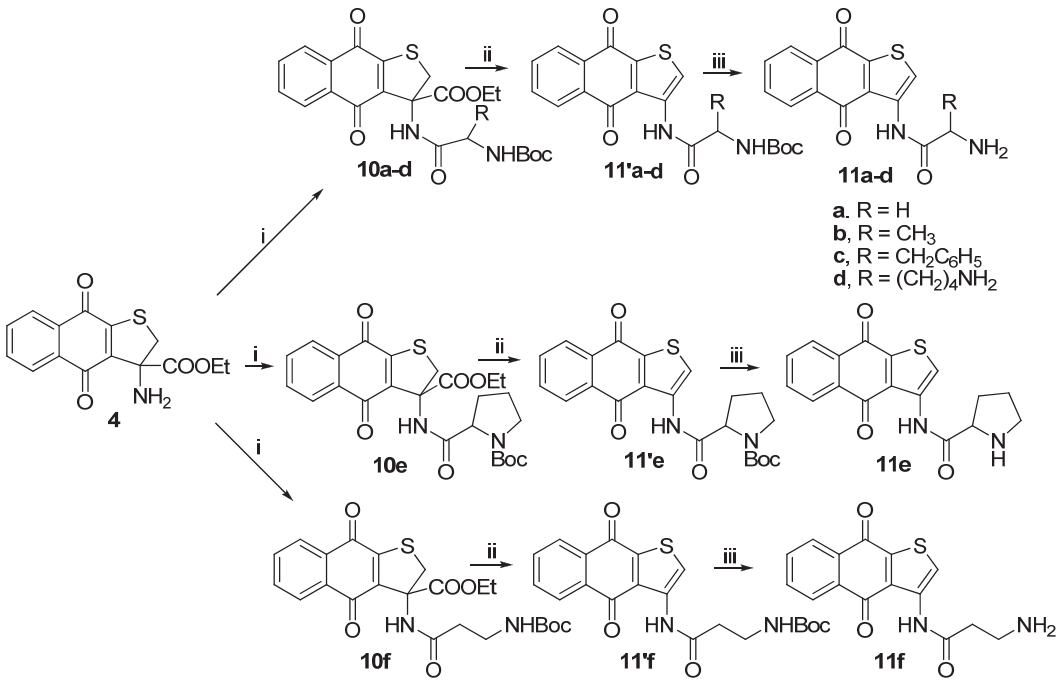

Figure 23. Reagents and conditions: i) Boc-Aaa-OH HBTU, HOBt, DIPEA in DMF, room temperature ii) DBU in MeOH/H20, room temperature, iii) TFA/DCM, TES.

Two homologue series of compounds containing a linear substituted-alkyl chain were synthesized from 3-(2′-chloro)acetamide-3-ethoxycarbonyl-2,3-dihydrothieno[2,3-*b*]naphtho-4,9-dione (**12**) and 3-(acrylamido)-3-ethoxycarbonyl-2,3-dihydrothieno[2,3-*b*]naphtho-4,9-dione (**13**) respectively, followed a similar methodology (Figure 24).

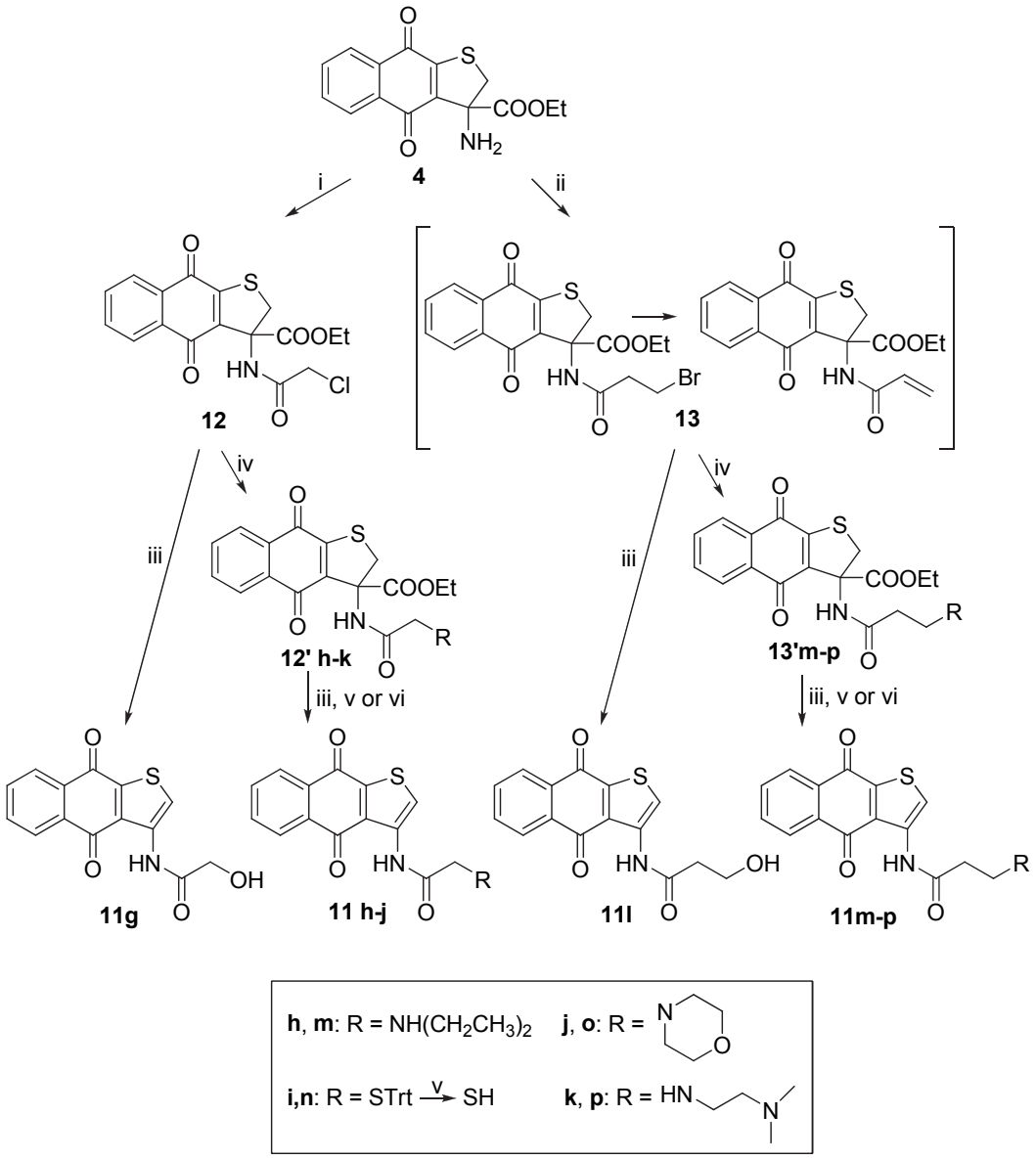

Figure 24. Reagents and conditions: i) chloroacetyl chloride, TEA in THF; ii) bromopropionyl chloride, TEA in THF, iii) DBU in MeOH/H2O, room temperature; iv) Nucleophilic reagents in THF, TEA, reflux temperature; v) then, for **11i** and **11n** 20% TFA in dichloromethane; vi) then, for **11j** and **11k**, **11m**, **11o**, and **11p** HCl (g)/diethyl ether solution.

Condensation of **4** with chloroacethyl chloride in THF, using triethylamine as base, afforded the (2′-chloro)acetamide derivative **12** with 92% yield. Under these conditions, the reaction of **4** with bromopropionyl chloride gave the 3-bromopropionamide intermediate

(90% yield), which partially evolved to *β*-elimination product 3-(acrylamido)-3-ethoxycarbonyl-2,3-dihydrothieno[2,3-*b*] naphtho-4,9-dione (**13**), during work-up of reaction. Decarboxylation performed on **12** and **13** intermediates gave directly the 2-hydroxyacetamide (**11g**) and 3-hydroxypropyonamide (**11l**) as final compound, respectively. Nucleophilic displacement of the chlorine atom (**12**) or Michael-type addiction to acrylamido moiety (**13**) using diethylamine, triphenylmethanethiol, morpholine or *N,N*-diethylethylendiamine, in THF and triethylamine at reflux, readily provided the corresponding acetamide (**12'h-k**) or propionamide (**13'm-p**) analogues. Basic hydrolysis of these derivatives afforded the corresponding decarboxylated compounds (**11h-j** and **11m-p**), except in the case of **12'k** (R = $HNCH_2CH_2N(CH_3)_2$). In fact, under the cited conditions, this intermediate gave the cyclic derivative 4-[(2-*N,N*-dimethyl)amino]ethylspiro[(dihydropirazin-2,5-dione)-6,3′-(2′,3′-dihydrothieno[2,3-*b*]naphtho-4′,9′-dione)] (**7**) previously described.[190] Then, final compounds presenting an amine functionality **11j**, **11k**, **11m**, **11o**, and **11p**, were treated with a solution of gaseous hydrochloric acid in diethyl ether to provide corresponding hydrochloride salts. This was found to both aid purification, and provide an improved solubility profile for the biological assays. The final thioacetamide **11i** and thiopropyonamide

11n derivatives were obtained after S-Trt deprotection using 20% TFA in dichloromethane in quantitative yields.

For the synthesis of compound **11k** and the urea-based derivatives **11q** and **11r** we chose an alternative route which implied the use of 3-amino-naptho[2,3-*b*]thiophene-4.9-dione (TNQ, **9**) as starting material (Figure 25). The condensation of **9**, obtained after deprotection of corresponding N-Boc TNQ (**14**) using 50% TFA in dichloromethane,[193] with chloroacethyl chloride afforded the (2′-chloro)acetamide intermediate **15** (88% yield). Reaction of **15** with diethylamine in THF and triethylamine at reflux, afforded the final derivative **11k**. Compounds **11q** and **11r** were obtained by treatment of **9** with triphosgene and TEA in THF followed by addiction of propylamine or *N,N*-dimethylethylendiamine. Also in this case, the use of **9** as starting material was necessary since the corresponding N-carbamoyl derivatives of DTNQ (compounds **6'**) evolved rapidly to spirohydantoin derivatives **6** under hydrolitic conditions.[189]

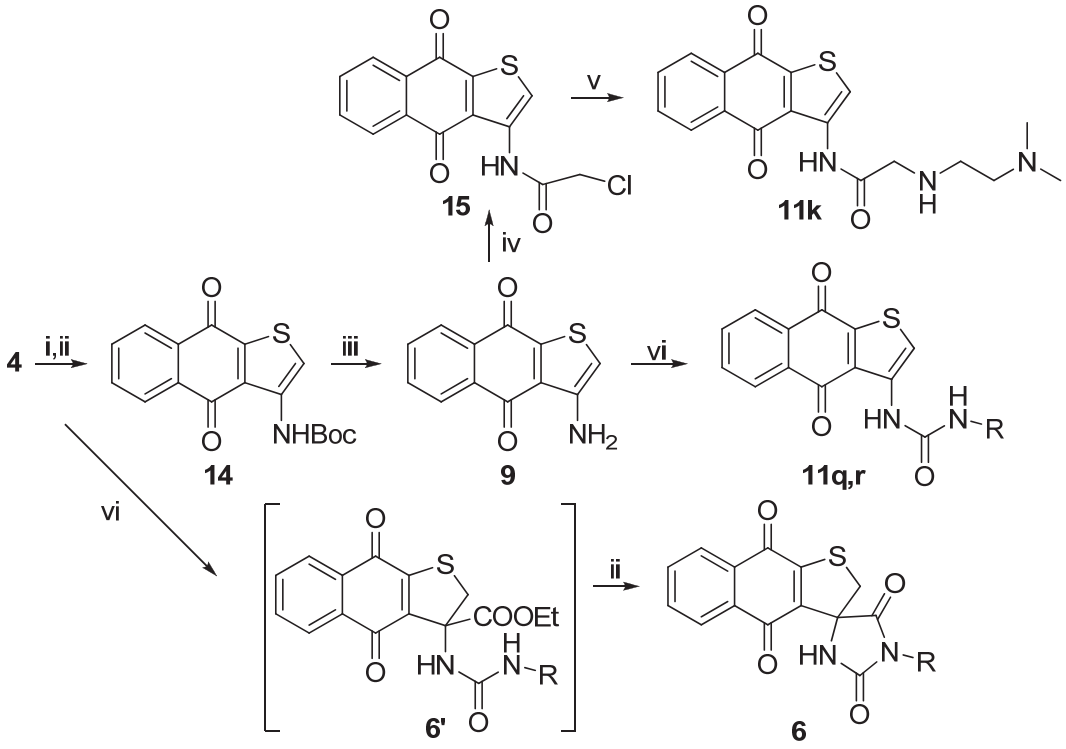

Figure 25. Reagents and conditions: i) (Boc)2O, ii) DBU in MeOH/H2O, room temperature; iii) 50% TFA/dichloromethane; iv) chloroacetyl chloride, TEA in THF; v) (N,N-dimethyl) ethylenediamine in THF, TEA, reflux temperature; vi) triphosgen, TEA, THF, room temperature, 10 min, then R-NH_2.

In Vitro Cytotoxicity. TNQ derivatives were first examined for antiproliferative activity against the MDA231 human breast carcinoma, SW 620 human colon carcinoma, and U937 human leukemic monocyte lymphoma cell lines, and the obtained IC_{50} values are summarized in Table 12. For comparative purposes, the template **9** and doxorubicin were also included in the assay.

Results in Table 12 confirmed the compound **9** as potential scaffold of new antitumoral agents with a cytotoxic activity into the micromolar range on three cell lines used in the assay. The improved antitumor activity and spectra of some of the newly synthesized

compounds, compared to **9**, demonstrated that chemical modification at C-3 was an effective approach to optimize the activity profiles of TNQ moiety. The wide activity range observed for compounds **11a-11r** (IC_{50} from 0.6 to >40 μM) indicated that the nature of substituents on amine group at C-3 position markedly affects the activity profile of these compounds. Incorporation through the 3-amino group of different amino acids was well tolerated in the case of linear amino acids such as glycine (**11a**). The presence of amino acids containing alkyl (Ala, **11b**) or benzyl (Phe, **11c**) side chain, relatively more rigid and more electron rich when compared to non substituted side chain, led to significant loss of activity, especially in the MDA231 cell line. This negative effect was more noteworthy with the introduction of an alkyl amino side chain (Lys, **11d**). The incorporation of Pro gave the derivative **11e**, which turned out to be the most active in the leukemic cell line (IC_{50} = 0.9 μM).

Table 12. Cytotoxic activities of 3-(amino)naphtho[2,3-b]thiophene-4,9-dione (9) and 3-[(acyl)amino]naphtho[2,3-b]thiophene-4,9-dione derivatives (11 a-f).

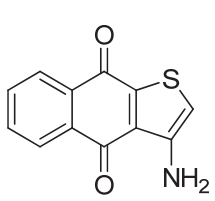

9

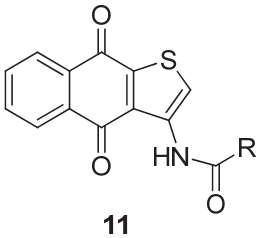

11

compd	R	IC$_{50}$ (□M) ±SD[a]			TopoII-activity[e]	
		MDA231[b]	SW620[c]	U937[d]	5μM	10μM
9		11.3±0.4	4.0±0.3	10.1±0.4		
11a	CH_2NH_2[f]	6.2±4.6	2.3±0.4	7.0±0.07		
11b	$CH(CH_3)NH_2$[f]	>40	12.4 ±1.5	9.1±0.2		
11c	$CH[CH_2(C_6H_5)]NH_2$[f]	>40	30.50±6.4	>40	+	+
11d	$CH[(CH_2)_4NH_2]NH_2$[f]	>40	>40	20±0.01		
11e	2-pyrrolidinyl[f]	6.7±2.5	5.4 ±0.1	0.9±0.06		
11f	$CH_2CH_2NH_2$[f]	3.7±0.9	0.8±0.27	1.7±0.01		
11g	CH_2OH	10.1±0.2	18.5 ±0.7	15.1±0.06		
11h	$CH_2N(CH_2CH_3)_2$[g]	8.5±0.12	4.0 ±0.14	5.1±0.07		
11i	CH_2SH	13.6±0.15	20.9 ±0.16	30.1±0.04		
11j	CH_2-morpholine[g]	7.1±0.2	10.8 ±0.12	4.3±0.02		
11k	$CH_2NH(CH_2)_2N(CH_3)_2$[g]	4.9±0.4	2.1±0.3	4.0±0.03		
11l	$(CH_2)_2OH$	9.2±0.6	20.3± 0.8	15±0.06		
11m	$(CH_2)_2N(CH_2CH_3)_2$[g]	2.5±0.1	1.5 ±0.2	1.1±0.01	+	+++
11n	$(CH_2)_2SH$	15.2±0.1	20.7 ±0.8	23.9±0.34		
11o	$(CH_2)_2$-morpholine[g]	10.1±1.3	20.1 ±0.3	7.2±0.07		
11p	$(CH_2)_2NH(CH_2)_2N(CH_3)_2$[g]	2.0±0.1	0.6 ± 0.08	1.3±0.03	++	+++
11q	$NH(CH_2)_2CH_3$[g]	9.5±0.52	6.5 ±1.20	10.1±0.50		
11r	$NH(CH_2)_2N(CH_3)_2$[g]	8.7± 0.30	5.9 ±0.20	9.8±0.20		
	Doxorubicin	1.13±0.01	0.12±0.01	0.93±0.01	0	0

[a] Data represent mean values (SD) for three independent determinations. [b] Human melanoma cell line. [c] Human colon carcinoma cell line. [d] Human leukemic monocyte lymphoma cell line. [e] The semiquantitative evaluation of TopoII-mediated DNA relaxation activity was as follows: +++, high; ++, intermediate; +, low; 0, absent. All the rest compounds were not tested. [f] Evaluated as TFA salts. [g] Evaluated as HCl salts.

Other interesting results were obtained with the incorporation of a primary or tertiary amine to the end of the ethyl side chains. Compounds **11f**, **11m**, and **11p** retained cytotoxic levels similar to those of doxorubicin on the SW 620 cell line, with IC$_{50}$ values of 0.8, 1.5, and 0.6 μM respectively, and maintained the activity on the

MDA231 and U937 cell lines within the micromolar range (2.0-3.7 μM and 1.1-1.7 μM, respectively). These derivatives were 2-5 fold more potent than their methylene homologues (**11a**, **11h**, and **11k**, respectively) on all the cell lines. Congeners with a hydroxyl (compounds **11g** and **11l**), thiol (compounds **11i** and **11n)** or morpholin (compounds **11j** and **11o**) groups were remarkably less potent compared to their primary and tertiary amine analogues.

Finally, the incorporation of an alkyl or alkylamino side chain through an ureide group led to a decrease of the activity in the resultant analogues **11q** and **11r**, respectively. These results imply a minor tolerance to structural modifications in this series compared to precedent series.

To further determine the antitumor spectra, the most potent compounds **11f**, **11m**, and **11p** were selected and screened against a panel of human tumor cell lines, including MDA-MB435 and SK-MEL 28 (melanoma), IGROV (ovarian), SF-295 and SNB-19 (glioblastoma), and Colo205, HT-29, and undifferentiated Caco-2 (colon). Differentiated Caco-2, a well accepted model of normal cell line due to its ability to acquire the phenotype of mature small-intestinal cell,[196, 197] was utilized to characterize a safety profile of the compounds at least in terms of "cell-selectivity".[198, 199]

As observed in Table 13, selected compounds were more potent than doxorubicin on the melanoma, colon and CNS human tumor cell lines, with IC_{50} values in the range 0.1–1.0 μM. Compounds **11m** and **11p** turned out to be the most active derivatives against SK-MEL 28 human melanoma cell line (IC_{50} = 0.6 and 0.3 μM, respectively) and were equipotent to doxorubicin (IC_{50} = 0.4 μM). Analogously to that observed in the previously described series,[189-191] these compounds showed a remarkable activity against tumoral cell lines generally highly resistant to treatment with doxorubicin. Compounds **11m** and **11p** presented a cytotoxic activity in the micromolar range against undifferentiated Caco-2 tumoral colon cell lines (IC_{50} = 0.8-1.0 μM), while showed to be 4-fold less active (IC_{50} = 3.8-4.1 μM) on differentiated Caco-2 cell line. These data indicated a good profile of cell-selectivity for our derivatives (Selectivity Index (SI) ~ 0.22) especially if they are compared with the high toxicity data obtained with doxorubicin (SI = 11.1).

Table 13. Inhibition of multiple human tumor cell lines by selected compound.

Origin of tumor	Cell line	IC_{50} (μM) ±SD[a]			
		11f	**11m**	**11p**	**Doxorubicin**
Melanoma	MDA-MB435	0.4±0.10	0.5±0.08	0.5±0.09	1.3±0.21
	SK-MEL 28	1.5±0.08	0.6±0.08	0.3±0.07	0.6±0.09
Ovarian	IGROV	1.2±0.30	2.5±0.10	2.0±0.20	1.3±0.30
Glioblastoma	SF-295	2.8±0.20	0.6±0.06	0.6±0.09	4.4±0.50
	SNB-19	1.6±0.60	0.7±0.04	0.9±0.10	0.8±0.05
Colon	Colo205	0.4±0.04	0.9±0.05	1.1±0.05	1.5±0.30
	HT-29	0.6±0.08	0.8±0.05	0.5±0.10	1.1±0.20
	Caco-2[b]	2.6±0.2	1.0±0.6	0.8±0.03	6.7±0.80
	Caco-2[c]	6.1 ±0.32	4.1±0.10	3.8 ±0.09	0.6±0.05
	SI[d]	0.43	0.25	0.21	11.1

[a] Data represent mean values (SD) for three independent determinations. [b] Pre confluent Caco-2 cell line. [c] Post confluent Caco-2 cell line. [d] SI = selectivity index (IC_{50} on undifferentiated Caco-2 cell line/IC_{50} on differentiated Caco-2 cell line ratio)

Subcellular distribution of TNQ derivatives in MCF-7 cell line.

Distribution of the labelled forms of our derivatives within the cell was investigated by confocal microscopy in MCF-7 cell line, using 50 nM of **11m** (IC_{50}= 0.5 μM) and **11p** (IC_{50} = 0.6 μM). As showed in Figure 26, these TNQ derivatives are clearly localized in the nuclei indicating a site of cytotoxic action similar to classic quinone-based intercalators.[200]

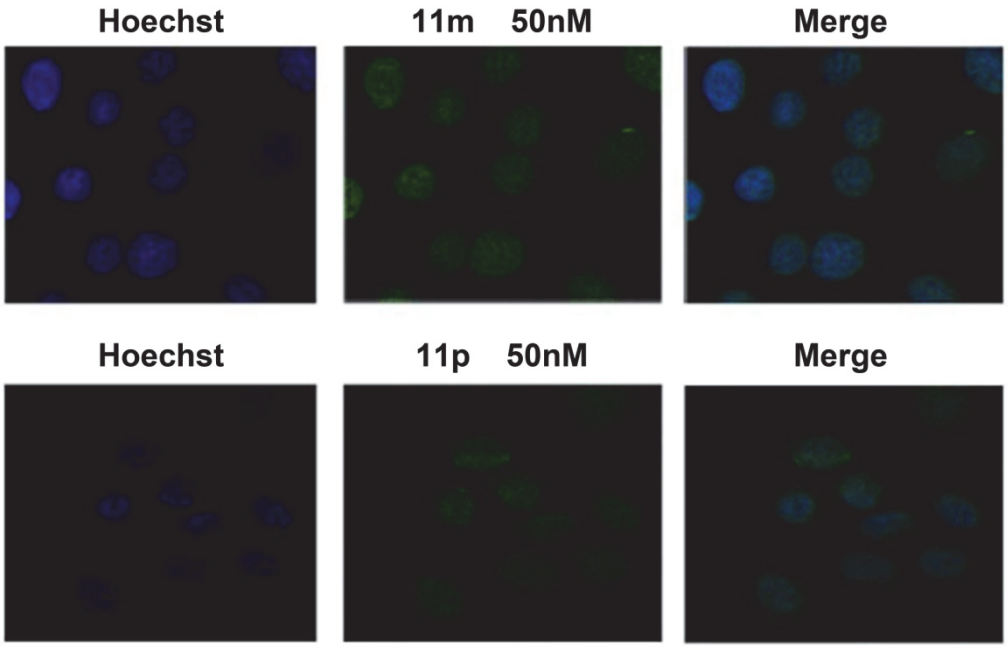

Figure 26. Distribution of labeled **11m** and **11p** in MCF-7 cells by confocal microscopy.

Topoisomerase inhibition. A number of quinone antitumor drugs are thought to be cytotoxic by virtue of their ability to stabilize a covalent topo II-DNA intermediate, the cleavable complex.[201] Topo II is an essential enzyme that plays an important role in DNA replication, repair, transcription, and chromosome segregation.[202] Topo II alters the topological state of nucleic acids by passing an intact DNA helix through a transient break which generates a separate DNA helix.[203, 204] We analyzed the possibility that compounds **11m** and **11p** could inhibit the activity of topo II. The effect of cytotoxic compounds **11m** and **11p** and of the inactive compound **11c** on the strand passage activity of topo II was determined by the enzyme-mediated negatively supercoiled pBR322 relaxation.[205]

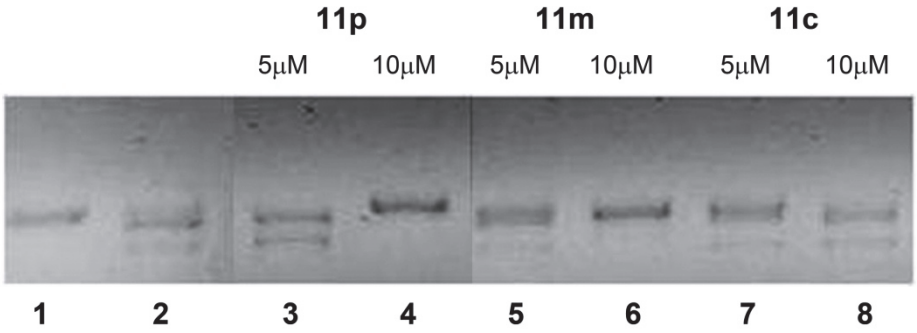

Figure 27. Effects of compounds **11p**, **11m** and **11c** on the topo II-mediated DNA cleavage. Supercoiled plasmid pBR 322 (0.5 pmol) was incubated with 1 unit of purified human topo II in the presence or absence of the tested agents: (lane 1), supercoiled DNA; (lane 2) relaxated DNA enzyme control; (lanes 3 and 4) 5 and 10 μM of compound **11p**; (lanes 5 and 6) 5 and 10 μM of compound **11m**; (lanes 7 and 8) 5 and 10 μM of compound **11c**.

As indicated in Figure 27, compounds **11m** and **11p** displayed significant inhibition of topo II mediated relaxation in a concentration-dependent mode, while **11c** does not inhibit this activity at the concentrations tested. These results, showed also in Table 12 as semi-quantitative form, parallel the cytotoxicity data enumerated in the same table, thus suggesting a behavior similar to classical intercalators. Moreover, at the assay concentrations, the doxorubicin showed a lack of activity (see Supporting Information) which agrees with the results described in different studies.[206, 207] These works show as the doxorubicin inhibits topo II only at the concentration range of 0.04 to 0.92 μM while at higher concentration the inhibition is either diminished or totally abolished.

DNA Binding Properties by NMR. Representative compounds, **11c**, **11m** and **11p**, were tested to see if they interact with DNA, using both saturation transfer difference (STD) [208] and water-ligand observed via gradient spectroscopy (WaterLOGSY) NMR techniques.[209] STD NMR and WaterLOGSY are techniques that can be used to characterize and identify binding. These techniques have become increasingly important as a tool in the investigation of biomolecular recognition phenomena.[210] In the STD NMR, resonances of the macromolecule are selectively saturated, and in a binding ligand, enhancements are observed in the difference (STD NMR) spectrum resulting from subtraction of this spectrum from a reference spectrum in which the macromolecule is not saturated. All the proton resonances of **11m** and **11p** were observed in the STD spectra acquired in the presence of poly(dG-dC)·poly(dG-dC) copolymer as DNA target (Figure 28), demonstrating that **11m**/ and **11p**/DNA interactions did occur. In contrast, the absence of the proton resonances of **11c** in its STD spectra (Figure 28) demonstrates that **11c** does not interact with DNA. The same results were obtained using the WaterLOGSY experiment. In this experiment, the large bulk water magnetization is partially transferred via the macromolecule-ligand complex to the free ligand. Due to the very different tumbling times of the free ligand and of the macromolecule-ligand complex, LOGSY

signals are typically negative for free ligands in solution, and relatively less negative or positive for binders in the presence of the macromolecule. Figure 29 shows the WaterLOGSY spectra of **11c**, **11m** and **11p** with and without the poly(dG-dC)·poly(dG-dC) copolymer. As observed, **11m** and **11p** signals became positive in the presence of DNA while **11c** signals remain negative demonstrating that **11m** and **11p** but not **11c** interact with the DNA polymer.

Furthermore, we applied the so-called DF-STD (differential frequency STD) spectroscopy,[211] to study the binding modes of **11m** and **11p** with the DNA. The method allows the discrimination of base-pair intercalators, minor-groove, and external binders. The approach is based on the comparison of two parallel sets of STD experiments performed under the same experimental conditions, in which saturation is centered either in the aromatic or in the low-field aliphatic spectral regions.

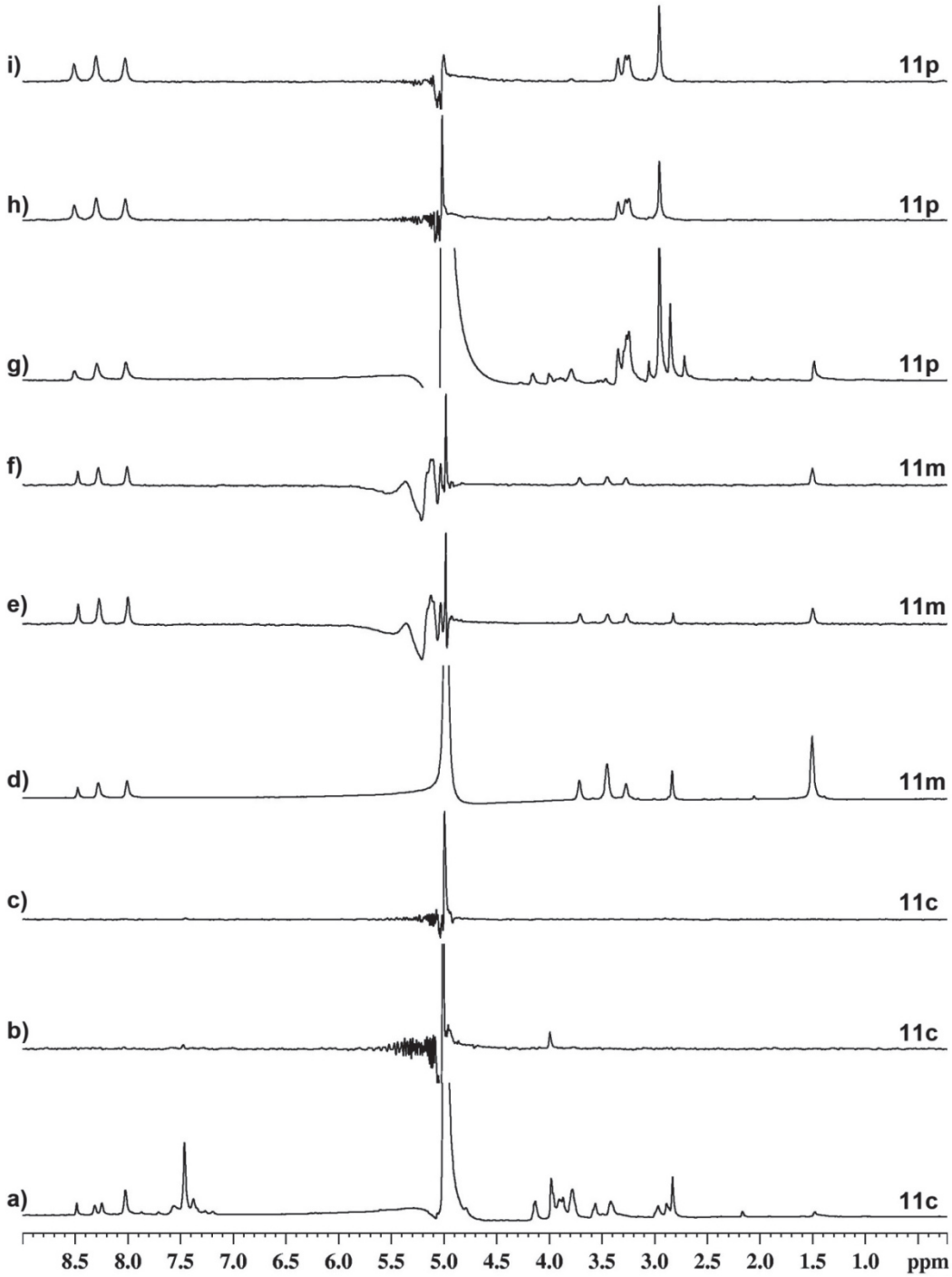

Figure 28. 1D proton spectra (a, d, g) and the corresponding STD NMR spectra recorded upon saturation at 10 ppm (b, e, h) and -1 ppm (c, f, i) of **11c**/, **11m**/, and **11p**/DNA complexes, respectively. The STD NMR spectra were plotted with the same noise level.

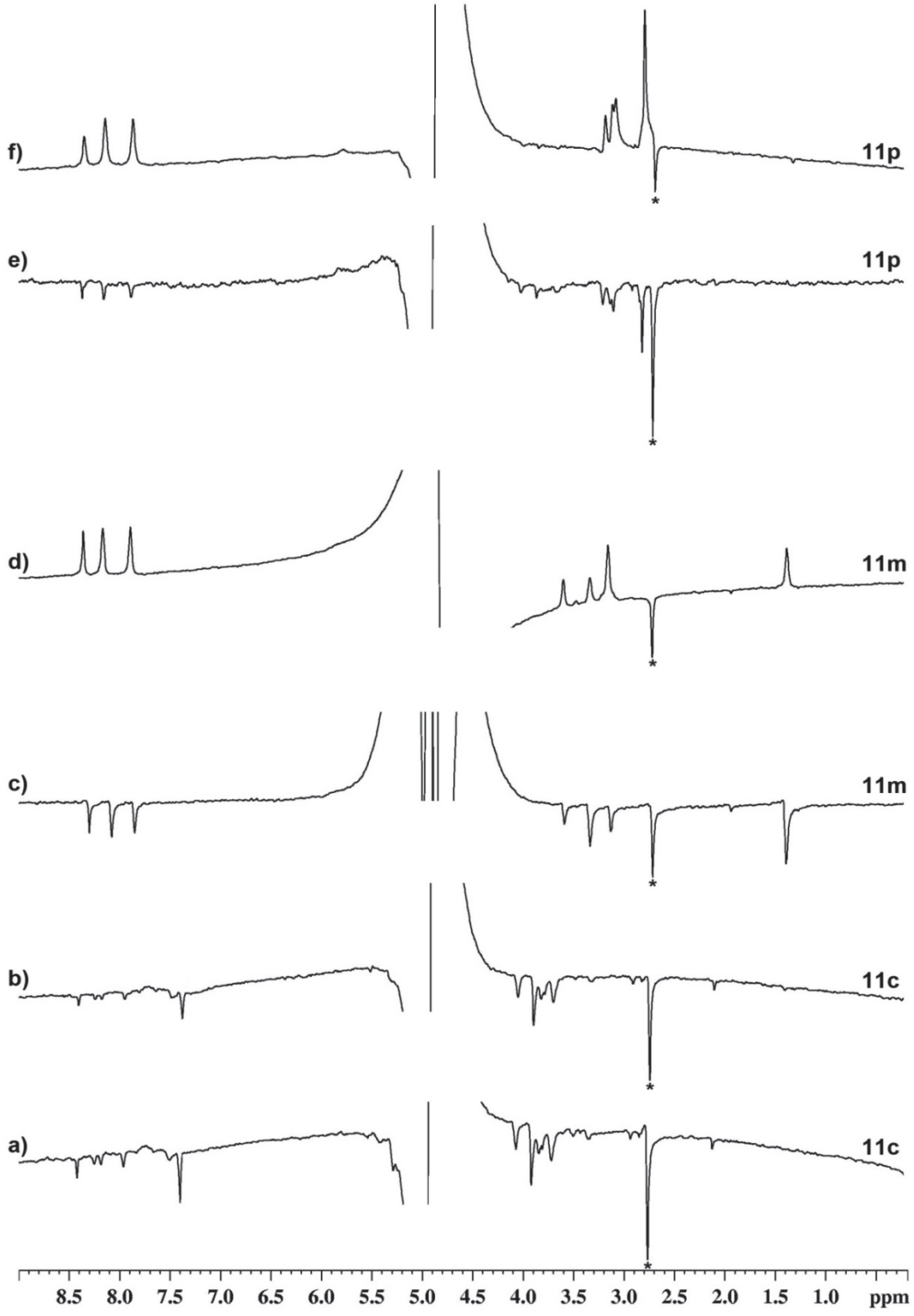

Figure 29. Water LOGSY spectra of **11c**, **11m**, and **11p** in the absence (b, d, e) or in the presence (a, c, e) of poly(dG-dC)•poly(dG-dC) copolymer.* DMSO residual signal.

A ligand making proximate contacts with aromatic base protons, such as an intercalator sandwiched by consecutive base pairs, would receive more saturation upon irradiation of DNA aromatic protons rather than irradiation of deoxyribose protons. The converse would be true for an external ligand. The "binding mode index" (BMI), a numerical parameter that expresses the relative sensitivity of ligand protons to the perturbation arising from base versus sugar/backbone saturation was used.[211] Three BMI ranges were defined in the original contribution:[211] $0 < BMI < 0.50$ for external (nonspecific) electrostatic backbone binding; $0.90 < BMI < 1.10$ for minor groove binding; and $1.20\ (0.90) < BMI < 1.50$ for base-pair intercalation. DF-STD analysis of compound **11m** gave different BMI values: BMI = 0.86, for the aliphatic signals; and BMI = 1.35 for the aromatic signals. This result can be explained assuming two different DNA binding modes for **11m**. An intercalative mode of binding is sustained by its tricyclic planar core, and an external backbone binding can be attributed to its side chain. This is similar to that observed for doxorubicin [211] and for compounds **7** and **8** in our previous works.[190, 191] Considering **11p**, BMI = 1.01 was measured for the aromatic protons and BMI = 0.90 for the aliphatics. These BMI values are compatible with both intercalative and minor groove binders.

Cell Cycle Effects. To investigate the cytotoxic effects of these derivatives in more detail, we examined the effects on cell cycle progression in CaCo-2 cell line. The percentage of these cells in G1, S, and G2/M phases was analyzed after 48 h of treatment with 1 μM of **11m**, **11p**, and **11c** (Figure 30). Under these conditions, the control cells were in the G1 phase 42%, G2/M phase 21%, and S phase 36%. The treatment with **11p** resulted in a significant accumulation of cells in the S phase while concomitantly the G1 populations decreased. About 53% of the CaCo-2 cells treated with this compound were arrested at the S phase. Under the same conditions, treatment with **11m** induces an weak increased of cell in both G2 and S phases and with compound **11c** tempts a less significant response.

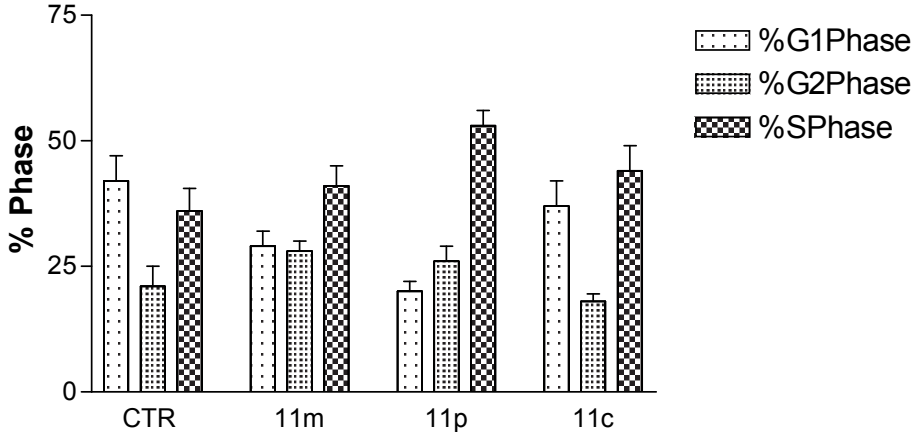

Figure 30. Effects of **11m**, **11p**, and **11c** on the distribution of Caco-2 cell populations data represent the percentage of cells in each cell cellular cycle phases. For **11m**: G1, 29%; G2/M, 28%; S, 41%; **11p**: G1, 20%; G2/M, 26%, S, 53%; **11c**: G1, 37%; G2/M , 18%, S, 44%.

Accordingly, treatment of Caco-2 cells with 1 μM of our derivatives for 48h induced an increase of cyclin A expression [212] only in the case of **11p** (43%, see Supporting Information) indicating that the cell cycle progression of cells in the S phase was prompted. The expression of cyclin A was not upset in treated Caco-2 cells with **11m** and **11c**.

Since cell division arrest is one of the prerequisites for cell differentiation,[213] we determined the effect of our molecules on Caco-2 differentiation. In Figure 31 we report alkaline phosphatase (ALP) activity, a marker of enterocytic differentiation correlated to post-confluent phase.[214]

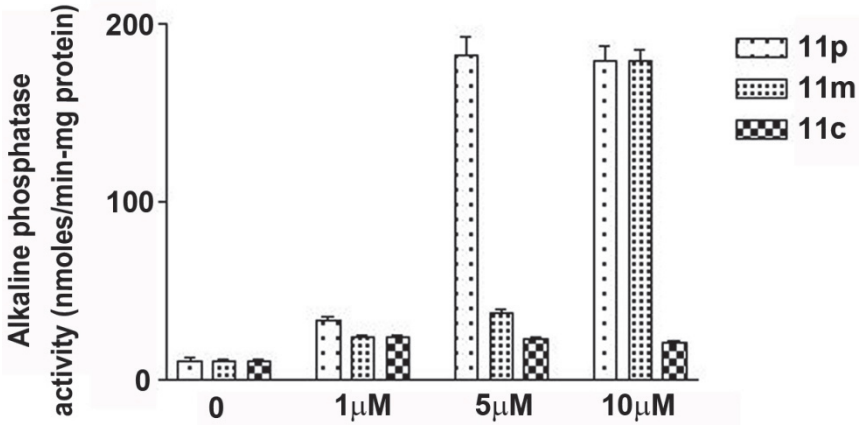

Figure 31. Differentiation of Caco-2 cells assessed by measurement of alkaline phosphatase activity after 48h of culture in the presence of 0, 1, 5, and 10 μM of **11p**, **11m** and **11c**.

Treatment of pre-confluent Caco-2 with 1μM **11p** increased ALP activity of 35% (p value< 0.005). A more significant increase of the

differentiation, with ALP augment of >180%, was only obtained by treatment of Caco-2 cells with 5 μM **11p** or 10 μM **11m** for 48 h. All these preliminary results suggested that, for this series, the cell growth inhibition was not related to cell cycle perturbation.

Modulation of heat shock protein (hsp) expression. Small heat shock proteins are involved in a variety of cellular processes including cell growth and differentiation.[215, 216] We previously reported the ability of a DTNQ analogue, compound **8**, to modulate the heat shock protein expression on Caco-2 cells.[192] In order to evaluate the behavior of the new synthesized derivatives, we carried out a study preliminary of the effect of **11m** and **11p** at 1 and 5μM on Hsp27 expression in Caco-2 cells for 48h. Hsp27 is weakly expressed in Caco-2 (Figure 32), and treatment of this cell line with **11p** led to significant dose-dependent increase of its expression. **11m** produced a weak enhanced of hsp27 expression at 1μM, which was not observed at 5μM.

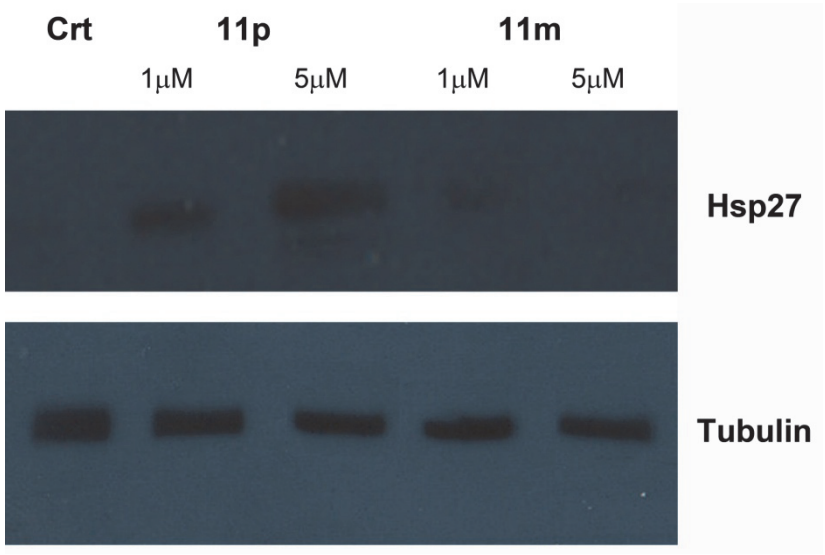

Figure 32. Effects of Caco-2 cells treatment with 1 and 5 μM of compounds **11p** and **11m** on hsp27 expression.

Cardiomyocyte cell viability. It is well known that the clinical use of anthracyclines, specially doxorubicin, in the treatment of many neoplastic diseases is limited by cumulative cardiotoxicty.[186] One of the cause of this effect has been attributed to the redox process involving the quinone system which results in the formation of reactive oxygen species and ultimately in myocyte death. In order to evaluate the potential toxicity of our quinone ring we examined the cell viability in cardiac derived H9C2 myocytes exposed to 1μM **11m** **11p** and doxorubicin for 24, 48, 72, 96 and 120 h. Previous studies reported in the literature used this cell line as a model system to evaluate the cardiotoxicity caused by doxorubicin.[217, 218] As show in Figure 33, treatment with doxorubicin induced cardiotoxicity in a time-dependent manner [186] while compounds **11m** and **11p**

maintained an good cell viability after 120 h (74 and 76%, respectively)

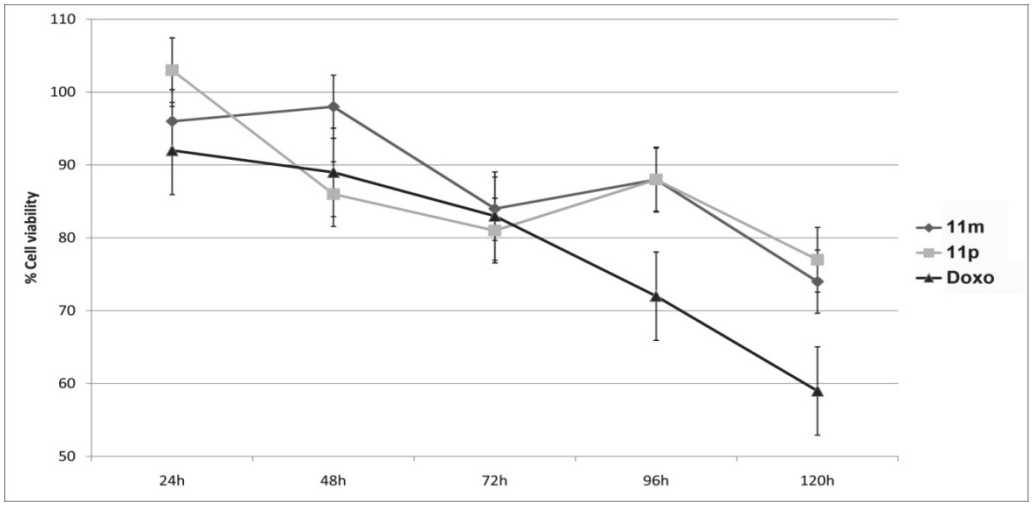

Figure 33. Results of cell viability assay of compounds 11m, 11p , and doxorubicin on H9C2 cells at concentration of 1μM.

The possible correlation [219] between these data and the preliminary results obtained with our products on the modulation of hsp27, will be object of more in-depth studies.

2.1.3 Conclusions

We report the synthesis and biological evaluation of a series of quinone-based derivatives, designed as conjugated structures linking a planar naphtho[2,3-*b*]thiophenedione core with different acyl-substituted groups. Among the designed molecules, compounds containing an 3-(diethylamino)propanamide (**11m**) or 3-(2-(dimethylamino)ethylamino)propanamide (**11p**) protonable side chain, showed a greater cytotoxic potency than doxorubicin against cell lines which were highly resistant to treatment with this drug, such as the melanoma (MDA-MB435), glioblastoma (SF-295) and colon (SW 620, Col205, and HT-29) human tumor cell lines,

Preliminary results about the mechanism of action indicate that these derivatives had a significant effect on topoisomerase II activity targeting the nuclear DNA, which is generally considered as an attractive target for anticancer therapy. The NMR results suggested that DNA interactions do occur for highly active compounds **11m** and **11p** but not for inactive compound **11c**. Experimental data indicate that **11m** and **11p** intercalate the DNA through their aromatic portion. Furthermore, a non intercalative mode of binding to DNA can also hold for **11p**. These data revealed significant similarities in the cytotoxic behavior and the site of action of these compounds compared to classical intercalators. However, tested compounds

showed a minor influence on the regulation of the cellular cycle and only derivative **11p** prolonged the S phase of the Caco-2 cell cycle inducing both delay of cell cycle progression in responsive cells and moderate cellular differentiation. This last compound showed also a high ability of increase hsp27 expression. Finally, the compounds under study affect the viability of H9C2 cells after chronic treatment at less extend compared to doxorubicin. Further development and more in-depth studies on mechanism of action of this series are in progress.

2.1.4 Experimental Section

***General**:* Reagents, starting materials, and solvents were purchased from commercial suppliers and used as received. Analytical TLC was performed on plates coated with a 0.25 mm layer of silica gel 60 F254 Merck and preparative TLC on 20×20 cm glass plates coated with a 0.5 mm layer of silica gel PF254 Merck. Flash and gravity chromatographic purification were performed using 230-400 mesh silica gel unless otherwise noted. Melting points were taken on a Kofler apparatus and are uncorrected. ^{1}H NMR and ^{13}C NMR spectra were recorded with a Varian-400 spectrometer, operating at 400 and 100 MHz, respectively. Chemical shifts are reported in δ values (ppm) relative to internal Me_4Si, and J values are reported in Hertz (Hz). ESI-MS experiments were performed on an Applied Biosystem API 2000 triple-quadrupole spectrometer. Combustion microanalyses were performed on a Carlo Erba CNH 1106 analyzer and all reported values are within 0.4% of calculated values. These elemental analyses confirmed ≥ 95% purity.

General procedure for the synthesis of 3-[(Acyl)amino]naphtho[2,3-b]thiophene-4,9-dione trifluoroacetate salts (11 a-f). The 3-amino-3-ethoxycarbonyl-2,3-dihydrothieno[2,3-*b*]naphtho-4,9-dione system (DTNQ) (1), the 3-(*N-tert*-butyloxyaminoacyl)amino-3-ethoxycarbonyl-2,3-dihydrothieno[2,3-

b]naphtho-4,9-dione (**10' a-f**), and the 3-(*N-tert*-butyloxyaminoacyl)aminonaphtho [2,3-*b*]thiophene-4,9-dione (**11**' **a-f**) derivatives were synthesized according to the references 12, 13, and 17 respectively. Then, TFA was added to a solution of decarboxylated Boc-protected derivatives (**11' a-f**) (0.1 mmol) in DCM (10 mL), using triethylsilane as scavenger. Stirring was continued for 3–4 h at room temperature, the reaction mixture was concentrated to half volume and ether was added. The title compounds as the trifluoroacetate salt, were collected by filtration as yellow solids.

3-[(Glycyl)amino]naphtho[2,3-b]thiophene-4,9-dione trifluoroacetate (11a). 45%, mp 207-208 °C. ^{1}H NMR (400 MHz, CD_3OD) δ 4.10 (s, 2H, CH_2,); 7.85–7.87 (m, 2H, H-6 and H-7); 8.20-8.23 (m, 2H, H-5 and H-8); 8.50 (s, 1H, H-2). ^{13}C NMR (100 MHz, CD_3OD) δ 45.7(*C*H_2), 119.2 (C-2); 127.5 (C-6 and C-7); 129.4 (C-3); 132.9 (C-8a); 134.2 (C-4a); 134.7 (C-5 and C-8); 135.9 (C-3a); 147.1 (C-9a); 171.8, 180.7 and 182.7 (C=O). ESI-MS *m*/*z* calcd for $C_{16}H_{11}F_3N_2O_5S$, 400.03; found, 400.11.

*3-[(L-phenylyl)amino]naphtho[2,3-b]thiophene-4,9-dione trifluoroacetate (**11c**).* 41%, mp 195-196 °C. ^{1}H NMR (400 MHz, CD_3OD) δ 2.96-3.07 (2 H, m, βCH_2), 4.44-4.47 (1 H, m, αCH), 7.12-7.22 (5 H, m, aryl), 7.87–7.89 (2 H, m, H-6 and H 7), 8.22–8.25 (2 H, m, H-5 and H 8), 8.47 (1H, s, H-2). ^{13}C NMR (100 MHz,

CD_3OD) δ 37.9 (β*C*H_2), 50.6 (αCH), 118.8 (C-2); 127.9 (C-6 and C-7); 125.9, 127.6, 128.3, 128.9 and 137.9 (aryl),131.4 (C-3); 133.6 (C-8a); 134.2 (C-4a); 134.9 (C-5 and C-8); 139.0 (C-3a); 142.5 (C-9a); 172.7 179.8 and 181.9 (C=O). ESI-MS *m*/*z* calcd for $C_{23}H_{17}F_3N_2O_5S$, 490.08; found, 490.01.

General procedure for the synthesis of N-(4,9-dioxo-4,9-dihydronaphtho[2,3-b]thiophen-3-yl)-3-(substituted)propanamide (11 m-p). To a solution of 13 (0.1-0.3 mmol) in THF (20 mL) were added *N*,*N*-diethylamine, or triphenylmethanethiol, or morpholine, or *N*,*N*-dimethylethylendiamine (1.1 equiv) and DIPEA (2 equiv). After stirring at reflux temperature for 12–24 h, the solvent was evaporated. Then, the residues (13' m-p) were dissolved into methanol–water (9:1, 20 mL) and DBU (5 equiv) was added dropwise to these solutions. The reaction mixtures were stirred for 0.5-1 h, then the solvents were evaporated and the reaction residues were dissolved in chloroform and washed with water and dried with Na_2SO_4. The corresponding free bases of compounds **11m**, 11n, and 11p were first purified by FC using DCM/Methanol 9/1 as eluent system. Then, the treatment with a HCl (g)/diethyl ether solution give the final compounds as hydrochloride saltsand yellow solids. Compound protected 11o was purified by FC using n-hexane/ethylacetate 3/2 as eluent. Then, the

final compound was obtained after Trt removal with a 50% TFA/DCM solution.

*3-(diethylamino)-N-(4,9-dioxo-4,9-dihydronaphtho[2,3-b]thiophen-3-yl)propanamide hydrochloride (**11m**)*. 43%, mp 201-202°C. ^{1}H NMR (400 MHz, CD_3OD) δ 1.36–1.40 (t, 6H, C*H*$_3$); 3.10-3.13 (m, 2H, C*H*$_2$); 3.30-3.34 (q, 4H, C*H*$_2$); 3.56-3.59 (m, 2H, C*H*$_2$); 7.85–7.87 (m, 2H, H-6 and H-7); 8.20-8.24 (m, 2H, H-5 and H-8); 8.48 (s, 1H, H-2). ^{13}C NMR (100 MHz, CD_3OD) δ 15.8 (*C*H$_3$), 35.8 (α*C*H$_2$), 47.9 (*C*H$_2$CH$_3$), 51.5 (βCH$_2$), 118.6 (C-2); 126.9 (C-6 and C-7); 129.2 (C-3); 132.7 (C-8a); 133.1 (C-4a); 134.8 (C-5 and C-8); 138.9 (C-3a); 145.0 (C-9a); 172.5, 178.9 and 182.6 (C=O). ESI-MS *m*/*z* calcd for $C_{19}H_{21}ClN_2O_3S$, 392.10; found, 390.17.

*3-(2-(dimethylamino)ethylamino)-N-(4,9-dioxo-4,9-dihydronaphtho[2,3-b]thiophen-3-yl) propanamide dihydrochloride (**11p**)*. 45%, mp 227-228 °C. ^{1}H NMR (400 MHz, CD_3OD) δ 2.98 (s, 6H, CH_3), 3.09-3.12 (t, 2H, α*C*H$_2$); 3.29-3.31 (m, 2H, *C*H$_2$N(Me)$_2$); 3.47-3.50(m, 2H, βCH$_2$) 3.50-3.53 (m, 2H, NHC*H*$_2$), 7.85-7.87 (m, 2H, H-6 and H-7); 8.20-8.25 (m, 2H, H-5 and H-8); 8.49 (s, 1H, H-2). ^{13}C NMR (100 MHz, CD_3OD) δ 32.1 (α*C*H$_2$), 42.4 (NH*C*H$_2$), 42.8 (*C*H$_3$),43.9 (βCH$_2$) 53.1 (*C*H$_2$N(Me)$_2$), 119.5 (C-2); 126.8 and 127.0 (C-6 and C-7); 129.0 (C-3); 132.9 (C-8a); 133.5 (C-4a); 134.2 and

134.3 (C-5 and C-8); 137.5 (C-3a); 144.0 (C-9a); 171.9, 178.9 and 182.5 (C=O). ESI-MS *m/z* calcd for $C_{19}H_{23}Cl_2N_3O_3S$, 443.08; found, 443.18.

Biology. Dulbecco's modified Eagle's medium (DMEM), fetal bovine serum (FBS), trypsin-EDTA solution (1 x) penicillin and streptomycin, phosphate-buffered saline (PBS) were from Cambrex Biosciences. 3-(4,5-Dimethylthiazol-2-yl)-2,5-diphenyltetrazolium bromide (MTT), propidium iodide (PI), Triton X-100, sodium citrate, formamide, mouse monoclonal anti-tubulin were purchased from Sigma (Milan, Italy). Rabbit polyclonal anti-cyclin A primary antibody were from Cell Signaling Technology (Celbio; Milan, Italy). ECL reagent was obtained from Amersham Pharmacia Biotech, UK.

Cell culture. Human breast MDA231, human colon carcinoma SW620, Colo205, HT-29, and Caco-2, human monocytic leukemia U937, human melanoma MDA-MB435 and SK-MEL28 human ovarian cancer IGROV, and human glioblastoma SF-295 and SNB-19 cell lines, were grown at 37 °C in Dulbecco's modified Eagle's medium containing 10 mM glucose (DMEM-HG) supplemented with 10% fetal calf serum and 100 units/ml each of penicillin and streptomycin and 2 mmol/L glutamine. In each experiment, cells were placed in fresh medium, cultured in the presence of synthesized compounds (from 0.1 to 25 mM) and followed for further analyses.

Cell Viability Assay. Cell viability for all cell lines was determined using the 3-[4,5-demethylthiazol-2,5-diphenyl-2H-tetrazolium bromide (MTT) colorimetric assay. The test is based on the ability of mitochondrial dehydrogenase to convert, in viable cells, the yellow MTT reagent (Sigma Chemical Co., St Louis, MO.) into a soluble blue formazan dye. Cells were seeded into 96-well plates to a density of 105 cells/100 μL well. After 24 h of growth to allow attachment to the wells, compounds were added at various concentrations (from 0.1 to 25 mM). After 24 or 48 h of growth and after removal of the culture medium, 100 μL/well of medium containing 1 mg/mL of MTT was added. Cell cultures were further incubated at 37 °C for 2 hrs in the dark. The solution was then gently aspirated from each well, and the formazan crystals within the cells were dissolved with 100 μL of DMSO. Optical densities were read at 550 nm using a Multiskan Spectrum Thermo Electron Corporation reader. Results were expressed as percentage relative to vehicle-treated control (0.5% DMSO was added to untreated cells) IC_{50} (concentration eliciting 50% inhibition) value were determined by linear and polynomial regression. Experiments were performed in triplicate.

Topo II-mediated supercoiled pBR322 relaxation. DNA relaxation assays were based on the procedure of Osheroff *et al.*[204]

Reaction buffer contained 10 mM Tris.HCl (pH 7.9), 50 mM KCl, 50 mM NaCl, 5 mM $MgCl_2$, 0.1 mM EDTA, and 15 μg/mL of bovine serum albumin (BSA), 0.15 μg supercoiled pBR322, 4 units of topo II in a total of 20 μL. Relaxation was employed at 37 °C for 6 min and stopped by the addition of 3 μL of stop solution (100 mM EDTA, 0.5% SDS, 50% glycerol, 0.05% bromophenol blue). Electrophoresis was carried out in a 1% agarose gel in 0.5 × TBE (89 mM Tris base, 89 mM boric acid and 2 mM EDTA) at 4 V/cm for 1 h. DNA bands were stained with 0.5 μg/mL of ethidium bromide (E.B.) solution and photographed through a Gel Document System GDS8000 (UVP). The amount of DNA bands was quantified by Gel 1D Intermediate software.

Confocal microscopy. For immunocytochemistry, cells were fixed in 0.04 g/liter paraformaldehyde for 30 min at 4 °C and permeabilized with 0.01 g/liter Triton X-100 for 30 min at 4 C. Cells were then washed and stained with Hoechst 33342 (Vector, Burlingame, CA). Images were acquired with a LSM510 inverted confocal microscope (Zeiss, Oberkochen, Germany) using 63X oil objective and processed using LSM software (Zeiss).

Flow Cytometry. Analysis of Cell Cycle. CaCo-2 cells were seeded in six multiwell plates at the density of 25 × 105 cells/plate. After 48 h of incubation with **11m**, and **11p** derivatives and

doxorubicin in DMEM without serum at 37 °C, cells were washed in PBS, pelleted in centrifuged, and directly stained in a propidium iodide (PI) solution (50 mg PI in 0.1% sodium citrate, 0.1% NP40, pH 7.4) for 30 min at 4 °C in the dark. Flow cytometric analysis was performed using a FACScan flow cytometer (Becton Dickinson, San Jose, CA). To evaluate cell cycle PI fluorescence was collected as FL2 (linear scale) by the ModFIT software (Becton Dickinson). For the evaluation of intracellular DNA content, at least 20000 events for each point were analyzed in at least three different experiments giving a s.d. less than 5%.

Western Blot Assay. The effects of **11m, 11p** and **11c** on expression of Ciclyn A and of **11m** and **11p** on HSP27, were determined by Western blots. Compounds stimulated and unstimulated (control) cell lysates were prepared using an ice cold lysis buffer (50 mMTris, 150 mM NaCl, 10 mM EDTA, 1% Triton) supplemented with a mixture of protease inhibitors containing antipain, bestatin, chymostatin, leupeptin, pepstatin, phosphoramidon, Pefabloc, EDTA, and aprotinin (Boehringer, Mannheim, Germany). Equivalent protein samples were resolved on 8–12% sodium dodecyl sulfate (SDS)-polyacrylamide gels and transferred to nitrocellulose membranes (Bio-Rad, Germany). For immunodetection, membranes were incubated overnight with specific antibody at the concentrations

indicated in manufacter's protocol (Santa Cruz Biotechnology). The two antibodies were diluted in Tris-buffered saline/Tween 20-1% milk powder. This step was followed by incubation with the corresponding horseradish peroxidase conjugated antibody (antirabbit-IgG 1:6000; Biosource, Germany). Bands were read by enhanced chemiluminescence (ECL-kit, Amersham, Germany).

Alkaline phosphatase activity. Alkaline phosphatase (ALP) activity was used as marker of the degree of cells differentiation. Attached and floating cells were washed and lysed with 0.25% sodium deoxycholate, essentially as described by Herz *et al*.[220] ALP activity was determined using Sigma Diagnostics ALP reagent (No. 245). Total cellular protein content of the samples was determined in a microassay procedure as described by Bradford [221] using the Coomassie Protein Assay Reagent Kit (Pierce). ALP activity was calculated as units of activity per mg of protein.

H9C2 cell viability. Cardiomyoblasts H9C2 were cultured in Dulbecco's minimal essential medium (DMEM, GIBCO) supplemented with 0.1 g/L fetal bovine serum (FBS, GIBCO) 200 mg/mL L-glutamine, 100 units/mL penicillin, and 10 mg/mL streptomycin (Sigma-Aldrich), at 37°C in 0.95 g/L air-0.05 g/L CO2. The H9C2 were studied between passages 4 and 10. The MTT-colorimetric assay (Invitrogen, San Diego, CA), was used to evaluate

cell proliferation in presence or absence of inhibitors. Briefly, H9C2 cells were plated into 96 multiwell at a density of 2000 cells/well in quadruplicate. Inhibitors (**11m**, **11p**, and Doxorubicin) were added to each well at a concentration of 1 μM for the indicated time points.. Then 10 μl of MTT reagent were added to each well, the plate was returned to cell culture incubator for 2 hours. The absorbance in each well, including the blanks, was measured at 570 nm in a microplate plate reader.

Statistical analysis. Data were expressed as mean ± standard deviation (SD). Statistical significance was assessed by Student-t test. P value adjustment for multiple comparisons was done by the Holm (sequential Bonferonni correction method). $P<0.05$ was considered statistically significant.

STD-NMR and WaterLOGSY Spectroscopy. STD-NMR [208] and WaterLOGSY [209] experiments were performed on a Varian Inova 700 MHz spectrometer at 25 °C. NMR samples were prepared by dissolving the ligand and the poly(dGdC)·poly(dG-dC) copolymer (Pharmacia Biochemicals) in H_2O/D_2O 9:1 (final volume 600 μL; D_2O 99.996%, CIL Laboratories) containing phosphate-buffered saline (100 mM) at pH 7.1. A high ligand–receptor molar excess (20:1) was used. In particular, the concentration of **11c**, **11m**, and **11p** was 1.0 mM, whereas that of the DNA was 50 μM, expressed as molarity of

phosphate groups. Water suppression was achieved by using the double-pulsed field gradient spin-echo (DPFGSE) scheme.[68] The STD effects of the individual protons were calculated for each compound relative to a reference spectrum with off-resonance saturation at δ = -16 ppm. Typically, 512 scans were recorded for each DF-STD spectrum (saturation time = 2 s). The relative STD effect was calculated for each signal as the difference between the intensity (expressed as S/N ratio) of one signal in the on-resonance STD spectrum and that of the same signal in the off-resonance NMR spectrum divided by the intensity of the same signal in the off-resonance spectrum. BMI values were obtained as ratio of the relative STD effects upon irradiation at 10.0 and -1.0 ppm.[210] The absence of STD effects in samples in which the DNA was not added ensured a selective macromolecule saturation. WaterLOGSY NMR experiments employed a 20 ms selective Gaussian 180° pulse at the water signal frequency and an NOE mixing time of 1.5 s.

Chapter 3 - SUPPORTING INFORMATION

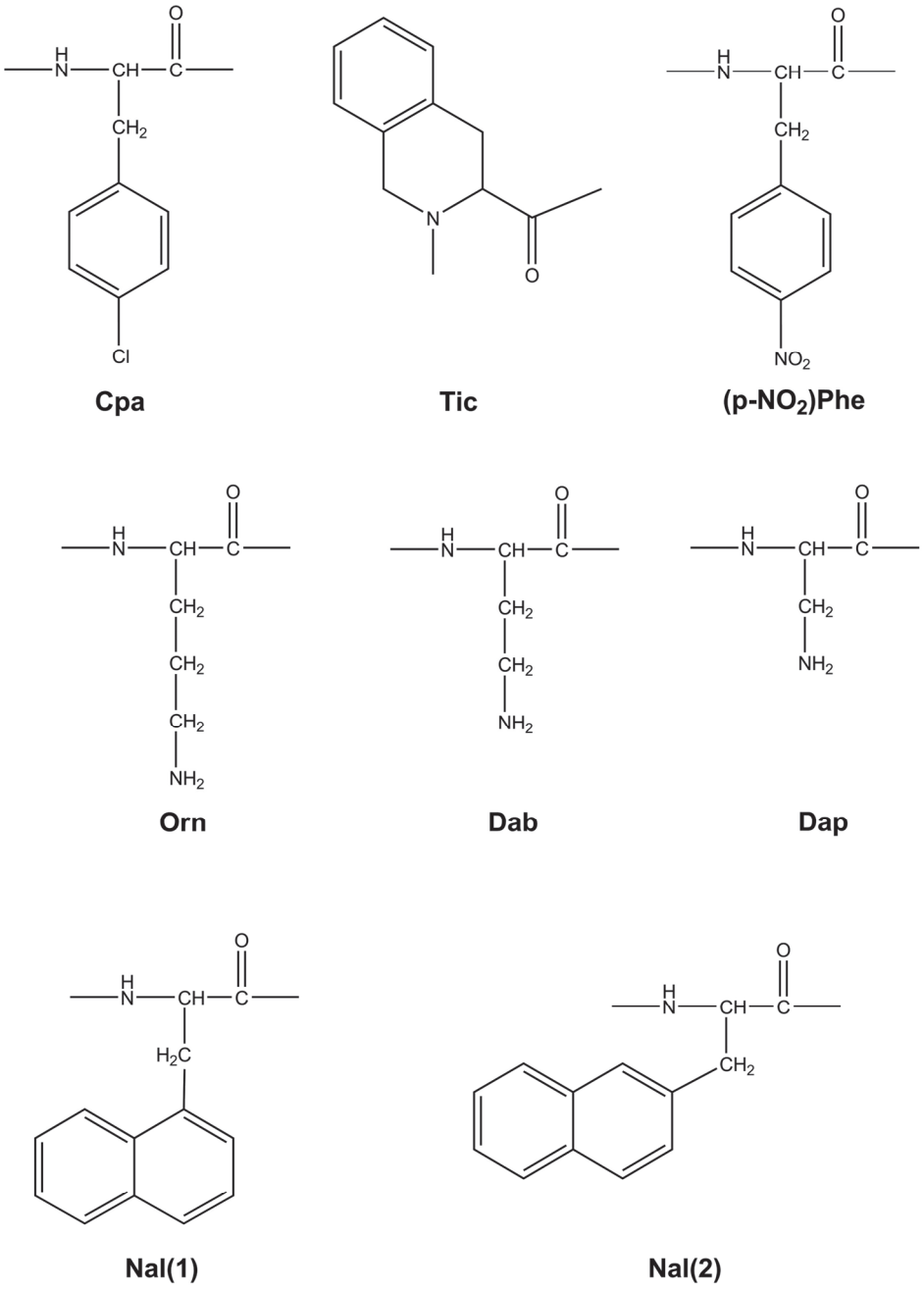

Figure S1. Chemical structures of the non-coded amino acids cited throughout the manuscript.

Table S1. Analytical Data for the P5U and Urantide Analogues

Peptide	Structure	HPLC[a]	MS (M+H)	
		k'	Found	Calcd
1	H-Ala-c[Pen-Phe-Trp-Lys-Tyr-Cys]-Val-OH	8.22	1045.80	1045.30
2	H-Ala-c[Pen-Phe-DTrp-Orn-Tyr-Cys]-Val-OH	8.16	1031.90	1031.27
3	H-Phe-c[Pen-Phe-Trp-Lys-Tyr-Cys]-Val-OH	8.31	1121.90	1121.40
4	H-Phe-c[Pen-Phe-DTrp-Orn-Tyr-Cys]-Val-OH	8.26	1108.10	1107.37
5	H-Cpa-c[Pen-Phe-Trp-Lys-Tyr-Cys]-Val-OH	8.33	1156.44	1155.85
6	H-Cpa-c[Pen-Phe-DTrp-Orn-Tyr-Cys]-Val-OH	8.30	1142.32	1141.82
7	H-Nal(1)-c[Pen-Phe-Trp-Lys-Tyr-Cys]-Val-OH	8.35	1171.98	1171.46
8	H-Nal(1)-c[Pen-Phe-DTrp-Orn-Tyr-Cys]-Val-OH	8.32	1158.10	1157.43
9	H-Nal(2)-c[Pen-Phe-Trp-Lys-Tyr-Cys]-Val-OH	8.35	1171.96	1171.46
10	H-Nal(2)-c[Pen-Phe-DTrp-Orn-Tyr-Cys]-Val-OH	8.31	1158.15	1157.43
11	H-(pNO_2)Phe-c[Pen-Phe-Trp-Lys-Tyr-Cys]-Val-OH	8.31	1167.01	1166.40
12	H-(pNO_2)Phe-c[Pen-Phe-DTrp-Orn-Tyr-Cys]-Val-OH	8.27	1152.97	1152.38
13	H-Tic-c[Pen-Phe-Trp-Lys-Tyr-Cys]-Val-OH	8.34	1134.03	1133.41
14	H-Tic-c[Pen-Phe-DTrp-Orn-Tyr-Cys]-Val-OH	8.31	1120.10	1119.38
15	H-Lys-c[Pen-Phe-Trp-Lys-Tyr-Cys]-Val-OH	8.12	1103.12	1102.39
16	H-Lys-c[Pen-Phe-DTrp-Orn-Tyr-Cys]-Val-OH	8.09	1089.11	1088.37

[a] k' = [(peptide retention time – solvent retention time)/solvent retention time].

Table S2. Amino Acid Analysis of the P5U and Urantide Analogues [a]

R-c[Pen-Phe-*Xaa*-*Yaa*-Tyr-Cys]-Val-OH

Peptide	R	Pen	Phe	Xaa[b]	Yaa[c]	Tyr	Cys	Val
1	0.97	N.D.	1.0	-	0.91	0.92	1.02	0.98
2	0.98	0.98	0.97	-	0.92	0.98	1.00	0.99
3	0.89	N.D.	0.98	-	1.00	1.00	0.98	0.97
4	0.92	0.98	0.93	-	0.92	0.93	0.97	1.02
5	0.96	N.D.	0.96	-	0.88	0.97	0.99	0.93
6	0.98	0.91	0.91	-	0.89	0.91	0.94	0.92
7	0.87	N.D.	0.96	-	0.97	0.95	0.91	0.89
8	0.91	N.D.	0.90	-	0.89	0.91	1.00	0.93
9	0.89	0.91	0.98	-	0.91	0.96	0.97	0.96
10	0.91	0.89	0.97	-	0.90	0.97	0.89	0.99
11	0.98	0.93	0.95	-	0.90	0.93	0.95	0.92
12	N.D.	0.92	0.93	-	0.94	0.91	0.93	0.94
13	0.93	N.D.	0.99	-	0.93	0.97	0.95	0.96
14	0.96	0.90	1.01	-	0.99	0.98	0.96	0.93
15	0.98	0.95	0.97	-	0.98	0.95	0.99	0.91
16	0.99	0.94	0.97	-	0.98	0.99	1.00	0.93

[a] The analyses were performed using an Applied Biosystems Model 420A amino acid analyzer with automatic hydrolysis (Vapor Phase at 160 ºC for 1 h 40 min using 6 N HCl) and a precolumn phenylthiocarbamyl-amino acid (PTC-AA) analysis. No correction is made for amino acid decomposition. [b]Trp was not well determined due to decomposition under these conditions. Other notations: "ND" (not determined) refers to the amino acid that could not be estimated due to unavailability of a standard sample. [c]Yaa = Lys (**1**,**3,5,7,9,11,13,15**), Orn (**2,4,6,8,10,12,14,16**);

Table S3. NMR Resonance Assignments[a] of Peptide **14** in SDS-d_{25} 200mM Solution.

residue	NH ($^3J_{\alpha N}$, exc, -Δδ/ΔT)[b]	$C^{\alpha}H$ ($^3J_{\alpha\beta}$)[b]	$C^{\beta}H$	Others
Tic 4		4.57 (5.5, 9.5)	3.22, 2.93	6.97(δ); 7.23(ε);
Pen 5	8.50 (8.8, f, 6.9)	5.14		1.32,1.13(γ)
Phe 6	9.05 (8.5, ms, 3.2)	4.71 (overl.)	2.98	7.08(δ);
D-Trp 7	8.18 (4.5, f, 6.3)	4.58 (9.0, 7.3)	3.19, 3.00	7.14(δ); 9.92, 7.67(ε); 7.51, 7.11(ζ); 7.20(η)
Orn 8	7.47 (5.9, f, 4.7)	4.09 (3.2, 7.3)	1.44, 1.13	0.97, 0.65(γ); 2.71,2.67(δ); 7.22(ε)
Tyr 9	8.07 (8.4, s, 2.7)	4.69 (5.3, 10.0)	2.99, 2.90	7.11(δ); 6.76(ε)
Cys 10	8.30 (8.7, f, 6.8)	5.38 (overl.)	2.89	
Val 11	8.14 (8.6, ms, 3.4)	4.40	2.05	0.88, 0.80(γ)

[a]Obtained at 25°C, pH = 5.5, with TSP (δ 0.00 ppm) as reference shift. Chemical shifts are accurate to ±0.02 ppm.

[b] $^3J_{\alpha N}$, and $^3J_{\alpha\beta}$ coupling constants in Hz. exc = N<u>H</u> exchange rate (f, fast; ms, moderately slow; s, slow;). -Δδ/ΔT = temperature coefficients (ppb/K).

Table S4. NMR Resonance Assignments[a] of Peptide **16** in SDS-d_{25} 200mM Solution.

residue	NH ($^3J_{\alpha N}$, exc, $-\Delta\delta/\Delta T$)[b]	$C^{\alpha}H$ ($^3J_{\alpha\beta}$)[b]	$C^{\beta}H$	Others
Lys 4		4.05 (8.7, 7.3)	1.71, 1.61	1.40, 1.26(γ); 1.68(δ); 2.96, 2.90(ε); 7.48(ζ)
Pen 5	8.26 (8.8, f, 6.7)	5.06		1.26, 1.06(γ)
Phe 6	9.21 (8.5, ms, 3.2)	4.69 (9.0, 6.0)	3.05, 2.90	7.13(δ)
D-Trp 7	8.55 (4.5, f, 6.3)	4.62 (9.1, 7.2)	3.24, 3.07	7.16(δ); 9.99, 7.66(ε); 7.51, 7.10(ζ); 7.18(η)
Orn 8	7.30 (5.9, f, 4.8)	4.11 (3.4, 7.1)	1.42, 1.01	0.87, 0.50(γ); 2.69,2.63(δ)
Tyr 9	8.09 (8.4, s, 2.7)	4.73 (5.5, 9.9)	3.05, 2.97	7.13(δ); 6.75(ε)
Cys 10	8.50 (8.7, f, 6.8)	5.44 (overl.)	2.87	
Val 11	8.39 (8.6, ms, 3.1)	4.46	2.27	1.01(γ)

[a]Obtained at 25°C, pH = 5.5, with TSP (δ 0.00 ppm) as reference shift. Chemical shifts are accurate to ±0.02 ppm.

[b] $^3J_{\alpha N}$ and $^3J_{\alpha\beta}$ coupling constants in Hz. exc = N<u>H</u> exchange rate (f, fast; ms, moderately slow; s, slow;). $-\Delta\delta/\Delta T$ = temperature coefficients (ppb/K).

NOE derived Upper Limit Constraints.

Peptide **14**

4	TIC	HA	5	PEN	HN	2.83
5	PEN	HN	5	PEN	QG1	3.71
5	PEN	HN	10	CYSS	HA	5.50
5	PEN	HA	6	PHE	HN	2.71
5	PEN	HA	10	CYSS	HA	2.65
5	PEN	HA	10	CYSS	QB	5.35
5	PEN	HA	11	VAL	HN	3.55
5	PEN	QG1	10	CYSS	HA	6.53
5	PEN	QG1	10	CYSS	QB	6.51
5	PEN	QG2	6	PHE	HN	5.85
5	PEN	QG2	7	DTRP	HN	6.50
5	PEN	QG2	10	CYSS	HA	6.40
5	PEN	QG2	10	CYSS	QB	7.03
6	PHE	HN	9	TYR	HN	4.26
6	PHE	HN	10	CYSS	HA	4.11
6	PHE	HA	7	DTRP	HN	2.71
7	DTRP	HN	7	DTRP	HB2	2.86
7	DTRP	HN	7	DTRP	HB3	3.02
7	DTRP	HN	7	DTRP	HD1	5.31
7	DTRP	HA	7	DTRP	HB2	2.83
7	DTRP	HA	7	DTRP	HB3	2.80
7	DTRP	HA	7	DTRP	HD1	4.01
7	DTRP	HA	7	DTRP	HE3	4.24
7	DTRP	HA	8	ORN	HN	2.59
7	DTRP	HA	9	TYR	HN	3.42
7	DTRP	HB2	7	DTRP	HD1	3.14
7	DTRP	HB2	7	DTRP	HE3	4.07
7	DTRP	HB2	8	ORN	HN	3.76
7	DTRP	HB3	7	DTRP	HD1	3.70
7	DTRP	HB3	7	DTRP	HE3	3.86
7	DTRP	HB3	8	ORN	HN	4.07
8	ORN	HN	8	ORN	HB2	3.52
8	ORN	HN	8	ORN	HB3	3.52
8	ORN	HN	8	ORN	QB	3.28
8	ORN	HN	8	ORN	HG2	4.35
8	ORN	HN	8	ORN	HG3	4.35
8	ORN	HN	8	ORN	QG	4.18
8	ORN	HN	8	ORN	HD2	5.50
8	ORN	HN	8	ORN	HD3	5.50
8	ORN	HN	9	TYR	HN	2.86
8	ORN	HA	8	ORN	HB2	3.05
8	ORN	HA	8	ORN	HB3	3.05
8	ORN	HA	8	ORN	QG	4.05
8	ORN	HA	9	TYR	HN	3.36
8	ORN	HA	9	TYR	QD	7.64
8	ORN	HB2	8	ORN	HE1	5.50
8	ORN	HB2	9	TYR	HN	4.51
8	ORN	HB2	9	TYR	QD	7.64
8	ORN	HB2	9	TYR	QE	7.63
8	ORN	HB3	8	ORN	HE1	5.50
8	ORN	HB3	9	TYR	HN	4.51
8	ORN	HB3	9	TYR	QD	7.64
8	ORN	HB3	9	TYR	QE	7.63
8	ORN	QB	9	TYR	HN	3.91
8	ORN	HG2	9	TYR	HN	5.50
8	ORN	HG2	9	TYR	QD	7.64
8	ORN	HG2	9	TYR	QE	7.63

8	ORN	HG3	9	TYR	HN	5.50
8	ORN	HG3	9	TYR	QD	7.64
8	ORN	HG3	9	TYR	QE	7.63
8	ORN	HD2	9	TYR	QE	7.63
8	ORN	HD3	9	TYR	QE	7.63
9	TYR	HN	9	TYR	HB2	2.90
9	TYR	HN	9	TYR	HB3	2.90
9	TYR	HN	9	TYR	QE	7.63
9	TYR	HA	9	TYR	HB2	3.08
9	TYR	HA	9	TYR	HB3	3.08
9	TYR	HA	10	CYSS	HN	3.11
10	CYSS	HA	11	VAL	HN	2.74
10	CYSS	HA	11	VAL	QQG	8.09
10	CYSS	QB	11	VAL	HN	4.08
10	CYSS	QB	11	VAL	QG1	7.40
10	CYSS	QB	11	VAL	QG2	7.40
11	VAL	HN	11	VAL	HB	3.95
11	VAL	HA	11	VAL	HB	2.86

Peptide **16**

4	LYS	HA	4	LYS	HG2	3.70
4	LYS	HA	4	LYS	HG3	3.70
4	LYS	HA	4	LYS	QG	3.52
4	LYS	HA	5	PEN	HN	2.80
4	LYS	HB2	5	PEN	HN	3.58
4	LYS	HB3	5	PEN	HN	3.58
4	LYS	QB	5	PEN	HN	3.39
4	LYS	HG2	4	LYS	HE2	4.29
4	LYS	HG2	4	LYS	HE3	4.29
4	LYS	HG2	4	LYS	QZ	6.44
4	LYS	HG3	4	LYS	HE2	4.29
4	LYS	HG3	4	LYS	HE3	4.29
4	LYS	HG3	4	LYS	QZ	6.44
4	LYS	QG	5	PEN	HN	6.38
5	PEN	HN	5	PEN	QG1	3.90
5	PEN	HA	6	PHE	HN	3.58
5	PEN	HA	10	CYSS	HA	3.02
5	PEN	HA	10	CYSS	QB	5.54
5	PEN	HA	11	VAL	HN	3.70
5	PEN	QG2	6	PHE	HN	4.73
5	PEN	QG2	7	DTRP	HN	5.69
5	PEN	QG2	9	TYR	HN	5.16
5	PEN	QG2	10	CYSS	HN	6.53
5	PEN	QG2	10	CYSS	HA	5.16
6	PHE	HN	6	PHE	HB2	3.73
6	PHE	HN	6	PHE	HB3	3.73
6	PHE	HN	6	PHE	QB	3.50
6	PHE	HN	9	TYR	HN	5.50
6	PHE	HN	10	CYSS	HA	3.89
6	PHE	HA	6	PHE	HB2	2.96
6	PHE	HA	6	PHE	HB3	2.96
6	PHE	HA	6	PHE	QB	2.76
6	PHE	HA	7	DTRP	HN	2.99
7	DTRP	HN	7	DTRP	HB2	3.08
7	DTRP	HN	7	DTRP	HB3	3.48
7	DTRP	HN	7	DTRP	HE3	5.50
7	DTRP	HA	7	DTRP	HB2	3.02
7	DTRP	HA	7	DTRP	HE3	3.39
7	DTRP	HA	8	ORN	HN	2.90
7	DTRP	HA	9	TYR	HN	3.55

```
 7 DTRP HB2     7 DTRP HD1     3.17
 7 DTRP HB2     8 ORN  HN      3.89
 7 DTRP HB3     7 DTRP HD1     3.42
 7 DTRP HB3     8 ORN  HN      4.32
 7 DTRP HE3     8 ORN  HN      4.57
 8 ORN  HN      8 ORN  HB2     3.55
 8 ORN  HN      8 ORN  HB3     3.55
 8 ORN  HN      8 ORN  QB      3.30
 8 ORN  HN      8 ORN  HG2     5.04
 8 ORN  HN      8 ORN  HG3     5.04
 8 ORN  HN      8 ORN  QG      4.73
 8 ORN  HN      9 TYR  HN      3.21
 8 ORN  HA      8 ORN  QG      3.97
 8 ORN  HA      9 TYR  HN      3.58
 8 ORN  HB2     9 TYR  QE      7.63
 8 ORN  HB3     9 TYR  QE      7.63
 8 ORN  QB      9 TYR  QE      7.30
 8 ORN  HG2     9 TYR  HN      5.50
 8 ORN  HG2     9 TYR  QE      7.63
 8 ORN  HG3     9 TYR  HN      5.50
 8 ORN  HG3     9 TYR  QE      7.63
 8 ORN  QG      9 TYR  QD      8.52
 8 ORN  HD2     9 TYR  QE      7.63
 8 ORN  HD3     9 TYR  QE      7.63
 9 TYR  HN      9 TYR  HB2     3.08
 9 TYR  HN      9 TYR  HB3     3.08
 9 TYR  HN      9 TYR  QE      7.63
 9 TYR  HN     10 CYSS HN      5.28
 9 TYR  HA     10 CYSS HN      3.08
10 CYSS HA     11 VAL  HN      3.08
10 CYSS QB     11 VAL  HN      4.30
10 CYSS QB     11 VAL  HA      5.20
11 VAL  HA     11 VAL  HB      2.86
```

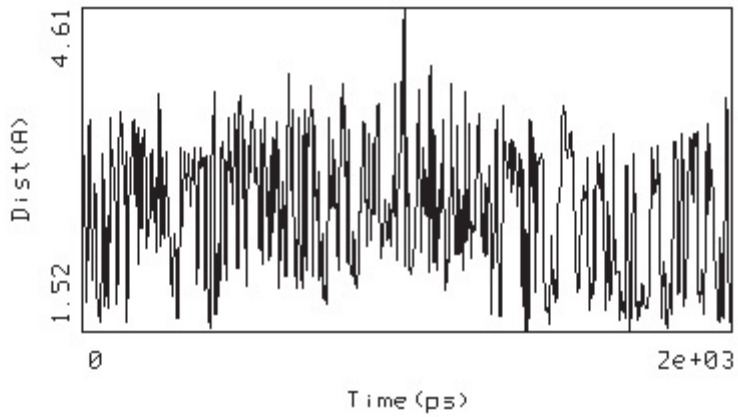

Figure S2. Results of MD simulations of *h*-UTR complexed with Urantide. Graphic shows plot of the monitored distance, in the complex, between the protonated N^{ε} of Orn^{8} in Urantide and the O^{δ} of Asp130 in *h*-UTR.

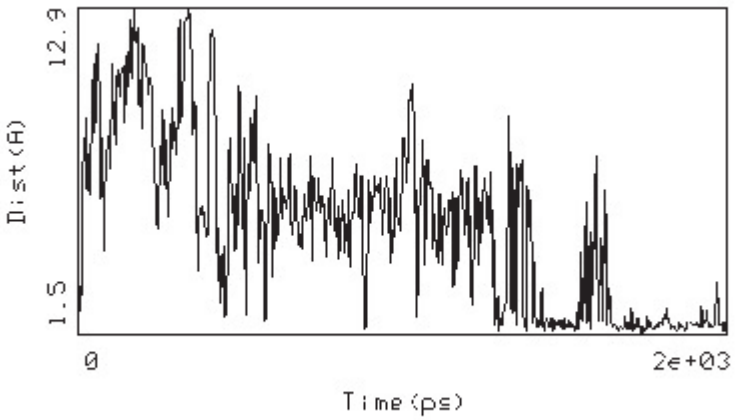

Figure S3. Distance between the OH oxygen of Tyr^{9} in Urantide and the side chain CO oxygen of Asn297 in *h*-UTR.

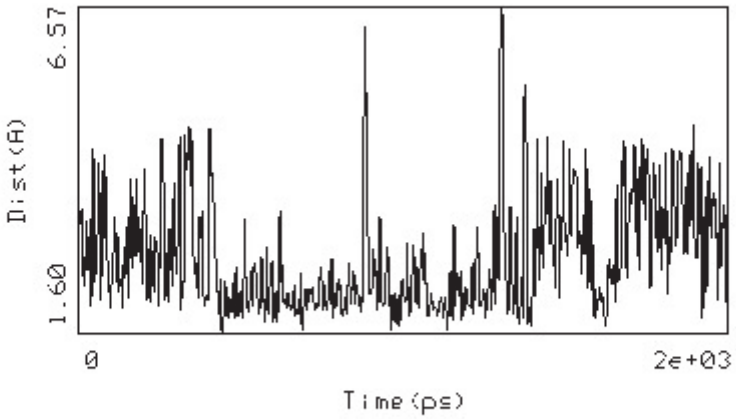

Figure S4. Distance between the OH oxygen of Tyr[9] in Urantide and the OH hydrogen of Thr301 in *h*-UTR.

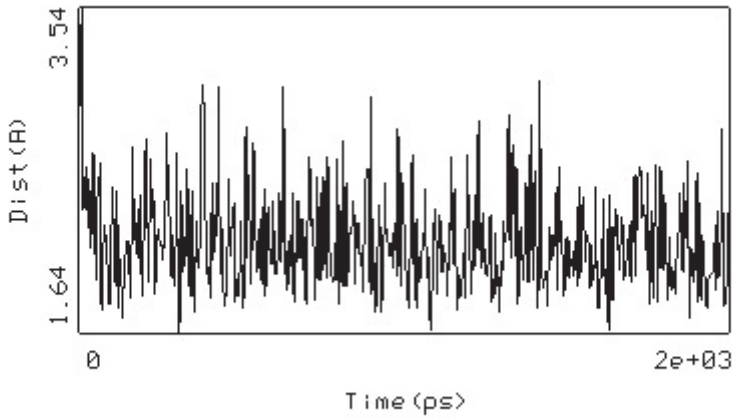

Figure S5. Distance between the the O^{δ} of Asp[4] in Urantide and the guanidinium group N^{η} of Arg206 in *h*-UTR.

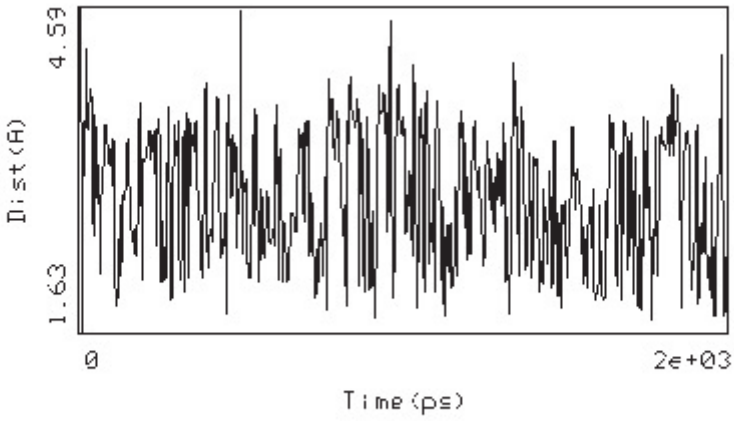

Figure S6. Distance between the protonated backbone NH_3 nitrogen of Asp^4 in Urantide and the backbone CO oxygen of Ala187 in *h*-UTR.

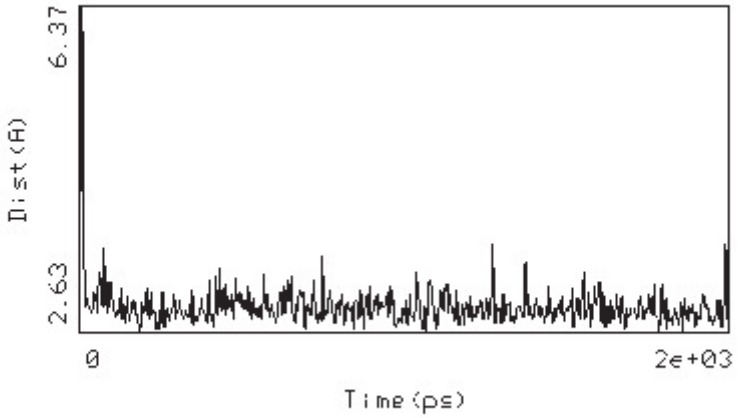

Figure S7. Distance between the protonated backbone NH_3 nitrogen of Asp^4 in Urantide and the backbone CO oxygen of Cys199 in *h*-UTR.

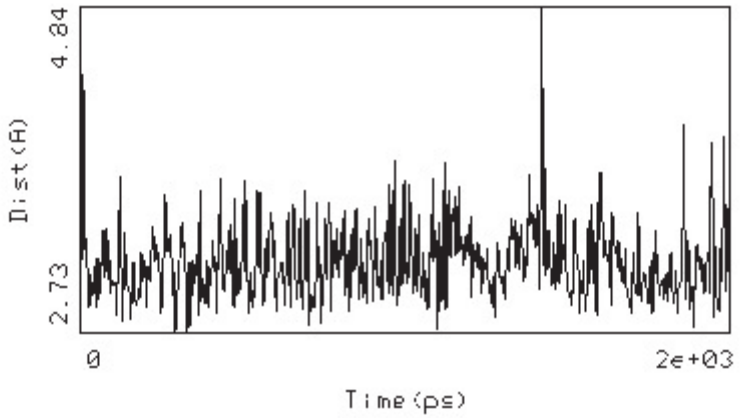

Figure S8. Distance between the protonated backbone NH_3 nitrogen of Asp^4 in Urantide and the backbone CO oxygen of Met188 in *h*-UTR.

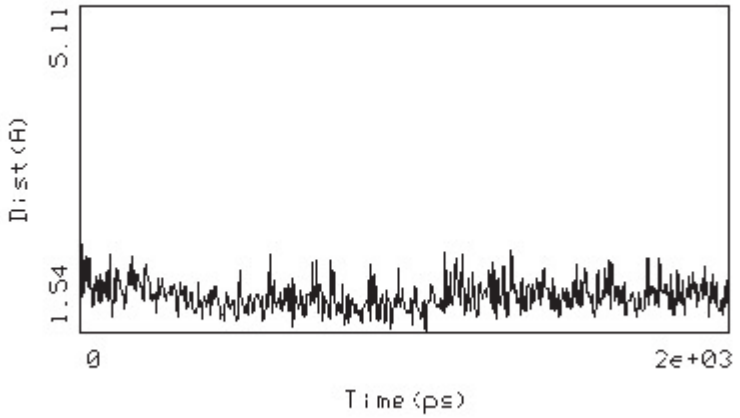

Figure S9. Distance between the negatively charged carboxyl group of Val^{11} in Urantide and the backbone NH hydrogen of Cys123 in *h*-UTR.

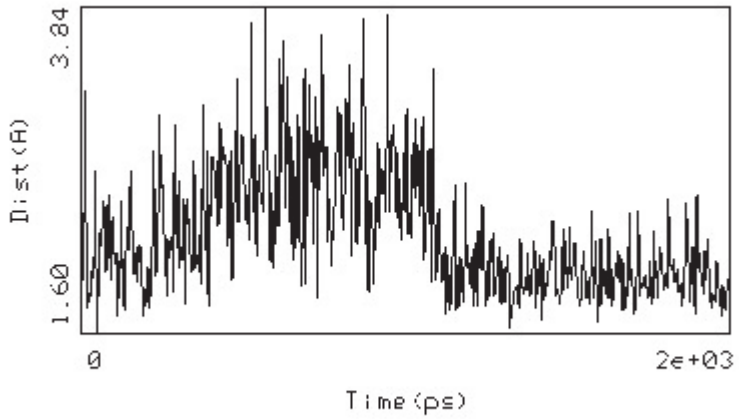

Figure S10. Distance between the negatively charged carboxyl group of Val[11] in Urantide and the backbone NH hydrogen of Cys199 in *h*-UTR.

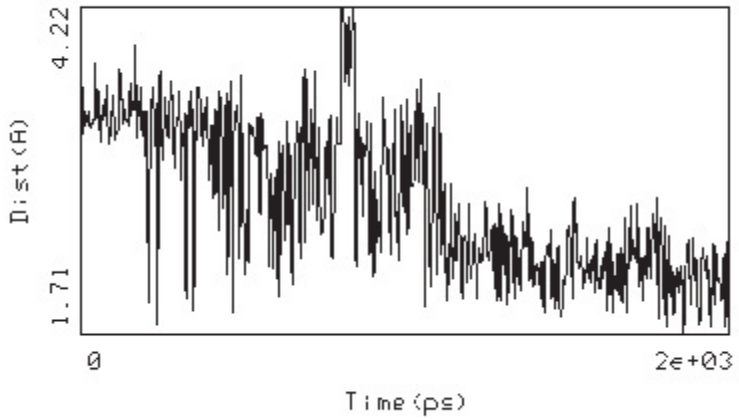

Figure S11. Distance between the negatively charged carboxyl group of Val[11] in Urantide and the backbone NH hydrogen of Arg189 in *h*-UTR.

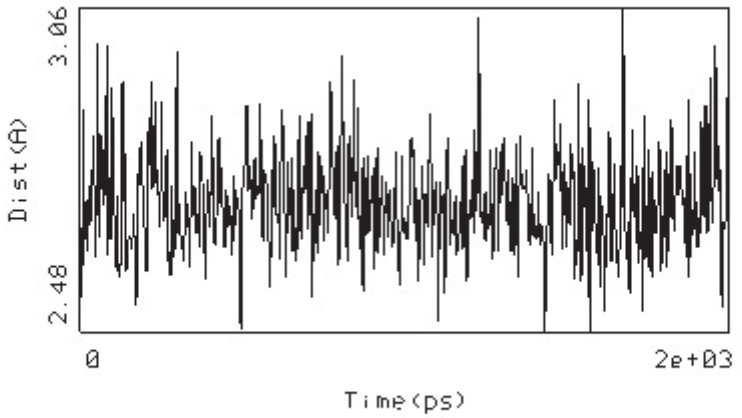

Figure S12. Distance between the protonated N^{ζ} of Lys^{8} in P5U and the O^{δ} of Asp130 in *h*-UTR.

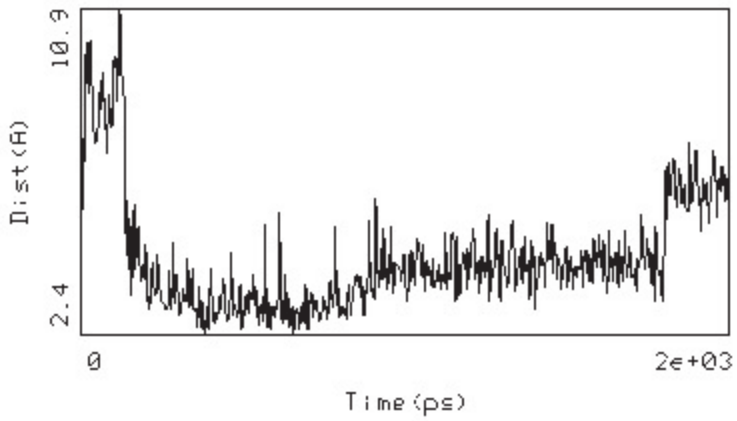

Figure S13. Distance between the the O^{δ} of Asp^{4} in P5U and the side chain NH_2^{ε} hydrogen of Gln285 in *h*-UTR.

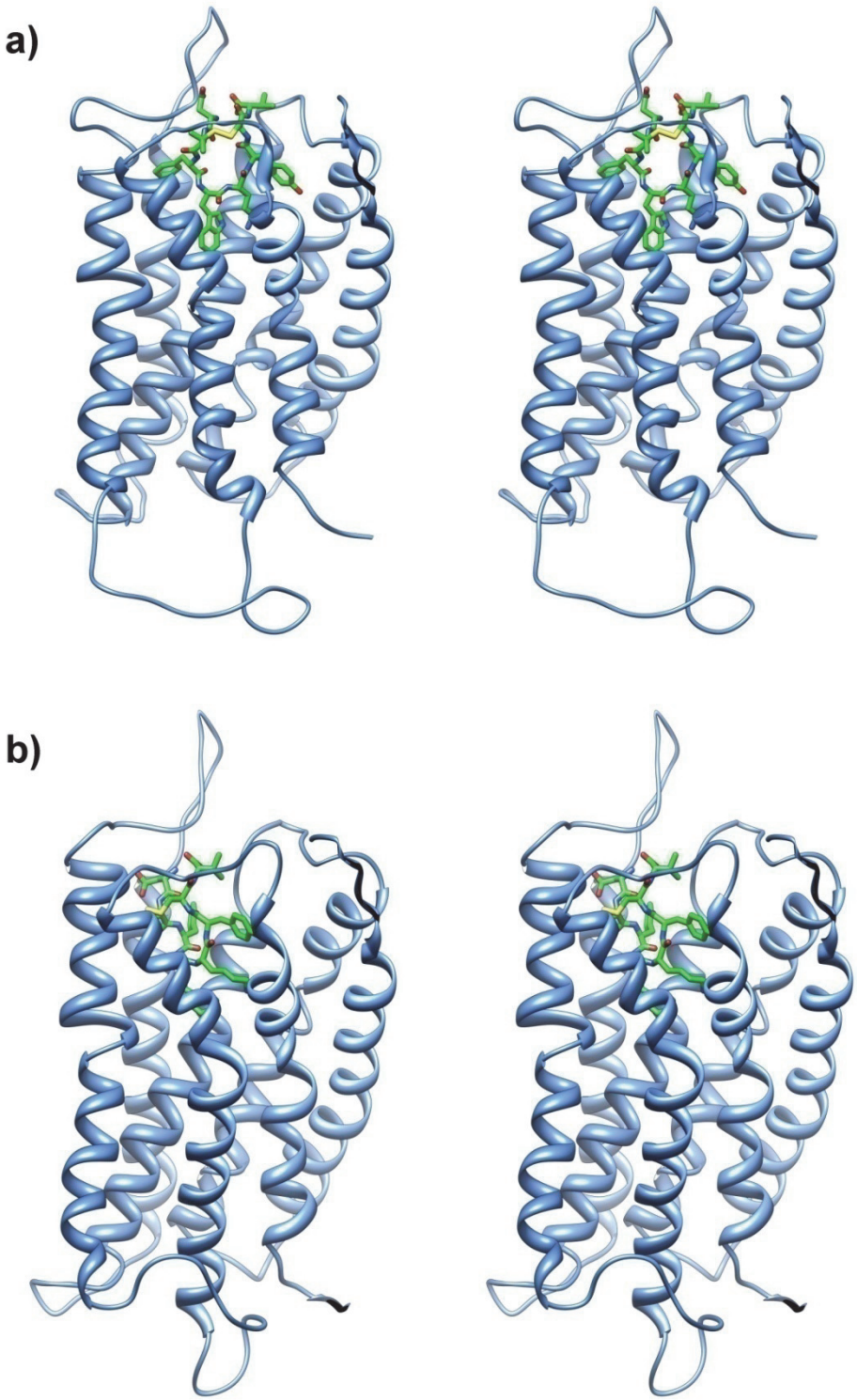

Figure S14. (a) Stereoview of Urantide/*h*-UTR$_a$ (a) and P5U/ *h*-UTR$_i$ (b) model complex. Urantide and P5U heavy atoms are colour coded (carbon, green; nitrogen, blue; oxygen, red; sulfur, yellow). Receptor backbones are represented in azure.

```
h-UTR   MALTPESPSSFPGLAATGSSVPEPPGGPNATLNSSWASPTEPSSLEDLVATGTIGTLLSA 60
r-UTR   MALSLESTTSFHMLTVSGSTVTELPGDSNVSLNSSWSGPTDPSSLKDLVATGVIGAVLSA 60
        ***: **.:**  *:.:**:*.* **..*.:*****:.**:****:******.**::***

h-UTR   MGVVGVVGNAYTLVVTCRSLRAVASMYVYVVNLALADLLYLLSIPFIVATYVTKEWHFGD 120
r-UTR   MGVVGMVGNVYTLVVMCRFLRASASMYVYVVNLALADLLYLLSIPFIIATYVTKDWHFGD 120
        *****:***.***** ** *** **********:**********:******:*****

h-UTR   VGCRVLFGLDFLTMHASIFTLTVMSSERYAAVLRPLDTVQRPKGYRKLLALGTWLLALLL 180
r-UTR   VGCRVLFSLDFLTMHASIFTLTIMSSERYAAVLRPLDTVQRSKGYRKLLVLGTWLLALLL 180
        *******.**************:*****************.*******.***********

                EL-II
h-UTR   TLPVMLAMRLVRRGPKSLCLPAWGPRAHRAYLTLLFATSIAGPGLLIGLLYARLARAYRR 240
r-UTR   TLPMMLAIQLVRRGSKSLCLPAWGPRAHRTYLTLLFGTSIVGPGLVIGLLYVRLARAYWL 240
        ***:***::*****.**************:******.***.****:*****.******

h-UTR   SQRASFKRARR-PGARALRLVLGIVLLFWACFLPFWLWQLLAQYHQA-PLAPRTARIVNY 298
r-UTR   SQQASFKQTRRLPNPRVLYLILGIVLLFWACFLPFWLWQLLAQYHEAMPLTPETARIVNY 300
        **:****::** *..*.* *:************************:* **:*.*******

h-UTR   LTTCLTYGNSCANPFLYTLLTRNYRDHLRGRVRGPGSGGGRGPVPS--LQPRARFQRCSG 356
r-UTR   LTTCLTYGNSCINPFLYTLLTKNYREYLRGRQRSLGSSCHSPGSPGSFLPSRVHLQQDSG 360
        ********** *********:***::**** *. **.      *.  * .*.::*: **

h-UTR   RSLSSCSPQPTDSLVLAPAAPARPAPEGPRAPA 389
r-UTR   RSLSSSSQQATETLMLSPVPRNGALL------- 386
        *****.* *.*::*:*:*..   .
```

Figure S15. Pairwise alignment of h-UTR and r-UTR. The conserved key residues used to align the sequences are shown in bold. In all sequence alignment figures, an asterisk (*) indicates an identical amino acid; punctuations indicate a "conserved" amino acid, which meets the criteria for either highly conservative substitutions (:) or semiconservative substitutions (.), as defined by CLUSTALW.

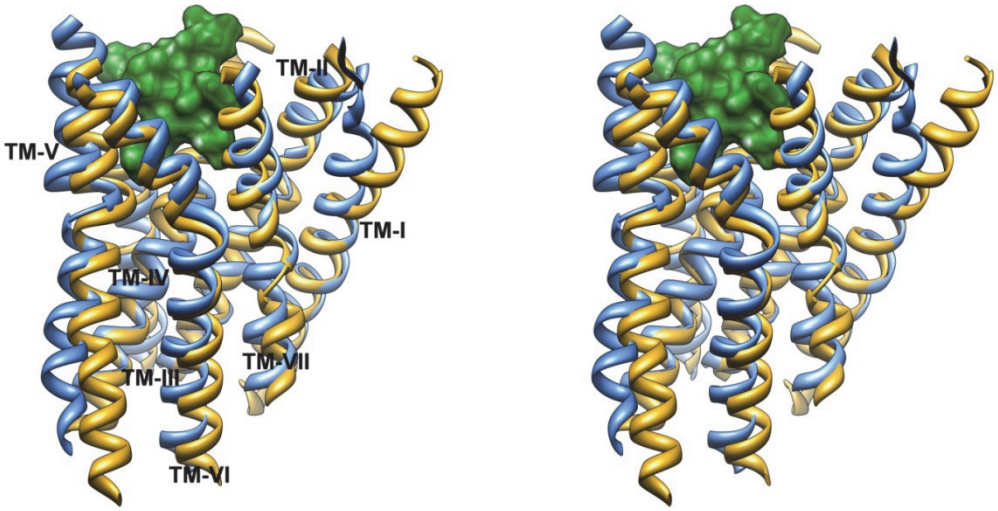

Figure S16. Stereoview of the TM domains of the *h*-UTR$_i$ model (azure) superimposed to β_2AR crystal structure (gold, PDB code 2RH1). Backbone heavy atoms of TM-II÷TM-VII were used for the superimposition. Bound urantide is shown as green surface.

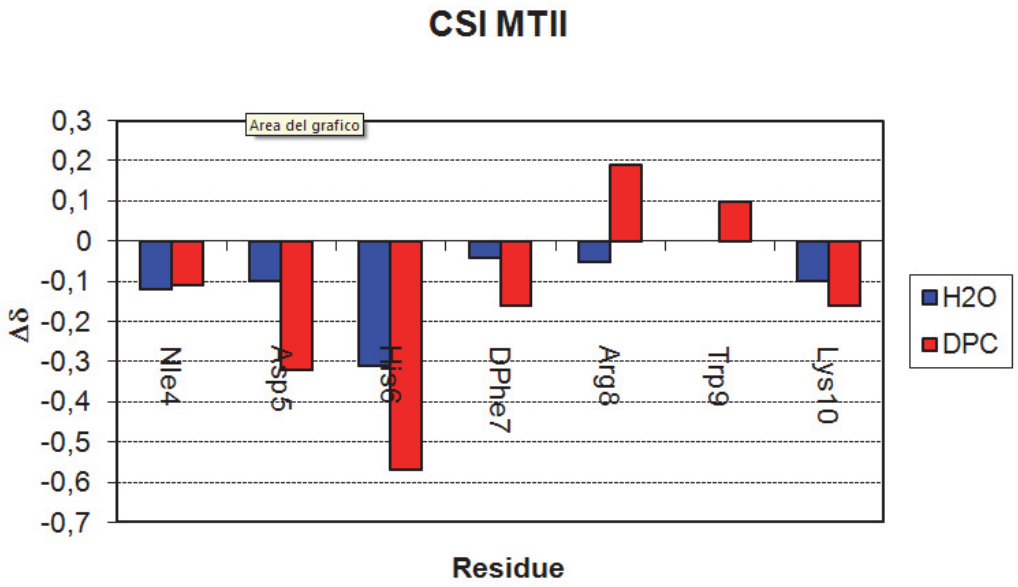

Figure S17. Chemical shift deviations from the random coil shift values (reference [110] of the manuscript) for Hα resonances at 25 °C.

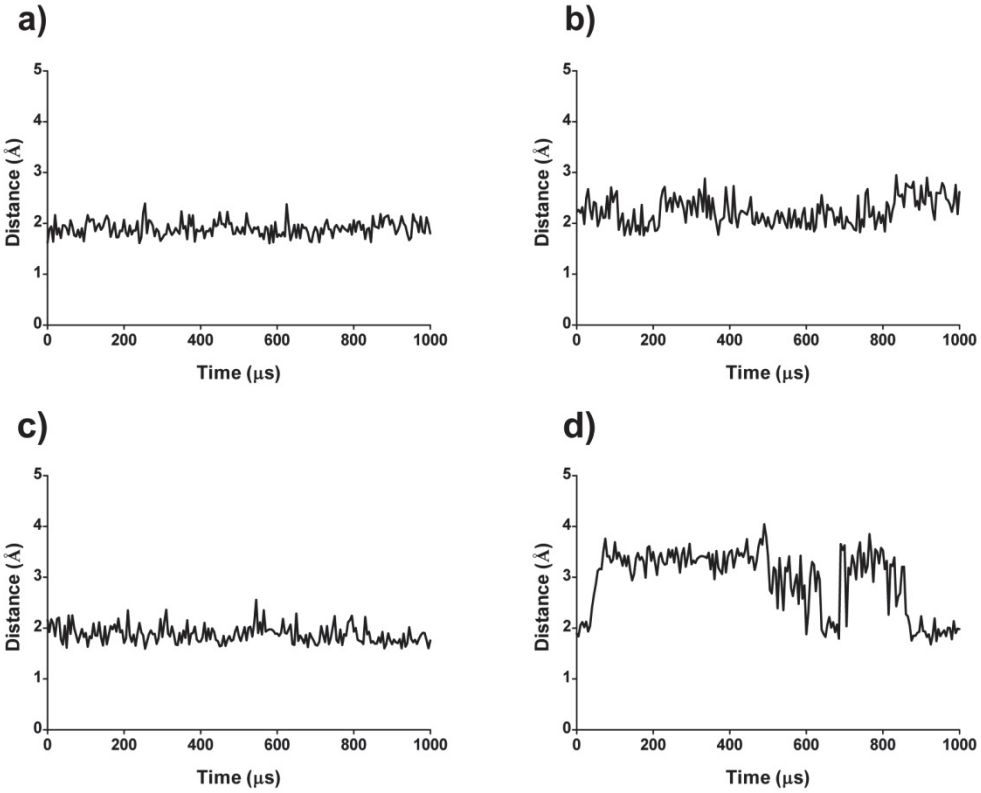

Figure S18. Results of MD simulations of *h*-MC4R$_a$ complexed with MTII. Graphic shows plot of the monitored distances, in the complex, between the protonated guanidinium N$^{\varepsilon}$ of Arg^{8} in MTII and the O$^{\varepsilon}$ of Glu100 (a), O$^{\delta}$ of Asp122 (b), Asp126 (c), and between N$^{\varepsilon}$ of His^{6} and the O$^{\varepsilon}$ of Glu100 (d).

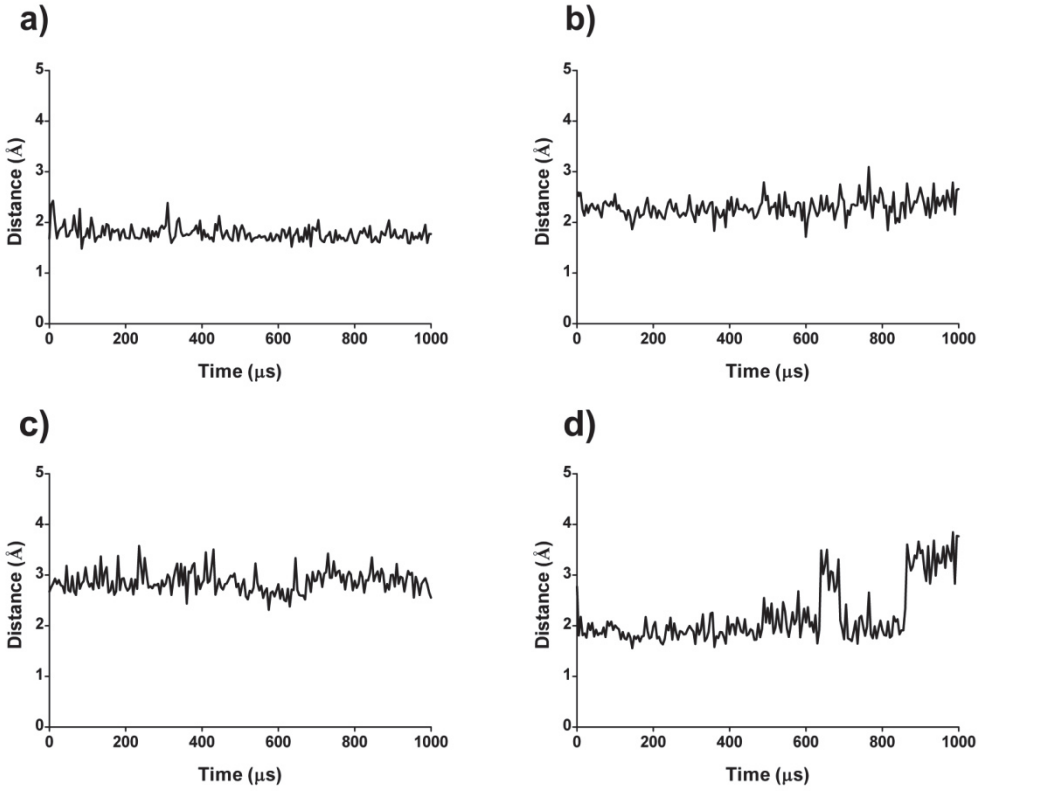

Figure S19. Results of MD simulations of *h*-MC4R$_i$ complexed with SHU9119. Graphic shows plot of the monitored distances, in the complex, between the protonated guanidinium N$^{\varepsilon}$ of Arg^{8} in SHU9119 and the O$^{\varepsilon}$ of Glu100 (a), O$^{\delta}$ of Asp122 (b), Asp126 (c), and between N$^{\varepsilon}$ of His^{6} and the O$^{\varepsilon}$ of Glu100 (d).

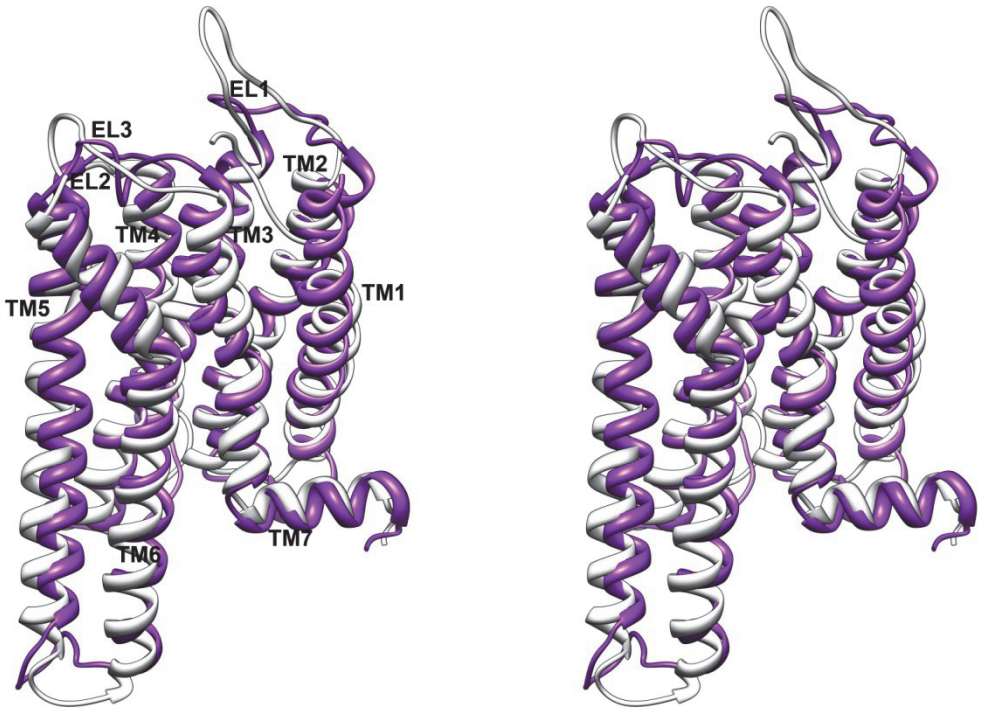

Figure S20. Stereoview of *h*-MC4R models in the "active" state proposed by Chapman *et al*. (violet ribbon; reference [129] of the manuscript) and that proposed by Mosberg *et al*. (grey ribbon; reference [114] of the manuscript). The *h*-MC4R models were superimposed using the backbone heavy atoms of TM residues.

Table S5. Analytical data of synthesized peptides MTII and SHU9119.

Code	M.W.	MS	HPLC[a,b]
MT-II	1024.22	1024.87	4.15
SHU9119	1074.28	1075.12	4.31

[a]HPLC column, Vydac 218TP1010, 1.0 x 25 cm, using a gradient of CH_3CN in 0.1% aqueous TFA (from 10 to 90% in 30 min) at a flow rate of 1.0 mL/min..
[b]k' = [(peptide retention time – solvent retention time)/solvent retention time].

Table S6. NMR Resonance Assignments[a] of Peptide MTII in H_2O Solution at 25 °C.

residue	NH ($^3J_{\alpha N}$, exc, $-\Delta\delta/\Delta T$)[b]	$C^{\alpha}H$	$C^{\beta}H$	Others
Nleu[4]	8.22 (6.6, f, 9.1)	4.20	1.65	1.26(γ); 0.85(ε)
Asp[5]	8.52 (7.5, f, 8.3)	4.63	2.89, 2.68	
His[6]	8.46 (7.0, f, 6.5)	4.40	3.16, 3.01	7.03(δ); 8.33(ε)
*D*Phe[7]	8.39 (7.1, f, 8.3)	4.57	3.15, 2.88	7.22(δ); 7.35(ε)
Arg[8]	7.89 (7.2, f, 6.3)	4.27	1.61, 1.57	1.32(γ); 3.08(δ); 7.10(ε)
Trp[9]	8.44 (6.7, f, 8.7)	4.65	3.31	7.27(δ); 10.15, 7.69(ε); 7.50, 7.33(ζ); 7.18(η)
Lys[10]	8.06 (8.1, f, 7.3)	4.22	1.75, 1.60	1.31, 1.23(γ); 1.51, 1.41(δ); 3.22, 3.17(ε); 7.91(ζ)

[a] Obtained at pH = 5, with TSP (δ 0.00 ppm) as reference shift. Chemical shifts are accurate to ±0.02 ppm.

[b] $^3J_{\alpha N}$ coupling constants in Hz. exc = N<u>H</u> exchange rate (f, fast; ms, moderately slow; s, slow;). $-\Delta\delta/\Delta T$ = temperature coefficients (ppb/K) calculated in the range 25-40 °C. Further signals: C<u>H</u>$_3$CO, 2.01; CON<u>H</u>$_2$, 6.65, 6.84.

Table S7. NMR Resonance Assignments[a] of Peptide SHU9119 in H_2O Solution at 25 °C.

residue	NH ($^3J_{\alpha N}$, exc, $-\Delta\delta/\Delta T$)[b]	$C^{\alpha}H$	$C^{\beta}H$	Others
Nleu[4]	8.18 (5.7, f, 8.3)	4.15	1.60	1.22(γ); 0.83(ε)
Asp[5]	8.46 (7.3, f, 8.1)	4.61	2.82, 2.63	
His[6]	8.41 (7.2, f, 6.0)	4.45	3.14, 2.96	6.95(δ); 8.04(ε)
*D*Nal[7]	8.53 (7.0, f, 8.3)	4.70	3.29, 3.06	7.65, 7.38(δ); 7.87(ε)
Arg[8]	7.93 (7.1, f, 6.8)	4.18	1.48, 1.39	1.05, 1.01(γ); 2.83(δ); 6.90(ε)
Trp[9]	8.39 (6.1, f, 9.1)	4.64	3.31, 3.27	7.26(δ); 10.13, 7.26(ε); 7.49, 7.33(ζ); 7.19(η)
Lys[10]	7.99 (8.8, f, 6.3)	4.21	1.74, 1.59	1.49(γ); 1.29, 1.19(δ); 3.18(ε); 7.91(ζ)

[a] Obtained at pH = 5, with TSP (δ 0.00 ppm) as reference shift. Chemical shifts are accurate to ±0.02 ppm.

[b] $^3J_{\alpha N}$ coupling constants in Hz. exc = N<u>H</u> exchange rate (f, fast; ms, moderately slow; s, slow;). $-\Delta\delta/\Delta T$ = temperature coefficients (ppb/K) calculated in the range 25-40 °C. Further signals: C<u>H</u>$_3$CO, 1.96; CON<u>H</u>$_2$, 6.65, 6.84.

Table S8. NMR Resonance Assignments[a] of Peptide MTII in H_2O Solution at 5 °C.

residue	NH ($^3J_{\alpha N}$, exc, $-\Delta\delta/\Delta T$)[b]	$C^{\alpha}H$	$C^{\beta}H$	Others
Nleu[4]	8.41 (6.0, f, 9.0)	4.18	1.64	1.23(γ); 0.83(ε)
Asp[5]	8.70 (7.5, f, 8.4)	4.63	2.90, 2.68	
His[6]	8.57 (6.4, f, 6.2)	4.38	3.16, 3.04	7.02(δ); 8.32(ε)
*D*Phe[7]	8.58 (6.8, f, 6.3)	4.13	3.16, 2.87	7.21(δ); 7.34(ε)
Arg[8]	8.00 (7.3, f, 6.2)	4.28	1.62, 1.56	1.29(γ); 3.07(δ); 7.17(ε)
Trp[9]	8.63 (6.4, f, 8.8)	4.65	3.30	7.27(δ); 10.24, 7.67(ε); 7.49, 7.33 (ζ); 7.17(η)
Lys[10]	8.17 (8.1, f, 7.4)	4.19	1.72, 1.58	1.31, 1.21(γ); 1.51, 1.39(δ); 3.23, 3.15(ε); 8.10(ζ)

[a] Obtained at pH = 5, with TSP (δ 0.00 ppm) as reference shift. Chemical shifts are accurate to ±0.02 ppm.

[b] $^3J_{\alpha N}$ coupling constants in Hz. exc = N<u>H</u> exchange rate (f, fast; ms, moderately slow; s, slow;). $-\Delta\delta/\Delta T$ = temperature coefficients (ppb/K) calculated in the range 5-15 °C. Further signals: C<u>H$_3$</u>CO, 1.99; CON<u>H$_2$</u>, 6.52, 6.94.

Table S9. NMR Resonance Assignments[a] of Peptide SHU9119 in H_2O Solution at 5 °C.

residue	NH ($^3J_{\alpha N}$, exc, $-\Delta\delta/\Delta T$)[b]	$C^{\alpha}H$	$C^{\beta}H$	Others
Nleu[4]	8.34 (5.7, f, 8.3)	4.14	1.59	1.23(γ); 0.82(ε);
Asp[5]	8.61 (7.2, f, 8.1)	4.60	2.83, 2.63	
His[6]	8.53 (6.5, f, 6.0)	4.44	3.14, 2.95	6.93(δ); 8.04(ε)
*D*Nal[7]	8.73 (6.7, f, 6.5)	4.70	3.29, 3.04	7.66, 7.40(δ); 7.85(ε)
Arg[8]	8.10 (7.1, f, 6.7)	4.16	1.48, 1.39	1.05, 0.97(γ); 2.82(δ); 6.95(ε)
Trp[9]	8.55 (6.2, f, 9.1)	4.63	3.29, 3.27	7.25(δ); 10.21(ε); 7.47, 7.33 (ζ); 7.16(η)
Lys[10]	8.09 (8.2, f, 6.3)	4.19	1.74, 1.59	1.49(γ); 1.29, 1.19(δ); 3.15(ε); 8.09(ζ)

[a] Obtained at pH = 5, with TSP (δ 0.00 ppm) as reference shift. Chemical shifts are accurate to ±0.02 ppm.

[b] $^3J_{\alpha N}$ coupling constants in Hz. exc = N<u>H</u> exchange rate (f, fast; ms, moderately slow; s, slow;). $-\Delta\delta/\Delta T$ = temperature coefficients (ppb/K) calculated in the range 5-15 °C. Further signals: C<u>H$_3$</u>CO, 1.96; CON<u>H$_2$</u>, 6.73, 6.96.

Table S10. NMR Resonance Assignments[a] of Peptide MTII in H_2O/DMSO Solution at -10 °C.

residue	NH ($^3J_{\alpha N}$, exc, $-\Delta\delta/\Delta T$)[b]	$C^{\alpha}H$	$C^{\beta}H$	Others
Nleu[4]	8.43 (6.4, f, 9.0)	4.18	1.60	1.21(γ); 0.83(ε)
Asp[5]	8.71 (6.8, f, 8.2)	4.60	2.90, 2.66	
His[6]	8.59 (6.4, f, 6.2)	4.33	3.17, 3.01	7.01(δ); 8.38(ε)
*D*Phe[7]	8.56 (7.0, f, 6.3)	4.52	3.16, 2.86	7.22(δ); 7.33(ε)
Arg[8]	7.99 (7.0, f, 6.6)	4.30	1.64, 1.58	1.33(γ); 3.08(δ); 7.25(ε)
Trp[9]	8.64 (6.0, f, 8.7)	4.63	3.30, 3.26	7.27(δ); 10.35, 7.68(ε); 7.47, 7.16(ζ); 7.23(η)
Lys[10]	8.25 (8.1, f, 7.3)	4.18	1.74, 1.58	1.32, 1.22(γ); 1.49, 1.37(δ); 3.19(ε); 8.11(ζ)

[a] Obtained at -10 °C, with TSP (δ 0.00 ppm) as reference shift. Chemical shifts are accurate to ±0.02 ppm.

[b] $^3J_{\alpha N}$ coupling constants in Hz. exc = N<u>H</u> exchange rate (f, fast; ms, moderately slow; s, slow;). $-\Delta\delta/\Delta T$ = temperature coefficients (ppb/K) calculated in the range -10 to 0 °C. Further signals: C<u>H</u>$_3$CO, 1.97; CON<u>H</u>$_2$, 6.59, 7.01.

.

Table S11. NMR Resonance Assignments[a] of Peptide SHU9119 in H_2O/DMSO Solution.

residue	NH ($^3J_{\alpha N}$, exc, $-\Delta\delta/\Delta T$)[b]	$C^{\alpha}H$	$C^{\beta}H$	Others
Nleu[4]	8.38 (5.8, f, 8.4)	4.14	1.56	1.18(γ); 0.79(ε);
Asp[5]	8.65 (6.7, f, 8.1)	4.58	2.85, 2.62	
His[6]	8.57 (6.4, f, 6.0)	4.36	3.15, 2.96	6.93(δ); 8.07(ε)
*D*Nal[7]	8.70 (6.7, f, 6.5)	4.67	3.30, 3.04	7.66, 7.39(δ); 7.86(ε)
Arg[8]	8.07 (7.0, f, 6.7)	4.21	1.53, 1.48	1.11, 1.08(γ); 2.90(δ); 7.09(ε)
Trp[9]	8.60 (6.1, f, 9.1)	4.63	3.29, 3.24	7.23(δ); 10.33, 7.26(ε); 7.46, 7.15(ζ); 7.23(η)
Lys[10]	8.17 (8.3, f, 6.3)	4.19	1.73, 1.58	1.24(γ); 1.48, 1.37(δ); 3.17(ε); 8.10(ζ)

[a] Obtained at -10 °C,with TSP (δ 0.00 ppm) as reference shift. Chemical shifts are accurate to ±0.02 ppm.

[b] $^3J_{\alpha N}$ coupling constants in Hz. exc = N<u>H</u> exchange rate (f, fast; ms, moderately slow; s, slow;). $-\Delta\delta/\Delta T$ = temperature coefficients (ppb/K) calculated in the range -10 to 0 °C. Further signals: C<u>H$_3$</u>CO, 1.94; CON<u>H$_2$</u>, 6.66, 7.02.

Table S12. NMR Resonance Assignments[a] of Peptide MTII in DPC 200mM Solution.

residue	NH ($^3J_{\alpha N}$, exc, $-\Delta\delta/\Delta T$)[b]	$C^{\alpha}H(J_{\alpha\beta(l)},J_{\alpha\beta(h)})$	$C^{\beta}H$	Others
Nleu[4]	8.23 (5.8, f, 7.6)	4.22 (8.6, 7.3)	1.69, 1.63	1.23(γ); 1.30(δ); 0.82(ε);
Asp[5]	8.70 (5.5, f, 5.0)	4.40 (6.1, 8.5)	3.13, 2.47	
His[6]	8.84 (6.0, f, 4.7)	4.14 (6.3, 7.2)	3.29, 3.15	7.12(δ); 8.51(ε)
*D*Phe[7]	8.21 (7.0, ms, 3.2)	4.46 (9.5, 5.2)	3.16, 2.92	7.19(δ); 7.22(ε); 7.16(ζ)
Arg[8]	7.49 (8.2, s, 1.4)	4.54 (ov.)	1.73, 1.70	1.52, 1.47(γ); 3.15(δ); 7.23(ε)
Trp[9]	8.72 (7.0, f, 8.9)	4.75 (9.0, 5.8)	3.33, 3.14	7.21(δ); 10.63, 7.61(ε); 7.46, 6.99(ζ); 7.07(η)
Lys[10]	8.19 (8.1, f, 5.3)	4.16 (5.2, 9.1)	1.73, 1.53	1.35, 1.28(γ); 1.42(δ); 3.20, 3.06(ε); 7.95(ζ)

[a] Obtained at 25°C, pH = 5, with TSP (δ 0.00 ppm) as reference shift. Chemical shifts are accurate to ±0.02 ppm.

[b] $^3J_{\alpha N}$ and $^3J_{\alpha\beta}$ coupling constants in Hz. exc = N<u>H</u> exchange rate (f, fast; ms, moderately slow; s, slow;). $-\Delta\delta/\Delta T$ = temperature coefficients (ppb/K) calculated in the range 25 – 40 °C. The subscripts (l) and (h) denote the coupling constant of the low- and high-field H_{β} signal, respectively. Further signals: C<u>H$_3$</u>CO, 1.93; CON<u>H$_2$</u>, 6.37, 7.08.

Table S13. NMR Resonance Assignments[a] of Peptide SHU9119 in DPC 200mM Solution

residue	NH ($^3J_{\alpha N}$, exc, $-\Delta\delta/\Delta T$)[b]	$C^{\alpha}H(J_{\alpha\beta(l)},J_{\alpha\beta(h)})$	$C^{\beta}H$	Others
Nleu[4]	8.18 (5.6, f, 7.8)	4.26 (8.6, 7.4)	1.69, 1.63	1.26(γ); 1.18(δ); 0.78(ε);
Asp[5]	8.73 (5.4, f, 5.7)	4.42 (6.0, 8.5)	3.13, 2.49	
His[6]	8.87 (6.1, f, 4.5)	4.16 (6.5, 7.3)	3.30, 3.16	7.12(δ); 8.39(ε)
*D*Nal[7]	8.38 (6.9, ms, 3.2)	4.57 (8.5, 7.2)	3.31, 3.11	7.65, 7.35(δ); 7.75(ε); 7.80(ζ); 7.80, 7.79(η); 7.43(θ)
Arg[8]	7.53 (8.2, s, 1.5)	4.55 (6.8, 8.0)	1.76, 1.69	1.52, 1.47(γ); 3.12(δ); 7.23(ε)
Trp[9]	8.74 (7.1, f, 8.5)	4.77 (9.0, 5.8)	3.35, 3.15	7.23(δ); 10.65, 7.63(ε); 7.47, 7.01(ζ); 7.08(η)
Lys[10]	8.22 (8.1, f, 5.8)	4.18 (5.2, 9.0)	1.74, 1.55	1.31(γ); 1.44, 1.37(δ); 3.22, 3.07(ε); 7.97(ζ)

[a] Obtained at 25°C, pH = 5, with TSP (δ 0.00 ppm) as reference shift. Chemical shifts are accurate to ±0.02 ppm.

[b] $^3J_{\alpha N}$ and $^3J_{\alpha\beta}$ coupling constants in Hz. exc = N<u>H</u> exchange rate (f, fast; ms, moderately slow; s, slow;). $-\Delta\delta/\Delta T$ = temperature coefficients (ppb/K) calculated in the range 25 - 40 °C. The subscripts (l) and (h) denote the coupling constant of the low- and high-field H_{β} signal, respectively. Further signals: C<u>H$_3$</u>CO, 1.90; CON<u>H$_2$</u>, 6.40, 7.10.

Table S14. NOE Derived Upper Limit Constraints of MTII in DPC solution

3	ACE	QH	5	ASP	HN	6.19
4	NLE	HN	4	NLE	HA	2.93
4	NLE	HN	4	NLE	HB2	3.92
4	NLE	HN	4	NLE	HB3	3.92
4	NLE	HN	4	NLE	QB	2.84
4	NLE	HN	4	NLE	QG	5.27
4	NLE	HN	4	NLE	QD	6.38
4	NLE	HN	5	ASP	HN	2.99
4	NLE	HA	4	NLE	HB2	2.96
4	NLE	HA	4	NLE	HB3	2.96
4	NLE	HA	4	NLE	QD	5.02
4	NLE	HA	4	NLE	QE	6.53
4	NLE	HA	5	ASP	HN	3.50
4	NLE	HA	6	HIS	HN	4.76
4	NLE	HB2	4	NLE	QE	6.53
4	NLE	HB2	5	ASP	HN	3.48
4	NLE	HB2	6	HIS	HN	4.72
4	NLE	HB3	4	NLE	QE	6.53
4	NLE	HB3	5	ASP	HN	3.48
4	NLE	HB3	6	HIS	HN	4.72
4	NLE	QB	4	NLE	QE	6.41
4	NLE	QB	5	ASP	HN	3.26
4	NLE	QB	6	HIS	HN	4.50
4	NLE	QG	5	ASP	HN	6.32
4	NLE	QG	6	HIS	HN	6.38
4	NLE	QG	7	DPHE	QD	8.50
4	NLE	QG	9	TRP	HE3	6.38
4	NLE	QG	9	TRP	HZ3	6.38
4	NLE	QD	5	ASP	HN	6.38
4	NLE	QD	9	TRP	HE3	6.38
4	NLE	QE	7	DPHE	QD	8.65
4	NLE	QE	9	TRP	HE3	6.53
5	ASP	HN	5	ASP	HA	2.55
5	ASP	HN	6	HIS	HN	3.17
5	ASP	HN	10	LYS	HZ1	5.50
5	ASP	HA	5	ASP	HB2	2.99
5	ASP	HA	5	ASP	HB3	2.99
5	ASP	HA	6	HIS	HN	3.60
5	ASP	HA	7	DPHE	HN	5.00
5	ASP	HA	10	LYS	HZ1	5.13
5	ASP	HB2	10	LYS	HE2	6.85
5	ASP	HB2	10	LYS	HE3	6.85
5	ASP	HB2	10	LYS	HZ1	3.11
5	ASP	HB3	10	LYS	HE2	6.85
5	ASP	HB3	10	LYS	HE3	6.85
5	ASP	HB3	10	LYS	HZ1	3.11
5	ASP	QB	8	ARG	HN	5.50
5	ASP	QB	10	LYS	QB	7.25
5	ASP	QB	10	LYS	QE	5.90
5	ASP	QB	10	LYS	HZ1	2.88
6	HIS	HN	6	HIS	HA	2.68
6	HIS	HN	6	HIS	HB2	3.42
6	HIS	HN	6	HIS	HB3	3.42
6	HIS	HN	6	HIS	HD2	5.25
6	HIS	HN	7	DPHE	HN	3.21
6	HIS	HN	8	ARG	HN	4.63
6	HIS	HA	6	HIS	HB2	2.77
6	HIS	HA	6	HIS	HB3	2.77
6	HIS	HA	6	HIS	HD2	4.60

6	HIS	HA	7	DPHE	HN	2.86
6	HIS	HA	7	DPHE	QD	7.62
6	HIS	HA	8	ARG	HN	4.88
6	HIS	QB	7	DPHE	HN	4.86
7	DPHE	HN	7	DPHE	HB2	2.83
7	DPHE	HN	7	DPHE	HB3	2.83
7	DPHE	HN	7	DPHE	QB	2.63
7	DPHE	HN	8	ARG	HN	3.50
7	DPHE	HA	8	ARG	HN	3.14
8	ARG	HN	9	TRP	HN	4.58
8	ARG	HA	8	ARG	QB	2.76
8	ARG	HA	8	ARG	HG2	4.04
8	ARG	HA	8	ARG	HG3	4.04
8	ARG	HA	9	TRP	HN	2.55
8	ARG	HB2	9	TRP	HN	3.24
8	ARG	HB3	9	TRP	HN	3.24
8	ARG	HG2	9	TRP	HN	5.25
8	ARG	HG3	9	TRP	HN	5.25
8	ARG	QG	9	TRP	HN	5.10
9	TRP	HN	9	TRP	HB2	2.90
9	TRP	HN	9	TRP	HB3	2.90
9	TRP	HN	9	TRP	QB	2.68
9	TRP	HN	9	TRP	HD1	5.20
9	TRP	HN	10	LYS	HN	4.61
9	TRP	HA	9	TRP	HD1	5.07
9	TRP	HA	9	TRP	HE3	4.67
9	TRP	HA	10	LYS	HN	2.93
9	TRP	HB2	9	TRP	HE3	3.64
9	TRP	HB2	10	LYS	HN	3.83
9	TRP	HB3	9	TRP	HE3	3.64
9	TRP	HB3	10	LYS	HN	3.83
9	TRP	QB	9	TRP	HD1	3.49
9	TRP	QB	9	TRP	HE3	3.42
9	TRP	QB	10	LYS	HN	3.63
9	TRP	HD1	10	LYS	HN	4.72
9	TRP	HD1	10	LYS	HA	5.50
9	TRP	HD1	11	CNH2	HN1	5.16
9	TRP	HE1	11	CNH2	HN1	5.50
10	LYS	HN	10	LYS	HA	2.90
10	LYS	HN	10	LYS	HB2	3.08
10	LYS	HN	10	LYS	HB3	3.08
10	LYS	HN	11	CNH2	HN1	4.35
10	LYS	HA	10	LYS	HB2	2.83
10	LYS	HA	10	LYS	HB3	2.83
10	LYS	HA	10	LYS	QB	2.63
10	LYS	HA	10	LYS	HG2	3.30
10	LYS	HA	10	LYS	HG3	3.30
10	LYS	HA	10	LYS	QG	2.95
10	LYS	HB2	11	CNH2	HN1	5.50
10	LYS	HB3	11	CNH2	HN1	5.50
10	LYS	HG2	10	LYS	HE2	4.04
10	LYS	HG2	10	LYS	HE3	4.04
10	LYS	HG2	10	LYS	HZ1	3.76
10	LYS	HG3	10	LYS	HE2	4.04
10	LYS	HG3	10	LYS	HE3	4.04
10	LYS	HG3	10	LYS	HZ1	3.76
10	LYS	QG	10	LYS	QE	3.23
10	LYS	QG	10	LYS	HZ1	3.41

ACE QH is the methyl group of the N-terminal acetyl funtion. CNH2 HN1 is one of the amide protons of the C-terminal carboxamide function.

Table S15. NOE Derived Upper Limit Constraints of SHU9119 in DPC solution

3	ACE	QH	5	ASP	HN	6.09
4	NLE	HN	4	NLE	HA	2.86
4	NLE	HN	4	NLE	HB2	3.90
4	NLE	HN	4	NLE	HB3	3.90
4	NLE	HN	4	NLE	QB	2.80
4	NLE	HN	4	NLE	QG	5.39
4	NLE	HN	4	NLE	QD	5.92
4	NLE	HN	5	ASP	HN	2.97
4	NLE	HA	4	NLE	HB2	2.96
4	NLE	HA	4	NLE	HB3	2.96
4	NLE	HA	4	NLE	QD	4.62
4	NLE	HA	5	ASP	HN	3.52
4	NLE	HA	6	HIS	HN	4.88
4	NLE	HB2	4	NLE	QE	6.25
4	NLE	HB2	5	ASP	HN	3.52
4	NLE	HB3	4	NLE	QE	6.25
4	NLE	HB3	5	ASP	HN	3.52
4	NLE	QB	4	NLE	QE	6.03
4	NLE	QB	5	ASP	HN	3.22
4	NLE	QB	6	HIS	HN	5.82
4	NLE	QB	7	DNAL	HN	5.67
4	NLE	QB	7	DNAL	QB	5.50
4	NLE	QG	5	ASP	HN	6.38
4	NLE	QG	9	TRP	HE3	6.38
4	NLE	QD	5	ASP	HN	6.38
4	NLE	QD	9	TRP	HE3	6.38
4	NLE	QE	5	ASP	HN	6.53
4	NLE	QE	9	TRP	HE3	6.53
5	ASP	HN	5	ASP	HA	2.55
5	ASP	HN	6	HIS	HN	3.08
5	ASP	HN	7	DNAL	HN	4.30
5	ASP	HN	10	LYS	HZ1	5.50
5	ASP	HA	5	ASP	HB2	2.90
5	ASP	HA	5	ASP	HB3	2.90
5	ASP	HA	5	ASP	QB	2.68
5	ASP	HA	6	HIS	HN	3.64
5	ASP	HA	7	DNAL	HN	4.98
5	ASP	HA	10	LYS	HZ1	5.07
5	ASP	HB2	10	LYS	HZ1	3.05
5	ASP	HB3	10	LYS	HZ1	3.05
5	ASP	QB	8	ARG	HN	5.50
5	ASP	QB	10	LYS	HZ1	2.85
6	HIS	HN	6	HIS	HA	2.71
6	HIS	HN	6	HIS	HB2	3.48
6	HIS	HN	6	HIS	HB3	3.48
6	HIS	HN	6	HIS	QB	3.20
6	HIS	HN	7	DNAL	HN	3.33
6	HIS	HN	8	ARG	HN	4.66
6	HIS	HA	6	HIS	HB2	2.72
6	HIS	HA	6	HIS	HB3	2.72
6	HIS	HA	6	HIS	HD2	4.51
6	HIS	HA	7	DNAL	HN	3.02
6	HIS	HA	8	ARG	HN	4.83
6	HIS	QB	7	DNAL	HN	4.80
7	DNAL	HN	7	DNAL	HB2	2.90
7	DNAL	HN	7	DNAL	HB3	2.90
7	DNAL	HN	7	DNAL	QB	2.66
7	DNAL	HN	8	ARG	HN	3.52
7	DNAL	HA	8	ARG	HN	3.24

8	ARG	HN	9	TRP	HN	4.52
8	ARG	HA	8	ARG	QB	2.78
8	ARG	HA	9	TRP	HN	2.59
8	ARG	HB2	9	TRP	HN	3.24
8	ARG	HB3	9	TRP	HN	3.24
9	TRP	HN	9	TRP	HB2	2.93
9	TRP	HN	9	TRP	HB3	2.93
9	TRP	HN	9	TRP	QB	2.69
9	TRP	HN	9	TRP	HD1	5.22
9	TRP	HN	10	LYS	HN	4.64
9	TRP	HA	9	TRP	HD1	5.04
9	TRP	HA	9	TRP	HE3	4.74
9	TRP	HA	10	LYS	HN	2.68
9	TRP	HB2	9	TRP	HE3	3.79
9	TRP	HB2	10	LYS	HN	3.84
9	TRP	HB3	9	TRP	HE3	3.79
9	TRP	HB3	10	LYS	HN	3.84
9	TRP	QB	9	TRP	HD1	3.49
9	TRP	QB	9	TRP	HE3	3.53
9	TRP	QB	10	LYS	HN	3.63
9	TRP	HD1	10	LYS	HN	5.04
9	TRP	HD1	10	LYS	HA	5.50
9	TRP	HD1	11	CNH2	HN1	5.18
9	TRP	HE1	11	CNH2	HN1	5.46
10	LYS	HN	10	LYS	HA	2.96
10	LYS	HN	10	LYS	HB2	3.14
10	LYS	HN	10	LYS	HB3	3.14
10	LYS	HN	11	CNH2	HN1	4.36
10	LYS	HA	10	LYS	HB2	2.86
10	LYS	HA	10	LYS	HB3	2.86
10	LYS	HA	10	LYS	QB	2.64
10	LYS	HB2	11	CNH2	HN1	5.50
10	LYS	HB3	11	CNH2	HN1	5.50
10	LYS	HG2	10	LYS	HE2	3.98
10	LYS	HG2	10	LYS	HE3	3.98
10	LYS	HG2	10	LYS	HZ1	3.73
10	LYS	HG3	10	LYS	HE2	4.08
10	LYS	HG3	10	LYS	HE3	4.08
10	LYS	HG3	10	LYS	HZ1	3.76
10	LYS	QG	10	LYS	HZ1	4.64

ACE QH is the methyl group of the N-terminal acetyl funtion. CNH2 HN1 is one of the amide protons of the C-terminal carboxamide function.

Table S16. Dihedral angles of the NMR structures of MTII and SHU9119

	MTII				SHU9119			
4	NLE	OMEGA	-178.8 +/-	6.4	4 NLE	OMEGA	169.1 +/-	2.4
4	NLE	PHI	-90.2 +/-	22.8	4 NLE	PHI	-78.6 +/-	24.4
4	NLE	CHI1	-125.6 +/-	44.7	4 NLE	CHI1	-134.5 +/-	32.7
4	NLE	CHI2	63.0 +/-	52.3	4 NLE	CHI2	119.8 +/-	54.9
4	NLE	CHI3	54.1 +/-	68.6	4 NLE	CHI3	98.8 +/-	111.5
4	NLE	PSI	-72.4 +/-	29.2	4 NLE	PSI	-57.9 +/-	27.6
5	ASP	OMEGA	-175.6 +/-	5.5	5 ASP	OMEGA	176.7 +/-	4.6
5	ASP	PHI	-118.0 +/-	25.6	5 ASP	PHI	-135.4 +/-	24.5
5	ASP	CHI1	-167.9 +/-	23.9	5 ASP	CHI1	-170.6 +/-	15.3
5	ASP	CHI2	-0.1 +/-	24.3	5 ASP	CHI2	10.1 +/-	29.5
5	ASP	PSI	-51.6 +/-	10.3	5 ASP	PSI	-63.8 +/-	7.9
6	HIS	OMEGA	173.0 +/-	5.6	6 HIS	OMEGA	-178.1 +/-	2.9
6	HIS	PHI	-164.6 +/-	4.0	6 HIS	PHI	-143.8 +/-	7.9
6	HIS	CHI1	-128.3 +/-	48.3	6 HIS	CHI1	-67.6 +/-	83.8
6	HIS	CHI2	-77.7 +/-	64.1	6 HIS	CHI2	-85.0 +/-	78.3
6	HIS	PSI	42.1 +/-	13.1	6 HIS	PSI	53.4 +/-	14.7
7	DPHE	OMEGA	-174.8 +/-	6.8	7 DNAL	OMEGA	-173.7 +/-	2.5
7	DPHE	PHI	87.7 +/-	24.4	7 DNAL	PHI	64.0 +/-	18.3
7	DPHE	CHI1	157.3 +/-	4.4	7 DNAL	CHI1	112.0 +/-	48.0
7	DPHE	CHI2	-118.5 +/-	84.2	7 DNAL	CHI2	101.6 +/-	36.4
7	DPHE	PSI	-55.4 +/-	23.0	7 DNAL	PSI	5.0 +/-	21.1
8	ARG	OMEGA	-179.2 +/-	6.5	8 ARG	OMEGA	-178.9 +/-	2.0
8	ARG	PHI	-79.4 +/-	6.0	8 ARG	PHI	-132.9 +/-	18.1
8	ARG	CHI1	-74.3 +/-	12.6	8 ARG	CHI1	-71.6 +/-	13.1
8	ARG	CHI2	-123.0 +/-	38.8	8 ARG	CHI2	-166.3 +/-	33.6
8	ARG	CHI3	-112.5 +/-	113.2	8 ARG	CHI3	174.0 +/-	56.6
8	ARG	CHI4	-168.3 +/-	45.0	8 ARG	CHI4	172.5 +/-	49.7
8	ARG	PSI	159.6 +/-	7.1	8 ARG	PSI	157.7 +/-	4.3
9	TRP	OMEGA	-175.4 +/-	7.7	9 TRP	OMEGA	179.9 +/-	2.7
9	TRP	PHI	-90.6 +/-	18.4	9 TRP	PHI	-68.2 +/-	25.0
9	TRP	CHI1	179.4 +/-	4.6	9 TRP	CHI1	-174.7 +/-	3.1
9	TRP	CHI2	-99.9 +/-	23.7	9 TRP	CHI2	-104.7 +/-	11.7
9	TRP	PSI	155.0 +/-	3.9	9 TRP	PSI	149.1 +/-	3.6
10	LYS	OMEGA	-172.8 +/-	4.1	10 LYS	OMEGA	-168.8 +/-	1.3
10	LYS	PHI	-92.1 +/-	11.5	10 LYS	PHI	-92.8 +/-	14.0
10	LYS	CHI1	-73.6 +/-	5.5	10 LYS	CHI1	-84.1 +/-	10.0
10	LYS	CHI2	173.0 +/-	43.8	10 LYS	CHI2	166.0 +/-	27.5
10	LYS	CHI3	172.6 +/-	4.2	10 LYS	CHI3	-175.0 +/-	6.9
10	LYS	CHI4	44.8 +/-	44.3	10 LYS	CHI4	59.7 +/-	68.3
10	LYS	PSI	88.3 +/-	26.1	10 LYS	PSI	97.2 +/-	8.8

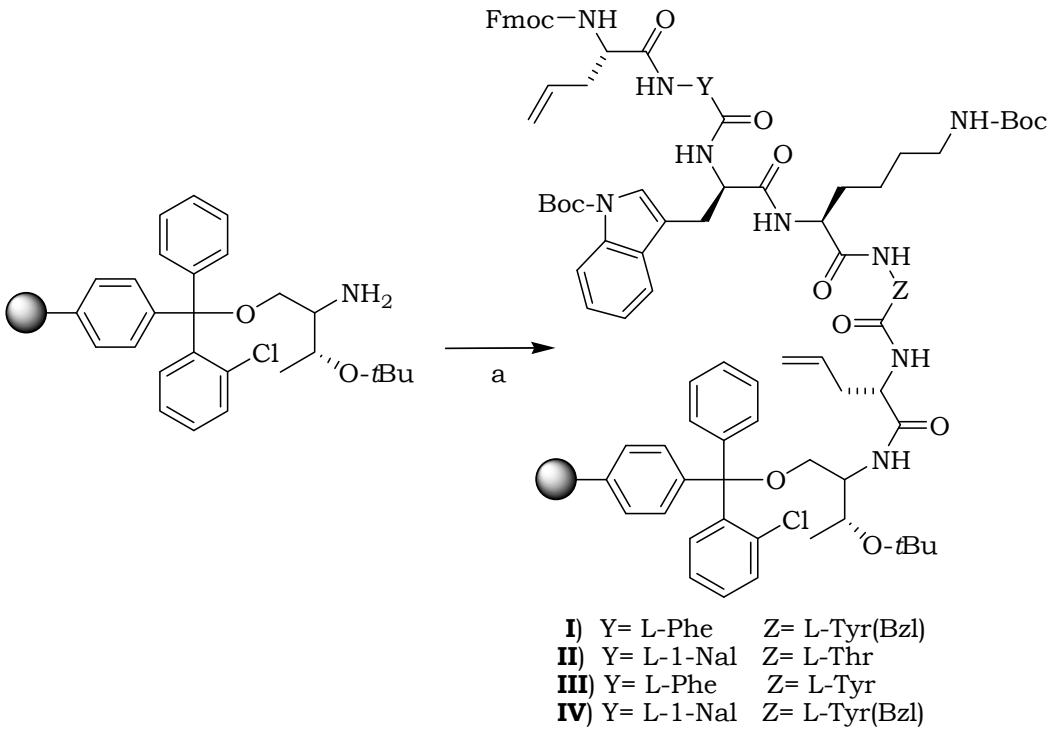

Scheme 1. Synthesis of linear peptides on H–l-Thr(t-Bu)–ol–2-chlorotrityl resin. a) *(i) Fmoc- L- Hag, HATU/NMM, 40 min r.t.; (ii) 20% piperidine in DMF (2 x 15 min); (iii) coupling with the amino acids.*

The resin aliquots containing the linear peptides were swollen for 2 h in anhydrous DCM. After two hours, the vessels were heated to 45 °C and a DCM solution of catalyst **9** (0.5 mole equiv. calculated on the basis of 0.5 mmol/g of peptide) was added. The suspension was then stirred for 48 h at 45 °C. The resin aliquots were washed with DCM, DMF, and MeOH, then swelled for 45 min at room temperature in DMF. Fmoc–Hag was deprotected (2.5 mL of 20% piperidine in DMF for 5 min, 4 time repeated) and coupled with Fmoc–D-Phe affording the on-resin peptides **4-8** which were deprotected and cleaved as previously described (Scheme 2).

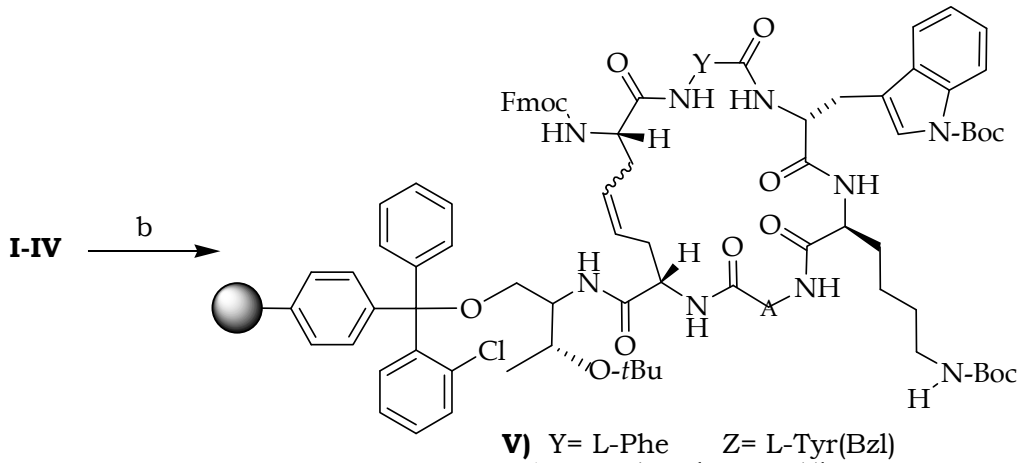

V) Y= L-Phe Z= L-Tyr(Bzl)
VI) Y= L-1-Nal Z= L-Thr
VII) Y= L-Phe Z= L-Tyr
VIII) Y= L-1-Nal Z= L-Tyr(Bzl)

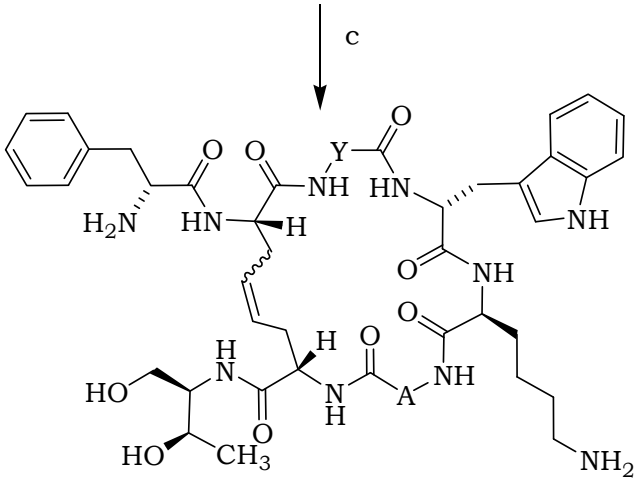

4) Y= L-Phe Z= L-Tyr(Bzl) *Z*-isomer
5) Y= L-1-Nal Z= L-Thr *Z*-isomer
6) Y= L-Phe Z= L-Tyr *E*-isomer
7) Y= L-Phe Z= L-Tyr *Z*-isomer
8) Y= L-1-Nal Z= L-Tyr(Bzl) *Z*-isomer

Scheme 2. Synthesis of ciclic octapeptides. b) *(i) Catalyst, 45 °C, 48 h; (ii) 20% piperidine in DMF, Fmoc-D-Phe/HATU/NMM 40 min, r.t.*
c) i) 20% piperidine in DMF; ii) Cleavage of ***5-7*** *by TFA/DCM/EDT/Phenol (94:2:2:2);* ***4*** *and* ***8*** *by TFA/DCM/EDT/Phenol (70:26:2:2).*

Table S17. RP-HPLC data of the purified analogues.

Compound	HPLC method [a]	Retention times (min.)[b]
4	45%-55% B in 20 min.	9.64
5	20%-60% B in 20 min.	13.26
6	32% B in 20 min.	13.03
7	30%-40% B in 20 min.	15.08
8	50%-60% B in 10 min.	7.02

[a] A: H_2O 0.1% TFA;B: CH_3CN 0.1% TFA. [b] R_t of the pure compounds.

Table S18. Mass Spectral data of the purified analogues.

Compound	$[M]^+$ calcd.	$[M+H]^+$ found	$[M+2H]^{2+}$	$[M+Na]^+$
4	1132.57	1133.53	567.6	1156.66
5	1030.53	1032.0	514.46	1054.98
6	1042.53	1043.55 (20%)	523,53 (100%)	1066.67
7	1042.53	1043.63 (20%)	522,35 (100%)	1066.67
8	1182.59	1184,04 (10%)	592,51 (100 %)	1206.94

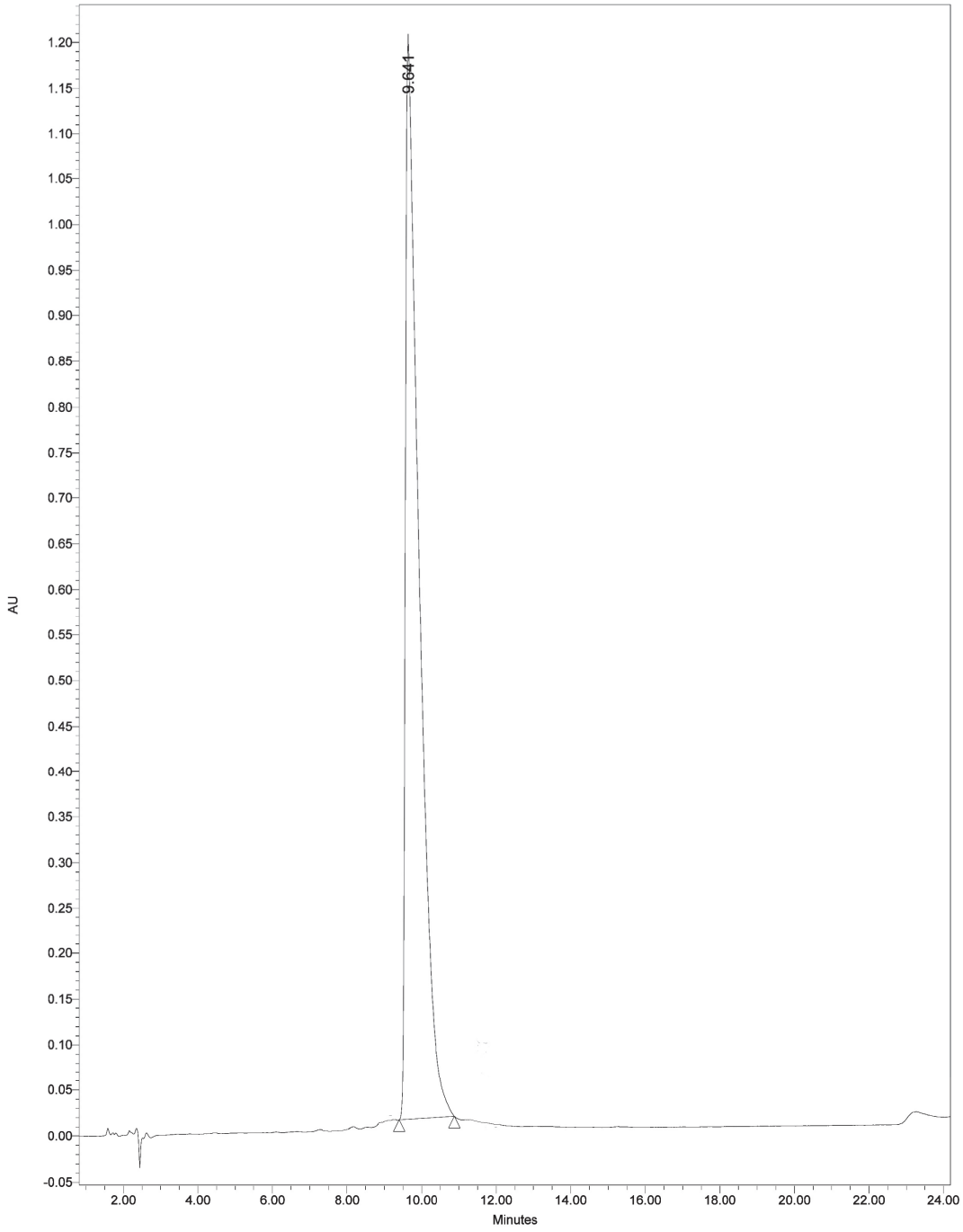

Figure S21. RP-HPLC trace of pure (**4**)

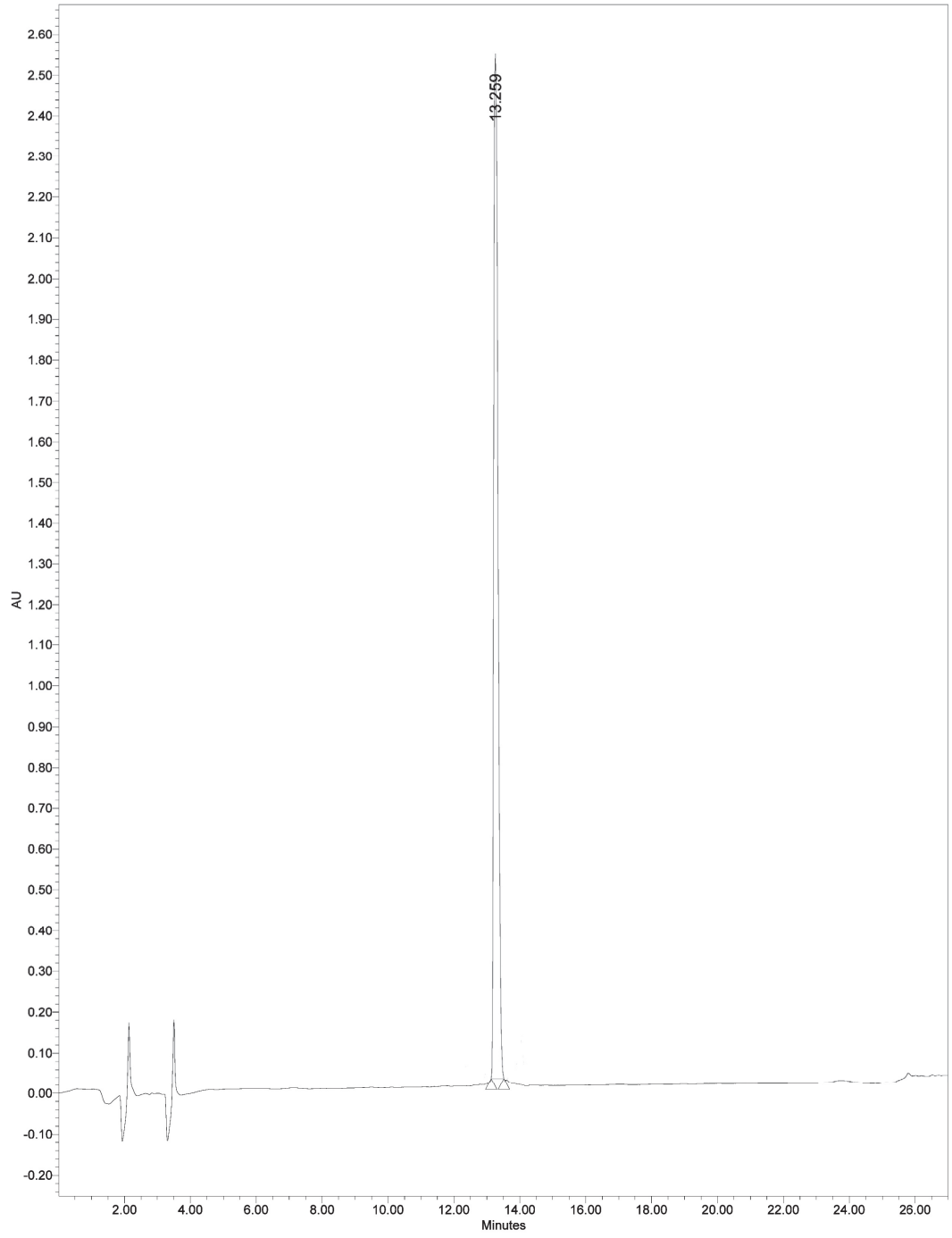

Figure S22. RP-HPLC trace of pure (5)

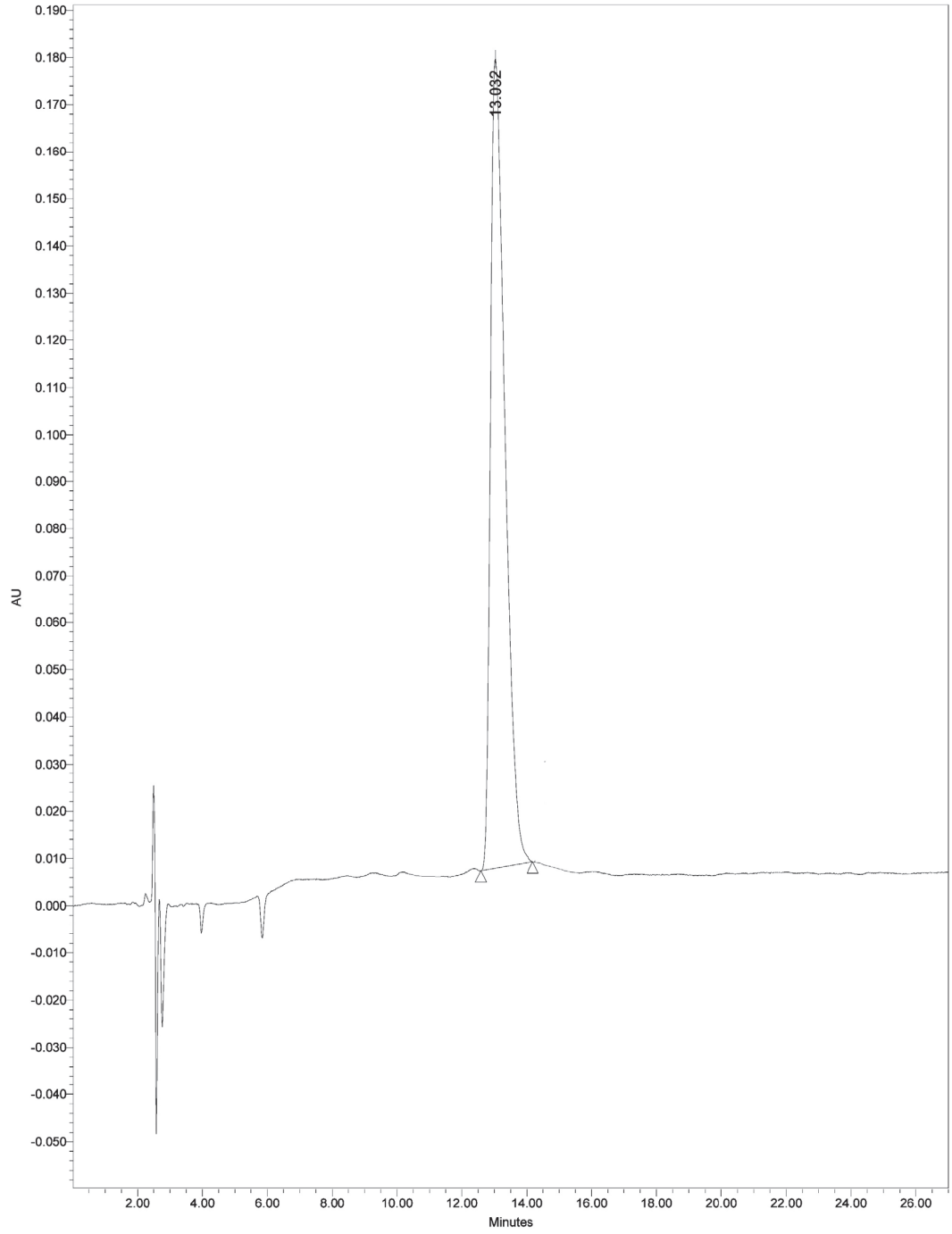

Figure S23. RP-HPLC trace of pure (**6**)-*E* isomer

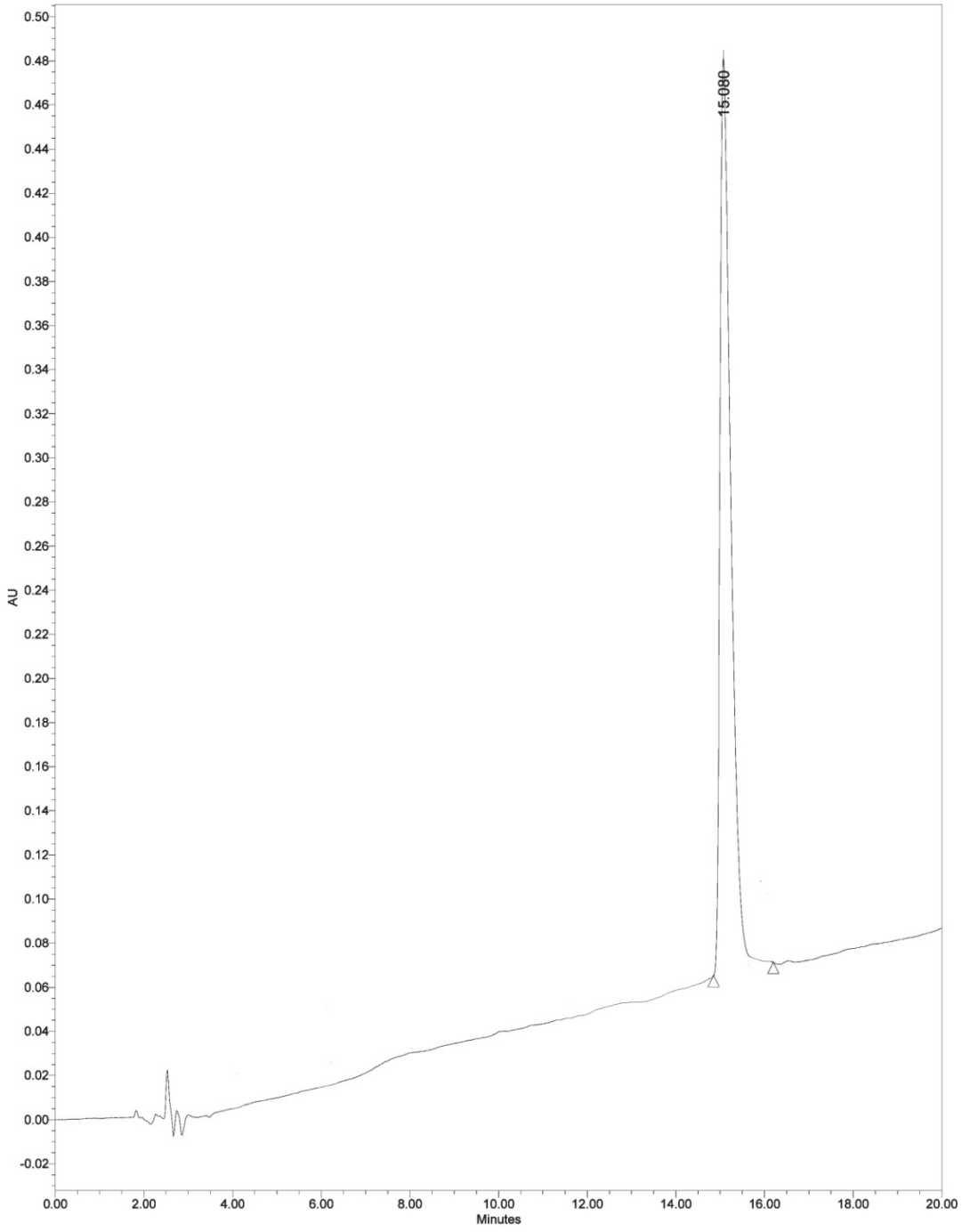

Figure S24. RP-HPLC trace of pure (**7**) *Z*-isomer

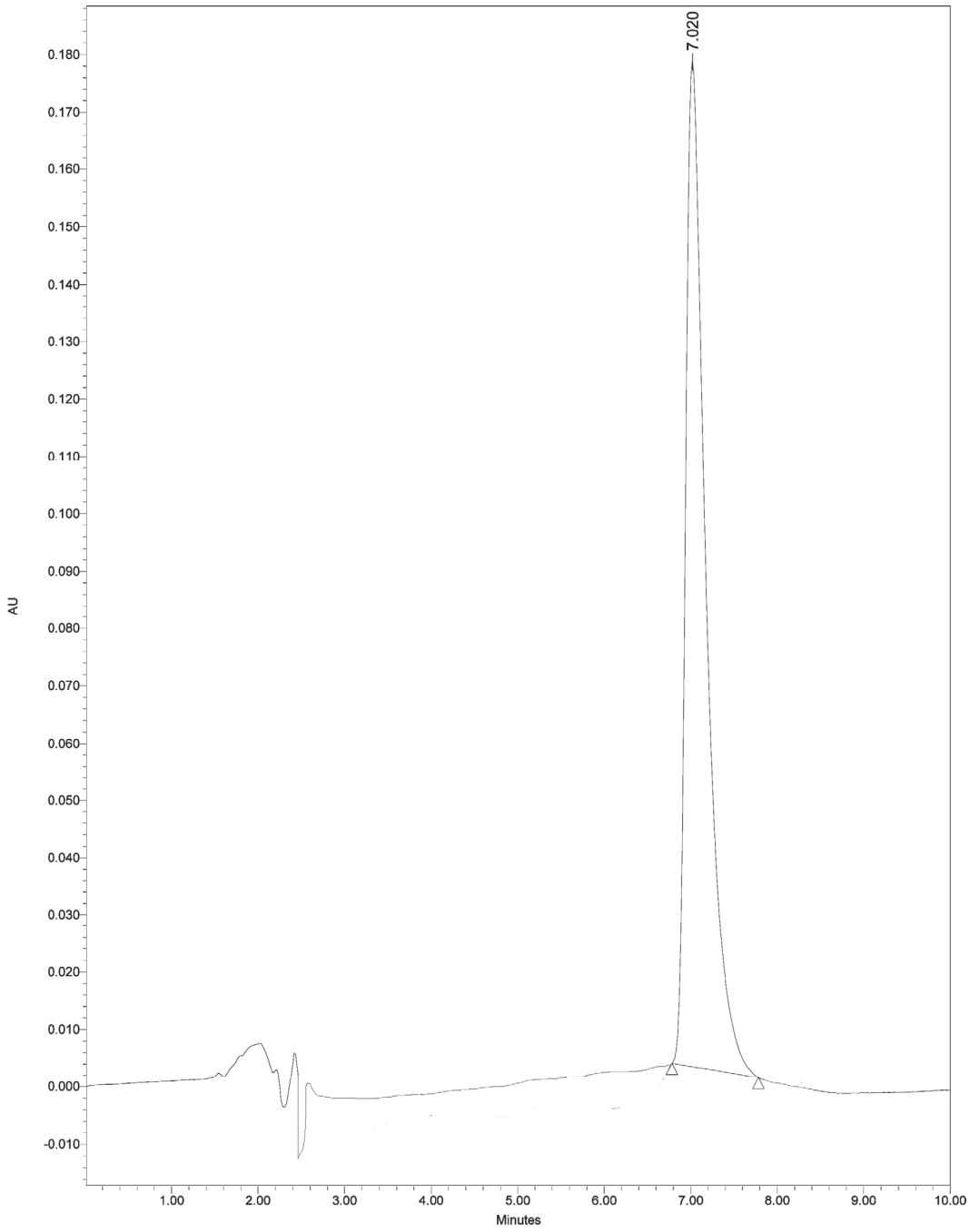

Figure S25. RP-HPLC trace of pure (**8**)

Table S19. NMR Resonance Assignments[a] of Peptide **3** in SDS-d_{25} 200mM Solution.

residue	NH ($^3J_{\alpha N}$, $-\Delta\delta/\Delta T$)[b]	$C^{\alpha}H$	$C^{\beta}H$	Others
D-Phe[2]		4.23	3.23, 3.10	7.26 (δ); 7.31(ε);
dhDsa-N[c]	8.02 (6.8, 6.7)	3.81	2.22	5.16(γ)
Phe[7]	7.00 (8.2, 6.2)	4.74	2.98	7.03(δ); 7.16(ε)
D-Trp[8]	8.09 (5.5, 6.5)	4.38	3.21, 3.09	7.21(δ);10.05, 7.68(ε);7.49, 7.14(ζ); 7.14(η)
Lys[9]	7.36 (5.9, 3.7)	4.09	1.44, 1.25	0.52, 0.43(γ); 1.39(δ); 2.76(ε)
Tyr(Bzl)[10]	7.67 (5.4, 2.6)	4.25	3.13, 2.87	7.09(δ); 6.89(ε);[d]
dhDsa-C[c]	7.15 (6.7, 3.0)	4.39	2.52, 2.23	5.27(γ)
Thr(ol)[15]	7.28 (6.9, 3.4)	3.80	3.95	1.15(γ); 3.68, 3.61 (ω)

[a]Obtained at 35 °C, pH = 5.5, with TSP (δ 0.00 ppm) as reference shift. Chemical shifts are accurate to ±0.02 ppm. [b] $^3J_{\alpha N}$ coupling constants in Hz. $-\Delta\delta/\Delta T$ = temperature coefficients (ppb/K). [c] dh-DSA-N: N-terminal portion of dehydrodiaminosuberic acid. dh-DSA-C: C-terminal portion of dehydrodiaminosuberic acid. [d] Other signals: CH_2: 5.09, 5.04, Arom: 7.44, 7.40, 7.30.

Table S20. NMR Resonance Assignments[a] of Peptide **4** in SDS-d_{25} 200mM Solution.

residue	NH ($^3J_{\alpha N}$, -Δδ/ΔT)[b]	$C^{\alpha}H$	$C^{\beta}H$	Others
D-Phe[2]		4.21	3.08; 3.29	7.25(δ); 7.32(ε)
dhDsa-N[c]	8.12 (8.2, 6.9)	3.79	2.32, 2.13	5.11(γ)
Phe[7]	6.94 (8.5, 5.3)	4.73	2.95, 2.90	6.84(δ); 7.02(ε)
D-Trp[8]	8.24 (4.7, 6.3)	4.61	3.34, 3.04	7.28(δ); 10.03, 7.89(ε); 7.50, 7.16(ζ); 7.15(η)
Lys[9]	7.51 (5.9, 4.7)	4.07	1.51, 1.37	0.68, 0.63(γ); 1.45 (δ); 2.82(ε); 7.37(ζ)
Tyr(Bzl)[10]	7.92 (6.5, 2.7)	4.41	3.09, 2.96	7.14(δ); 6.89(ε);[d]
dhDsa-C[c]	7.61 (7.1, 5.8)	4.27	2.44, 2.12	5.20(γ)
Thr(ol)[15]	7.40 (7.6, 5.4)	3.84	3.95	1.14(γ); 3.71, 3.63 (ω)

[a]Obtained at 35 °C, pH = 5.5, with TSP (δ 0.00 ppm) as reference shift. Chemical shifts are accurate to ±0.02 ppm. [b] $^3J_{\alpha N}$ coupling constants in Hz. -Δδ/ΔT = temperature coefficients (ppb/K). [c] dh-DSA-N: N-terminal portion of dehydrodiaminosuberic acid. dh-DSA-C: C-terminal portion of dehydrodiaminosuberic acid. [d] Other signals: CH_2: 5.03; Arom: 7.43, 7.39, 7.32.

Table S21. NMR Resonance Assignments[a] of Peptide **5** in SDS-d_{25} 200mM Solution.

residue	NH ($^3J_{\alpha N}$, $-\Delta\delta/\Delta T$)[b]	$C^{\alpha}H$	$C^{\beta}H$	Others
D-Phe[2]		4.24	3.24, 3.14	7.31(δ)
dhDsa-	7.96 (8.1, 7.9)	4.23	2.45, 2.29	5.29(γ)
1-Nal[7]	8.13 (7.5, 6.3)	4.73	3.54, 3.42	7.69(ζ); 8.18, 7.42(δ); 7.45(ε)
D-Trp[8]	7.31 (4.8, 6.3)	4.04	2.59, 2.28	6.88(δ);9.86, 7.07(ε);7.43, 6.98(ζ); 7.11(η)
Lys[9]	7.90 (6.2, 4.6)	3.88	1.50, 1.25	0.58, 0.32(γ); 1.33(δ); 2.69, 2.65(ε); 7.24(ζ)
Thr[10]	8.04 (6.1, 2.7)	4.04	4.22	1.25(γ)
dhDsa-	7.76 (7.5, 6.0)	4.36	2.41, 2.22	5.39(γ)
Thr(ol)[15]	7.26 (8.0, 6.4)	3.77	3.83	1.05(γ); 3.63, 3.53 (ω)

[a]Obtained at 35 °C, pH = 5.5, with TSP (δ 0.00 ppm) as reference shift. Chemical shifts are accurate to ±0.02 ppm. [b] $^3J_{\alpha N}$ coupling constants in Hz. $-\Delta\delta/\Delta T$ = temperature coefficients (ppb/K). [c] dh-DSA-N: N-terminal portion of dehydrodiaminosuberic acid. dh-DSA-C: C-terminal portion of dehydrodiaminosuberic acid.

Table S22. NMR Resonance Assignments[a] of Peptide **6** in SDS-d_{25} 200mM Solution.

residue	NH ($^3J_{\alpha N}$, $-\Delta\delta/\Delta T$)[b]	$C^{\alpha}H$	$C^{\beta}H$	Others
D-Phe[2]		4.21	3.24, 3.07	7.26(δ); 7.31(ε)
dhDsa-	7.87 (6.7, 7.7)	3.96	2.18	5.21(γ)
Phe[7]	7.27 (8.3, 6.7)	4.67	2.92	6.98(δ); 7.16(ε)
D-Trp[8]	7.81 (5.3, 6.6)	4.43	3.07, 2.97	7.11(δ); 10.01, 7.58(ε); 7.44, 7.08(ζ); 7.15(η)
Lys[9]	7.66 (6.0, 3.8)	3.95	1.31, 1.24	0.54, 0.36(γ); 1.34(δ); 2.71(ε); 7.31(ζ)
Tyr[10]	7.98 (5.3, 2.8)	4.22	3.04, 2.86	6.77(ε); 7.03(γ)
dhDsa-	7.27 (6.8, 3.1)	4.31	2.49, 2.30	5.33(γ)
Thr(ol)[15]	7.31 (6.9, 3.8)	3.78	3.94	1.14(γ); 3.66, 3.59 (ω)

[a]Obtained at 35 °C, pH = 5.5, with TSP (δ 0.00 ppm) as reference shift. Chemical shifts are accurate to ±0.02 ppm. [b] $^3J_{\alpha N}$ coupling constants in Hz. $-\Delta\delta/\Delta T$ = temperature coefficients (ppb/K). [c] dh-DSA-N: N-terminal portion of dehydrodiaminosuberic acid. dh-DSA-C: C-terminal portion of dehydrodiaminosuberic acid.

Table S23. NMR Resonance Assignments[a] of Peptide **7** in SDS-d_{25} 200mM Solution.

residue	NH ($^3J_{\alpha N}$, $-\Delta\delta/\Delta T$)[b]	$C^{\alpha}H$	$C^{\beta}H$	Others
D-Phe[2]		4.23	3.29, 3.10	7.28(δ); 7.34(ε)
dhDsa-	8.12 (8.2, 6.9)	3.80	2.42, 2.11	5.29(γ)
Phe[7]	6.97 (8.1, 6.6)	4.73	2.89, 2.76	6.67(δ); 6.95(ε); 7.03(ζ)
D-Trp[8]	8.16 (4.8, 6.8)	4.74	3.34, 3.00	7.29(δ); 9.99, 7.89(ε); 7.45, 7.18(ζ); 7.21(η)
Lys[9]	7.83 (6.9, 4.3)	3.94	1.41	0.74, 0.61(γ); 1.46(δ); 2.81(ε); 7.33(ζ)
Tyr[10]	8.36 (6.4, 2.6)	4.41	3.14, 2.88	7.12(δ); 6.79(ε)
dhDsa-	7.53 (7.2, 5.9)	4.28	2.49, 1.93	5.43(γ)
Thr(ol)[15]	7.44 (7.5, 5.5)	3.83	3.96	1.15(γ); 3.70, 3.61 (ω)

[a]Obtained at 35 °C, pH = 5.5, with TSP (δ 0.00 ppm) as reference shift. Chemical shifts are accurate to ±0.02 ppm. [b] $^3J_{\alpha N}$ coupling constants in Hz. $-\Delta\delta/\Delta T$ = temperature coefficients (ppb/K). [c] dh-DSA-N: N-terminal portion of dehydrodiaminosuberic acid. dh-DSA-C: C-terminal portion of dehydrodiaminosuberic acid.

Table S24. NMR Resonance Assignments[a] of Peptide **8** in SDS-d_{25} 200mM Solution.

residue	NH ($^3J_{\alpha N}$, -Δδ/ΔT)[b]	$C^{\alpha}H$	$C^{\beta}H$	Others
D-Phe[2]		4.26	3.30, 3.17	7.31(δ); 7.37(ε)
dhDsa-N[c]	8.12 (8.1, 6.8)	4.20	2.34	5.19(γ)
1-Nal[7]	7.60 (8.4, 5.4)	4.93	3.64, 3.53	7.67(ζ); 8.22, 7.31(δ); 7.80(ε)
D-Trp[8]	8.22 (4.8, 6.3)	4.10	3.03, 2.72	7.12(δ); 10.00, 7.46(ε); 7.51, 7.15(ζ); 7.14(η)
Lys[9]	6.64 (6.9, 4.6)	4.00	1.29, 0.93	0.22, 0.08(γ); 1.27(δ); 2.69(ε)
Tyr(Bzl)[10]	7.83 (6.5, 2.6)	4.43	3.06, 2.91	7.09(δ); 6.87(ε);[d]
dhDsa-C[c]	7.95 (7.1, 5.7)	4.44	2.45, 2.35	5.37(γ)
Thr(ol)[15]	7.51 (7.6, 5.9)	3.85	3.97	1.15(γ); 3.71, 3.62 (ω)

[a]Obtained at 35 °C, pH = 5.5, with TSP (δ 0.00 ppm) as reference shift. Chemical shifts are accurate to ±0.02 ppm. [b] $^3J_{\alpha N}$ coupling constants in Hz. -Δδ/ΔT = temperature coefficients (ppb/K). [c] dh-DSA-N: N-terminal portion of dehydrodiaminosuberic acid. dh-DSA-C: C-terminal portion of dehydrodiaminosuberic acid. [d] Other signals: CH_2: 5.05, 5.02, Arom: 7.47, 7.42, 7.35.

Table S25. NOE Derived Upper Limit Constraints of Compound **3**

Atom1	Atom2	Upper Limit	Violation
2 DPHE HA	3 DHS HN	2.52	
2 DPHE HB2	3 DHS HN	5.31	
2 DPHE HB3	3 DHS HN	5.31	
2 DPHE QB	3 DHS HN	4.49	
3 DHS HN	3 DHS QB	3.84	
3 DHS HA	14 DHS HG	4.60	
3 DHS HA	7 PHE HN	2.40	
3 DHS HG	14 DHS HA	3.58	
3 DHS HG	14 DHS QB	3.21	
7 PHE HN	10 TBZ HB2	2.99	
7 PHE HA	8 DTRP HN	2.83	
7 PHE QB	8 DTRP HN	3.93	
7 PHE QD	8 DTRP HN	6.69	
8 DTRP HN	8 DTRP HB2	2.86	
8 DTRP HN	8 DTRP HB3	2.86	
8 DTRP HN	8 DTRP QB	2.64	
8 DTRP HN	8 DTRP HD1	5.50	
8 DTRP HA	8 DTRP HD1	4.97	
8 DTRP HA	8 DTRP HE3	2.70	
8 DTRP HA	9 LYS HN	2.40	
8 DTRP HB2	8 DTRP HD1	3.70	
8 DTRP HB2	8 DTRP HE3	4.19	
8 DTRP HB2	9 LYS HN	4.60	
8 DTRP HB3	8 DTRP HD1	3.70	
8 DTRP HB3	8 DTRP HE3	4.19	
8 DTRP HB3	9 LYS HN	4.60	
8 DTRP QB	8 DTRP HD1	3.13	
8 DTRP QB	8 DTRP HE3	3.70	
8 DTRP QB	9 LYS HN	4.18	
8 DTRP HD1	9 LYS QG	6.38	
8 DTRP HE1	9 LYS QG	6.38	
8 DTRP HE1	9 LYS QD	6.38	
8 DTRP HE1	9 LYS QE	6.38	
8 DTRP HE1	15 THO HA	5.50	
8 DTRP HZ2	9 LYS QE	6.38	
9 LYS HN	9 LYS HA	2.91	
9 LYS HN	9 LYS HB2	2.60	
9 LYS HN	9 LYS HB3	3.74	
9 LYS HN	9 LYS HG2	3.45	
9 LYS HN	9 LYS HG3	3.45	
9 LYS HN	9 LYS QG	3.21	
9 LYS HN	10 TBZ HN	3.03	
9 LYS HA	9 LYS HG2	3.76	
9 LYS HA	9 LYS HG3	3.76	
9 LYS HA	9 LYS QG	3.35	
9 LYS HA	9 LYS QD	6.38	

9 LYS HA	10 TBZ HN	3.56	
9 LYS HA	15 THO HN	4.80	
9 LYS HA	15 THO QG2	6.53	
9 LYS HB2	10 TBZ HN	3.54	
9 LYS HB2	10 TBZ QD	7.64	
9 LYS HB3	10 TBZ HN	3.69	
9 LYS HB3	10 TBZ QD	7.64	
9 LYS HG2	10 TBZ HN	5.50	
9 LYS HG3	10 TBZ HN	5.50	
9 LYS QG	10 TBZ QE	8.51	
10 TBZ HN	10 TBZ HB2	2.63	
10 TBZ HN	10 TBZ HB3	3.60	
10 TBZ HN	10 TBZ QE	6.83	
10 TBZ HN	14 DHS HN	2.60	
10 TBZ HN	15 THO HN	4.83	
10 TBZ HA	14 DHS HN	3.35	0.10
14 DHS HN	14 DHS HA	2.91	
14 DHS HN	14 DHS HB2	3.02	
14 DHS HN	14 DHS HB3	3.90	
14 DHS HN	14 DHS HG	5.07	
14 DHS HA	14 DHS HG	4.04	
14 DHS HA	15 THO HN	3.50	
14 DHS HB2	15 THO HN	3.72	
14 DHS HB3	15 THO HN	4.49	
15 THO HN	15 THO HA	2.85	
15 THO HN	15 THO HB	3.05	
15 THO HA	15 THO HB	2.40	

3 DHS: N-terminal portion of dehydrodiaminosuberic acid. 14 DHS: C-terminal portion of dehydrodiaminosuberic acid.
TBZ: Tyr(Bzl). THO: Threoninol. [b] Violations (Å) observed for the mean structure of the ensemble.

Table S26. NOE derived Upper Limit Constraints. Compound **4**

Atom1[a]	Atom2	Upper Limit	Violation[b]		
			Helix	Extend	Ensemble
2 DPHE HA	3 DHS HN	2.59			
2 DPHE QD	3 DHS HA	7.62			
3 DHS HN	3 DHS HB2	3.24			
3 DHS HN	3 DHS HB3	3.24			
3 DHS HN	3 DHS QB	3.02			
3 DHS HA	3 DHS HB2	2.74			
3 DHS HA	3 DHS HB3	2.74			
3 DHS HA	3 DHS QB	2.48			
3 DHS HA	3 DHS HG	3.75		0.40	
3 DHS HA	14 DHS HG	5.10			
3 DHS HA	7 PHE HN	2.40			
3 DHS HA	7 PHE QD	7.62			
3 DHS HA	14 DHS HA	3.30	1.20		0.28
3 DHS QB	3 DHS HG	2.75			
3 DHS HG	14 DHS HA	4.72			
7 PHE HN	7 PHE HB2	3.73			
7 PHE HN	7 PHE HB3	3.73			
7 PHE HN	7 PHE QB	3.35			
7 PHE HN	14 DHS HA	4.01	1.38		0.39
7 PHE HA	8 DTRP HN	2.49			
7 PHE QB	8 DTRP HN	3.93			
7 PHE QD	8 DTRP HN	7.28			
8 DTRP HN	8 DTRP HB2	2.68			
8 DTRP HN	8 DTRP HB3	2.68			
8 DTRP HN	8 DTRP QB	2.42			
8 DTRP HN	8 DTRP HD1	5.28			
8 DTRP HA	8 DTRP HE3	2.83			
8 DTRP HA	9 LYS HN	2.40			
8 DTRP HA	10 TBZ HN	3.83			
8 DTRP HB2	8 DTRP HD1	3.70			
8 DTRP HB2	8 DTRP HE3	4.22			
8 DTRP HB2	9 LYS HN	4.40			
8 DTRP HB3	8 DTRP HD1	3.70			
8 DTRP HB3	8 DTRP HE3	4.22			
8 DTRP HB3	9 LYS HN	4.40			
8 DTRP QB	8 DTRP HD1	3.16			
8 DTRP QB	9 LYS HN	4.20			
8 DTRP QB	8 DTRP HE3	3.60			
8 DTRP HD1	9 LYS QG	6.38			
8 DTRP HE3	9 LYS HN	4.01			
9 LYS HN	9 LYS HB2	2.50			
9 LYS HN	9 LYS HB3	3.70			
9 LYS HN	9 LYS QG	3.49			
9 LYS HN	10 TBZ HN	3.00			
9 LYS HA	9 LYS HG2	3.83			
9 LYS HA	9 LYS HG3	3.83			

9 LYS HA	9 LYS QG	3.32			
9 LYS HA	10 TBZ HN	3.46			
9 LYS HA	15 THO HN	5.44		2.80	0.46
9 LYS HA	15 THO QG2	6.53		2.10	0.33
9 LYS HB2	10 TBZ HN	3.60	0.74		
9 LYS HB3	10 TBZ HN	4.10	0.20		
9 LYS QG	10 TBZ HN	6.38			
9 LYS QG	10 TBZ QD	7.52		1.02	
10 TBZ HN	10 TBZ HB2	2.83			
10 TBZ HN	10 TBZ HB3	3.14			
10 TBZ HN	14 DHS HN	2.95		0.36	
10 TBZ HA	14 DHS HN	2.62	0.82		0.27
10 TBZ HA	15 THO HN	5.31			
10 TBZ HB2	14 DHS HN	4.01		0.40	
10 TBZ HB3	14 DHS HN	3.86		0.58	
10 TBZ QD	14 DHS HN	6.68			
10 TBZ QD	14 DHS HA	6.05	0.74		
10 TBZ QD	15 THO QG2	7.27	0.52		
14 DHS HN	14 DHS HB2	2.52			
14 DHS HN	14 DHS HB3	3.29	0.43		
14 DHS HN	14 DHS HG	5.01			
14 DHS HN	15 THO HN	3.16		1.16	0.12
14 DHS HA	14 DHS HG	3.76			
14 DHS HA	15 THO HN	2.65	0.59		
14 DHS HB2	15 THO HN	3.83		0.77	
14 DHS HB3	15 THO HN	4.41			
15 THO HN	15 THO HB	3.70			
15 THO HN	15 THO QG2	4.61			
15 THO HA	15 THO HB	2.54			

[a] 3 DHS: N-terminal portion of dehydrodiaminosuberic acid. 14 DHS: C-terminal portion of dehydrodiaminosuberic acid. TBZ: Tyr(Bzl). THO: Threoninol.
[b] Violations (Å) observed for the mean structure of the family I (helix), family II (extended) and an ensemble of 20 structures of both families (ensemble).

Table S27. NOE Derived Upper Limit Constraints of Compound **5**

Atom1[a]	Atom2	Upper Limit	Violation		
			Helix	Extend	Ensemble
2 DPHE HA	3 DHS HN	2.40			
2 DPHE HB2	3 DHS HN	3.86			
2 DPHE HB3	3 DHS HN	3.86			
2 DPHE QB	3 DHS HN	3.62			
2 DPHE QD	3 DHS HN	7.62			
3 DHS HN	3 DHS HB2	3.24			
3 DHS HN	3 DHS HB3	3.24			
3 DHS HN	3 DHS QB	3.24			
3 DHS HN	3 DHS HG	4.35			
3 DHS HN	7 NAL HN	3.79			
3 DHS HA	3 DHS HG	3.48		0.66	
3 DHS HA	14 DHS HG	4.38			
3 DHS HA	7 NAL HN	2.43			
3 DHS HA	14 DHS HA	3.25	1.25		0.32
3 DHS QB	14 DHS HN	5.77			
3 DHS HG	7 NAL HN	5.50			
3 DHS HG	14 DHS HA	4.88			
3 DHS HG	14 DHS QB	4.31			
7 NAL HN	7 NAL HB2	2.71			
7 NAL HN	7 NAL HB3	2.74			
7 NAL HN	7 NAL HD1	5.50			
7 NAL HN	8 DTRP HN	4.48			
7 NAL HN	14 DHS HA	3.82	1.57		0.46
7 NAL HN	14 DHS QB	5.00			
7 NAL HA	8 DTRP HN	2.40			
7 NAL HB2	7 NAL HD1	2.74			
7 NAL HB2	7 NAL HD3	2.49			
7 NAL HB2	8 DTRP HN	4.11			
7 NAL HB3	7 NAL HD1	2.86			
7 NAL HB3	7 NAL HD3	2.52			
7 NAL HB3	8 DTRP HN	3.92			
7 NAL HZ	8 DTRP HE3	5.50			
7 NAL HE3	8 DTRP HE3	5.50			
7 NAL HD3	8 DTRP HN	4.82			
8 DTRP HN	8 DTRP HB2	2.83			
8 DTRP HN	8 DTRP HB3	2.83			
8 DTRP HN	8 DTRP QB	2.53			
8 DTRP HN	8 DTRP HD1	5.50			
8 DTRP HA	8 DTRP HD1	4.82			
8 DTRP HA	8 DTRP HE3	3.02			
8 DTRP HA	9 LYS HN	2.43			
8 DTRP HB2	9 LYS HN	4.32			
8 DTRP HB3	9 LYS HN	4.32			
8 DTRP QB	8 DTRP HE3	4.38			
8 DTRP QB	9 LYS HN	3.80			
8 DTRP HD1	9 LYS HN	5.50			

8 DTRP HE3	9 LYS HN	5.16			
8 DTRP HE3	9 LYS HA	5.37			
8 DTRP HE1	9 LYS QG	6.38			
8 DTRP HE1	9 LYS QD	6.38			
8 DTRP HZ2	9 LYS QD	6.38			
9 LYS HN	9 LYS HB2	2.60			
9 LYS HN	9 LYS HB3	3.71			
9 LYS HN	9 LYS HG2	4.14			
9 LYS HN	9 LYS HG3	4.14			
9 LYS HN	9 LYS QG	3.71			
9 LYS HN	10 THR HN	2.77			
9 LYS HA	9 LYS QG	3.91			
9 LYS HA	9 LYS QD	6.38			
9 LYS HA	10 THR HN	3.33			
9 LYS HA	14 DHS HN	5.50			
9 LYS HA	15 THO HN	5.35		2.90	0.41
9 LYS QB	10 THR HN	5.51			
10 THR HN	10 THR HA	2.90			
10 THR HN	10 THR HB	3.21			
10 THR HN	14 DHS HN	2.89		0.42	
10 THR HA	10 THR HB	2.83			
10 THR HA	14 DHS HN	2.57	0.88		0.31
10 THR HA	15 THO HN	5.34			
10 THR HB	14 DHS HN	3.61			
10 THR QG2	14 DHS HN	6.53			
14 DHS HN	14 DHS HB2	2.86			
14 DHS HN	14 DHS HB3	3.39	0.33		
14 DHS HN	14 DHS HG	4.85			
14 DHS HN	15 THO HN	3.22		1.20	0.14
14 DHS HA	14 DHS HG	3.86			
14 DHS HA	15 THO HN	2.55	0.68		
14 DHS HB2	15 THO HN	3.80		0.80	
14 DHS HB3	15 THO HN	4.39			
15 THO HN	15 THO HB	3.58			
15 THO HA	15 THO HB	2.40			

[a] 3 DHS: N-terminal portion of dehydrodiaminosuberic acid. 14 DHS: C-terminal portion of dehydrodiaminosuberic acid. NAL: 1-naphtylalanine. THO: Threoninol. [b] Violations (Å) observed for the mean structure of the family I (helix), family II (extended) and an ensemble of 20 structures of both families (ensemble).

Table S28. NOE Derived Upper Limit Constraints of Compound **8**

Atom1[a]	Atom2	Upper Limit	Violation		
			Helix	Extend	Ensemble
2 DPHE HA	3 DHS HN	2.52			
3 DHS HA	3 DHS HG	3.64		0.53	
3 DHS HA	7 NAL HN	2.71			
3 DHS HA	14 DHS HA	3.31	1.19		0.30
3 DHS HG	7 NAL HN	5.50			
3 DHS HG	14 DHS HB2	4.42			
7 NAL HN	7 NAL HB2	3.39			
7 NAL HN	7 NAL HB3	3.45			
7 NAL HN	14 DHS HA	3.87	1.52		0.19
7 NAL HA	7 NAL HD1	3.95			
7 NAL HA	8 DTRP HN	2.46			
7 NAL HB2	7 NAL HD1	3.08			
7 NAL HB3	7 NAL HD1	3.05			
8 DTRP HN	8 DTRP HB2	2.83			
8 DTRP HN	8 DTRP HB3	2.83			
8 DTRP HN	8 DTRP QB	2.53			
8 DTRP HN	8 DTRP HD1	5.06			
8 DTRP HA	8 DTRP HD1	4.98			
8 DTRP HA	8 DTRP HE3	2.71			
8 DTRP HA	9 LYS HN	2.59			
8 DTRP HA	10 TBZ HN	3.76			
8 DTRP HA	10 TBZ QD	7.64			
8 DTRP HA	10 TBZ QE	7.63			
8 DTRP HB2	8 DTRP HD1	3.45			
8 DTRP HB2	8 DTRP HE3	4.04			
8 DTRP HB2	9 LYS HN	4.11			
8 DTRP HB3	8 DTRP HD1	3.45			
8 DTRP HB3	8 DTRP HE3	4.04			
8 DTRP HB3	9 LYS HN	4.11			
8 DTRP QB	8 DTRP HD1	3.26			
8 DTRP QB	9 LYS HN	3.93			
8 DTRP HD1	9 LYS HG2	5.22			
8 DTRP HD1	9 LYS HG3	5.22			
8 DTRP HD1	9 LYS QG	4.92			
8 DTRP HE3	9 LYS HN	4.11			
8 DTRP HE3	9 LYS QG	6.38			
8 DTRP HE3	10 TBZ QE	7.51	0.38		
8 DTRP HE1	9 LYS QD	6.38			
8 DTRP HE1	9 LYS QE	6.38			
8 DTRP HZ2	9 LYS QE	6.38			
9 LYS HN	9 LYS HB2	2.61			
9 LYS HN	9 LYS HB3	3.69			
9 LYS HN	9 LYS HG2	4.11			
9 LYS HN	9 LYS HG3	4.11			
9 LYS HN	9 LYS QG	3.84			
9 LYS HN	10 TBZ HN	2.93			

9 LYS HN	10 TBZ QD	7.64			
9 LYS HA	9 LYS QG	3.88			
9 LYS HA	9 LYS QD	5.45			
9 LYS HA	10 TBZ HN	3.45			
9 LYS HA	14 DHS HN	5.00			
9 LYS HA	15 THO HN	5.50		2.76	0.48
9 LYS HA	15 THO QG2	6.51		2.10	0.35
9 LYS HB2	10 TBZ HN	3.66	0.68		
9 LYS HB3	10 TBZ HN	4.16	0.20		
9 LYS QB	10 TBZ QD	8.52			
9 LYS QG	10 TBZ HN	5.50			
9 LYS QG	10 TBZ QE	7.63			
10 TBZ HN	10 TBZ HB2	2.90			
10 TBZ HN	10 TBZ HB3	3.57			
10 TBZ HN	10 TBZ QE	7.63			
10 TBZ HN	14 DHS HN	2.98		0.34	
10 TBZ HA	10 TBZ HB2	2.93			
10 TBZ HA	10 TBZ HB3	2.74			
10 TBZ HA	14 DHS HN	2.64	0.82		0.23
10 TBZ HB2	14 DHS HN	3.95		0.46	
10 TBZ HB3	14 DHS HN	3.82		0.63	
14 DHS HN	14 DHS HB2	2.96			
14 DHS HN	14 DHS HB3	3.39	0.33		
14 DHS HN	14 DHS HG	4.51			
14 DHS HN	15 THO HN	3.21		1.21	0.13
14 DHS HA	14 DHS HB2	2.93			
14 DHS HA	14 DHS HB3	2.83			
14 DHS HA	14 DHS HG	3.81			
14 DHS HA	15 THO HN	2.66	0.58		
14 DHS HB2	15 THO HN	3.86		0.75	
14 DHS HB3	15 THO HN	4.43			
15 THO HN	15 THO HB	3.58			
15 THO HN	15 THO QG2	4.88			
15 THO HA	15 THO HB	2.40			

[a] 3 DHS: N-terminal portion of dehydrodiaminosuberic acid. 14 DHS: C-terminal portion of dehydrodiaminosuberic acid. NAL: 1-naphtylalanine. TBZ: Tyr(Bzl). THO: Threoninol. [b] Violations (Å) observed for the mean structure of the family I (helix), family II (extended) and an ensemble of 20 structures of both families (ensemble).

Table S29. Microanalysis data for the all final products

		Found (%)				Calculated (%)			
Comp.	Formula	C	H	N	S	C	H	N	S
11a	$C_{16}H_{11}F_3N_2O_5S$	48.00	2.77	7.00	8.01	48.15	2.89	7.05	8.08
11b	$C_{17}H_{13}F_3N_2O_5S$	49.28	3.16	6.76	7.74	49.39	3.03	6.66	7.63
11c	$C_{23}H_{17}F_3N_2O_5S$	56.32	3.49	5.71	6.54	56.24	3.59	5.74	6.63
11d	$C_{22}H_{21}F_6N_3O_7S$	45.13	3.62	7.18	5.48	45.01	3.70	7.21	5.51
11e	$C_{19}H_{15}F_3N_2O_5S$	51.82	3.43	6.36	7.28	51.68	3.47	6.27	7.41
11f	$C_{17}H_{13}F_3N_2O_5S$	49.28	3.16	6.76	7.74	49.13	3.12	6.84	7.87
11g	$C_{14}H_9NO_4S$	58.53	3.16	4.88	11.16	58.42	3.25	4.97	10.98
11h	$C_{18}H_{19}ClN_2O_3S$	57.06	5.05	7.39	8.46	56.96	5.14	7.30	8.59
11i	$C_{18}H_{17}ClN_2O_4S$	55.03	4.36	7.13	8.16	55.00	4.40	7.16	8.24
11j	$C_{14}H_9NO_3S_2$	55.43	2.99	4.62	21.14	55.35	2.95	4.69	21.26
11k	$C_{18}H_{21}Cl_2N_3O_3S$	50.24	4.92	9.76	7.45	50.12	5.01	9.69	7.58
11l	$C_{15}H_{11}NO_4S$	59.79	3.68	4.65	10.64	59.68	3.63	4.72	10.71
11m	$C_{19}H_{21}ClN_2O_3S$	58.08	5.39	7.13	8.16	57.98	5.44	7.02	8.29
11n	$C_{19}H_{19}ClN_2O_4S$	56.09	4.71	6.88	7.88	56.00	4.76	6.78	8.01
11o	$C_{15}H_{11}NO_3S_2$	56.76	3.49	4.41	20.21	56.64	3.55	4.30	20.34
11p	$C_{19}H_{23}Cl_2N_3O_3S$	51.35	5.22	9.46	7.22	51.42	5.24	9.39	7.36
11q	$C_{16}H_{14}N_2O_3S$	61.13	4.49	8.91	10.20	61.18	4.53	8.82	10.31
11r	$C_{17}H_{18}ClN_3O_3S$	53.75	4.78	11.06	8.44	53.83	4.68	11.11	8.38

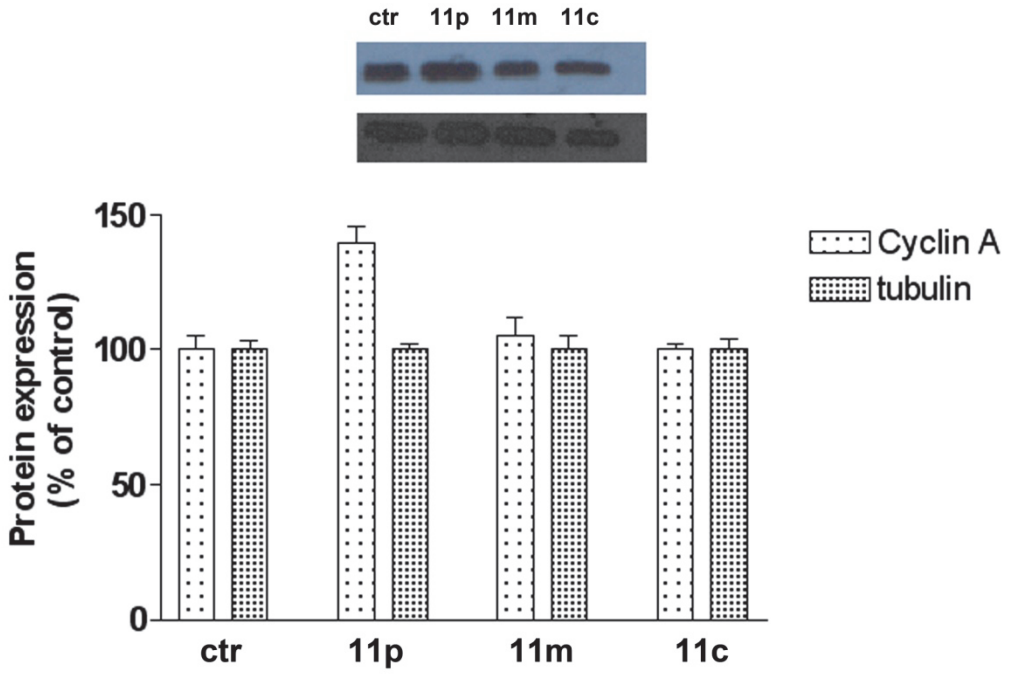

Figure S26. Expression of cyclin A in control cells and upon treatment with 11p, 11m, and 11c (1 μM) for 48h

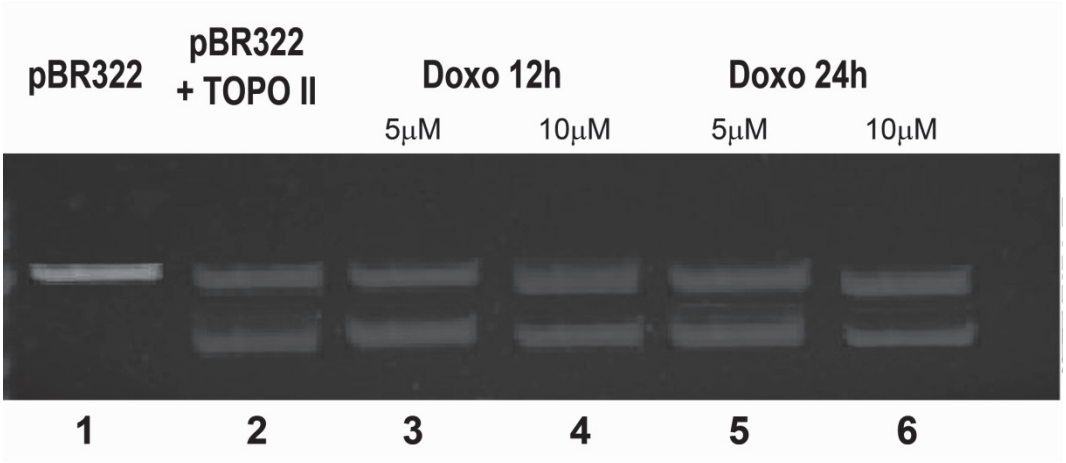

Figure S27. Effects of doxorubicin on the topo II-mediated DNA cleavage

References

[1] D. Pearson, J.E. Shively, B.R. Clark, I.I. Geschwind, M. Barkley, R.S. Nishioka, H.A. Bern, Urotensin II: a Somatostain-like Peptide in the Caudal Neurosecretory System of Fishes, Proc Natl Acad Sci U S A, 77 (**1980**) 5021-5024.

[2] J.M. Conlon, F. O'Harte, D.D. Smith, M.C. Tonon, H. Vaudry, Isolation and primary structure of urotensin II from the brain of a tetrapod, the frog Rana ridibunda, Biochem Biophys Res Commun, 188 (**1992**) 578-583.

[3] Y. Coulouarn, I. Lihrmann, S. Jegou, Y. Anouar, H. Tostivint, J.C. Beauvillain, J.M. Conlon, H.A. Bern, H. Vaudry, Cloning of the cDNA encoding the urotensin II precursor in frog and human reveals intense expression of the urotensin II gene in motoneurons of the spinal cord, Proc Natl Acad Sci U S A, 95 (**1998**) 15803-15808.

[4] Y. Coulouarn, S. Jegou, H. Tostivint, H. Vaudry, I. Lihrmann, Cloning, sequence analysis and tissue distribution of the mouse and rat urotensin II precursors, FEBS Lett, 457 (**1999**) 28-32.

[5] M. Mori, T. Sugo, M. Abe, Y. Shimomura, M. Kurihara, C. Kitada, K. Kikuchi, Y. Shintani, T. Kurokawa, H. Onda, O. Nishimura, M. Fujino, Urotensin II is the Endogenous Ligand of a G-protein Coupled Orphan Receptor, SENR (GPR14), Biochem Biophys Res Commun, 265 (**1999**) 123-129.

[6] N.A. Elshourbagy, S.A. Douglas, U. Shabon, S. Harrison, G. Duddy, J.L. Sechler, Z. Ao, B.E. Maleeff, D. Naselsky, J. Disa, N.V. Aiyar, Molecular and pharmacological characterization of genes encoding urotensin-II peptides and their cognate G-protein-coupled receptors from the mouse and monkey, Br J Pharmacol, 136 (**2002**) 9-22.

[7] R.S. Ames, H.M. Sarau, J.K. Chambers, R.N. Willette, N.V. Aiyar, A.M. Romanic, C.S. Louden, J.J. Foley, C.F. Sauermelch, R.W. Coatney, Z. Ao, J. Disa, S.D. Holmes, J.M. Stadel, J.D. Martin, W.S. Liu, G.I. Glover, S. Wilson, D.E. McNulty, C.E. Ellis, N.A. Elshourbagy, U. Shabon, J.J. Trill, D.W. Hay, E.H. Ohlstein, D.J. Bergsma, S.A. Douglas, Human urotensin-II is a potent vasoconstrictor and agonist for the orphan receptor GPR14, Nature, 401 (**1999**) 282-286.

[8] T. Sugo, Y. Murakami, Y. Shimomura, M. Harada, M. Abe, Y. Ishibashi, C. Kitada, N. Miyajima, N. Suzuki, M. Mori, M. Fujino, Identification of urotensin II-related peptide as the urotensin II-immunoreactive molecule in the rat brain, Biochem Biophys Res Commun, 310 (**2003**) 860-868.

[9] D. Chatenet, C. Dubessy, J. Leprince, C. Boularan, L. Carlier, I. Segalas-Milazzo, L. Guilhaudis, H. Oulyadi, D. Davoust, E. Scalbert, B. Pfeiffer, P. Renard, M.C. Tonon, I. Lihrmann, P. Pacaud, H. Vaudry, Structure-activity relationships and structural conformation of a novel urotensin II-related peptide, Peptides, 25 (**2004**) 1819-1830.

[10] N. Chartrel, J.M. Conlon, F. Collin, B. Braun, D. Waugh, M. Vallarino, S.L. Lahrichi, J.E. Rivier, H. Vaudry, Urotensin II in the central nervous system of the frog Rana ridibunda: immunohistochemical localization and biochemical characterization, J Comp Neurol, 364 (**1996**) 324-339.

[11] Y. Coulouarn, C. Fernex, S. Jegou, C.E. Henderson, H. Vaudry, I. Lihrmann, Specific expression of the urotensin II gene in sacral motoneurons of developing rat spinal cord, Mech Dev, 101 (**2001**) 187-190.

[12] G. Pelletier, I. Lihrmann, H. Vaudry, Role of androgens in the regulation of urotensin II precursor mRNA expression in the rat brainstem and spinal cord, Neuroscience, 115 (**2002**) 525-532.

[13] G. Pelletier, I. Lihrmann, C. Dubessy, V. Luu-The, H. Vaudry, F. Labrie, Androgenic down-regulation of urotensin II precursor, urotensin II-related peptide precursor and androgen receptor mRNA in the mouse spinal cord, Neuroscience, 132 (**2005**) 689-696.
[14] E. Novellino, P. Grieco, M. Caraglia, A. Budillon, R. Franco, S.R. Addeo, Peptidic and non Peptidic Ligands for Immunodetection of Urotensin-II Receptor., PCT Int. Appl., (**2008**) 21pp WO 2008095995.
[15] J.J. Maguire, A.P. Davenport, Is Urotensin-II the New Endothelin? , Br J Pharmacol, 137 (**2002**) 579-588.
[16] S.A. Douglas, E.H. Ohlstein, Human Urotensin-II, the Most Potent Mammalian Vasoconstrictor Identified to Date, as a Therapeutic Target for the Management of Cardivascular Diseases, Trends Cardiovasc Med 10 (**2000**) 229-237.
[17] S.A. Douglas, Human Urotensin-II as a Novel Cardiovascular Target: "Heart" of the Matter or Simply a Fish "Tail?", Curr Opin Pharmacol, 3 (**2003**) 159-167.
[18] R.A. Silvestre, E.M. Egido, R. Hernandez, J. Leprince, D. Chatenet, H. Tollemer, N. Chartrel, H. Vaudry, J. Marco, Urotensin-II is present in pancreatic extracts and inhibits insulin release in the perfused rat pancreas, Eur J Endocrinol, 151 (**2004**) 803-809.
[19] T. Djordjevic, R.S. BelAiba, S. Bonello, J. Pfeilschifter, J. Hess, A. Gorlach, Human urotensin II is a novel activator of NADPH oxidase in human pulmonary artery smooth muscle cells, Arterioscler Thromb Vasc Biol, 25 (**2005**) 519-525.
[20] Y. Matsumoto, M. Abe, T. Watanabe, Y. Adachi, T. Yano, H. Takahashi, T. Sugo, M. Mori, C. Kitada, T. Kurokawa, M. Fujino, Intracerebroventricular administration of urotensin II promotes anxiogenic-like behaviors in rodents, Neurosci Lett, 358 (**2004**) 99-102.
[21] H. Itoh, D. McMaster, K. Lederis, Functional receptors for fish neuropeptide urotensin II in major rat arteries, Eur J Pharmacol, 149 (**1988**) 61-66.
[22] S. Flohr, M. Kurz, E. Kostenis, A. Brkovich, A. Fournier, T. Klabunde, Identification of nonpeptidic urotensin II receptor antagonists by virtual screening based on a pharmacophore model derived from structure-activity relationships and nuclear magnetic resonance studies on urotensin II, J Med Chem, 45 (**2002**) 1799-1805.
[23] W.A. Kinney, H.R. Almond Jr, J. Qi, C.E. Smith, R.J. Santulli, L. de Garavilla, P. Andrade-Gordon, D.S. Cho, A.M. Everson, M.A. Feinstein, P.A. Leung, B.E. Maryanoff, Structure-function analysis of urotensin II and its use in the construction of a ligand-receptor working model, Angew Chem Int Ed Engl, 41 (**2002**) 2940-2944.
[24] A. Brkovic, A. Hattenberger, E. Kostenis, T. Klabunde, S. Flohr, M. Kurz, S. Bourgault, A. Fournier, Functional and binding characterizations of urotensin II-related peptides in human and rat urotensin II-receptor assay, J Pharmacol Exp Ther, 306 (**2003**) 1200-1209.
[25] P. Labarrere, D. Chatenet, J. Leprince, C. Marionneau, G. Loirand, M.C. Tonon, C. Dubessy, E. Scalbert, B. Pfeiffer, P. Renard, B. Calas, P. Pacaud, H. Vaudry, Structure-activity relationships of human urotensin II and related analogues on rat aortic ring contraction, J Enzyme Inhib Med Chem, 18 (**2003**) 77-88.
[26] D.H. Coy, W.J. Rossowski, B.L. Cheng, J.E. Taylor, Structural requirements at the N-terminus of urotensin II octapeptides, Peptides, 23 (**2002**) 2259-2264.

[27] E. Lescot, R. Bureau, S. Rault, Nonpeptide Urotensin-II receptor agonists and antagonists: review and structure-activity relationships, Peptides, 29 (**2008**) 680-690.
[28] V.J. Hruby, Designing Peptide Receptors Agonists and Antagonists, Nature Review Drug Discovery, 1 (**2002**) 847-858.
[29] A. Carotenuto, P. Grieco, P. Rovero, E. Novellino, Urotensin-II receptor antagonists, Curr Med Chem, 13 (**2006**) 267-275.
[30] P. Grieco, A. Carotenuto, P. Campiglia, E. Zampelli, R. Patacchini, C.A. Maggi, E. Novellino, P. Rovero, A new, potent urotensin II receptor peptide agonist containing a Pen residue at the disulfide bridge, J Med Chem, 45 (**2002**) 4391-4394.
[31] R. Patacchini, P. Santicioli, S. Giuliani, P. Grieco, E. Novellino, P. Rovero, C.A. Maggi, Urantide: an ultrapotent urotensin II antagonist peptide in the rat aorta, Br J Pharmacol, 140 (**2003**) 1155-1158.
[32] V. Camarda, W. Song, E. Marzola, M. Spagnol, R. Guerrini, S. Salvadori, D. Regoli, J.P. Thompson, D.J. Rowbotham, D.J. Behm, S.A. Douglas, G. Calo, D.G. Lambert, Urantide mimics urotensin-II induced calcium release in cells expressing recombinant UT receptors, Eur J Pharmacol, 498 (**2004**) 83-86.
[33] P. Grieco, A. Carotenuto, P. Campiglia, L. Marinelli, T. Lama, R. Patacchini, P. Santicioli, C.A. Maggi, P. Rovero, E. Novellino, Urotensin-II receptor ligands. From agonist to antagonist activity, J Med Chem, 48 (**2005**) 7290-7297.
[34] A. Carotenuto, P. Grieco, P. Campiglia, E. Novellino, P. Rovero, Unraveling the active conformation of urotensin II, J Med Chem, 47 (**2004**) 1652-1661.
[35] J.M. Stewart, J.D. Yang, Solid Phase Peptide Synthesis, Pierce Chemical, Rockford, IL, **1984**.
[36] K. Wüthrich, NMR of Proteins and Nucleic Acids, John Wiley & Sons, Inc, New York, **1986**.
[37] U. Piantini, O.W. Sorensen, R.R. Ernst, Multiple quantum filters for elucidating NMR coupling network, J Am Chem Soc, 104 (**1982**) 6800-68001.
[38] D. Marion, K. Wuthrich, Application of phase sensitive two-dimensional correlated spectroscopy (COSY) for measurements of 1H-1H spin-spin coupling constants in proteins, Biochem Biophys Res Commun, 113 (**1983**) 967-974.
[39] L. Braunschweiler, R.R. Ernst, Coherence transfer by isotropic mixing: application to proton correlation spectroscopy, J Magn Reson, 53 (**1983**) 521-528.
[40] J. Jenner, B.H. Meyer, P. Bachman, R.R. Ernst, Investigation of exchange processes by two-dimensional NMR spectroscopy, J Chem Phys, 71 (**1979**) 4546-4553.
[41] C. Bartels, T.H. Xia, M. Billeter, P. Guntert, K. Wuthrich, The Program Xeasy for Computer-Supported Nmr Spectral-Analysis of Biological Macromolecules, J Biomol Nmr, 6 (**1995**) 1-10.
[42] K. Palczewski, T. Kumasaka, T. Hori, C.A. Behnke, H. Motoshima, B.A. Fox, I. Le Trong, D.C. Teller, T. Okada, R.E. Stenkamp, M. Yamamoto, M. Miyano, Crystal structure of rhodopsin: A G protein-coupled receptor, Science, 289 (**2000**) 739-745.
[43] A. Lavecchia, S. Cosconati, E. Novellino, Architecture of the human urotensin II receptor: comparison of the binding domains of peptide and non-peptide urotensin II agonists, J Med Chem, 48 (**2005**) 2480-2492.
[44] B.J. Holleran, M.E. Beaulieu, C.D. Proulx, P. Lavigne, E. Escher, R. Leduc, Photolabelling the urotensin II receptor reveals distinct agonist- and partial-agonist-binding sites, Biochem J, 402 (**2007**) 51-61.

[45] D.S. Goodsell, G.M. Morris, A.J. Olson, Automated docking of flexible ligands: applications of AutoDock, J Mol Recognit, 9 (**1996**) 1-5.
[46] G.M. Morris, D.S. Goodsell, R.S. Halliday, R. Huey, W.E. Hart, R.K. Belew, A.J. Olson, Automated docking using a Lamarckian genetic algorithm and an empirical binding free energy function, J Comput Chem, 19 (**1998**) 1639-1662.
[47] R. Huey, G.M. Morris, A.J. Olson, D.S. Goodsell, A semiempirical free energy force field with charge-based desolvation, J Comput Chem, 28 (**2007**) 1145-1152.
[48] C.B. Fowler, I.D. Pogozheva, A.L. Lomize, H. LeVine, 3rd, H.I. Mosberg, Complex of an active mu-opioid receptor with a cyclic peptide agonist modeled from experimental constraints, Biochemistry, 43 (**2004**) 15796-15810.
[49] E. Marzola, V. Camarda, M. Batuwangala, D.G. Lambert, G. Calo, R. Guerrini, C. Trapella, D. Regoli, R. Tomatis, S. Salvadori, Structure-activity relationship study of position 4 in the urotensin-II receptor ligand U-II(4-11), Peptides, 29 (**2008**) 674-679.
[50] L. Moroder, R. Romano, W. Guba, D.F. Mierke, H. Kessler, C. Delporte, J. Winand, J. Christophe, New evidence for a membrane-bound pathway in hormone receptor binding, Biochemistry, 32 (**1993**) 13551-13559.
[51] D.F. Sargent, R. Schwyzer, Membrane Lipid Phase as Catalyst for Peptide-Receptor Interactions. , Proc Natl Acad Sci U S A, 83 (**1986**).
[52] B. Gysin, R. Schwyzer, Head group and structure specific interactions of enkephalins and dynorphin with liposomes: investigation by hydrophobic photolabeling, Arch Biochem Biophys, 225 (**1983**) 467-474.
[53] M. Dhanasekaran, M.M. Palian, I. Alves, L. Yeomans, C.M. Keyari, P. Davis, E.J. Bilsky, R.D. Egleton, H.I. Yamamura, N.E. Jacobsen, G. Tollin, V.J. Hruby, F. Porreca, R. Polt, Glycopeptides related to beta-endorphin adopt helical amphipathic conformations in the presence of lipid bilayers, J Am Chem Soc, 127 (**2005**) 5435-5448.
[54] R.D. Egleton, E.J. Bilsky, G. Tollin, M. Dhanaseharan, J. Lowery, I. Alves, P. Davis, F. Porreca, Y.H. I., L. Yeomans, C.M. Keyari, R. Polt, Biousian glycopeptides penetrate the blood-brain-barrier, Tetrahedron Asymmetry 16 (**2005**) 65-75.
[55] T. Yamamoto, P. Nair, N.E. Jacobsen, P. Davis, S.W. Ma, E. Navratilova, S. Moye, J. Lai, H.I. Yamamura, T.W. Vanderah, F. Porreca, V.J. Hruby, The importance of micelle-bound states for the bioactivities of bifunctional peptide derivatives for delta/mu opioid receptor agonists and neurokinin 1 receptor antagonists, J Med Chem, 51 (**2008**) 6334-6347.
[56] E. Lescot, J. Sopkova-de Oliveira Santos, N. Colloc'h, J. Rodrigo, I. Milazzo-Segalas, R. Bureau, S. Rault, Three-dimensional model of the human urotensin-II receptor: docking of human urotensin-II and nonpeptide antagonists in the binding site and comparison with an antagonist pharmacophore model, Proteins, 73 (**2008**) 173-184.
[57] V. Cherezov, D.M. Rosenbaum, M.A. Hanson, S.G. Rasmussen, F.S. Thian, T.S. Kobilka, H.J. Choi, P. Kuhn, W.I. Weis, B.K. Kobilka, R.C. Stevens, High-resolution crystal structure of an engineered human beta2-adrenergic G protein-coupled receptor, Science, 318 (**2007**) 1258-1265.
[58] T. Warne, M.J. Serrano-Vega, J.G. Baker, R. Moukhametzianov, P.C. Edwards, R. Henderson, A.G. Leslie, C.G. Tate, G.F. Schertler, Structure of a beta1-adrenergic G-protein-coupled receptor, Nature, 454 (**2008**) 486-491.

[59] V.P. Jaakola, M.T. Griffith, M.A. Hanson, V. Cherezov, E.Y. Chien, J.R. Lane, A.P. Ijzerman, R.C. Stevens, The 2.6 angstrom crystal structure of a human A2A adenosine receptor bound to an antagonist, Science, 322 (**2008**) 1211-1217.
[60] S. Boivin, L. Guilhaudis, I. Milazzo, H. Oulyadi, D. Davoust, A. Fournier, Characterization of urotensin-II receptor structural domains involved in the recognition of U-II, URP, and urantide, Biochemistry, 45 (**2006**) 5993-6002.
[61] S. Boivin, I. Segalas-Milazzo, L. Guilhaudis, H. Oulyadi, A. Fournier, D. Davoust, Solution structure of urotensin-II receptor extracellular loop III and characterization of its interaction with urotensin-II, Peptides, 29 (**2008**) 700-710.
[62] A.A. Boucard, S.S. Sauve, G. Guillemette, E. Escher, R. Leduc, Photolabelling the rat urotensin II/GPR14 receptor identifies a ligand-binding site in the fourth transmembrane domain, Biochem J, 370 (**2003**) 829-838.
[63] R. Guerrini, V. Camarda, E. Marzola, M. Arduin, G. Calo, M. Spagnol, A. Rizzi, S. Salvadori, D. Regoli, Structure-activity relationship study on human urotensin II, J Pept Sci, 11 (**2005**) 85-90.
[64] V. Camarda, M. Spagnol, W. Song, R. Vergura, A.L. Roth, J.P. Thompson, D.J. Rowbotham, R. Guerrini, E. Marzola, S. Salvadori, P. Cavanni, D. Regoli, S.A. Douglas, D.G. Lambert, G. Calo, In vitro and in vivo pharmacological characterization of the novel UT receptor ligand [Pen5,DTrp7,Dab8]urotensin II(4-11) (UFP-803), Br J Pharmacol, 147 (**2006**) 92-100.
[65] A. Misika, V.J. Hruby, Optimization of Disulfide Bond Formation, Pol J Chem, 68 (**1994**) 893-899.
[66] T.P. Kenakin, Competitive antagonism, 3rd ed. Lippincott-Raven Press, Philadelphia, **1997**.
[67] Y. Cheng, W.H. Prusoff, Relationship Between the Inhibition Constant (Ki) and the Concentration of Inhibitor which Causes 50 per Cent Inhibition (I50) of an Enzymatic Reaction, Biochem Pharmacol, 22 (**1973**) 3099-3108

[68] T.L. Hwang, A.J. Shaka, Water suppression that works. Excitation sculpting using arbitrary wave-forms and pulsed-field gradients, J Magn Reson, 112 (**1995**) 275-279.
[69] L. Mueller, P. E: COSY, a simple alternative to E. COSY, J Magn Reson, 72 (**1987**) 191-196.
[70] D.J. States, R.A. Haberkorn, D.J. Ruben, A two-dimensional nuclear overhauser experiment with pure absorption phase in four quadrants, J Magn Reson, 48 (**1982**) 286-292.
[71] P. Guntert, C. Mumenthaler, K. Wuthrich, Torsion angle dynamics for NMR structure calculation with the new program DYANA, J Mol Biol, 273 (**1997**) 283-298.
[72] R. Koradi, M. Billeter, K. Wuthrich, MOLMOL: a program for display and analysis of macromolecular structures, J Mol Graph, 14 (**1996**) 51-55, 29-32.
[73] J.R. Maple, U. Dinur, A.T. Hagler, Derivation of force fields for molecular mechanics and dynamics from ab initio energy surfaces, Proc Natl Acad Sci U S A, 85 (**1988**) 5350-5354.
[74] R.A. Laskowski, M.W. MacArthur, D.S. Moss, T.J. M., PROCHECK: A Program to Check the Stereochemical Quality of Protein Structures. , J Appl Crystallogr, 26 (**1993**) 283-291.
[75] A.L. Morris, M.W. MacArthur, E.G. Hutchinson, J.M. Thornton, Stereochemical quality of protein structure coordinates, Proteins, 12 (**1992**) 345-364.

[76] E.F. Pettersen, T.D. Goddard, C.C. Huang, G.S. Couch, D.M. Greenblatt, E.C. Meng, T.E. Ferrin, UCSF Chimera--a visualization system for exploratory research and analysis, J Comput Chem, (**2004**) 1605-1612.
[77] V. Chhajlani, J.E. Wikberg, Molecular cloning and expression of the human melanocyte stimulating hormone receptor cDNA, FEBS Lett, 309 (**1992**) 417-420.
[78] K.G. Mountjoy, L.S. Robbins, M.T. Mortrud, R.D. Cone, The cloning of a family of genes that encode the melanocortin receptors, Science, 257 (**1992**) 1248-1251.
[79] L. Roselli-Rehfuss, K.G. Mountjoy, L.S. Robbins, M.T. Mortrud, M.J. Low, J.B. Tatro, M.L. Entwistle, R.B. Simerly, R.D. Cone, Identification of a receptor for gamma melanotropin and other proopiomelanocortin peptides in the hypothalamus and limbic system, Proc Natl Acad Sci U S A, 90 (**1993**) 8856-8860.
[80] K.G. Mountjoy, M.T. Mortrud, M.J. Low, R.B. Simerly, R.D. Cone, Localization of the melanocortin-4 receptor (MC4-R) in neuroendocrine and autonomic control circuits in the brain, Mol Endocrinol, 8 (**1994**) 1298-1308.
[81] I. Gantz, Y. Konda, T. Tashiro, Y. Shimoto, H. Miwa, G. Munzert, S.J. Watson, J. DelValle, T. Yamada, Molecular cloning of a novel melanocortin receptor, J Biol Chem, 268 (**1993**) 8246-8250.
[82] I. Gantz, H. Miwa, Y. Konda, Y. Shimoto, T. Tashiro, S.J. Watson, J. DelValle, T. Yamada, Molecular cloning, expression, and gene localization of a fourth melanocortin receptor, J Biol Chem, 268 (**1993**) 15174-15179.
[83] I. Gantz, Y. Shimoto, Y. Konda, H. Miwa, C.J. Dickinson, T. Yamada, Molecular cloning, expression, and characterization of a fifth melanocortin receptor, Biochem Biophys Res Commun, 200 (**1994**) 1214-1220.
[84] R.D. Cone, The Melanocortin Receptors, Human Press, Totowa NJ, **2000**.
[85] L.E. Pritchard, A.V. Turnbull, A. White, Pro-opiomelanocortin processing in the hypothalamus: impact on melanocortin signalling and obesity, J Endocrinol, 172 (**2002**) 411-421.
[86] H.B. Schioth, V. Chhajlani, R. Muceniece, V. Klusa, J.E. Wikberg, Major pharmacological distinction of the ACTH receptor from other melanocortin receptors, Life Sci, 59 (**1996**) 797-801.
[87] T.K. Sawyer, P.J. Sanfilippo, V.J. Hruby, M.H. Engel, C.B. Heward, J.B. Burnett, M.E. Hadley, 4-Norleucine, 7-D-phenylalanine-alpha-melanocyte-stimulating hormone: a highly potent alpha-melanotropin with ultralong biological activity, Proc Natl Acad Sci U S A, 77 (**1980**) 5754-5758.
[88] F. Al-Obeidi, V.J. Hruby, A.M. Castrucci, M.E. Hadley, Design of potent linear alpha-melanotropin 4-10 analogues modified in positions 5 and 10, J Med Chem, 32 (**1989**) 174-179.
[89] C. Haskell-Luevano, G. Nikiforovich, S.D. Sharma, Y.K. Yang, C. Dickinson, V.J. Hruby, I. Gantz, Biological and conformational examination of stereochemical modifications using the template melanotropin peptide, Ac-Nle-c[Asp-His-Phe-Arg-Trp-Ala-Lys]-NH2, on human melanocortin receptors, J Med Chem, 40 (**1997**) 1738-1748.
[90] D. Lu, D. Willard, I.R. Patel, S. Kadwell, L. Overton, T. Kost, M. Luther, W. Chen, R.P. Woychik, W.O. Wilkison, et al., Agouti protein is an antagonist of the melanocyte-stimulating-hormone receptor, Nature, 371 (**1994**) 799-802.
[91] M.M. Ollmann, B.D. Wilson, Y.K. Yang, J.A. Kerns, Y. Chen, I. Gantz, G.S. Barsh, Antagonism of central melanocortin receptors in vitro and in vivo by agouti-related protein, Science, 278 (**1997**) 135-138.

[92] J.E. Wikberg, Melanocortin receptors: perspectives for novel drugs, Eur J Pharmacol, 375 (**1999**) 295-310.
[93] H. Wessells, K. Fuciarelli, J. Hansen, M.E. Hadley, V.J. Hruby, R. Dorr, N. Levine, Synthetic melanotropic peptide initiates erections in men with psychogenic erectile dysfunction: double-blind, placebo controlled crossover study, J Urol, 160 (**1998**) 389-393.
[94] S. Chaki, S. Okuyama, Involvement of melanocortin-4 receptor in anxiety and depression, Peptides, 26 (**2005**) 1952-1964.
[95] S.C. Benoit, M.W. Schwartz, J.L. Lachey, M.M. Hagan, P.A. Rushing, K.A. Blake, K.A. Yagaloff, G. Kurylko, L. Franco, W. Danhoo, R.J. Seeley, A novel selective melanocortin-4 receptor agonist reduces food intake in rats and mice without producing aversive consequences, J Neurosci, 20 (**2000**) 3442-3448.
[96] N. Xi, The MC4 Receptor as a drug discovery target, Drugs Future, 31 (**2006**) 163-173.
[97] W. Fan, B.A. Boston, R.A. Kesterson, V.J. Hruby, R.D. Cone, Role of melanocortinergic neurons in feeding and the agouti obesity syndrome, Nature, 385 (**1997**) 165-168.
[98] H. Wessells, D. Gralnek, R. Dorr, V.J. Hruby, M.E. Hadley, N. Levine, Effect of an alpha-melanocyte stimulating hormone analog on penile erection and sexual desire in men with organic erectile dysfunction, Urology, 56 (**2000**) 641-646.
[99] A.V. Vergoni, A. Bertolini, Role of melanocortins in the central control of feeding, Eur J Pharmacol, 405 (**2000**) 25-32.
[100] L.H. Van der Ploeg, W.J. Martin, A.D. Howard, R.P. Nargund, C.P. Austin, X. Guan, J. Drisko, D. Cashen, I. Sebhat, A.A. Patchett, D.J. Figueroa, A.G. DiLella, B.M. Connolly, D.H. Weinberg, C.P. Tan, O.C. Palyha, S.S. Pong, T. MacNeil, C. Rosenblum, A. Vongs, R. Tang, H. Yu, A.W. Sailer, T.M. Fong, C. Huang, M.R. Tota, R.S. Chang, R. Stearns, C. Tamvakopoulos, G. Christ, D.L. Drazen, B.D. Spar, R.J. Nelson, D.E. MacIntyre, A role for the melanocortin 4 receptor in sexual function, Proc Natl Acad Sci U S A, 99 (**2002**) 11381-11386.
[101] C. Lubrano-Berthelier, M. Cavazos, B. Dubern, A. Shapiro, C.L. Stunff, S. Zhang, F. Picart, C. Govaerts, P. Froguel, P. Bougneres, K. Clement, C. Vaisse, Molecular genetics of human obesity-associated MC4R mutations, Ann N Y Acad Sci, 994 (**2003**) 49-57.
[102] G.S. Yeo, E.J. Lank, I.S. Farooqi, J. Keogh, B.G. Challis, S. O'Rahilly, Mutations in the human melanocortin-4 receptor gene associated with severe familial obesity disrupts receptor function through multiple molecular mechanisms, Hum Mol Genet, 12 (**2003**) 561-574.
[103] Y.X. Tao, D.L. Segaloff, Functional characterization of melanocortin-4 receptor mutations associated with childhood obesity, Endocrinology, 144 (**2003**) 4544-4551.
[104] Q. Hong, R.K. Bakshi, J. Dellureficio, S. He, Z. Ye, P.H. Dobbelaar, I.K. Sebhat, L. Guo, J. Liu, T. Jian, R. Tang, R.N. Kalyani, T. Macneil, A. Vongs, C.I. Rosenblum, D.H. Weinberg, Q. Peng, C. Tamvakopoulos, R.R. Miller, R.A. Stearns, D. Cashen, W.J. Martin, A.S. Chen, J.M. Metzger, H.Y. Chen, A.M. Strack, T.M. Fong, E. Maclntyre, L.H. Van der Ploeg, M.J. Wyvratt, R.P. Nargund, Optimization of privileged structures for selective and potent melanocortin subtype-4 receptor ligands, Bioorg Med Chem Lett, 20 (**2010**) 4483-4486.
[105] B.E. Wisse, M.W. Schwartz, D.E. Cummings, Melanocortin signaling and anorexia in chronic disease states, Ann N Y Acad Sci, 994 (**2003**) 275-281.

[106] V.J. Hruby, D. Lu, S.D. Sharma, A.L. Castrucci, R.A. Kesterson, F.A. al-Obeidi, M.E. Hadley, R.D. Cone, Cyclic lactam alpha-melanotropin analogues of Ac-Nle4-cyclo[Asp5, D-Phe7,Lys10] alpha-melanocyte-stimulating hormone-(4-10)-NH2 with bulky aromatic amino acids at position 7 show high antagonist potency and selectivity at specific melanocortin receptors, J Med Chem, 38 (**1995**) 3454-3461.
[107] M. Chen, M. Cai, D. McPherson, V. Hruby, C.M. Harmon, Y. Yang, Contribution of the transmembrane domain 6 of melanocortin-4 receptor to peptide [Pro5, DNal (2')8]-gamma-MSH selectivity, Biochem Pharmacol, 77 (**2009**) 114-124.
[108] F. Al-Obeidi, S.D. O'Connor, C. Job, V.J. Hruby, B.M. Pettitt, NMR and quenched molecular dynamics studies of superpotent linear and cyclic alpha-melanotropins, Journal of Peptide Research, 51 (**1998**) 420-431.
[109] J. Ying, K.E. Kover, X. Gu, G. Han, D.B. Trivedi, M.J. Kavarana, V.J. Hruby, Solution structures of cyclic melanocortin agonists and antagonists by NMR, Biopolymers, 71 (**2003**) 696-716.
[110] D.S. Wishart, B.D. Sykes, F.M. Richards, The chemical shift index: a fast and simple method for the assignment of protein secondary structure through NMR spectroscopy, Biochemistry, 31 (**1992**) 1647-1651.
[111] A.L. Fink, Protein folding in cryosolvents and at subzero temperatures, Methods Enzymol, 131 (**1986**) 173-185.
[112] K.G.R. Pachler, Nuclear magnetic resonance study of some alpha-amino acids–II. Rotational isomerism, Spectrochim Acta, 20 (**1964**) 581-587.
[113] M.T. Cung, M. Marraud, Conformational dependence of the vicinal proton coupling constant for the Calpha-Cbeta bond in peptides, Biopolymers, 21 (**1982**) 953-967.
[114] I.D. Pogozheva, B.X. Chai, A.L. Lomize, T.M. Fong, D.H. Weinberg, R.P. Nargund, M.W. Mulholland, I. Gantz, H.I. Mosberg, Interactions of human melanocortin 4 receptor with nonpeptide and peptide agonists, Biochemistry, 44 (**2005**) 11329-11341.
[115] B.X. Chai, I.D. Pogozheva, Y.M. Lai, J.Y. Li, R.R. Neubig, H.I. Mosberg, I. Gantz, Receptor-antagonist interactions in the complexes of agouti and agouti-related protein with human melanocortin 1 and 4 receptors, Biochemistry, 44 (**2005**) 3418-3431.
[116] K. Konvicka, F. Campagne, H. Weinstein, Interactive construction of residue-based diagrams of proteins: the RbDe web service, Protein Eng, 13 (**2000**) 395-396.
[117] S.F. Sousa, P.A. Fernandes, M.J. Ramos, Protein-ligand docking: current status and future challenges, Proteins, 65 (**2006**) 15-26.
[118] Y. Yang, M. Chen, Y. Lai, I. Gantz, K.E. Georgeson, C.M. Harmon, Molecular determinants of human melanocortin-4 receptor responsible for antagonist SHU9119 selective activity, J Biol Chem, 277 (**2002**) 20328-20335.
[119] Y.K. Yang, T.M. Fong, C.J. Dickinson, C. Mao, J.Y. Li, M.R. Tota, R. Mosley, L.H. Van Der Ploeg, I. Gantz, Molecular determinants of ligand binding to the human melanocortin-4 receptor, Biochemistry, 39 (**2000**) 14900-14911.
[120] C. Haskell-Luevano, R.D. Cone, E.K. Monck, Y.P. Wan, Structure activity studies of the melanocortin-4 receptor by in vitro mutagenesis: identification of agouti-related protein (AGRP), melanocortin agonist and synthetic peptide antagonist interaction determinants, Biochemistry, 40 (**2001**) 6164-6179.
[121] K. Hogan, S. Peluso, S. Gould, I. Parsons, D. Ryan, L. Wu, I. Visiers, Mapping the binding site of melanocortin 4 receptor agonists: a hydrophobic

pocket formed by I3.28(125), I3.32(129), and I7.42(291) is critical for receptor activation, J Med Chem, 49 (**2006**) 911-922.
[122] M. Chen, M. Cai, C.J. Aprahamian, K.E. Georgeson, V. Hruby, C.M. Harmon, Y. Yang, Contribution of the conserved amino acids of the melanocortin-4 receptor in [corrected] [Nle4,D-Phe7]-alpha-melanocyte-stimulating [corrected] hormone binding and signaling, J Biol Chem, 282 (**2007**) 21712-21719.
[123] J. Oosterom, W.A. Nijenhuis, W.M. Schaaper, J. Slootstra, R.H. Meloen, W.H. Gispen, J.P. Burbach, R.A. Adan, Conformation of the core sequence in melanocortin peptides directs selectivity for the melanocortin MC3 and MC4 receptors, J Biol Chem, 274 (**1999**) 16853-16860.
[124] C. Haskell-Luevano, S. Hendrata, C. North, T.K. Sawyer, M.E. Hadley, V.J. Hruby, C. Dickinson, I. Gantz, Discovery of prototype peptidomimetic agonists at the human melanocortin receptors MC1R and MC4R, J Med Chem, 40 (**1997**) 2133-2139.
[125] B.A. Fleck, N. Ling, C. Chen, Substituted NDP-MSH peptides paired with mutant melanocortin-4 receptors demonstrate the role of transmembrane 6 in receptor activation, Biochemistry, 46 (**2007**) 10473-10483.
[126] H.J. Dyson, M. Rance, R.A. Houghten, P.E. Wright, R.A. Lerner, Folding of immunogenic peptide fragments of proteins in water solution. II. The nascent helix, J Mol Biol, 201 (**1988**) 201-217.
[127] L. Doedens, F. Opperer, M. Cai, J.G. Beck, M. Dedek, E. Palmer, V.J. Hruby, H. Kessler, Multiple N-methylation of MT-II backbone amide bonds leads to melanocortin receptor subtype hMC1R selectivity: pharmacological and conformational studies, J Am Chem Soc, 132 (**2010**) 8115-8128.
[128] S.W. Lin, T.P. Sakmar, Specific tryptophan UV-absorbance changes are probes of the transition of rhodopsin to its active state, Biochemistry, 35 (**1996**) 11149-11159.
[129] K.L. Chapman, G.K. Kinsella, A. Cox, D. Donnelly, J.B. Findlay, Interactions of the melanocortin-4 receptor with the peptide agonist NDP-MSH, J Mol Biol, 401 (**2010**) 433-450.
[130] J.H. Park, P. Scheerer, K.P. Hofmann, H.W. Choe, O.P. Ernst, Crystal structure of the ligand-free G-protein-coupled receptor opsin, Nature, 454 (**2008**) 183-187.
[131] P. Scheerer, J.H. Park, P.W. Hildebrand, Y.J. Kim, N. Krauss, H.W. Choe, K.P. Hofmann, O.P. Ernst, Crystal structure of opsin in its G-protein-interacting conformation, Nature, 455 (**2008**) 497-502.
[132] M.A. Bednarek, M.V. Silva, B. Arison, T. MacNeil, R.N. Kalyani, R.R. Huang, D.H. Weinberg, Structure-function studies on the cyclic peptide MT-II, lactam derivative of alpha-melanotropin, Peptides, 20 (**1999**) 401-409.
[133] M.A. Bednarek, T. Macneil, R.N. Kalyani, R. Tang, L.H. Van der Ploeg, D.H. Weinberg, Analogs of MTII, lactam derivatives of alpha-melanotropin, modified at the N-terminus, and their selectivity at human melanocortin receptors 3, 4, and 5, Biochem Biophys Res Commun, 261 (**1999**) 209-213.
[134] R.A. Adan, J. Oosterom, R.F. Toonen, M.V. Kraan, J.P. Burbach, W.H. Gispen, Molecular pharmacology of neural melanocortin receptors, Receptors Channels, 5 (**1997**) 215-223.
[135] M. Chen, C.J. Aprahamian, A. Celik, K.E. Georgeson, W.T. Garvey, C.M. Harmon, Y. Yang, Molecular characterization of human melanocortin-3 receptor ligand-receptor interaction, Biochemistry, 45 (**2006**) 1128-1137.

[136] M.K. Cho, C.J. Lee, C.H. Lee, S.Z. Li, S.K. Lim, J.H. Baik, W. Lee, Structure and function of the potent cyclic and linear melanocortin analogues, J Struct Biol, 150 (**2005**) 300-308.
[137] S. Lim, S. Li, C. Lee, C. Yoon, J. Baik, W. Lee, Minimization of MC1R selectivity by modification of the core structure of alpha-MSH-ND, Chem Biol, 8 (**2001**) 857-870.
[138] Z. Xiang, I.D. Pogozheva, N.B. Sorenson, A.M. Wilczynski, J.R. Holder, S.A. Litherland, W.J. Millard, H.I. Mosberg, C. Haskell-Luevano, Peptide and small molecules rescue the functional activity and agonist potency of dysfunctional human melanocortin-4 receptor polymorphisms, Biochemistry, 46 (**2007**) 8273-8287.
[139] C.J. Lee, J.H. Yun, S.K. Lim, W. Lee, Solution structures and molecular interactions of selective melanocortin receptor antagonists, Mol Cells, 30 (**2010**) 551-556.
[140] X. Yang, Z. Wang, W. Dong, L. Ling, H. Yang, R. Chen, Modeling and docking of the three-dimensional structure of the human melanocortin 4 receptor, J Protein Chem, 22 (**2003**) 335-344.
[141] A. Wilczynski, X.S. Wang, R.M. Bauzo, Z. Xiang, A.M. Shaw, W.J. Millard, N.G. Richards, A.S. Edison, C. Haskell-Luevano, Structural characterization and pharmacology of a potent (Cys101-Cys119, Cys110-Cys117) bicyclic agouti-related protein (AGRP) melanocortin receptor antagonist, J Med Chem, 47 (**2004**) 5662-5673.
[142] A. Wilczynski, X.S. Wang, C.G. Joseph, Z. Xiang, R.M. Bauzo, J.W. Scott, N.B. Sorensen, A.M. Shaw, W.J. Millard, N.G. Richards, C. Haskell-Luevano, Identification of putative agouti-related protein(87-132)-melanocortin-4 receptor interactions by homology molecular modeling and validation using chimeric peptide ligands, J Med Chem, 47 (**2004**) 2194-2207.
[143] E.G. Hutchinson, J.M. Thornton, PROMOTIF--a program to identify and analyze structural motifs in proteins, Protein Sci, 5 (**1996**) 212-220.
[144] R. Burgus, P. Brazeau, W.W. Vale, Isolation and determination of the primary structure of somatostatin (a somatotropin release inhibiting factor) of bovin hypothalamic origin, Advances in Human Growth Hormone Research, U. S. Government Printing Office, DHEW, Publ No. (NIH), 74-612 (**1973**) 144-158.
[145] G. Weckbecker, I. Lewis, R. Albert, H.A. Schmid, D. Hoyer, C. Bruns, Opportunities in somatostatin research: biological, chemical and therapeutic aspects, Nat Rev Drug Discov, 2 (**2003**) 999-1017.
[146] J. Erchegyi, R. Cescato, C.R. Grace, B. Waser, V. Piccand, D. Hoyer, R. Riek, J.E. Rivier, J.C. Reubi, Novel, potent, and radio-iodinatable somatostatin receptor 1 (sst1) selective analogues, J Med Chem, 52 (**2009**) 2733-2746.
[147] C.R. Grace, J. Erchegyi, S.C. Koerber, J.C. Reubi, J. Rivier, R. Riek, Novel sst2-selective somatostatin agonists. Three-dimensional consensus structure by NMR, J Med Chem, 49 (**2006**) 4487-4496.
[148] M. Gairi, P. Saiz, S. Madurga, X. Roig, J. Erchegyi, S.C. Koerber, J.C. Reubi, J.E. Rivier, E. Giralt, Conformational analysis of a potent SSTR3-selective somatostatin analogue by NMR in water solution, J Pept Sci, 12 (**2006**) 82-91.
[149] C.R. Grace, S.C. Koerber, J. Erchegyi, J.C. Reubi, J. Rivier, R. Riek, Novel sst(4)-selective somatostatin (SRIF) agonists. 4. Three-dimensional consensus structure by NMR, J Med Chem, 46 (**2003**) 5606-5618.
[150] W. Bauer, U. Briner, W. Dopfener, R. Haller, R. Huguenin, P. Marbach, T.J. Petcher, J. Pless, SMS 201-995: a very potent and selective analogue of somatostatin with prolonged action, Life Sci, 31 (**1982**) 1133-1140.

[151] M. Ginj, J.S. Schmitt, J. Chen, B. Waser, J.C. Reubi, M. de Jong, S. Schulz, H.R. Maecke, Design, synthesis, and biological evaluation of somatostatin-based radiopeptides, Chem Biol, 13 (**2006**) 1081-1090.
[152] M. Ginj, H. Zhang, B. Waser, R. Cescato, D. Wild, X. Wang, J. Erchegyi, J. Rivier, H.R. Macke, J.C. Reubi, Radiolabeled somatostatin receptor antagonists are preferable to agonists for in vivo peptide receptor targeting of tumors, Proc Natl Acad Sci U S A, 103 (**2006**) 16436-16441.
[153] M. de Jong, W.A. Breeman, D.J. Kwekkeboom, R. Valkema, E.P. Krenning, Tumor imaging and therapy using radiolabeled somatostatin analogues, Acc Chem Res, 42 (**2009**) 873-880.
[154] J. Fichna, A. Janecka, Synthesis of target-specific radiolabeled peptides for diagnostic imaging, Bioconjug Chem, 14 (**2003**) 3-17.
[155] A. Carotenuto, D. D'Addona, E. Rivalta, M. Chelli, A.M. Papini, P. Rovero, M. Ginanneschi, Synthesis of a dicarba-analogue of octreotide keeping the type II' beta-turn of the farmacophore in water solution, Lett Org Chem, 2 (**2005**) 274-279.
[156] D. D'Addona, A. Carotenuto, E. Novellino, V. Piccand, J.C. Reubi, A. Di Cianni, F. Gori, A.M. Papini, M. Ginanneschi, Novel sst5-selective somatostatin dicarba-analogues: synthesis and conformation-affinity relationships, J Med Chem, 51 (**2008**) 512-520.
[157] F. Barragan, V. Moreno, V. Marchan, Solid-phase synthesis and DNA binding studies of dichloroplatinum(ii) conjugates of dicarba analogues of octreotide as new anticancer drugs, Chem Commun (Camb), (**2009**) 4705-4707.
[158] B.H. Arison, R. Hirschmann, D.F. Veber, Inferences about the conformation of somatostatin at a biologic receptor based on NMR studies, Bioorg Chem, 7 (**1978**) 447-451.
[159] D. Wild, J.S. Schmitt, M. Ginj, H.R. Macke, B.F. Bernard, E. Krenning, M. De Jong, S. Wenger, J.C. Reubi, DOTA-NOC, a high-affinity ligand of somatostatin receptor subtypes 2, 3 and 5 for labelling with various radiometals, Eur J Nucl Med Mol Imaging, 30 (**2003**) 1338-1347.
[160] G. Melacini, Q. Zhu, M. Goodman, Multiconformational NMR analysis of sandostatin (octreotide): equilibrium between beta-sheet and partially helical structures, Biochemistry, 36 (**1997**) 1233-1241.
[161] J.D. Tyndall, B. Pfeiffer, G. Abbenante, D.P. Fairlie, Over one hundred peptide-activated G protein-coupled receptors recognize ligands with turn structure, Chem Rev, 105 (**2005**) 793-826.
[162] G. Melacini, Q. Zhu, G. Osapay, M. Goodman, A refined model for the somatostatin pharmacophore: conformational analysis of lanthionine-sandostatin analogs, J Med Chem, 40 (**1997**) 2252-2258.
[163] S.F. Brady, W.J. Paleveda, B.H. Arison, R. Saperstein, E.J. Brady, K. Raynor, T. Reisine, D.F. Veber, R.M. Freidinger, Approaches to peptidomimetics which serve as surrogates for the cis amide bond: novel disulfide-constrained bicyclic hexapeptide analogs of somatostatin, Tetrahedron, 49 3449-3466.
[164] I. Lewis, W. Bauer, R. Albert, N. Chandramouli, J. Pless, G. Weckbecker, C. Bruns, A novel somatostatin mimic with broad somatotropin release inhibitory factor receptor binding and superior therapeutic potential, J Med Chem, 46 (**2003**) 2334-2344.
[165] E. Pohl, A. Heine, G.M. Sheldrick, Z. Dauter, K.S. Wilson, J. Kallen, W. Huber, P.J. Pfaffli, Structure of octreotide, a somatostatin analogue, Acta Crystallogr D Biol Crystallogr, 51 (**1995**) 48-59.

[166] G. Interlandi, Backbone conformations and side chain flexibility of two somatostatin mimics investigated by molecular dynamics simulations, Proteins, 75 (**2009**) 659-670.
[167] J.C. Reubi, B. Waser, J.C. Schaer, J.A. Laissue, Somatostatin receptor sst1-sst5 expression in normal and neoplastic human tissues using receptor autoradiography with subtype-selective ligands, Eur J Nucl Med, 28 (**2001**) 836-846.
[168] M.C. Zatelli, E. degli Umberti, The significance of new somatostatin analogs as therapeutic agents Curr Opin Investig Drugs, 10 (**2009**) 1025-1031.
[169] A. Ben-Shlomo, S. Melmed, Pasireotide--a somatostatin analog for the potential treatment of acromegaly, neuroendocrine tumors and Cushing's disease, IDrugs, 10 (**2007**) 885-895.
[170] R. Cescato, K.A. Loesch, B. Waser, H.R. Macke, J.E. Rivier, J.C. Reubi, A. Schonbrunn, Agonist-biased signaling at the sst2A receptor: the multi-somatostatin analogs KE108 and SOM230 activate and antagonize distinct signaling pathways, Mol Endocrinol, 24 (**2010**) 240-249.
[171] P. Antunes, M. Ginj, M.A. Walter, J. Chen, J.C. Reubi, H.R. Maecke, Influence of different spacers on the biological profile of a DOTA-somatostatin analogue, Bioconjug Chem, 18 (**2007**) 84-92.
[172] H.P. Nothacker, Z. Wang, A.M. McNeill, Y. Saito, S. Merten, B. O'Dowd, S.P. Duckles, O. Civelli, Identification of the natural ligand of an orphan G-protein-coupled receptor involved in the regulation of vasoconstriction, Nat Cell Biol, 1 (**1999**) 383-385.
[173] M.M. Malagon, M. Molina, M.D. Gahete, M. Duran-Prado, A.J. Martinez-Fuentes, F.J. Alcain, M.C. Tonon, J. Leprince, H. Vaudry, J.P. Castano, R. Vazquez-Martinez, Urotensin II and urotensin II-related peptide activate somatostatin receptor subtypes 2 and 5, Peptides, 29 (**2008**) 711-720.
[174] J.C. Reubi, J.C. Schar, B. Waser, S. Wenger, A. Heppeler, J.S. Schmitt, H.R. Macke, Affinity profiles for human somatostatin receptor subtypes SST1-SST5 of somatostatin radiotracers selected for scintigraphic and radiotherapeutic use, Eur J Nucl Med, 27 (**2000**) 273-282.
[175] R. Cescato, J. Erchegyi, B. Waser, V. Piccand, H.R. Maecke, J.E. Rivier, J.C. Reubi, Design and in vitro characterization of highly sst2-selective somatostatin antagonists suitable for radiotargeting, J Med Chem, 51 (**2008**) 4030-4037.
[176] V.T. De Vita, S. Hellman, S.A. Rosenberg, Cancer: Principles and Practice of Oncology, 6th ed., Lippincott, Williams and Wilkins, Philadelphia, PA, **2001**.
[177] J.H. Doroshow, Anthracyclines and anthracenediones. In. Cancer chemotherapy and biotherapy: principles and practice, Lippincott, Williams and Wilkins, Philadelphia, PA, **2001**.
[178] J.W. Lown, Anthracycline and anthraquinone anticancer agents: current status and recent developments, Pharmacol Ther, 60 (**1993**) 185-214.
[179] M. Binaschi, M. Bigioni, A. Cipollone, C. Rossi, C. Goso, C.A. Maggi, G. Capranico, F. Animati, Anthracyclines: selected new developments, Curr Med Chem Anticancer Agents, 1 (**2001**) 113-130.
[180] J.T. Thigpen, Innovations in anthracycline therapy: overview, Community Oncol., 2 (**2005**) 3-7.
[181] R. Martinez, L. Chacon-Garcia, The search of DNA-intercalators as antitumoral drugs: what it worked and what did not work, Curr Med Chem, 12 (**2005**) 127-151.

[182] R.D. Baird, S.B. Kaye, Drug resistance reversal--are we getting closer?, Eur J Cancer, 39 (**2003**) 2450-2461.
[183] R. Krishna, L.D. Mayer, Multidrug resistance (MDR) in cancer. Mechanisms, reversal using modulators of MDR and the role of MDR modulators in influencing the pharmacokinetics of anticancer drugs, Eur J Pharm Sci, 11 (**2000**) 265-283.
[184] E.M. Leslie, R.G. Deeley, S.P. Cole, Multidrug resistance proteins: role of P-glycoprotein, MRP1, MRP2, and BCRP (ABCG2) in tissue defense, Toxicol Appl Pharmacol, 204 (**2005**) 216-237.
[185] J. Serrano, C.M. Palmeira, D.W. Kuehl, K.B. Wallace, Cardioselective and cumulative oxidation of mitochondrial DNA following subchronic doxorubicin administration, Biochim Biophys Acta, 1411 (**1999**) 201-205.
[186] G. Minotti, P. Menna, E. Salvatorelli, G. Cairo, L. Gianni, Anthracyclines: molecular advances and pharmacologic developments in antitumor activity and cardiotoxicity, Pharmacol Rev, 56 (**2004**) 185-229.
[187] I. Gomez-Monterrey, P. Campiglia, O. Mazzoni, E. Novellino, M.V. Diurno, Cycloaddition reactions of thiazolidine derivatives. An approach to the synthesis of new functionalized heterocyclic systems, Tetrahedron Lett, 42 (**2001**) 5755-5757.
[188] I. Gomez-Monterrey, P. Campiglia, P. Grieco, M.V. Diurno, A. Bolognese, P. La Colla, E. Novellino, New benzo[g]isoquinoline-5,10-diones and dihydrothieno [2,3-b]naphtho-4,9-dione derivatives: Synthesis and biological evaluation as potential antitumoral agents, Bioorgan Med Chem, 11 (**2003**) 3769-3775.
[189] I. Gomez-Monterrey, G. Santelli, P. Campiglia, D. Califano, F. Falasconi, C. Pisano, L. Vesci, T. Lama, P. Grieco, E. Novellino, Synthesis and cytotoxic evaluation of novel spirohydantoin derivatives of the dihydrothieno[2,3-b]naphtho-4,9-dione system, J Med Chem, 48 (**2005**) 1152-1157.
[190] I. Gomez-Monterrey, P. Campiglia, A. Carotenuto, P. Stiuso, A. Bertamino, M. Sala, C. Aquino, P. Grieco, S. Morello, A. Pinto, P. Ianelli, E. Novellino, Spiro[(dihydropyrazin-2,5-dione)-6,3 '-(2 ',3 '-dihydrothieno[2,3-b]naphtho-4 ',9 '-dione)]-based cytotoxic agents: Structure-activity relationship studies on the substituent at N4-position of the diketopiperazine domain, Journal of Medicinal Chemistry, 51 (**2008**) 2924-2932.
[191] I. Gomez-Monterrey, P. Campiglia, A. Carotenuto, D. Califano, C. Pisano, L. Vesci, T. Lama, A. Bertamino, M. Sala, A.M. di Bosco, P. Grieco, E. Novellino, Design, synthesis, and cytotoxic evaluation of a new series of 3-substituted spiro[(dihydropyrazine-2,5-dione)-6,3'-(2',3'-dihydrothieno[2,3-b]naphtho- 4',9'-dione)] derivatives, J Med Chem, 50 (**2007**) 1787-1798.
[192] I. Gomez-Monterrey, P. Campiglia, A. Bertamino, C. Aquino, M. Sala, P. Grieco, A. Dicitore, D. Vanacore, A. Porta, B. Maresca, E. Novellino, P. Stiuso, A novel quinone-based derivative (DTNQ-Pro) induces apoptotic death via modulation of heat shock protein expression in Caco-2 cells, Br J Pharmacol, 160 (**2010**) 931-940.
[193] P. Campiglia, C. Aquino, A. Bertamino, N. De Simone, M. Sala, S. Castellano, M. Santoriello, P. Grieco, E. Novellino, I.M. Gomez-Monterrey, Unprecedented synthesis of a novel amino quinone ring system via oxidative decarboxylation of quinone-based alpha,alpha-amino esters, Org Biomol Chem, 8 (**2010**) 622-627.
[194] Y. Kita, M. Kirihara, J. Sekihachi, R. Okunaka, M. Sasho, S. Mohri, T. Honda, S. Akai, Y. Tamura, K. Shimooka, Synthetic anthracyclines: regiospecific

total synthesis of D-ring thiophene analogues of daunomycin, Chem Pharm Bull (Tokyo), 38 (**1990**) 1836-1843.
[195] A.P. Krapcho, M.E. Petry, M.P. Hacker, Heterosubstituted anthracene-9,10-dione analogues. The synthesis and antitumor evaluation of 5,8-bis[(aminoalkyl)amino]naphtho[2,3-b] thiophene-4,9-diones, J Med Chem, 33 (**1990**) 2651-2655.
[196] M. Rousset, The human colon carcinoma cell lines HT-29 and Caco-2: two in vitro models for the study of intestinal differentiation, Biochimie, 68 (**1986**) 1035-1040.
[197] R. Stierum, M. Gaspari, Y. Dommels, T. Ouatas, H. Pluk, S. Jespersen, J. Vogels, K. Verhoeckx, J. Groten, B. van Ommen, Proteome analysis reveals novel proteins associated with proliferation and differentiation of the colorectal cancer cell line Caco-2, Biochim Biophys Acta, 1650 (**2003**) 73-91.
[198] A.V. Kamath, J.M. Darling, M.E. Movis, Choline uptake in human intestinal Caco2 cells is carrier mediated, J Nutr, 133 (**2003**) 2607-2611.
[199] A.A. Cotter, C. Jewell, K.D. Cashman, The effect of oestrogen and dietary phyto-oestrogens on transepithelial calcium transport in human intestinal-like Caco-2 cells, Br J Nutr, 89 (**2003**) 755-765.
[200] D.A. Gewirtz, A critical evaluation of the mechanisms of action proposed for the antitumor effects of the anthracycline antibiotics adriamycin and daunorubicin, Biochem Pharmacol, 57 (**1999**) 727-741.
[201] K.R. Hande, Topoisomerase II inhibitors, Update Cancer Ther, 3 (**2008**) 13-26.
[202] J.C. Wang, DNA topoisomerases, Annu Rev Biochem, 65 (**1996**) 635-692.
[203] L. Bjergbaek, P. Kingma, I.S. Nielsen, Y. Wang, O. Westergaard, N. Osheroff, A.H. Andersen, Communication between the ATPase and cleavage/religation domains of human topoisomerase IIalpha, J Biol Chem, 275 (**2000**) 13041-13048.
[204] K.D. Bromberg, C. Hendricks, A.B. Burgin, N. Osheroff, Human topoisomerase IIalpha possesses an intrinsic nucleic acid specificity for DNA ligation. Use of 5' covalently activated oligonucleotide substrates to study enzyme mechanism, J Biol Chem, 277 (**2002**) 31201-31206.
[205] N. Osheroff, E.R. Shelton, D.L. Brutlag, DNA topoisomerase II from Drosophila melanogaster. Relaxation of supercoiled DNA, J Biol Chem, 258 (**1983**) 9536-9543.
[206] K.M. Tewey, T.C. Rowe, L. Yang, B.D. Halligan, L.F. Liu, Adriamycin-induced DNA damage mediated by mammalian DNA topoisomerase II, Science, 226 (**1984**) 466-468.
[207] A. Bodley, L.F. Liu, M. Israel, R. Seshadri, Y. Koseki, F.C. Giuliani, S. Kirschenbaum, R. Silber, M. Potmesil, DNA Topoisomerase II-mediated Interaction of Doxorubicin and Daunorubicin Congeners with DNA, Cancer Res, 49 5969-5978.
[208] M. Mayer, B. Meyer, Characterization of ligand binding by saturation transfer difference NMR spectroscopy, Angew Chem Int Ed Engl, 38 (**1999**) 1784-1788.
[209] C. Dalvit, P. Pevarello, M. Tato, M. Veronesi, A. Vulpetti, M. Sundstrom, Identification of compounds with binding affinity to proteins via magnetization transfer from bulk water, J Biomol Nmr, 18 (**2000**) 65-68.
[210] M. Pellecchia, I. Bertini, D. Cowburn, C. Dalvit, E. Giralt, W. Jahnke, T.L. James, S.W. Homans, H. Kessler, C. Luchinat, B. Meyer, H. Oschkinat, J. Peng,

H. Schwalbe, G. Siegal, Perspectives on NMR in drug discovery: a technique comes of age, Nat Rev Drug Discov, 7 (**2008**) 738-745.
[211] S. Di Micco, C. Bassarello, G. Bifulco, R. Riccio, L. Gomez-Paloma, Differential-frequency saturation transfer difference NMR spectroscopy allows the detection of different ligand-DNA binding modes, Angew Chem Int Ed Engl, 45 (**2005**) 224-228.
[212] C.H. Yam, T.K. Fung, R.Y. Poon, Cyclin A in cell cycle control and cancer, Cell Mol Life Sci, 59 (**2002**) 1317-1326.
[213] Q.M. Ding, T.C. Ko, B.M. Evers, Caco-2 intestinal cell differentiation is associated with G1 arrest and suppression of CDK2 and CDK4, Am J Physiol, 275 (**1998**) 1193-1200.
[214] H. Matsumoto, R.H. Erickson, J.R. Gum, M. Yoshioka, E. Gum, Y.S. Kim, Biosynthesis of alkaline phosphatase during differentiation of the human colon cancer cell line Caco-2, Gastroenterology, 98 (**1990**) 1199-1207.
[215] S.W. Carper, J.J. Duffy, E.W. Gerner, Heat shock proteins in thermotolerance and other cellular processes, Cancer Res, 47 (**1987**) 5249-5255.
[216] S.M. Davidson, M.T. Loones, O. Duverger, M. Morange, The developmental expression of small HSP, Prog Mol Subcell Biol, 28 (**2002**) 103-128.
[217] T. L'Ecuyer, Z. Allebban, R. Thomas, R. Vander Heide, Glutathione S-transferase overexpression protects against anthracycline-induced H9C2 cell death, Am J Physiol Heart Circ Physiol, 286 (**2004**) H2057-2064.
[218] G. Corna, P. Santambrogio, G. Minotti, G. Cairo, Doxorubicin paradoxically protects cardiomyocytes against iron-mediated toxicity: role of reactive oxygen species and ferritin, J Biol Chem, 279 (**2004**) 13738-13745.
[219] S. Turakhia, C.D. Venkatakrishnan, K. Dunsmore, H. Wong, P. Kuppusamy, J.L. Zweier, G. Ilangovan, Doxorubicin-induced cardiotoxicity: direct correlation of cardiac fibroblast and H9c2 cell survival and aconitase activity with heat shock protein 27, Am J Physiol Heart Circ Physiol, 293 (**2007**) H3111-3121.
[220] F. Herz, A. Schermer, M. Halwer, L.H. Bogart, Alkaline phosphatase in HT-29, a human colon cancer cell line: influence of sodium butyrate and hyperosmolality, Arch Biochem Biophys, 210 (**1981**) 581-591.
[221] M.M. Bradford, A rapid and sensitive method for the quantitation of microgram quantities of protein utilizing the principle of protein-dye binding, Anal Biochem, 72 (**1976**) 248-254.